THE UNIVERSITY OF CHICAGO

PARTICLE ACCELERATION, PROPAGATION, AND DETECTION: A JOURNEY FROM THE KINETIC STRUCTURE OF PLASMA PHYSICS TO PARTICLE TRANSPORT ON COSMIC SCALES

A DISSERTATION SUBMITTED TO
THE FACULTY OF THE DIVISION OF THE PHYSICAL SCIENCES
IN CANDIDACY FOR THE DEGREE OF
DOCTOR OF PHILOSOPHY

DEPARTMENT OF ASTRONOMY & ASTROPHYSICS

BY
ROSTOM MBAREK

CHICAGO, ILLINOIS
AUGUST 2022

Thanks to Scott and Damiano for their continued support.

Thanks to Samah for keeping me human.

Thanks to my family for staying healthy.

Thanks to soccer for keeping me healthy.

Table of Contents

List of Figures

List of Tables

Abstract

PART I The origin of Ultra-High-Energy Cosmic Rays (UHECRs) and the highest-energy astrophysical neutrinos remains as one of the most prominent unresolved questions in astrophysics. Part of my research can shed light on such phenomena employing a thorough bottom-up approach to understand the spectra of UHECRs, and neutrinos from Active Galactic Nucleus (AGN) jets. My frameworks account for i) particle injection, ii) particle acceleration, iii) spectra of UHECRs, iv) the effects of losses on UHECRs, v) the resulting neutrino spectral features, and vi) potentially lepton cooling and its ensuing radiation spectrum. I study these effects from the large structures of AGN jets employing magnetohydrodynamic (MHD) simulations to the kinetic scales of the plasma relevant for lepton acceleration using Particle-in-Cell (PIC) simulations. My results are backed by original theories that govern particle acceleration.

I developed a framework—agnostic to particle acceleration mechanisms—where trajectories are integrated via standard PIC techniques in relativistic state-of-the-art 3D MHD jet simulations to explore particle energization. I then enhanced this particle acceleration framework by including subgrid scattering (SGS) to characterize the role of small-scale magnetic irregularities that are not captured in MHD simulations. The results I obtain are consistent with current UHECR phenomenology in terms of spectral slope, chemical composition, and anisotropy. I then augment this framework with realistic photon field prescriptions to study

the effects of losses on accelerated particles, and the expected spectrum of neutrinos produced by typical AGN jets. This enabled me to set constraints on the anisotropy and maximum expected neutrino flux from AGN jets. I also study the effect of relativistic asymmetric reconnection on particle energization in relativistic astrophysical systems, such as jets, analytically and with kinetic PIC simulations. In a nutshell, I present the first steps in understanding asymmetric reconnection in the relativistic plasma regime.

PART II I complement these studies by propagating particles employing similar methods in magnetic fields over distances normalized to the particle Larmor radii to examine the impact of the magnetic field and its coherence length on the delay incurred during propagation and deflection angles. While applying these methods to UHECR propagation, we find that the delay incurred by UHECRs on their way to Earth is comparable to AGN duty cycles, making correlation studies with AGNs challenging. These propagation considerations could potentially be important for galactic propagation as they have similar predictive powers for galactic cosmic rays. The confinement time of galactic CRs could also be measured in a more direct manner using CR isotope ratios. I have been heavily involved with the High Energy Light Isotope eXperiment (HELIX) to obtain an observationally motivated value for the confinement time of CRs in the galaxy. HELIX is a magnet spectrometer designed to make measurements of the composition of light CR isotopes. This NASA funded experiment is a set of high-precision particle detectors designed specifically to make measurements of significant isotopic abundance ratios such as Beryllium isotopes in the energy range $\sim$0.2 GeV/n to $\sim$10 GeV/n, a range that is not accessible to any current or planned instrument.

Part I

Cosmic Rays: An Overview

Chapter 1

Basic Cosmic Ray Phenomenology

1.1 What are Cosmic Rays?

In 1912, Viktor Hess noted that electrometers on balloon flights were discharging at a higher rate with increasing altitude. This experiment earned him the discovery of Cosmic Rays (CRs), what he believed to be "extraterrestrial radiation"[1]. The term "ray" in CRs is misleading considering that CRs are not photons, but this term dates back to the days of Robert Millikan who believed CRs to be photons and coined this term.

CRs include all astrophysical charged particles including protons, electrons, positrons, and nuclei with different charge Z. The most remarkable feature of the CR spectrum is that is is well fit by a broken power-law over an extended energy range, as shown in Figure 1.1. The CR power law spectrum extends over 11 orders of magnitude, to almost 10^{21}eV! Particle acceleration up to these highest energies will be discussed more in detail in the following chapters.

Nowadays, in addition to direct measurements, CR research relies on input from astronomical observations (γ-ray, radio etc), particle physics, and plasma

1. It is worth noting that in 1911, Domenico Pacini noted a similar effect but with decreasing discharge with increasing depth in submarines (Pacini, 1912).

physics to answer astrophysical questions that are not only related to CR acceleration and origin, but also to (to mention a few):

- The origin of galactic winds and other large-scale interstellar flows
- The mechanisms driving magnethydrodynamic (MHD) waves, which are intrinsically related to interstellar turbulence
- The origin of astrophysical neutrinos
- The effect of CRs on galaxy formation
- The effect of CRs on weather

Over the past 15 years, improved experimental techniques have enabled a substantial evolution in the quality of the spectra and composition of CRs. Challenges have even shifted in some instances to theoretical interpretation as experimental uncertainties continue to dwindle.

1.2 Spectrum Main Features

Figure 1.1 shows the main features of the CR spectrum including:

The knee As shown in Figure 1.1, the "knee" is an evident feature of the CR spectrum occurring at around 3×10^{15} eV, where data suggest that the CR flux has a cutoff in rigidity. Although quite apparent, one needs to keep in mind there has not been clear direct measurements of the CR spectrum at the knee as most measurements are based on reconstructed secondary particle showers. It is worth noting that the spectrum exhibits a greater steepening above the knee than the all-particle spectrum. This steepening is also dependent on the chemical composition. This suggests that nuclei with atomic number Z are accelerated up to a maximum energy $E_{\max} \propto Z$, which leads to a heavier and heavier composition above 3×10^{15} eV (e.g., Hörandel, 2005; Bartoli et al., 2015; Dembinski et al., 2017).

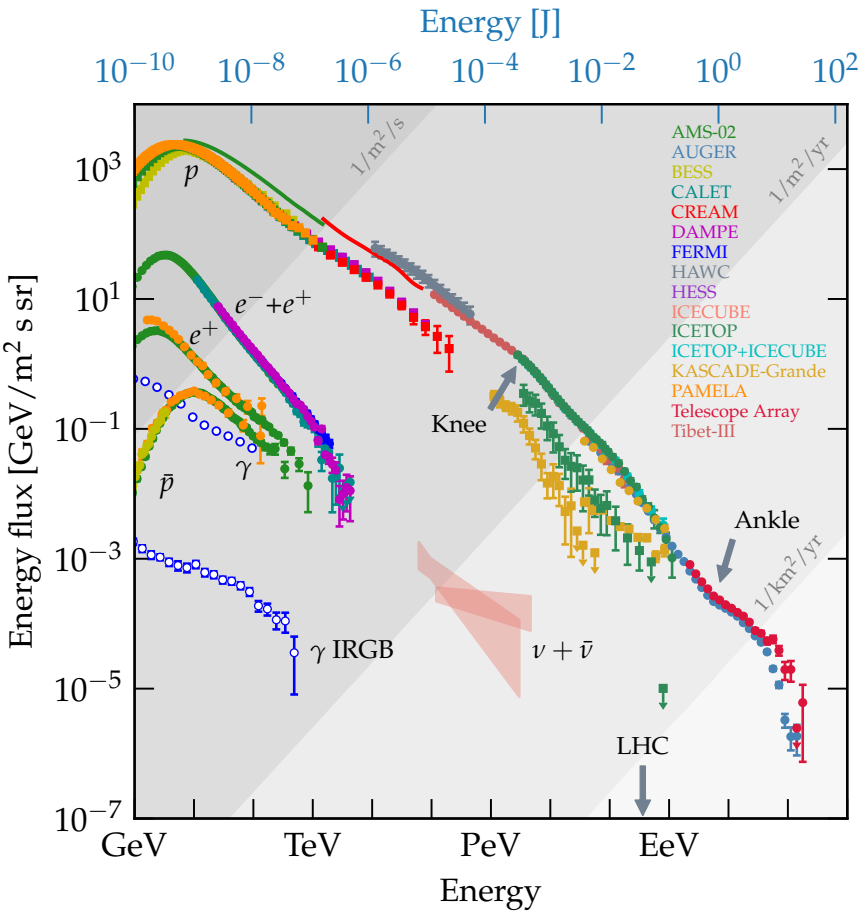

Figure 1.1: The CR Spectrum as of 2020 measured by several experiments (Verzi, 2019; Alfaro et al., 2017; Aartsen et al., 2019; Bertaina et al., 2015; Grebenyuk et al., 2019; Matthews & Telescope Array Collaboration, 2017; Amenomori et al., 2008; Budnev et al., 2020; Archer et al., 2018; Shikaze et al., 2007; Adriani et al., 2011; Aguilar et al., 2015; An et al., 2019). Credit: Carmelo Evoli.

The second knee There is no clear energy at which the transition between galactic and extragalactic CRs occurs. Many studies, however, agree that the transition should occur at $\sim 3 \times 10^{17}$eV known as the "second knee" because of the steepening that occurs at this energy. The origin of particles at the second knee could be similar to that of the knee because of a steepening of the spectrum of heavy nuclei. This suggests a rigidity dependent acceleration mechanism of galactic CRs. The Kascade-Grande experiment has reported a spectrum of particles below the second knee that is lighter than the all-particle spectrum (Apel et al., 2013b), suggesting that particles between $3 \times 10^{15} - 10^{17}$ev result from a Peters cycle. This was later strengthened from a composition analysis using coincident surface from IceCube which suggests that the CR mass increases the knee (Aartsen et al., 2019).

The ankle A flattening of the spectrum at around 3×10^{18}eV called the ankle associated with a lighter CR composition has been detected by Auger and Telescope Array (See Figure 1.2 for more details). There is no consensus on the origin of the ankle feature. It has been initially suggested that protons from Bethe–Heitler pair production interactions could reproduce the lighter element dominance of the power spectrum (Berezinsky et al., 2006; Hillas, 1967), however, the detection of heavier elements with increasing energy (Aab et al., 2017a) refutes this model. Other studies have modeled the UHECR spectrum as a superposition of heavy nuclei and a light element with softer spectra (Aloisio et al., 2014a). More recent studies have attributed the light element spectra to the effects of photodisintegration on heavy UHECRs (e.g. Unger et al., 2015).

The dip at the highest energies A steep decline in the UHECR flux above 5×10^{19}eV is observed. This could be caused by the interaction between UHECRs and the cosmic background radiation (CMB), named the Greisen-Zatsepin-Kuzmin (GZK) cutoff (Greisen, 1966; Zatsepin & Kuz'min, 1966) such that $p + \gamma_{\mathrm{CMB}} \rightarrow$

$p + \pi^0$. However, this is not the only possible interaction, as pair production interactions $p + \gamma_{\rm CMB} \rightarrow p + \pi^+ \rightarrow p + e^+e^-$ could also be significant as they start being relevant at $\sim 10^{18}$eV.

1.3 Fermi Acceleration

It is almost impossible to discuss CR acceleration without mentioning Fermi acceleration. In his famous set of papers (Fermi, 1949, 1954), Enrico Fermi presented an acceleration mechanism that explained energy transfer from magnetized irregularities to charged particles. This is the so called Fermi II mechanism, where particles experience head-on and tail-on collisions thereby gaining and losing energy. On average, particles gain energy $\Delta E/E = (4/3)(V/c)^2$ (V is the velocity of the magnetized structures) because head-on collisions are more likely. This mechanism is quite slow considering that the velocity $V \ll c$.

If we consider the same picture in the context of shocks, particles see the shock as approaching whether it is moving from downstream to upstream or the other way around. This enables consistent head-on collisions $\Delta E/E \propto (V/c)$ and a greater energy gain. The linear aspect of energy gain in this regime gave it the designation Fermi I or diffusive shock acceleration (DSA). The particle spectrum in this case is a power law in momentum space with a slope that is quite close to what is observed in supernova remnants (SNRs). See Blasi (2013) and Amato (2014) for more details.

Nonlinear Diffusive Shock Acceleration Efficient CR acceleration through DSA in SNRs requires strong and turbulent magnetic fields so that CRs are confined close to the shock. Magnetic fields in the vicinity of SNRs must be amplified by a large factor compared to the average value in the interstellar medium (ISM) to confine CRs and accelerate them up to the knee. Present nonlinear theories include the effects of i) CR pressure on the shock, ii) plasma wave generated from

CRs streaming upstream of the shock, and iii) the reaction of the new amplified magnetic field on the shock and particle acceleration (Amato, 2014).

1.4 Galactic vs. Extragalactic CRs

One of the simplest and most powerful applications of Fermi acceleration is the constraint on the gyroradius of the accelerated particle as it approaches the source's size. As the gyroradius increases, particles are not as easily confined magnetically and cannot get more accelerated. The *Hillas criterion* (Cavallo, 1978; Hillas, 1984) takes this effect into account such that:

$$D_{\rm kpc} B_{\mu\rm G} \beta \gtrsim \frac{100}{Z} \frac{E}{10^{20}\,\rm eV}. \tag{1.1}$$

Equation 1.1 expresses the minimum combination of size D and magnetic field B (in kpc and in μG) necessary, but not sufficient, to accelerate a nucleus of charge Z up to energy E (in units of 10^{20} eV) in a flow with speed βc. One can easily find constraints on the potential sources of CRs such that CRs above 10^{19}eV cannot be accelerated in known galactic sources based on equation 1.1.

The focus of this thesis will be mostly on the highest energy extragalactic CRs, but it is worth mentioning that galactic CRs below 10^{17} eV are thought to be accelerated in supernova remnants (SNRs) through diffusive shock acceleration (see 1.3), a Fermi I process (DSA; e.g., Bell, 1978; Blandford & Ostriker, 1978; Berezhko & Völk, 2007; Caprioli et al., 2010a; Ptuskin et al., 2010; Caprioli & Spitkovsky, 2014), which is consistent with observations of individual SNRs such as Tycho (Morlino & Caprioli, 2012; Slane et al., 2014), IC 443, and W44 (Ackermann et al., 2013). Particles gain energy each time they traverse the SNR shock to generate power law spectra. Accounting for the number of SNRs and supernova rate in the Milky Way, we can determine whether these objects have sufficient energy to supply the observed CR spectrum. It is widely believed that

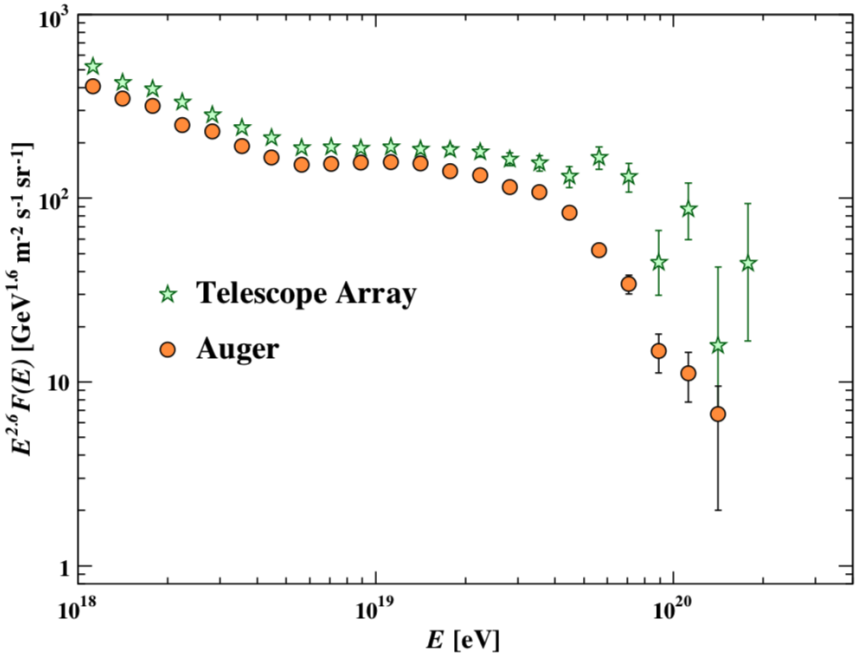

Figure 1.2: UHECR data from the Telescope Array and Pierre Auger experiments featuring the ankle (Compare with Figure 1.1) (Particle-Data-Group et al., 2020).

a few percent of SNR energy is sufficient to power the observed spectrum.

Ultra-high-energy cosmic rays (UHECRs) with energies between $\sim 10^{18}$ eV and $\sim 10^{20}$ eV are expected to be from extragalactic origin. In subsequent chapters, a more thorough discussion of UHECR sources, origin and acceleration mechanism will be provided. Generally speaking, the sources and acceleration mechanism of UHECRs remain much less clear that galactic CRs. The Pierre Auger Observatory has enabled a better understanding of the UHECR spectrum by showing evidence that the highest-energy bins should contain nuclei heavier than hydrogen and helium (Aab et al., 2014a,b; Abbasi et al., 2015; Aab et al., 2017b). While at $\sim 10^{18}$ eV the composition is proton only, at $\sim 3 \times 10^{19}$ eV the UHECR composition is nitrogen-like, outlining a scenario where the UHECR composition becomes heavier as the energy increases, with a possible contribution from iron close to the highest-energy cutoff (Dembinski et al., 2019; Heinze et al., 2019). When statistics, limitations of current nuclear interaction models, and pipeline analy-

ses are taken into account, this scenario is not at odds with Telescope Array data, which is also consistent with a lighter chemical composition on the whole energy range (Pierog, 2013; Abbasi et al., 2015).

Based on energetics and luminosity arguments, γ-ray bursts (GRBs; e.g., Vietri, 1995; Waxman, 1995), tidal disruption events (TDEs; e.g., Farrar & Piran, 2014a), newly-born millisecond pulsars (e.g., Blasi et al., 2007; Fang et al., 2012), and active galactic nuclei (AGNs; e.g., Ostrowski, 2000; Murase et al., 2012; Matthews et al., 2019) have been suggested as possible sources of particles up to $\sim 10^{20}$ eV. However, the actual mechanism(s) through which acceleration should proceed are not well delineated, and are mostly back-of-the-envelope estimates of the maximum energy achievable in a given system based on applications of the Hillas criterion (See equation 1.1).

For relativistic flows, this criterion corresponds to a constraint on the particle Larmor radius, $\mathcal{R}(E) \lesssim D$, and applies to both stochastic and one-shot acceleration mechanisms. In some cases, well-defined acceleration mechanisms (e.g., DSA, magnetic reconnection, shear acceleration) are also considered, but calculations require large extrapolations and parameterization of poorly constrained ingredients such as particle injection and/or scattering.

DSA at nonrelativistic shocks is a very robust acceleration process, but shocks on stellar (e.g., SNRs) and galactic scales (e.g., the wind termination shock) have hard times reaching the highest CR energies (e.g., Bell et al., 2013; Cardillo et al., 2015; Bustard et al., 2017); the interplay of multiple nonrelativistic shocks in the backflowing material of AGN lobes (e.g., Matthews et al., 2019) and accretion shocks in galaxy clusters (e.g., Kang et al., 1996) may be more promising, though. DSA at relativistic shocks, which applies to GRBs, TDEs, and AGN internal shocks, has been shown to be generally less efficient and much slower than its nonrelativistic counterpart (e.g., Sironi & Spitkovsky, 2011a; Sironi et al.,

2013; Araudo et al., 2018; Bell et al., 2018). Magnetic reconnection in newly born millisecond pulsars is another popular CR acceleration mechanism; pulsars can generate large voltages between poles and equator, but it is not clear if/how particles could manage to cross magnetic field lines and tap the full potential drop. Stochastic turbulent acceleration and shear acceleration at the jet/cocoon interface in relativistic jets have also been suggested (e.g., Hardcastle et al., 2009; O'Sullivan et al., 2009; Ostrowski, 2000; Kimura et al., 2018);

Any acceleration mechanism that produces spectra E^{-2} or steeper is strongly disfavored if acceleration has to start from "thermal" particles, since the energetic constraint is already demanding at $E \gtrsim 10^{18}$ eV and a spectrum steeper than E^{-2} would have most of the power in low-energy particles. Kinetic simulations have recently shown that DSA at nonrelativistic shocks naturally boosts the injection of heavy nuclei, in agreement with the elemental abundances of Galactic CRs (Caprioli et al., 2017); however, test-particle DSA only leads to spectra $\propto E^{-2}$ or steeper, and the standard non-linear theory of DSA (e.g., Jones & Ellison, 1991; Malkov & O'C. Drury, 2001), which predicts flatter spectra as a consequence of the back-reaction of accelerated particles, is at odds with the steep γ-ray spectra observed in SNRs (Caprioli, 2012, 2011). This list of possible UHECR sources and acceleration mechanisms is far from being comprehensive (for reviews see, e.g., Aharonian et al., 2002; Kotera & Olinto, 2011; Blandford et al., 2014), but it is safe to say that there is no consensus on where and how UHECRs are produced.

1.5 Cosmic Ray Propagation

Here, we mainly discuss CR propagation in the galaxy and have a more involved discussion of extra galactic propagation of UHECRs in Part II.

1.5.1 Diffusive transport

Secondary-to-primary ratios

The escape time $\tau_{\rm esc}$ is the time that CRs spend in the galaxy before escaping. The ratio of light element fluxes can inform us on the grammage that particles traversed $X = n\mu v\tau_{\rm esc}(E)$ (where n is the mean gas density in the disc plus halo, μ the mean mass of gas, and v the speed of particles) and thus enable better constraints of $\tau_{\rm esc}$. Assuming a standard chemical composition in the ISM, a proton with energy 10GeV has a typical escape time $\tau_{\rm esc} \sim 90(\frac{H}{3\rm kpc})$Myr (Blasi, 2013), where H is the galaxy halo size. This is the best evidence for a diffusive propagation of CRs in the glaxy considering that $\tau_{\rm esc}$ exceeds the ballistic propagation time scale by ~ 3 orders of magnitude. We can then introduce a diffusion coefficient D associated with CRs propagation in the galaxy such that $\tau_{\rm esc} \sim H^2/D$ (More details in Blasi (2013)).

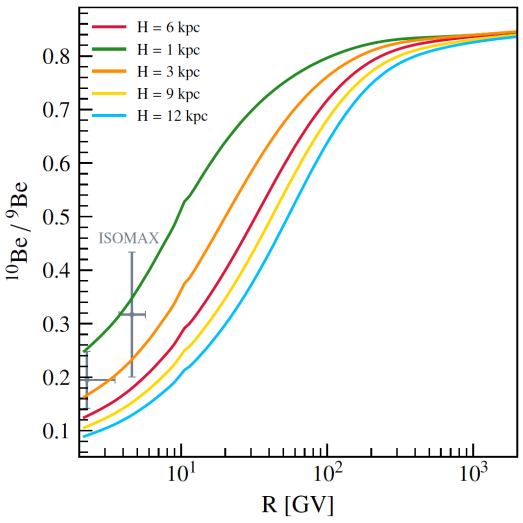

Figure 1.3: Predicted ^{10}Be/^{9}Be ratio for different values of the halo size H as a function of rigidity (Evoli et al., 2019) (See text for more details).

1.5.2 Importance of CR ratio measurements in Confinement measurements

We distinguish between "primary" CRs (Electrons, protons and He, and other nuclei synthesized in stars), which are accelerated at astrophysical sources, and "secondaries" (are not abundant end-products of stellar nucleosynthesis e.g. Li,

Be) which are generated by the interaction of primaries with the ISM via spallation during propagation. The elemental secondary-to-primary ratios are a commonly employed observable that measures the relative abundance of source-produced CRs against the abundance of secondary species. For example, the Boron to Carbon ratio B/C probes the total material pathlength through which CRs travel before they reach Earth (Swordy et al., 1990; Engelmann et al., 1990; et al., 2008). In the context of the standard diffusion-convection model, these ratios are typically proportional to H/D, where H is the CR halo size and D is the diffusion coefficient. Secondary-to-primary ratios are of great value in analyzing CR histories and can even carry signatures of reacceleration processes at around 1 GeV/n (Webber, 1997, 2000). However, models based only on these ratios can lead to large degeneracies in the parameter space because they are only sensitive to H/D, which leaves the confinement time (proportional to H^2/D through the same set of equations) weakly constrained.

Radioactive isotope ratios

Radioactive isotope ratios serve a complementary and crucial role in unraveling the fundamental properties of CRs. We can derive the lifetime of CRs in the Galaxy from the measurements of radioactive isotopes, and subsequently determine the power required to sustain the energy density of CRs in the Galaxy (e.g. Gaisser et al., 2016). These "clock" isotopes can provide model constraints which are independent of those derived from the abundances of stable secondaries. With a half-life of 1.39 Myr (Granger et al., 2013), $^{10}\mathrm{Be}$ is one of the most important isotopes because it is conducive to testing CR confinement times in the galaxy. Additionally, $^{10}\mathrm{Be}/^{9}\mathrm{Be}$ is determined by the propagation history of CRs in the ISM because Be is not produced by stellar nucleosynthesis. Together with constraints from secondary/primary ratios, we can estimate the diffusion coefficient and halo

size of the galaxy (Simon, 1999; Strong et al., 2007; Simpson & Garcia-Munoz, 1988) from the confinement time measurements. Figure 1.3 (Evoli et al., 2019) shows models of the expected $^{10}\mathrm{Be}/^{9}\mathrm{Be}$ ratio for different values of H as a function of the rigidity of the CR in gigavolts. The rigidity $R = pc/Ze = B\rho$—where p is the momentum, Z is the charge of the particle, c is the speed of light, B is the magnetic field, and ρ is the gyroradius—is intrinsically related to the particle momentum and is a measure of the resistance of charged particles to deflections by magnetic fields. The models are compared with data points from ISOMAX (et al., 2004). We can see that we need an accuracy better than 30% in the $^{10}\mathrm{Be}/^{9}\mathrm{Be}$ ratio to discriminate between H = 3 and H = 6kpc, and a 10% accuracy to discriminate between H = 6 and H = 9kpc. Clearly, we cannot constrain H, and thus precise measurements of the $^{10}\mathrm{Be}/^{9}\mathrm{Be}$ ratio are much needed.

Chapter 2

Cosmic Ray Detection

Direct measurements of CRs are made primarily from Helium balloon detectors and probes in spacecraft. Other methods rely on ground observations with large apertures and long exposure times to detect rarer and more energetic particles. Such experiments detect air showers that are produced when high energy hadrons interact with the atmosphere to produce secondary particle showers. Other indirect detection methods rely on synchrotron and Inverse Compton photons to probe CRs in remote regions. Indeed, synchrotron radiation, bremsstrahlung, and inverse-Compton produce photons that are directly associated with CR interactions in SNRs for instance. Among the active experiments actively observing SNRs, we have for instance at GeV energies Fermi-LAT and AGILE and at TeV energies HESS, MAGIC, and VERITAS.

2.1 Direct Detection

CRs can be directly detected in the energy range from 10^3 to roughly 10^{15}eV with balloon and space-borne experiments.

2.1.1 Techniques

The main techniques that are used to detect CRs are:

Transition radiation As relativistic particles traverse an interface of two media with two dielectric constants, they emit transition radiation. The intensity of radiation is proportional to the energy

Calorimeters The main idea behind calorimeters is to detect the hadronic and/or electromagnetic shower of secondary particles that ensues the interaction of the particle with a dense material to measure the energy deposited from scintillation.

Cherenkov radiation Relativistic particles that traverse a medium with a velocity greater greater than the speed of light, emit Cherenkov light in a cone with a certain angle. Measurements of the angle and the refractive index of the material enables us to infer the velocity of the particle.

2.1.2 CR detectors

In this section, we use the example of the The Alpha Magnetic Spectrometer (AMS-02) detector to discuss different subsystems that employ most of the techniques discussed above. AMS-02 is a particle-physics detector aboard the International Space Station (ISS), that aims to detect dark matter, antimatter, and performs precision measurements of cosmic rays.

The AMS instrument (See Figure 2.1) is composed of these different subsystems, which cover most of the detection techniques discussed above.

Magnet Spectrometer The magnetic field in magnets bends in opposite directions charged particles/antiparticles. The magnetic fields are used to separate particles and antiparticles. From the radius of curvature, we can measure the particle momentum.

Transition Radiation Detector (TRD) The TRD identifies electrons and positrons among other CRs. Its goal is to identify particles through the detection of the X-rays emitted by light particles. X-rays are produced when the particle crosses

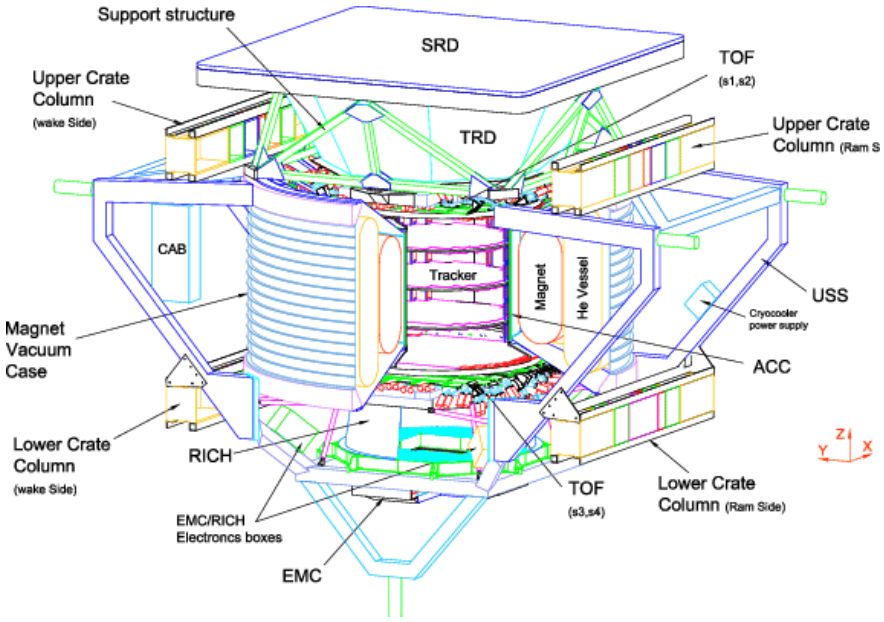

Figure 2.1: Layout of the AMS-02 detector with its different components as discussed more in detail in the text (Credit NASA).

several interfaces characterized by an abrupt change in index of refraction. The TRD is able to tell the difference between an electron and a proton. At high energy, protons with about 940 (MeV) of mass, electrons with 0.5 MeV, pions and muons with about 100 MeV, all will look the same. They will have about the same momentum, so the Tracker can't distinguish them. The TRD is able to tell the difference between an electron and a proton since at high energy an electron will emit X-rays while crossing the TRD detector while a proton will not.

Time-of-Flight System (ToF) The TOF warns the sub-detectors of incoming CRs. The ToF is the detector's stopwatch. It is able to measure with a high level of precision (150 ps) the particle transit time into the detector. Its main goal is to warn the other sub-detectors of the incoming of an incident CRs. The distance between Upper and Lower ToF is a few meters, the ToF is able to measure particles velocity up to 98% of the speed of light!

Ring-Imaging Cherenkov Detector (RICH) The RICH estimates the particles velocity with a high accuracy (0.1%). Cherenkov radiation consists of photons

emitted along a characteristic cone whose angular aperture is directly related to the particle velocity and with the index of refraction of the material. Velocity derives from pattern recognition of photons distributed over geometrical shapes as circles, ellipses, arcs or crescents produced by the Cherenkov effect.

The silicon tracker The Silicon Tracker is the only sub-detector able to separate positive particles from negative particles from the direct measurement of the trajectory deflection. Tracker is also one of the three sub-detectors – with ToF and RICH – able to evaluate the absolute charge (Z) of a particle, contributing to the chemical distinction capability of the AMS-02 spectrometer. The Silicon Tracker measures with a high precision (10 μm) the position of passage of a particle at 8 different position along the track.

Electromagnetic Calorimeter (ECAL) the ECAL measures energy of incoming electrons, positrons and γ-rays The positron has the same proton charge and sign, but a 1/2000 mass. Since a high-energy positron could have the same rigidity of a low-energy proton, they cannot be separated by a magnetic field. ECAL is a heavy-lead brick in which Incident particles interact in such a dense material producing a shower of low-energy particles. The shape of the shower identifies the particle kind (proton or positron) and the particle total energy. ECAL is also able to measure directly high energy photons with an accurate energy and direction determination.

2.2 Indirect Detection

These measurements rely on the showers of secondary particles produced by primary cosmic-rays interacting with the atmosphere. Particles can be detected using this technique above roughly 10^{13}eV. The Auger and Telescope Array (TA) experiments have relied on particle showers to study the UHECR spectrum. The longitudinal profile enables a calorimetric measurement of the original UHECR

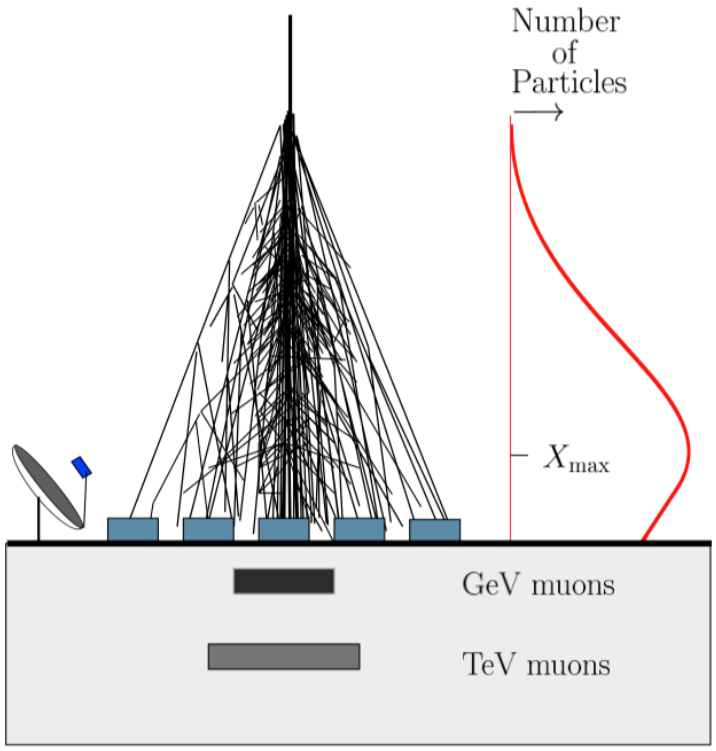

Figure 2.2: When particles interact with the atmosphere, they initiate a hadronic and electromagnetic cascade. Detector arrays sample the hadronic shower reaching the ground and telescopes collect the Cherenkov and nitrogen fluorescent light. The energy of the primary CR is measured calorimetrically using the longitudinal profile of the shower. (Anchordoqui, 2019)

energy and the depth maximum $X_{\max}$, enables us to study the composition of UHECRs.

Figure 2.2 shows what happens to primary CRs as they penetrate in the atmosphere. Particle air showers are created when an incident primary cosmic ray interacts with nuclei in the atmosphere producing secondary and tertiary etc... particles. The air shower, or cascade, starts developing a longitudinal component as more and more secondary particles are created and the energy per particle decreases. These air shower particles excite atmospheric nitrogen which cause ultraviolet (UV) fluorescence.

The size of the shower depends on the angle of incidence of the primary CRs and its energy. Primary particles with energy $> 10^{18}$eV can create showers with millions of particles with a diameter that reaches hundreds of meters. Scintillation counters or Cherenkov light emitted in water tanks can be used to detect the secondary electrons and muons. These detectors are usually separated depending on the energy of the CRs to be detected (10 m to 1 km). The particle's primary energy can be detected from the density of particle showers or sensing the UV light produced via interactions of CRs in the atmosphere to probe the longitudinal development of the shower.

Part II

Particle Acceleration in Active Galactic Nuclei: From the Large Structures of Jets to the Kinetic Scale of Plasma Turbulence

Chapter 3

Espresso Acceleration of Ultra-high-energy Cosmic Rays in the Jets of Active Galactic Nuclei

3.1 Bottom-up Acceleration of Ultra-high-energy Cosmic Rays

The origin of the highest-energy cosmic rays (CRs) is one of the most prominent unresolved questions in astrophysics. The goal of part of my work is to build a solid theoretical framework where parameterizations are reduced to a minimum, if not eliminated, and UHECR acceleration is followed bottom-up from injection to the highest energies in an astrophysical source described in the most realistic way.

Espresso Reacceleration in AGNs AGNs are excellent candidates as UHECR sources: an AGN jet with radius of hundreds of parsecs and B of a few tens of μG satisfies the Hillas criterion up to the highest energies for iron nuclei (equation 1.1). Also, AGN luminosities are consistent with the energy injection rate required to sustain the flux of UHECRs, $Q_{\rm UHECR} \sim 5 \times 10^{43}$ erg Mpc^{-3} yr^{-1} (e.g., Katz et al., 2013), as extensively discussed, e.g., in Caprioli (2018) and references therein. In

fact, assuming a typical density of AGNs $n_{\rm AGN} \approx 10^{-4}$ Mpc^{-3}, 10%-20% of which is radio-loud (e.g., Jiang et al., 2007), the luminosity of each AGN in UHECRs has to be

$$\tilde{\mathcal{L}} \approx \frac{Q_{\rm UHECR}}{n_{\rm AGN}} \approx 10^{40}\ {\rm erg\ s^{-1}}. \tag{3.1}$$

Such a luminosity is smaller than the bolometric luminosity of typical AGNs, $\mathcal{L}^{\rm bol}_{\rm AGN} \approx 10^{42}-10^{45}$erg s^{-1} (e.g., Woo & Urry, 2002; Lusso et al., 2012). Note that the upper end of this luminosity distribution is populated by powerful Fanaroff-Riley II (FR II) galaxies, which have number densities $n_{\rm FRII} \approx 10^{-7}$ Mpc^{-3} and hence $\tilde{\mathcal{L}} \approx 10^{43}$ erg s^{-1}. However, the ultimate source of energy that can be exploited to accelerate UHECRs is the jet power, which is a factor of 10–100 larger than $\mathcal{L}^{\rm bol}_{\rm AGN}$ (e.g., Ghisellini et al., 2009).

Caprioli (2015a), hereafter C15, suggested that UHECRs may be produced in relativistic AGN jets through a very general mechanism dubbed *espresso* acceleration. The basic idea is that CR *seeds* accelerated up to 10^{17} eV in SNRs can penetrate into a relativistic jet and—independently of their exact trajectory—receive a *one-shot* boost of a factor of $\sim \Gamma^2$ in energy, where Γ is the Lorentz factor of the relativistic flow (the *steam*). With $\Gamma \gtrsim 30$, as inferred from multiwavelength observations of powerful blazars (e.g., Tavecchio et al., 2010; Zhang et al., 2014), a single *espresso* shot may be sufficient to boost the energy of galactic CRs by a factor $\Gamma^2 \gtrsim 10^3$, transforming the highest-energy galactic CRs at 10^{17} eV in the highest-energy UHECRs at 10^{20} eV.

The most appealing feature of the *espresso* mechanism is its simplicity: CR seeds undergo a Compton-like scattering with a relativistic "wall" (the jet magnetic field), and the resulting energy gain is of order Γ^2 if the initial and final directions of flight, differ by more than $\pi/2$. A close relative of this process is the first upstream–downstream–upstream cycle for a particle accelerated at a relativistic shock (e.g., Vietri, 1995; Achterberg et al., 2001); the idea was also applied in

blazar shocks assuming DSA and large-angle scattering, which in principle leads to multiple Γ^2 boosts (e.g., Stecker et al., 2007).

In the *espresso* framework, no assumptions are made on particle pitch-angle scattering (diffusion) or on the properties of the underlying magnetic turbulence, differently from the stochastic models that rely on repeated acceleration at the jet interface (e.g., Ostrowski, 1998, 2000; Fang & Murase, 2018a; Kimura et al., 2018) or on multiple DSA in the jet cocoon (Matthews et al., 2019). In any stochastic model, the maximum energy critically depends on the rate at which CRs diffuse back to the acceleration sites, and in turn on the amplitude and spectrum of the magnetic turbulence at Larmor-radius scales, which is hard to constrain observationally.

C15 also pointed out that any reacceleration model that uses galactic CRs as seeds naturally predicts a match between the chemical composition at/above the knee and that of UHECRs: given a rigidity cutoff at a few PV, the UHECR spectrum should be proton dominated at 10^{18} eV and increasingly heavier at higher energies, consistent with experimental data. This argument was put originally forward in the context of the *espresso* mechanism but has been applied to other frameworks, too (e.g., Fang & Murase, 2018a; Kimura et al., 2018).

Reacceleration Efficiency Before diving into more detailed calculations, it is worth going through a simple estimate of the energetics of the galactic CR reacceleration. We express the seed luminosity by considering the luminosity of the Milky Way in Galactic CRs, $\mathcal{L}_{\rm MW}^{\rm GCR} \approx 5 \times 10^{40}$erg s^{-1} (e.g., Hillas, 2005) and scaling it proportionally to the SN rate, $\zeta_{\rm MW} \sim 2$ SNe century^{-1} for our Galaxy. Considering an injected spectrum $\propto E^{-2}$, which contains the same energy per decade, allows us to work with the total seed luminosity rather than the luminosity in PeV particles; if the seed injection spectrum were steeper, $\propto E^{-2.3}$ as in the Milky Way (Blasi et al., 2012; Aguilar et al., 2016), the energy density in seeds at the

knee would be about one order of magnitude smaller.

Then, we estimate the fraction of the seeds that can be reprocessed by the jet. C15 (§3.2) gives the flux of CRs in the galactic halo that goes through the lateral surface of the jet, which reads

$$\Phi \approx 0.02 \Delta\theta \left(\frac{H}{R_{\rm gal}} \right)^2 , \tag{3.2}$$

where H is the minimum between the halo scale height and the jet length $L_{\rm jet}$, $R_{\rm gal}$ is the galaxy radius, and $\Delta\theta$ is the jet semi-aperture in degrees. If the CR scale height is comparable with $R_{\rm gal}$, we can put $H \sim L_{\rm jet}$; therefore, for $L_{\rm jet}/R_{\rm gal} \gtrsim 1$ and $\Delta\theta \approx 2^\circ$, we obtain $\Phi \gtrsim 0.04$. We comment on such assumptions in the next section.

Since the energy of the CR knee should not differ much from galaxy to galaxy (C15), galactic CRs need to gain a factor $\mathcal{E} \approx 10^3$ in energy to be promoted to UHECR; hence, the total luminosity in reaccelerated seeds can be estimated as

$$\mathcal{L}_{\rm AGN}^{\rm UHECR} \approx \mathcal{E} \mathcal{L}_{\rm MW}^{\rm GCR} \frac{\zeta \Phi}{\zeta_{\rm MW}} \approx 2 \times 10^{42} \, \frac{\zeta}{\zeta_{\rm MW}} \frac{\Phi}{0.04} \, {\rm erg \ s^{-1}}. \tag{3.3}$$

For our reference parameters, $\mathcal{L}_{\rm AGN}^{\rm UHECR} \gg \tilde{\mathcal{L}}$ (equation 3.1) for a Milky Way-like AGN host. Due to the contribution of type Ia SNe, the SN rate per unit of stellar mass is roughly the same in spiral and elliptical galaxies (e.g., Turatto et al., 1994); therefore, one can have $\zeta \gg \zeta_{\rm MW}$ both in starburst and in massive elliptical galaxies, the latter being the typical AGN hosts. Moreover, it is plausible that the larger the SN/seed production rate, the stronger the interstellar magnetic turbulence and hence the longer the seed confinement time.

Dependence on the AGN Type A natural question is what kinds of AGNs are the best candidates for *espresso* acceleration. Let us consider acceleration to $\sim 10^{20}$eV, first. If such energies had to be achieved with one shot only, the jet

Lorentz factor would need to be $\Gamma \gtrsim 30$, and such large Lorentz factors are typically inferred in blazars and radio-loud quasars (e.g., Tavecchio et al., 2010; Zhang et al., 2014). If a few *espresso* cycles were allowed (say, N), significantly lower values of Γ would suffice because the energy gain scales as Γ^{2N}. Since AGN jets typically have bulk flows $\Gamma \gtrsim 5$, and possibly even spines with $\Gamma \gtrsim 10$ (Chiaberge et al., 2001; Ghisellini et al., 2005; Lister et al., 2019), even ordinary Seyfert galaxies could in principle accelerate UHECRs.

In terms of required UHECR luminosity per single AGN (Equation 3.3), it is likely that radio-quiet AGNs may not be powerful enough to contribute substantially to the UHECR flux (e.g., Kimura et al., 2018). When considering radio-loud AGNs, one has to distinguish between FR I jets, which are typically decelerated to nonrelativistic bulk flows within 1 kpc (e.g., Wardle & Aaron, 1997; Arshakian & Longair, 2004; Mullin & Hardcastle, 2009), and FR II jets, which rather show $\Gamma \gtrsim 10$ at kiloparsec scales and beyond (e.g., Sambruna et al., 2002a; Siemiginowska et al., 2002a; Tavecchio et al., 2004; Harris & Krawczynski, 2006a).

FR I jets may have $H \lesssim 0.1 R_{\rm gal}$ and reprocess a fraction of the galactic seeds smaller than FR II jets (Equation 3.2), but still be able to satisfy the condition in Equation 3.3. In such galaxies, the jet Lorentz factor may be of order of a few, and UHECR production would critically rely on the cocoon magnetic turbulence to be strong enough to allow a few acceleration cycles; for Γ as low as $\gtrsim 3$, $N \gtrsim 3$ *espresso* shots would be sufficient to promote galactic CRs to UHECRs. Instead, if the jet velocity becomes subrelativistic, *espresso* acceleration morphs into stochastic acceleration (Fang & Murase, 2018a; Kimura et al., 2018). For instance, $N \gtrsim 12$ for a jet bulk flow of $\simeq 0.5c$ and $\Gamma \simeq 1.33$ (see equation 10 of Caprioli, 2018).

On the other hand, radio-loud FR II AGNs, despite being quite rare, are both powerful and extended enough to easily satisfy the energetic constraints for production of UHECRs via reacceleration of galactic CR seeds. Also, the large Lorentz

factors persisting over kiloparsec scales provide the ideal conditions for *espresso* acceleration to occur, even via one/two shots only.

One final note: the boost of 10^3 in energy and the corresponding requirements on Γ, are based on the assumption that the knee energy of galactic CRs is the same in every galaxy (Caprioli, 2015a); it is indeed possible that the knee energy may be a factor of a few to 10 larger in some AGN hosts (for instance in galaxies with prominent winds; see, e.g., Bustard et al., 2017), which would significantly reduce the requirements on the jet Lorentz factors in such environments.

Open Questions The *espresso* scenario has been corroborated with analytical calculations of CR trajectories in idealized jet structures, which confirmed that the vast majority of the trajectories lead to $\sim \Gamma^2$ boosts regardless of the radial and longitudinal jet structures (Caprioli, 2018). Nevertheless, analytical calculations cannot answer some fundamental questions, such as:

- In a realistic jet, what is the fraction of CR seeds that can undergo *espresso* acceleration?
- Do particles typically get a boost of Γ^2? Is it possible to undergo more than one shot and thus exceed such an estimate?
- Is acceleration up to the Hillas limit generally achievable?
- How does the spectrum of reaccelerated particles compare with the injected one?
- Are reaccelerated particles released isotropically, or are they beamed along the jet?

3.1.1 Particle Trajectories and Energy Gain in Cylindrical Jets

The basic idea behind the *espresso* acceleration is that particles with Larmor radii large enough can penetrate into relativistic jets and experience the potential

drop associated with the strong motional electric field, as seen from the laboratory frame. In C15 it was argued that particles on average gain a factor of Γ^2 in energy, where Γ is the jet Lorentz factor, provided that the ingoing and outgoing flight directions are uncorrelated, which requires particles to perform at least one-quarter of gyration in the flow before being released.

In this section, we use either an analytical Hamiltonian formalism (Caprioli, 2018) or a direct numerical approach to study particle trajectories and energy evolution in idealized jet structures; the main goal is to assess acceleration in nonhomogeneous and finite jets.

Throughout the paper, we denote quantities in the laboratory and flow frames, respectively, with Q and Q', and initial/final quantities with the subscripts $_{\rm i/f}$.

The Analytical Approach

We use cylindrical coordinates (r,ϕ,z) and consider a cylindrical jet with radius $R_{\rm jet}$, with a magnetic field that is purely toroidal in the flow frame, $\boldsymbol{B'} = -B'(r)\boldsymbol{\phi}$, corresponding to a potential vector:

$$\boldsymbol{A'}(\boldsymbol{r}) = A'(r)\boldsymbol{z}, \quad \text{with} \quad \mathrm{A'(r)} = -\int_0^{\mathrm{r}} \mathrm{B'(r')dr'}; \tag{3.4}$$

The flow has a velocity $\beta\boldsymbol{z} = v/c\boldsymbol{z}$ in the laboratory frame, where v and c are the speed of the flow and speed of light, respectively; $\Gamma \equiv (1-\beta^2)^{-1/2}$ is the flow Lorentz factor. The potential vector transforms as $\boldsymbol{A} = \Gamma\boldsymbol{A'}$, which means that B_ϕ is larger by a factor of Γ in the laboratory frame.

We consider the Hamiltonian of a particle with mass m, charge q, and Lorentz factor γ' in the flow frame:

$$\mathcal{H}' = \sqrt{P_r'^2 + \frac{P_\phi'^2}{r^2} + [P_z' - qA'(r)]^2 + m} = \gamma' m, \tag{3.5}$$

where $P'_r = \gamma' m\dot{r}$, $P'_\phi = \gamma' m r^2 \dot{\phi}$, and $P'_z = \gamma' m\dot{z} + qA'$ are the canonical momenta. $\mathcal{H}'$, P'_ϕ, and P'_z are conserved quantities because $\mathcal{H}'$ is independent of t, ϕ, and z. Let us then consider a relativistic particle in the laboratory frame with initial energy E_i and momentum

$$\boldsymbol{p}_\mathrm{i} \simeq E_\mathrm{i}(-\xi_\mathrm{i}\sqrt{1-\mu_\mathrm{i}^2}; \sqrt{(1-\mu_\mathrm{i}^2)(1-\xi_\mathrm{i}^2)}; \mu_\mathrm{i}) \tag{3.6}$$

where $\mu_\mathrm{i} \equiv p_z/|\boldsymbol{p}|$ and $\xi_\mathrm{i} \equiv p_r/|\boldsymbol{p}|$ define the cosines of the flight angles with respect to $\boldsymbol{z}$ and $-\boldsymbol{r}$.

If we restrict ourselves to cases with $\xi_\mathrm{i} = 1$, which correspond to $P'_\phi = 0$ and hence to planar orbits, the initial momentum is $\boldsymbol{p}_\mathrm{i} \simeq E_\mathrm{i}(-\sqrt{1-\mu_\mathrm{i}^2}; 0; \mu_\mathrm{i})$ and the energy gain in the laboratory frame achieved by truncating the orbit at an arbitrary time t_f reads (Caprioli, 2018):

$$\begin{aligned}\mathcal{E} \equiv \frac{E_\mathrm{f}}{E_\mathrm{i}} =& \Gamma^2(1-\beta\mu_\mathrm{i})(1+\beta\mu'_\mathrm{f}) \\ =& (1-\beta\mu_\mathrm{i})\left\{1 + \frac{\Gamma^2\beta}{\alpha'}\left[1 - \frac{A(r)}{A(R_\mathrm{jet})}\right]\right\},\end{aligned} \tag{3.7}$$

where

$$\alpha' \equiv \frac{\mathcal{R}'}{R_\mathrm{jet}} = \frac{E'}{q\langle B'\rangle_r R_\mathrm{jet}} = \Gamma^2\alpha_\mathrm{i} = \alpha_\mathrm{f}. \tag{3.8}$$

$\mathcal{R}'$ is the average particle Larmor radius, $A'(r) \equiv r\langle B'\rangle_r$, $\langle B'\rangle_r$ being the radially averaged toroidal magnetic field. Equation 3.7 illustrates that the energy gain in the laboratory frame is due to the potential energy tapped by particles that penetrate into the jet: the closer they get to $r = 0$ (where $A' = 0$), the larger the gain. For $\mu_\mathrm{i} \neq 1$ and in the limit $\beta \to 1$, $\Gamma^2 \gg \alpha'$ one has:

$$\mathcal{E} \approx \frac{\Gamma^2}{\alpha'}\left[1 - \frac{A(r)}{A(R_\mathrm{jet})}\right]. \tag{3.9}$$

In general, the energy gain of a particle that travels back and forth between R_jet

and some minimum r oscillates between 1 and a value $\mathcal{E}_{\rm max}$ that depends on the initial Larmor radius. The *average* energy gain along the orbit, $\langle\mathcal{E}\rangle$, obeys $\mathcal{E}_{\rm max} \geq \langle\mathcal{E}\rangle \geq \mathcal{E}_{\rm max}/2$ for any increasing profile of $B(r)$, and the maximum energy gain depends on the initial Larmor radius of the particle.

In calculating $\mathcal{E}_{\rm max}$ using equation 3.7, we distinguish the cases $\alpha' > 1/2$ and $\alpha' < 1/2$, corresponding to final Larmor radii smaller or larger than the jet radius, in the flow frame. Note that α' is constant over the gyration, but it corresponds to different $\alpha_{\rm i}$ and $\alpha_{\rm f}$ in the laboratory frame.

1. $\alpha' < 1/2$: Particles get back to $r = R_{\rm jet}$ after one gyration; for planar orbits, the maximum energy is achieved at $r = r_{\rm min}$ where $P_r = 0$ and the momentum is entirely along the z-direction. The maximum energy gain reads as:

$$\mathcal{E}_{\rm max} = \Gamma^2(1 - \beta\mu_{\rm i})(1 + \beta) \simeq 2\Gamma^2. \tag{3.10}$$

2. $\alpha' > 1/2$: Particles are not well magnetized and cross the entire flow; the maximum gain is achieved for $A(r = 0) = 0$ and reads as:

$$\mathcal{E}_{\rm max} = (1 - \beta\mu_{\rm i})\left[1 + \frac{\Gamma^2\beta}{\alpha'}\right] \simeq \frac{\Gamma^2}{\alpha'} = \frac{1}{\alpha_{\rm i}}, \tag{3.11}$$

   i.e., $\alpha_{\rm f} \simeq 1$, which means that particles gain energy up to the Hillas limit.

The energy gain does not depend much on the pitch angle $\mu_{\rm i}$ as long as it is not very close to 1. Finally, for $\xi_{\rm i} < 1$ orbits are nonplanar and have a finite constant P_ϕ; in this case, particles do not reach $r = 0$ because of the centrifugal barrier, but the corrections to equation 3.10 and 3.11 are small, $\mathcal{O}(1/\Gamma^2)$ (Caprioli, 2018).

The Numerical Approach

In this section we numerically integrate orbits on top of a prescribed electromagnetic configuration for which an analytical solution cannot be easily found. Particles are propagated using the relativistic Boris algorithm (e.g., Birdsall & Langdon, 1991a), which ensures long-term stability of the orbits; we have also tried the Vay pusher (Vay, 2008), which is known to perform better in relativistic flows, and it led to consistent results.

We consider the more general case of a cylindrical jet with $\Gamma_0 = 10$ and length $L_{\rm jet} = 200 R_{\rm jet}$. The Lorentz factor outside the jet is set up with a sharp exponential radial profile such that $\Gamma(r > R_{\rm jet}) = \Gamma_0 e^{-10(r/R_{\rm jet}-1)}$ until it reaches $\Gamma = 1$ for continuity purposes. We set a toroidal magnetic field inspired by the one generated by a current-carrying homogeneous wire, which goes as r inside the jet and as $1/r$ outside, i.e.,

$$\boldsymbol{B}(r \leq R_{\rm jet}, z) = B(R_{\rm jet}, z) \frac{r}{R_{\rm jet}} \boldsymbol{\phi}, \tag{3.12}$$

$$\boldsymbol{B}(r \geq R_{\rm jet}, z) = B(R_{\rm jet}, z) \frac{R_{\rm jet}}{r} \boldsymbol{\phi} \tag{3.13}$$

$$B(R_{\rm jet}, z) = B_0 \frac{L_{\rm jet} - z}{L_{\rm jet}} \tag{3.14}$$

The magnetic field also decreases linearly along the jet, as suggested by radio observations (e.g., O'Sullivan & Gabuzda, 2009), which allows particles to eventually leave the jet.

Throughout the paper, we consider two possible orientations of the jet toroidal magnetic field, $B_\phi \lessgtr 0$, which physically correspond to the jet current along z being $J_z \lessgtr 0$ and call them case A and case B, respectively. The sign of B_ϕ depends on the direction of the poloidal field in the material that is accreted on the black hole (e.g., Begelman et al., 1984), as recently shown also by first-principle

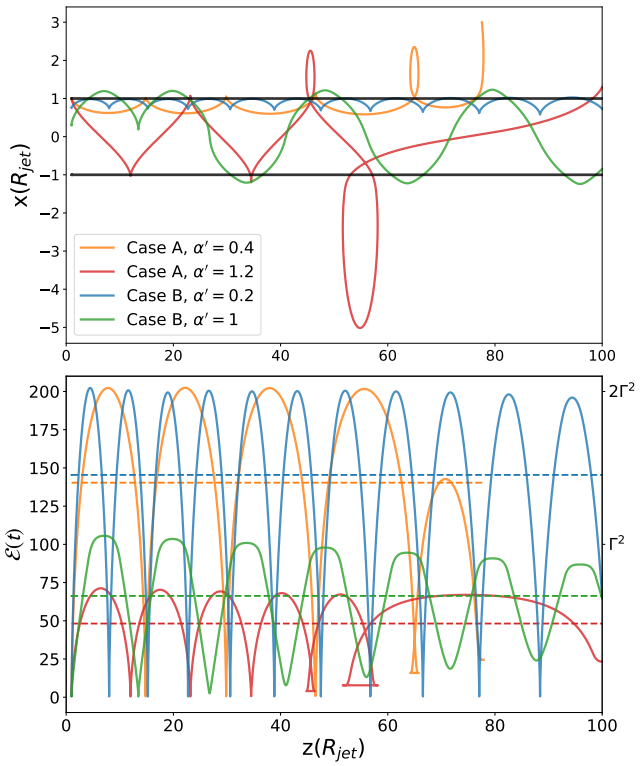

Figure 3.1: 2D projection of the trajectories (top panel) of four representative particles and their corresponding energy gain $\mathcal{E}$ (bottom panel). The horizontal solid lines in the top panel mark the jet boundaries, while the dashed lines in the bottom panel represent the average energy gain $\langle \mathcal{E} \rangle$ for each particle (color coded).

particle-in-cell simulations (Parfrey et al., 2019), which in general does not have a preferential direction. One possible model that breaks such a symmetry is the "cosmic battery" mechanism (Contopoulos & Kazanas, 1998); in this picture radiative losses induce a drag between electrons and protons in the accretion disk, which generates a toroidal current and hence a fixed sign of the poloidal field that is accreted onto the black hole. The cosmic battery would lead to a counterclockwise toroidal magnetic field ($J_z < 0$, $B_\phi < 0$, case A), provided that the accreted material does not have its own magnetic field in excess of the battery-generated one. In the absence of a definitive motivation to fix the signs of J_z and B_ϕ, we leave both possibilities open and discuss how our results differ between case A and case B.

Figure 3.1 shows the projection of the orbit on the $x - z$ plane (top panel) and the energy gain $\mathcal{E}$ (bottom panel) for four particles with $\mu_\mathrm{i} = 0$, $\xi_\mathrm{i} = 1$, and different initial Larmor radii parameterized by $\alpha' = \mathcal{R}'/R_\mathrm{jet}$, as in the legend; we also consider both jet polarizations, which lead to concave/convex trajectories. *Espresso* acceleration occurs for both toroidal magnetic field directions, as attested by the energy gain oscillating between 1 and $\mathcal{E}_\mathrm{max}$ during one orbit. Particles with $\alpha' < 1/2$ reach a maximum energy gain $\mathcal{E}_\mathrm{max} \sim 2\Gamma^2$, in agreement with equation 3.10, while particles with $\alpha' > 1/2$ gain energy until their Larmor radius becomes comparable with R_jet (see equation 3.11). The dashed lines in the bottom panel of Figure 3.1 show the orbit-averaged energy gain $\langle\mathcal{E}\rangle$, which is always a fraction of order one of the maximum energy gain $\mathcal{E}_\mathrm{max}$.

To further test the effect of the magnetic field on the trajectories, we have added a poloidal component to the field, comparable in strength to the toroidal one, and found that the induced $\mathbf{B} \times \boldsymbol{\nabla} B$ drift has no appreciable effect on the particle energy gain.

Nonhomogeneous Jets

In general, relativistic jets do not have a uniform Lorentz factor as we have assumed so far. The interaction of the jet with the ambient medium creates regions that are pinch unstable (e.g., Hardee, 2000; Mignone et al., 2010; Tchekhovskoy & Bromberg, 2016a), which leads to the formation of clumps where the Lorentz factor is larger, separated by slower regions along the jet spine (e.g., Agudo et al., 2001; Hardcastle et al., 2016). This feature is commonly found also in high-resolution MHD simulations, so it is worth singling out the effects of such inhomogeneities on particle orbits.

We consider particles initialized with $\mu_{\rm i} = 0$ and different values of $\alpha' \in [0.05, 0.4]$ in a region of finite extent $H = 2.5R_{\rm jet}$ that has $\Gamma = 10$; beyond $x = H$, we set $\Gamma = 5$. The top panel of Figure 3.2 illustrates such a flow profile (gray scale), along with the trajectories of the propagated particles. Their maximum energy gain (bottom panel) is the expected $2\Gamma^2 \simeq 200$ for $\alpha' \lesssim \bar{\alpha}' \simeq 0.16$ and increasingly smaller for larger Larmor radii. The critical value $\bar{\alpha}'$ can be understood in the following way: in order to achieve the maximum energy boost, a particle needs to stay in the high-Γ flow for at least one quarter of a gyration, i.e., for a time $T_{\rm acc} \gtrsim \Gamma\pi/(2\Omega')$, where $\Omega' \equiv \mathcal{R}'/c$ is the gyration frequency in the flow frame. Since, during this time, the particle travels a distance $\Delta z = T_{\rm acc}c = \pi\alpha' R_{\rm jet}\Gamma/2$ along z, $\bar{\alpha}'$ corresponds to the energy for which $T_{\rm acc}c = H$.

In summary, the conditions

$$\mathcal{R}_{\rm i} \lesssim \frac{R_{\rm jet}}{2\Gamma^2}; \quad \mathcal{R}_{\rm i} \lesssim \frac{2}{\pi}\frac{H}{\Gamma^3} \approx \frac{H}{\Gamma^3} \tag{3.15}$$

express the constraints on the transverse ($R_{\rm jet}$) and longitudinal (H) sizes of a region with Lorentz factor Γ that allow particles with initial Larmor radius $\mathcal{R}_{\rm i}$ to achieve the maximum theoretical energy boost $\sim \Gamma^2$. Both conditions can phys-

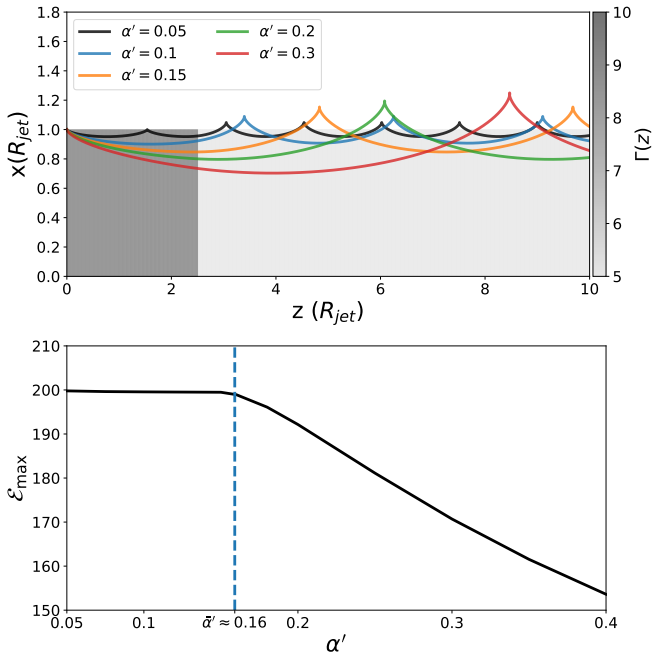

Figure 3.2: Top panel: trajectories of five particles with different Larmor radii (equation 3.8) in a jet with a variable $\Gamma(z)$ as shown on the colormap. Bottom panel: maximum energy gain $\langle \mathcal{E}_{\rm max} \rangle$ for a range of particles with different α'; $\bar{\alpha}' \simeq 0.16$ is the maximum Larmor radius that allows particles to complete at least one-quarter of a gyration in the high-Γ region and thus achieve the largest boost.

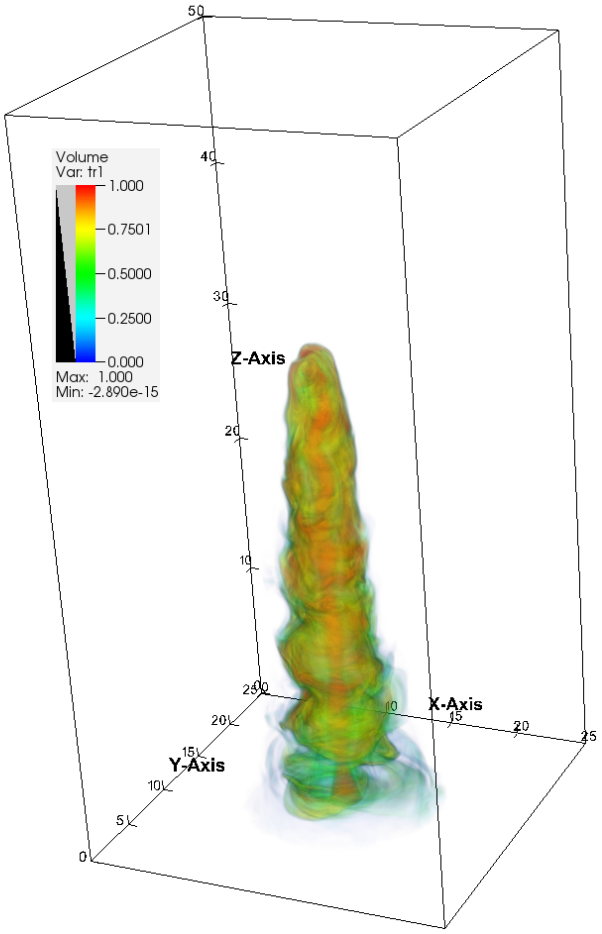

Figure 3.3: 3D MHD simulation of a relativistic jet launched with Lorentz factor $\Gamma_0 = 7$. The rendering shows the variable τ, a tracer of the relative local abundance of jet/ambient material; $\tau = 1$ and $\tau = 0$ indicate pure jet and ambient material, respectively. Lengths are in units of jet diameter ($2R_{\rm jet}$).

ically be interpreted as the Hillas criterion in the transverse and longitudinal directions, where in the longitudinal direction particles see a relativistically contracted region. Note that both conditions correspond to requiring the *final* Larmor radius $\mathcal{R}_{\rm f}$ to be at most comparable to the size of the system.

3.1.2 Propagation in a Full MHD Simulation

In order to properly capture all the properties of a realistic astrophysical jet, we performed 3D MHD simulations with the PLUTO code (Mignone et al., 2012), which includes adaptive mesh refinement (AMR). A relativistic magnetized jet is

launched in an unmagnetized uniform ambient medium, with a setup similar to the simulations presented in (Mignone et al., 2010). The jet is launched along the z-direction through a cylindrical nozzle with a magnetization radius $R_{\rm jet}$ in a box that measures $48R_{\rm jet}$ in the x- and y-directions and $100R_{\rm jet}$ in the z-direction. The grid has $512 \times 512 \times 1024$ cells with four AMR levels, which allows us to resolve the instabilities at the jet–ambient medium interface in great detail. The characteristics of the system are specified by the jet/ambient density contrast ψ, the launching Lorentz factor of the jet Γ_0, and the jet sonic and Alfvénic Mach numbers $M_s \equiv c/c_s$ and $M_A \equiv c/v_A$, where c_s and v_A are the sound speed and Alfvén speed, respectively; our fiducial parameters are $\psi = 10^{-3}$, $\Gamma_0 = 7$, M_s =3, and $M_A = 1.67$. The jet is initialized with a purely toroidal magnetic field component such that:

$$B_\phi(r) \propto \begin{cases} r & \text{for } r < R_{\rm jet} \\ 1/r & \text{for } R_{\rm jet} < r < 2R_{\rm jet} \\ 0 & \text{for } r > 2R_{\rm jet} \end{cases}$$

The overall jet structure does not depend on the details of the initial magnetic field (except for the sign of B_ϕ), since MHD simulations self-consistently produce a balance between toroidal and poloidal components that is directly connected to the jet stability, (see, e.g. Tchekhovskoy & Bromberg (2016a) and references therein). Finally, we scale the magnetic field with respect to its initial value at the magnetization radius $B(r = R_{\rm jet}) \equiv B_0$, which is defined by the chosen Alfvénic Mach number.

The simulations considered in this work cannot cover all the possible realizations of an AGN jet. For instance, varying the galactic density/temperature profile is known to affect the jet shape (e.g., Tchekhovskoy & Bromberg, 2016a), and it is likely that varying the jet Lorentz factor, luminosity, and magnetization may lead to diverse jet morphologies. Nevertheless, our fiducial simulation and

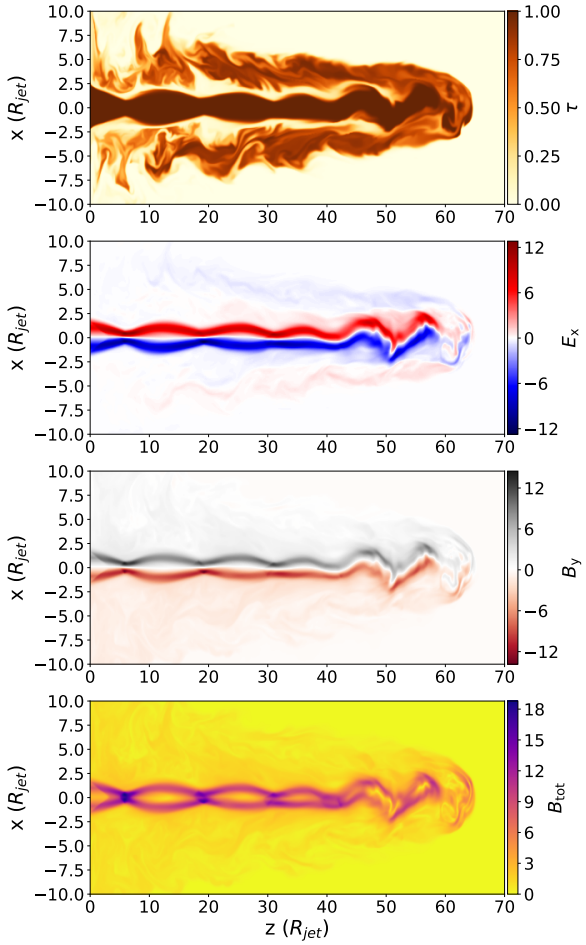

Figure 3.4: From top to bottom: 2D maps ($y = 0$) of: τ, a tracer of the relative abundance of jet/ambient material; $E_{\rm x}$, a proxy for the radial component of E; $B_{\rm y}$, proxy for the toroidal component of B; and modulus of B in units of B_0.

the analytical formalism of §3.1.1 allow us to characterize the general features of the acceleration mechanism in relativistic jets.

Figure 3.3 shows the volume rendering of the tracer variable τ for our benchmark run; τ represents the local fraction of jet material, such that $\tau = 0$ corresponds to pure ambient medium and $\tau = 1$ to pure jet medium. Jet and ambient material are well mixed, attesting that the Kelvin–Helmholtz instability in the cocoon and the wobbling of the jet lead to an effective mass entrainment (e.g., Mignone et al., 2010; Tchekhovskoy & Bromberg, 2016a). This means that galactic-like CRs embedded in the ambient medium can also be easily entrained

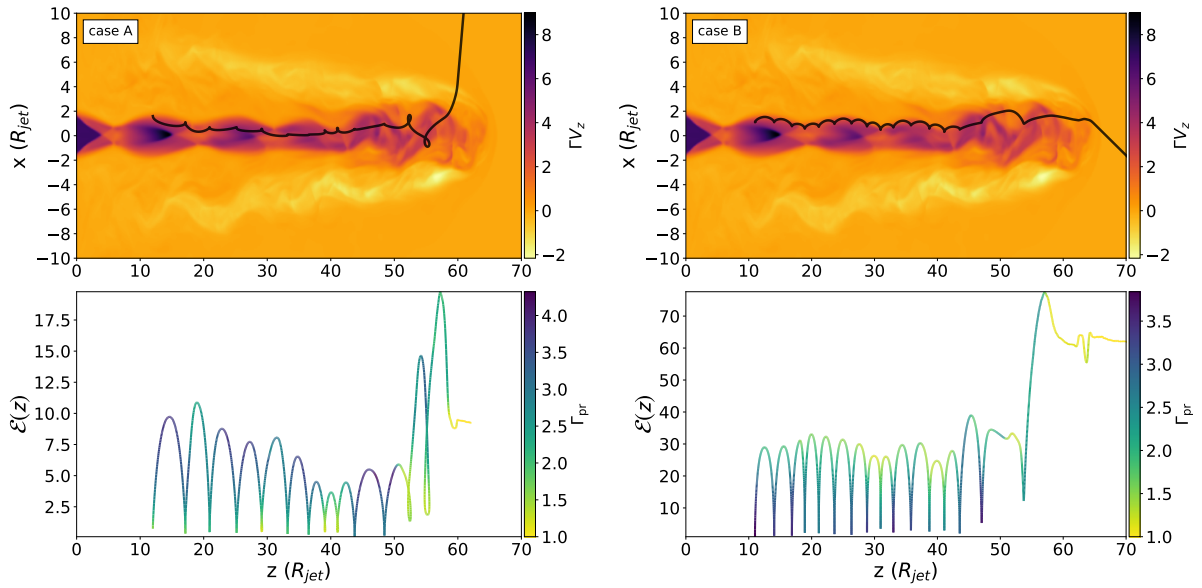

Figure 3.5: Trajectory and energy gain for representative particles in case A (left panels) and B (right panels). Top panels: particle trajectory overplotted on the 4-velocity component Γv_z of the flow. Bottom panels: energy evolution as a function of position along z, color coded with the instantaneous Lorentz factor probed, $\Gamma_{\rm pr}$. Case A and case B particles are initialized with $\alpha_{\rm i} = 0.42$ and $\alpha_{\rm i} = 0.13$, respectively, and both gain energy up to the Hillas limit, i.e., $\alpha_{\rm f} \simeq 5.9$ and $\alpha_{\rm f} \simeq 6.34 \approx \alpha_{\rm H}$. Note how both particles gain energy well in excess of $\Gamma_{\rm pr}^2$ through two *espresso* shots.

and be brought in contact with the most relativistic jet layers even without diffusing. Figure 3.4 shows 2D maps of E_x and B_y, which in the considered plane ($y = 0$) correspond in modulus to the radial and toroidal components of the electric and magnetic field, respectively. These variables trace the morphology of the different jet regions (the spine, for $r/R_{\rm jet} \lesssim 2$, and the cocoon, for $2 \lesssim r/R_{\rm jet} \lesssim 6$). We can see that the motional electric field $E_r \simeq v_z B_\phi$ reverses its sign between the two regions. This ultimately affects trajectories and fate of the reaccelerated particles, as we will explain more in detail in the following sections.

Particle Trajectories

For both case A and case B, we propagate ∼100,000 test-particle protons with a broad range of initial Larmor radii $\mathcal{R}$ and positions; the trajectories of nuclei

with charge $q = Ze$ can be derived simply by considering protons with the same rigidity $\rho \equiv E/q$, whose Larmor radius is $\mathcal{R} = \frac{E}{ZeB} = \frac{\rho}{B}$. We account for the two possible orientations of the toroidal magnetic field by flipping the sign of the propagated particles, so we can use the same MHD background and consider both case A ($B_\phi < 0$) and B ($B_\phi > 0$). We initialize protons with normalized Larmor radii logarithmically spaced in the interval $\alpha_{\rm i} = \frac{\rho}{B_0 R_{\rm jet}} \in [10^{-3.6}, 8]$ in order to cover an extended range of initial rigidities up to the Hillas limit, where particles should traverse the entire flow without significant acceleration. We notice that the actual strength of the magnetic field in the spine is larger than B_0 (see Figure 3.4): averaging over the regions where $\Gamma \geq 2$ returns $B_{\rm eff} \sim 7.2 B_0$, so that the effective Hillas condition (equation 3.15) is met for $\alpha_{\rm H} \sim 7.2$.

Particles are initialized at linearly spaced positions $(r_{\rm i}, \phi_{\rm i}, z_{\rm i})$ around the spine of the jet such that $r_{\rm i}/R_{\rm jet} \in [0.2, 5]$, $z_{\rm i}/R_{\rm jet} \in [2, 60]$ and $\phi_{\rm i} \in [0, 2\pi]$. The initial pitch angles are also linearly spaced with $\mu_{\rm i} \in [-0.5, 0.5]$ and $\xi_{\rm i} \in [-1, 1]$ (see definitions in §3.1.1).

Particle trajectories in the MHD jet show many features common with those discussed above for simplified jets. Figure 3.5 illustrates two examples of *espresso*-accelerated particles for case A and case B (left and right panels, respectively). The top panels show the particle trajectories overplotted on a 2D slice of the z component of the flow velocity, while the bottom panels show their energy gain $\mathcal{E}$ as a function of z; the color code indicates the instantaneous Lorentz factor that they probe, $\Gamma_{\rm pr}$.

The case A particle (left panels) gains a factor of $\sim \Gamma_{\rm pr}^2$ in energy during its first gyrations, where $\Gamma_{\rm pr} \lesssim 3.6$, and then encounters a major jet kink at $z \gtrsim 54 {\rm R_{jet}}$, which fosters another energy boost, though with a smaller Γ. Eventually, the particle loses some energy in crossing the cocoon and escapes the system with the canonical $\sim \Gamma_{\rm pr}^2$ energy gain. The case-B particle (right panels) first gains a

factor of $\sim 2\Gamma_{\rm pr}^2$, then undergoes another boost around $55 - 60R_{\rm jet}$, and is finally released with a total energy gain $\mathcal{E} \sim 50$, well in excess of $\Gamma_{\rm pr}^2$. Both particles gain energy up to the Hillas limit, though: the case A particle has an initial Larmor radius $\alpha_{\rm i} = 0.42$ and escapes the jet with $\alpha_{\rm f} \simeq 5.9 \approx \alpha_{\rm H}$, while the case B particle is initialized with $\alpha_{\rm i} = 0.13$ and escapes the jet with $\alpha_{\rm f} \simeq 6.34 \approx \alpha_{\rm H}$. It is important to stress that acceleration occurs when particles plunge into the relativistic flows, and neither at the interface between the spine and the cocoon, where the velocity shear is the largest (the boundary between the red and blue regions in Figure 3.5), nor in wake shocks.

These paradigmatic particle trajectories show that, regardless of the sign of the motional electric field, (i) energization occurs because of *espresso* acceleration, and not because of stochastic or diffusive processes; (ii) energy gains significantly larger than $\Gamma_{\rm pr}^2$ are possible and are favored by a nonuniform, turbulent jet that allows multiple acceleration cycles; (iii) crossing the cocoon, which has an electric potential opposite to the jet's, induces some energy losses that are generally smaller than the gain due to *espresso* acceleration; and (iv) particles tend to gain energy up to the Hillas limit.

Energy Gain Dependence on Γ

It is crucial to point out that, even if the jet is launched with $\Gamma_0 = 7$, most of the jet material moves with typical Lorentz factors smaller than Γ_0. The histogram in Figure 3.6 shows the distribution of Lorentz factors in the relativistic flow (defined as regions where $\Gamma \geq 2$). Only a few percent of the jet (in volume) moves with $\Gamma \sim \Gamma_0$, most of the material having $\Gamma \lesssim 5$; more precisely, the mean value of Γ in the relativistic regions, which we use to define an effective $\Gamma_{\rm eff}$, is ~ 3.2. Regions with $\Gamma > 7$ are rare and a consequence of the jet pinching.

Figure 3.6 also shows the average $\mathcal{E}_{\rm max}$ as a function of the largest Lorentz fac-

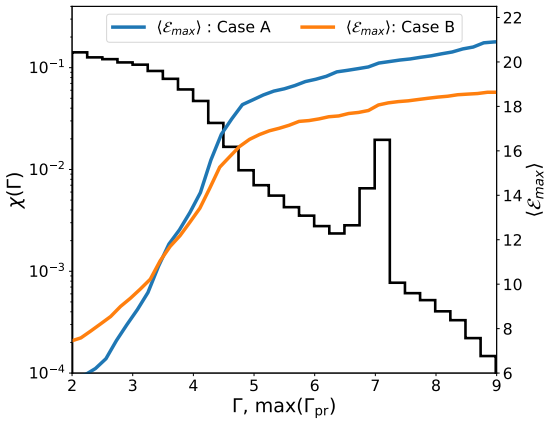

Figure 3.6: Maximum energy gain averaged on particles with $\mathcal{E} \geq 2$ ($\langle \mathcal{E}_{\rm max} \rangle$, right axis), as a function of the maximum Γ probed by each particle ($\Gamma_{\rm pr}$). χ (left axis) represents the filling factor of regions with a given value of Γ in the jet spine. Note that, even if the jet is launched with $\Gamma_0 = 7$, most of the jet has a $\Gamma \leq 4$ with an average value $\Gamma_{\rm eff} \sim 3.2$; the particle energy gain flattens for $\Gamma_{\rm pr} \gtrsim \Gamma_{\rm eff}$ because of the longitudinal Hillas criterion (Equation 3.15).

tor that particles probe along their trajectories. We can distinguish two regimes of acceleration depending on whether regions with a given Γ have a large/small filling factor. On average, particles that experience regions with $\Gamma \lesssim \Gamma_{\rm eff}$ achieve the full Γ^2 energy boost, while the energy gain saturates to $\mathcal{E} \approx 15 - 20$ for particles that probe regions with larger Lorentz factors. The explanation for this trend hinges on the longitudinal condition in equation 3.15, which may be easily violated for the most relativistic regions. For instance, in our MHD simulation a typical particle with $\alpha \sim 0.01$ would need a region with $\Gamma \gtrsim 7$ that is as large as $\gtrsim 6 R_{\rm jet}$ to be fully boosted, while in reality these regions are rare and/or much smaller.

In summary, particle energy gains are consistent with the *espresso* prediction of $\mathcal{E} \gtrsim \Gamma_{\rm eff}^2$, where $\Gamma_{\rm eff}$ is the largest Lorentz factor that has a nonnegligible filling factor; by the same token, $\Gamma_{\rm eff}$ should also be the characteristic Lorentz factor inferred from multiwavelength observations of AGN jets.

Strictly speaking, CR seeds live in the ambient medium, but the vigorous mass

entrainment effectively convects them inside the cocoon (Figure 3.3). On top of such a convective entrainment, seeds should diffuse through the ambient/jet interface thanks to both large-scale and microscopic turbulence. The role of large-scale turbulence is captured by the high resolution of our MHD simulation, while subgrid magnetic fluctuations are not accounted for in the present work. In order for particles to be *espresso* accelerated, they need to reach the relativistic regions of the jet and the rate of percolation of seed particles into the jet spine may be enhanced by pitch-angle scattering due to small-scale fluctuations; therefore, our results can be viewed as a *lower limit* on the jet effectiveness in injecting seeds into the *espresso* mechanism.

Figure 3.7 illustrates the correlation between the particle initial position and final energy gain for seeds with $\alpha_{\rm i} = 0.2$, $\mu_{\rm i} = 0$, and $\xi_{\rm i} = 1$. The top panel shows the distribution of $\Gamma(x, z)$ in a slice at $y = 0$, while the middle and bottom panels show the maps of $\mathcal{E}(x, z)$ for case A and case B, respectively. In both cases particles typically gain at least a factor of $\sim \Gamma_{\rm eff}^2$ in energy, but particles initialized in the highly relativistic regions generally gain even more; the same trend is observed regardless of the initial parameters. The motivation for this correlation is that after the first acceleration shot the particle momentum is preferentially along $+z$ ($\mu \approx 1$), which tends to reduce the energy gain of the following cycles (see equation 3.7); therefore, the possibility of having multiple shots relies on large-scale jet perturbations, in particular spine kinks and jet wobbling. Also, pitch-angle scattering due to small-scale turbulence generally helps breaking the correlation between in- and out-going angles, thereby fostering multiple acceleration cycles.

Energy Distribution of the Accelerated Particles

Figure 3.8 shows the spectrum of the escaping particles (solid black line), divided in the spectra produced by particles with a given initial $\alpha_{\rm i}$ (color lines). Four fea-

tures are noteworthy, (i) low-energy particles can be *espresso*-accelerated multiple times; for them energy gains $\mathcal{E} \gtrsim 100$ are common; (ii) the fraction of particles that are not reaccelerated increases at both extremes of the $\alpha_{\rm i}$ range; the optimal rigidity range for reacceleration is $\alpha_{\rm i} \in\sim [0.01, 1]$; (iii) the final spectrum is truncated at $\alpha_{\rm H} \sim 7.2$, a manifestation of the Hillas criterion; (iv) the final spectrum tends to be flatter than the injected one because particles pile up close to the Hillas limit.

We have already discussed how seeds with $\alpha \gtrsim 1$ do not gain much energy because they cannot complete one gyration in the flow; here we notice that for smaller and smaller $\alpha_{\rm i}$ the peaks in the color histograms in Figure 3.8 are more and more marked, attesting that a larger and larger fraction of the particles is not reaccelerated, the reason being that it is hard for low-energy particles to penetrate deep into the jet spine. The low-energy particles that manage to be reaccelerated often exhibit a double-*espresso* shot with $\mathcal{E} \gtrsim 100$, but do not necessarily make it up to the Hillas limit. This may be due to the limited dynamical range achievable in 3D MHD simulations: a realistic AGN may show multiple kinks and accommodate even three or more shots and pile even more particles up at the Hillas limit. In general, we expect that the spectrum of reaccelerated particles should become rather flat at low energies, consistent with modeling the UHECR flux and composition (e.g., Gaisser et al., 2013; Aloisio et al., 2014b; Taylor, 2014).

Energy Gain Dependence on Initial Positions

Multiple acceleration also shots ease the requirement of having $\Gamma = 30$ for producing UHECRs starting from Galactic CRs that have a knee at a few PeV (C15), in the sense that the required energy gain $\mathcal{E} \sim 10^3$ could be achieved even in AGNs with smaller $\Gamma_{\rm eff}$. Since the maximum energy gain scales as $\Gamma_{\rm eff}^{2N}$, where N is the number of *espresso* cycles, even a moderate $\Gamma_{\rm eff} \gtrsim 3$ and 3-4 shots could lead to UHECR production. By the same token, multiple shots could provide $\mathcal{E} \gtrsim 3 \times 10^3$

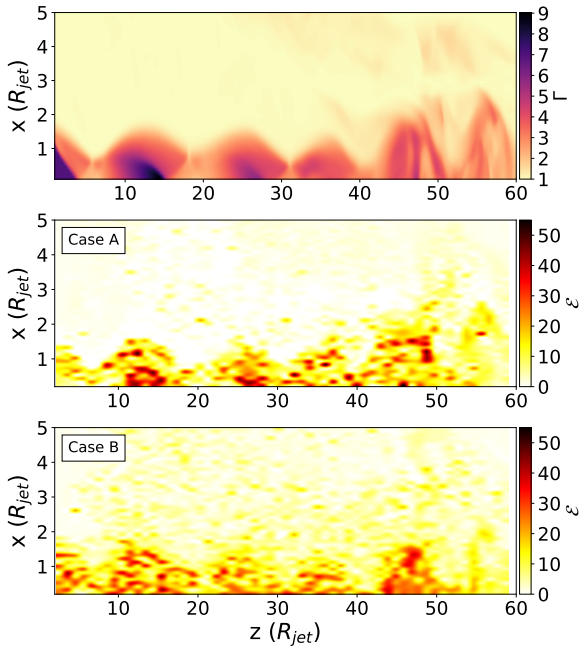

Figure 3.7: 2D slices showing the correlation between the local value of Γ (top panel) and the energy gain of particles initialized with $\alpha_{\rm i} = 0.2$, $\mu_{\rm i} = 0$, and $\xi_{\rm i} = 1$ in the $x - z$ plane (middle and bottom panels: case A and case B, respectively). Generally, larger energy gains are achieved for seeds that make it to regions where Γ is larger.

and thus allow nitrogen and oxygen nuclei to reach the canonical 10^{20} eV, relaxing the need to have iron nuclei at the highest energies.

Espresso and Stochastic Acceleration Processes

It is worth discussing how the energization process that we observe is distinct from other processes suggested in the literature, such as stochastic shear acceleration, DSA in the cocoon, and turbulent acceleration (e.g., Ostrowski, 2000; O'Sullivan et al., 2009; Hardcastle et al., 2009; Kimura et al., 2018; Matthews et al., 2019).

First of all, in our simulations all of the accelerated particles gain energy through one or at most two/three shots. Their trajectories closely resemble the ordered gyrations outlined in §3.1.1 (Figure 3.5), with no evidence of spatial random walk and pitch-angle scattering between two successive shots. Multiple shots are typically due to large-scale kinks in the jet, rather than to pitch-angle diffusion.

In stochastic shear acceleration, instead, particles are expected to be accelerated at the interface between the cocoon and the jet (Ostrowski, 1998, 2000; Kimura et al., 2018) and to diffuse throughout the cocoon; the same random walk in the cocoon should also be present if acceleration were due to second-order Fermi processes (e.g., Hardcastle et al., 2009; O'Sullivan et al., 2009) or DSA in the backflowing material (Matthews et al., 2019). However, in our simulations, acceleration always occurs *within the jet* (i.e., in relativistic regions where $\tau = 1$, i.e., pure jet material), consistently with the *espresso* scenario.

These results suggest that, when an ultrarelativistic jet spine is present, such as in FR II and in subkiloparsec scales of FR I AGNs, acceleration proceeds via the *espresso* mechanism, typically up to the Hillas limit. Our simulations cannot exclude that stochastic acceleration might play some role when the jet becomes trans/nonrelativistic, although such processes have never been quantified

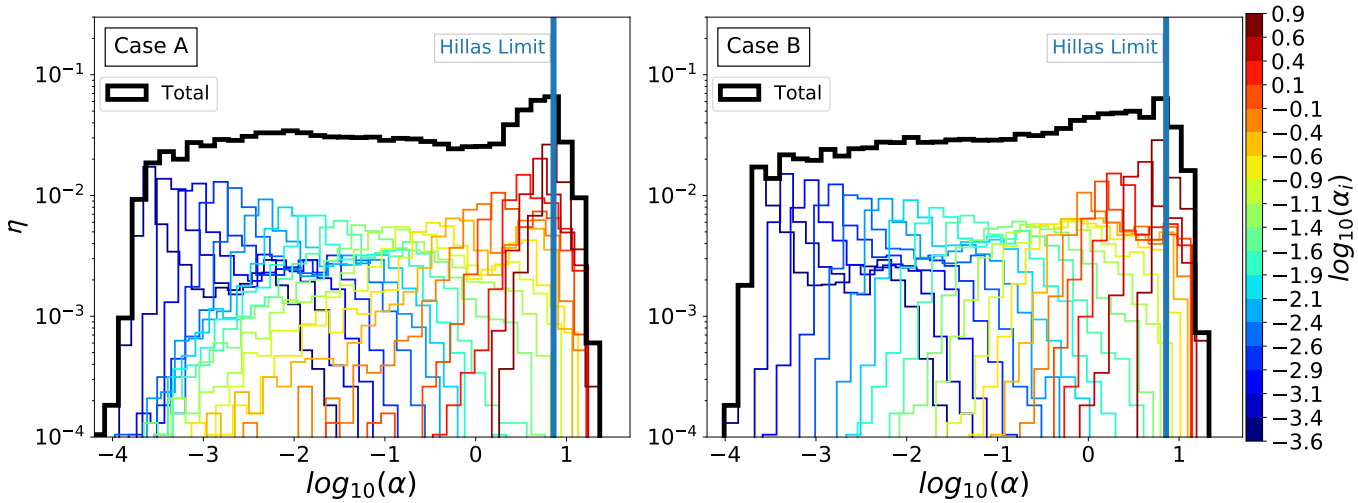

Figure 3.8: Distribution of the Larmor radii of reaccelerated particles obtained for an injection spectrum flat in the interval $\alpha_{\rm i} \in [10^{-3.6}, 8]$, for both case A and case B (left and right panels, respectively). The thick black line shows the cumulative spectrum, while colored histograms correspond to initial Larmor radii as in the color bar. Seeds with $\alpha_{\rm i} \lesssim 1$ can undergo boosts as large as $\sim 50-100 \gg \Gamma_{\rm eff}^2$, while for $\alpha_{\rm i} \gtrsim 1$ the energy gain is smaller and saturates at $\alpha_{\rm H} \approx 8$ (Hillas criterion; see equation 3.9).

via bottom-up calculations in environments with self-consistent MHD configurations, but only with Monte Carlo simulations where jet/cocoon structures are prescribed and pitch-angle scattering imposed by hand.

Our simulations, while showing that espresso acceleration in relativistic jets *can* be more prominent than stochastic processes for UHECR production, of course cannot prove that stochastic acceleration cannot ever matter. For instance, it is possible that stochastic acceleration might reenergize the seed population and/or produce lower-energy particles responsible for the observed radio emission (e.g., Stawarz & Ostrowski, 2002).

3.1.3 *Espresso* Acceleration in Astrophysical Jets

Let us now consider the results above in the context of typical AGN jets and for different species in seed CRs. In the MHD simulation, Larmor radii are normalized to the jet radius and the initial magnetic field; if we set $R_{\rm jet} \sim 15$ pc and

$B_0 \sim 1\mu$G, we can associate physical rigidities to the propagated particles, and the rigidity of the knee, $\rho_{\rm knee} \simeq 3 \times 10^6$ GV, would correspond to $\alpha \simeq 0.2$. In this section we focus only on particles that have initial rigidities $\rho_{\rm i} \in 3 \times [10^3, 10^6]$ GV.

Following C15, we parameterize the energy flux of galactic CR seeds below the knee as

$$\phi_s(E) = K_s \left(\frac{E}{10^{12}\ {\rm eV}} \right)^{-q_s}, \tag{3.16}$$

where we consider the CR species s =[H, He, C/N/O, Fe] as grouped according to their effective atomic number $Z_s = [1, 2, 7, 26]$ and mass $A_s = [1, 4, 14, 56]$. The normalizations are chosen according to the abundance ratios at 10^{12} eV such that $K_s/K_H \sim$ [1, 0.46, 0.30, 0.14]. The spectral slope observed at Earth is $q_H \simeq 2.7$ for protons and $q_{s\neq H} \simeq 2.6$ for heavier ions, a manifestation of the so-called *discrepant hardening* (Ahn et al., 2010; Caprioli et al., 2011). However, a conservation argument suggests that seeds in the galactic halo must have a spectrum parallel to the injection one, which should be significantly harder and closer to the universal spectrum produced at strong SNR shocks ($q_s = 2$, e.g., Bell, 1978; Blandford & Ostriker, 1978) or at most $q_s = 2.2 - 2.3$ as suggested by γ-ray observations of young SNRs (Caprioli, 2011, 2012), anisotropy constraints (Blasi & Amato, 2012a,b), and secondary/primary abundances in Galactic CRs (e.g., Aguilar et al., 2016). A value of q_s closer to the injection slope may also be realized in galaxies denser or bigger than the Milky Way, where spallation losses may dominate over diffusive escape (see the discussion in Caprioli, 2018). For these reasons, we initialize the seeds with the abundances above, $q_s = 2$, and introduce an abrupt rigidity cutoff at $\rho_{\rm knee} = 3 \times 10^6$ GV to facilitate the discrimination between seeds and reaccelerated particles.

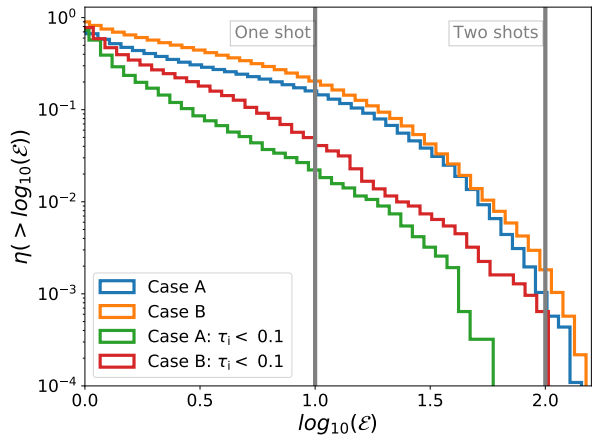

Figure 3.9: Cumulative distribution of the energy gains of particles with initial rigidity $\rho_i \in 3\times[10^3, 10^6]$ GV, for both case A and case B. Upper curves correspond to particles initialized in the whole domain (see §3.1.2), while lower curves consider only particles initialized in regions where $\tau \leq 0.1$, i.e., in the entrained ambient medium. The two vertical lines correspond to single- and double-*espresso* shots with Lorentz factor $\Gamma_{\rm eff}$.

Injection Efficiency

Figure 3.9 shows the cumulative distribution of the final energy gains of particles with $\rho_i \in 3 \times [10^3, 10^6]$ GV, for both case A and case B. If we consider the whole injection domain defined in §3.1.2 (upper curves), we find that $\sim 38\%$ ($\sim 53\%$) of case A (B) particles gain at least a factor of 2 in energy, and about $\sim 14\%$ ($\sim 18\%$) of case A (B) particles gain a factor of $\Gamma_{\rm eff}^2$. Also, $\sim 0.06\%$ ($\sim 0.18\%$) of the particles achieve an energy gain of 100 or more in case A (B), corresponding to $\mathcal{E} \gtrsim \Gamma_{\rm eff}^4$, i.e., two full *espresso* shots. The particles that do not gain much energy belong to the extremes of the range of initial rigidities: they either traverse the spine of the jet without gyrating because of their large Larmor radius, or had a Lorentz factor too small to enter the flow.

Including all the particles in the domain means assuming that particles can diffuse from ambient to jet medium, filling the domain in a uniform fashion. Instead, assuming that seeds are confined to the entrained ambient material only

(regions with $\tau < 0.1$) returns a *lower limit* on the fraction of seeds that can be reprocessed by the jet (bottom curves in Figure 3.9). In this case we find that $\sim 14\%$ ($\sim 27\%$) of case A (B) particles gain at least a factor of 2 in energy, and about $\sim 2\%$ ($\sim 4\%$) of case A (B) particles gain a factor of $\Gamma_{\rm eff}^2$, as shown in Figure 3.9. We also find that $\sim 0.06\%$ of the particles in case B achieve an energy gain of 100, while particles in case A do not make it up to such a threshold. While it is indeed possible that the sign of the toroidal magnetic field may affect the fraction of particles that get multiple shots, diffusion is expected to be effective at some level in realistic systems. The fractions quoted above do not depend much on the chosen range of rigidity, but it is clear from Figure 3.8 that the injection efficiency would be quite larger if we only considered particles with $\alpha_{\rm i} \gtrsim 0.01$. In summary, we conclude that a fraction $\eta \approx 3 - 20\%$ of the seeds has to be reprocessed by at least one shot, and that about 0.05–0.1% can undergo two or more shots. Since a fraction $\eta \gtrsim 10^{-4}$ is needed to account for the UHECR flux in the one-shot scenario (C15), we conclude that realistic AGN jets should be able to reaccelerate enough CR seeds to produce UHECRs.

FR I jets tend to wobble and exhibit multiple kinks (e.g., Mignone et al., 2010; Tchekhovskoy & Bromberg, 2016a), which may favor multiple acceleration cycles and allow the acceleration of UHECRs in sources such as Centaurus A (see the discussion in §3.1.2).

The Spectrum of Released Particles

The *espresso* model predicts that the chemical composition observed in galactic CRs, which is increasingly heavy above 10^{13} eV and dominated by iron nuclei around 10^{17} eV (e.g., Hörandel et al., 2006; Kampert & Unger, 2012), should be mapped into UHECRs. Auger observations suggest a proton-dominated flux at 10^{18} eV and a heavier composition at higher energies, which is consistent with

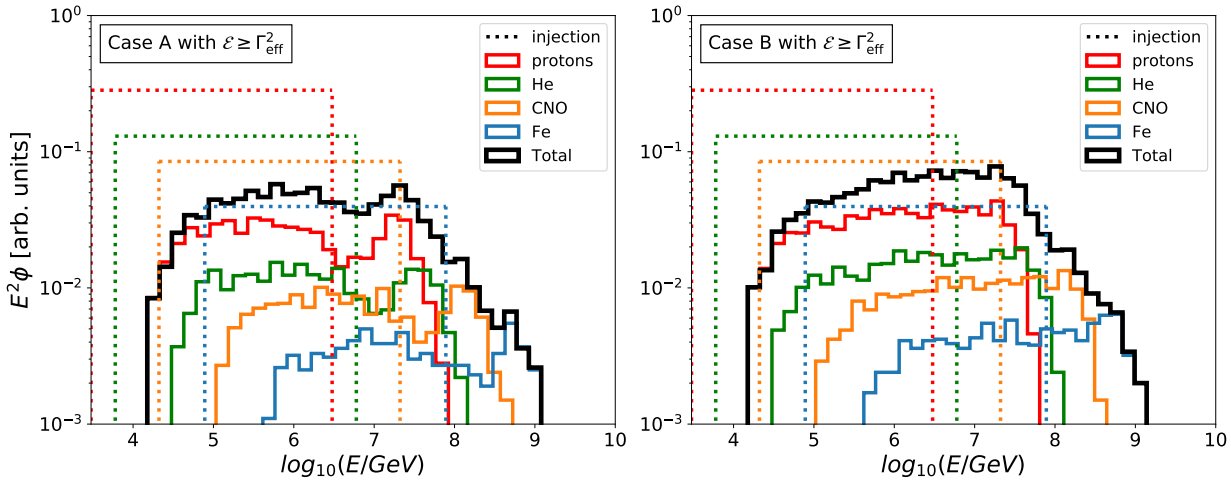

Figure 3.10: Energy spectrum of the particles that undergo at least one *espresso* shot and escape the jet (solid lines), assuming the injection spectrum in equation 3.16 (dotted lines). The thick black line illustrates the all-particle spectrum. Left and right panels correspond to case A and case B, respectively.

such a scenario. Figure 3.10 shows the energy spectrum produced in our fiducial MHD jet once galactic CRs are initialized as discussed above. We only consider particles that gained $\mathcal{E} \gtrsim \Gamma_{\rm eff}^2$ to eliminate reacclerated particles that should not contribute to the UHECR flux.

The cutoffs of seed species are boosted up in energy by a factor of $\Gamma_{\rm eff}^2 \sim 10$, consistently with the results in §3.1.2, and spectra exhibit a high-energy tail because of the particles that underwent multiple acceleration cycles. Below the cutoffs spectra are still power laws: parallel to the seed ones in case A, and slightly harder than the seed ones in case B (see also Figure 3.8). Modeling the UHECR flux and composition above 10^{18} eV (e.g., Gaisser et al., 2013; Aloisio et al., 2014b; Taylor, 2014) favors rather hard injection spectra ($\propto E^{-1.5}$ or flatter), which may seem hard to obtain with *espresso* reacceleration. Nevertheless, since particles tend to pile up close to the Hillas limit and since particles with $\alpha_{\rm i} \ll 1$ are hardly reaccelerated, the spectrum of accelerated particles naturally flattens at low energies (see Figure 3.8), in agreement with the models above, which assume single power law injection spectra.

Unfortunately, the limited effective Lorentz factor and the intrinsic Hillas limit of our simulations do not allow particles to be accelerated beyond 10^{18} eV; since the proton spectrum cuts off quite close to the seed iron spectrum, we cannot directly observe the typical light–heavy–light–heavy modulation predicted in C15, either. In other words, the resolution of our fiducial MHD simulation forces us to initialize knee CRs with a Larmor radius that is too close to the jet scales for accommodating the $\mathcal{E} \sim 10^3$ energy gain required to produce 10^{20} eV particles. The extrapolation of our results to jets with larger Lorentz factors and/or with larger dynamical range between the seed rigidities and the jet extent is straightforward and is discussed in the following sections.

Dependence on the Jet Lorentz Factor

Although we initialized our fiducial jet with $\Gamma_0 = 7$, the Lorentz factor that we would infer from a multiwa velength analysis of its emission would be smaller (see Figure 3.6). Radio observations do not rule out the existence of an extended, ultrarelativistic jet spine even in ordinary AGNs (e.g. Chiaberge et al., 2001; Ghisellini et al., 2005); moreover, they suggest that FR I and FR II spines should have no appreciable differences in their initial Lorentz factors (Giovannini et al., 2001; Casandjian & Grenier, 2008). In general, high-resolution relativistic MHD simulations (e.g. Mignone et al., 2010) show that the relativistic spine may extend for hundreds of jet radii up to the termination shock at the jet's head; even if deceleration is observed in the outer layers of jets, the Lorentz factor of the spine typically remains unchanged from the injection value (Rossi et al., 2008). This picture should mainly apply to FR II jets since the relativistic component exceeds many kiloparsecs in length as we discuss in section 3.1. Modeling hyper-relativistic flows in 3D MHD simulations is extremely challenging, so we resort to extrapolating our findings to realistic jets by scaling the measured energy gain with the

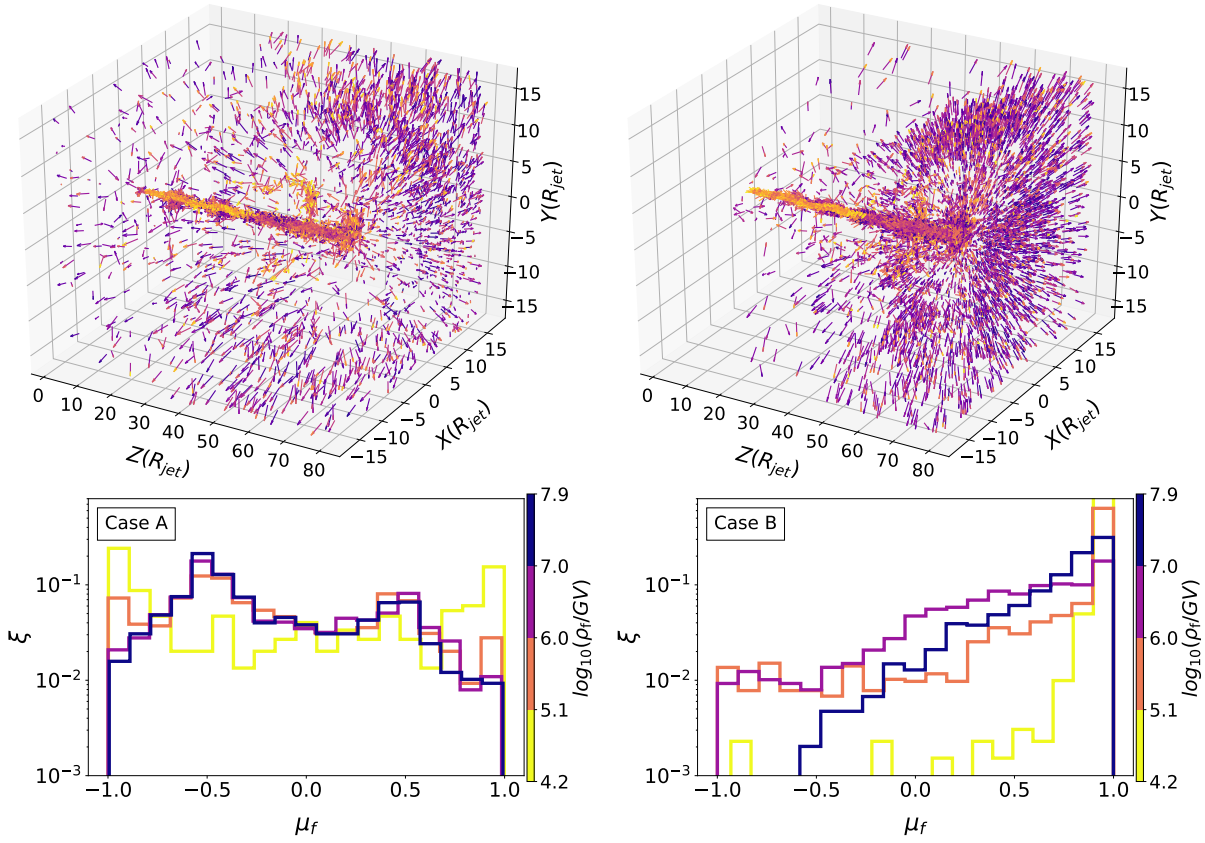

Figure 3.11: Top panels: final direction of flight for *espresso*-accelerated particles with $\mathcal{E} \gtrsim \Gamma_{\rm eff}^2$ and $\rho_{\rm i} \in 3 \times [10^3, 10^6]$ GV. Bottom panels: distribution of the corresponding cosines of the final angle of flight. Particles are color coded according to their final rigidity, as in the colorbar. In case A (left panels) particles are released quasi-isotropically, while in case B they are beamed along the jet axis; such a difference can be ascribed to the sign of the motional electric field in the cocoon, which controls the final escape direction.

jet Lorentz factor.

From figure 3.6 we see that the typical energy gain increases as $\mathcal{E} \propto \Gamma^2$ up to $\Gamma_{\rm eff} \sim 3.2$ and then levels off because the filling factor of regions with $\Gamma \gtrsim \Gamma_{\rm eff}$ is small. By the same token, it is reasonable that also a multiwa velength analysis would preferentially highlight regions with $\Gamma \lesssim \Gamma_{\rm eff}$; the most relativistic regions of the jet may still be the source of the jet fast variability and produce interesting relativistic effects (e.g., Giannios et al., 2009, and references therein). If the results above were extrapolated to the typical Lorentz factors inferred in

powerful AGNs, i.e., for $\Gamma_{\rm eff} \approx \Gamma_{\rm AGN}$, about 10% of the CR seeds should consistently achieve energy gains as large as $\Gamma_{\rm AGN}^2$ (Figure 3.9), which would saturate the Hillas limit and produce the highest-energy CRs.

As discussed in C15, it is reasonable that the knee rigidity $\rho_{\rm knee} \approx 3$ PeV does not depend much on the host galaxy. Assuming that the highest-energy galactic CRs are produced in SNRs around the Sedov stage, and that in the interstellar medium there is roughly equipartition between magnetic energy and thermal gas motions, one finds $\rho_{\rm knee} \propto n_g^{1/6} M_g^{1/2}$, where n_g and M_g are the number density and total mass of the galaxy considered. Moreover, since the elemental composition is determined by the intrinsic dependence of ion injection into DSA (Caprioli et al., 2017), the elemental composition of seeds in other galaxies should resemble the one in the Milky Way, too. Finally, it is also possible that multiple episodes of AGN activity produced circumgalactic halos much more turbulent than the Galactic one, which results is a more effective confinement of both CRs accelerated in SNRs and low-energy reaccelerated ones. Such an effect may change the slope and normalization of the seed spectrum, but it would systematically go in the direction of making it flatter and enhanced.

Angular Distribution of Reaccelerated Particles

A natural question is whether we should expect a correlation between the UHECR directions of arrival and the local AGN population; such a question is intimately connected to how particles are released from their sources, i.e., whether reaccelerated particles are strongly beamed along the jet or not. In the first case, UHECRs might preferentially come from AGN jets that point at us (from BL-Lac and flat-spectra-radio quasars), while in the second case all radio-loud AGNs may contribute, generally producing a more isotropic signal.

Intergalactic (and possibly galactic) magnetic fields may scramble the UHECR

trajectories enough to break any correlation, but magnetic turbulence and hence scattering rates are quite uncertain in this respect. With our simulations we can however quantify if reaccelerated particles are preferentially released quasi-isotropically or beamed along the jet axis.

Figure 3.11 shows how reaccelerated particles with $\mathcal{E} > \Gamma_{\rm eff}^2$ are released. The vectors in the top panels illustrate the final directions of flight and the bottom panels show the distribution of $\mu_{\rm f}$, the cosine of the angle between the final particle velocity and the z-axis; colors correspond to different energy bins. The lowest-energy particles (yellow arrows) tend to remain confined close to the jet spine, while higher-energy particles are released with significantly different angular distributions in case A and case B. Case A particles escape quasi-isotropically, while case B ones are strongly beamed along the jet axis. The very reason for this discrepancy hinges on the sign of the radial electric field in the cocoon, $E_r = v_z B_\phi$, which reverses its sign in the two cases. In fact, particles preferentially move along the $+z$-direction while in the spine, but their final direction is determined by the deflection they experience after leaving the relativistic regions and entering the cocoon, where the flow is in the $-z$-direction (top panel of Figure 3.5). A different sign of B_ϕ in the jet produces a radial electric field that either disperses ($E_r > 0$, case A) or collimates ($E_r < 0$, case B) the flux of particles that escape the jet (Figure 3.4). Therefore, the final anisotropy of the particles is not determined by pitch-angle scattering in the cocoon turbulence, but rather by the global sign of the motional electric field. Note that also in case B about half of the highest-energy particles escape within an angle of $\sim 30^\circ$, a bit larger than the canonical relativistic beaming of $\sim \Gamma_{\rm eff}^{-1} \sim 20^\circ$. Also considering that the sign of B_ϕ might as well change during the AGN lifetime, we conclude that the UHECR emission is not necessarily beamed along the jet as strongly as its γ-ray emission.

The Potential Role of Nuclei Photodisintegration

Photodisintegration inside or around the sources may destroy heavy ions and, in general, affect the spectra of escaping UHECRs in a different way for protons and other species. For ballistic propagation, even the intense radiation fields in the broad line region of the most luminous AGNs should not affect the UHECR spectrum appreciably (e.g., Dermer, 2007). Nevertheless, Unger et al. (2015) pointed out that—in the presence of magnetic irregularities that scatter and increase the UHECR confinement time in/around their sources —heavy ions may easily be photodisintegrated. They also argue that the products of such a disintegration naturally account for the light composition observed below 10^{18} eV, with the Galactic to extragalactic transition populated with secondary protons, mainly. Fang & Murase (2018a) recently suggested that photodisintegration, photomeson production by secondary nucleons, and Bethe-Heitler pair production processes may also account for the flux of high-energy neutrinos measured by IceCube and for the GeV gamma-ray background measured by Fermi.

Relaxing the assumption that all the UHECR species are produced with the same slope also relaxes the requirement that the UHECR injection spectrum has to be quite flat (e.g., Gaisser et al., 2013; Aloisio et al., 2014b; Taylor, 2014). In fact, it may be possible to reproduce the transition between Galactic and extragalactic CRs starting with relatively steep seed spectra (e.g., $\propto E^{-2}$, with a low-rigidity cutoff for heavy nuclei and the contribution of secondary protons around 10^{18} eV. Note that this still does not explain the reason why the Galactic and extragalactic components connect so smoothly, despite their different sources and transport properties. On the other hand, a single-source scenario for all of the CRs is strongly disfavored by the observed modulation in the chemical composition.

A detailed account for photodisintegration inside or in proximity of the jet is beyond the goal of this paper, but it is reasonable that heavy ions shot towards the black hole will be preferentially disintegrated by being exposed to the intense radiation fields in the AGN broad-line region and/or in the dusty torus. In general, we see that the trajectories of lower energy UHECRs are far from being ballistic, especially for the lower-energy particles that propagate toward the jet base, so we expect photodisintegration to act as a high-pass filter that may make the UHECR injection spectrum flatter at low energies in the central regions of radio-loud quasars.

Correlation between UHECR Arrival Directions and Local AGNs

The results of §3.1.3 suggest that the jet cocoon is crucial for scattering escaping particles and potentially isotropizing them. More evolved jets with larger lobes and/or larger separation of scales between the relativistic spine and the cocoon may be even more effective in this respect. The typical size of AGN lobes (tens to hundreds of kiloparsecs) is in fact much larger than the particle Larmor radius even at the highest rigidities ($\mathcal{R} \sim 1$kpc at 10^{18}V in a μG field). Note that this does not mean that the Hillas limit is larger in the lobes, since there flows are nonrelativistic and the maximum energy scales with the flow β.

The astrophysical implication of a quasi-isotropic particle release is that we may receive UHECRs also from nearby AGNs whose jets do not point in our direction, i.e., nonblazar AGNs. For instance, Centaurus A is usually classified as a FR I AGN with $\Gamma \lesssim 7$, despite likely hosting a very relativistic jet with $\Gamma \approx 15 - 20$ (e.g., Chiaberge et al., 2001) and could be a source of UHECRs (e.g., Wykes et al., 2013).

It is still possible that a few powerful AGNs may contribute in a more prominent way to the UHECR flux on top of a background that is quasi-isotropic, a notewor-

thy feature being the dipole measured by Auger (Aab et al., 2017a, 2018a). The only marginal (3.4σ post-trial) evidence for a hotspot has been reported by the Telescope Array Collaboration for events above 5.7×10^{19} eV (Abbasi et al., 2014); such a hotspot correlates with the position of Mrk 421, one of the most powerful blazars in the local universe with a bolometric luminosity of $L_{\rm bol} \approx 2 \times 10^{44}\,{\rm erg\ s^{-1}}$ and a luminosity distance of about $134\,{\rm Mpc}$ (see Caprioli, 2018, for a more extended discussion).

In summary, several different considerations suggest that, even if *espresso* acceleration in AGN jets were the main mechanism for generating UHECRs, their direction of arrival should not necessarily correlate with the most powerful nearby blazars: (i) reaccelerated particles may be released almost isotropically, hence also non-blazar AGNs may contribute; (ii) when just a few shots are allowed, even AGN jets with moderate $\Gamma \gtrsim 3$ produce UHECRs (note that the Hillas criterion does not depend on Γ); (iii) self-confinement and propagation delay may offset the UHECR arrival with respect to the signature of a prominent jet activity.

3.2 *Espresso* and Stochastic Acceleration of Ultra-high-energy Cosmic Rays in Relativistic Jets

Our high-resolution MHD simulations (run with PLUTO, see Mignone et al., 2007; Rossi et al., 2008), which use adaptive mesh refinement (Mignone et al., 2012), can capture large-scale magnetic fluctuations self-consistently. Still, they cannot account for the potential role of smaller-scale turbulence, below the grid resolution, in particle scattering. In this paper we introduce sub-grid scattering (SGS) in the whole computational domain via a Monte Carlo approach: we propagate particles on the grid with a standard Boris pusher (e.g., Birdsall & Langdon, 1991b), while prescribing a finite probability per unit time for particles to change their pitch angle with respect to the local magnetic field. Introduc-

ing SGS effectively includes an additional stochastic process with respect to our previous analysis, so we refer to the extra acceleration that one may obtain as (a type of) stochastic acceleration. Stretching the inverse-Compton analogy even further, adding SGS makes the environment more Compton-thick and fosters the comptonization of the seeds, without changing the maximum achievable energy.

This approach allows us to investigate the role of stochastic acceleration, which is fostered by increased scattering, in realistic AGN jets. Understanding the properties of the resulting spectra that depend on the assumed level of SGS is particularly important because the actual diffusion rate in different jet regions is effectively a free parameter in any model and can hardly be constrained by observations. In particular, we address the following questions:

- Does SGS have an impact on the fraction of seeds that can be reaccelerated?
- Do particles typically gain more energy in the presence of SGS?
- Does the maximum achievable energy depend on the scattering rate?
- What is the relative importance of *espresso* and stochastic acceleration?

We find that adding SGS increases the percolation rate into the high-Γ regions of the jet and helps to break the correlation between in- and out-going angles (Caprioli, 2015b, 2018), and hence facilitates multiple *espresso* acceleration cycles. Both effects go in the direction of increasing the acceleration efficiency; therefore, the results of MC19 can be seen as a *lower limit* on the effectiveness of the jet at accelerating particles.

Furthermore, adding SGS fosters stochastic shear acceleration at the jet/cocoon interface as well as diffusive shock acceleration in the jet backflows, two energization mechanisms potentially responsible for the production of UHECRs, as suggested, e.g., by Ostrowski (1998, 2000); Liu et al. (2017); Fang & Murase (2018b);

Kimura et al. (2018); Tavecchio (2021) and O'Sullivan et al. (2009); Matthews et al. (2019), respectively.

The plan of the section is the following: in §3.2.1 we analyze the effects of SGS on trajectory patterns, energy gains, and energy spectra. In §3.2.2, we discriminate between particles that underwent stochastic or *espresso* acceleration and assess the maximum energy that can be achieved through each mechanism, showing how the highest-energy particles are invariably *espresso* accelerated. Finally, we summarize the implications of our results for astrophysical applications in §3.2.3.

3.2.1 Trajectories and Spectra of Released Particles

We carry out our analysis using 3D relativistic MHD simulations performed with PLUTO, which includes adaptive mesh refinement (Mignone et al., 2012; Rossi et al., 2008). We consider the same initial conditions as in MC19 in order to single out the role of small-scale scattering on top of a known situation (Please refer to MC19 for more details on the MHD simulation setup and properties of the jet). The jet is launched with Lorentz factor $\Gamma_0 = 7$ along $\hat{z}$ through a nozzle with a magnetization radius $R_{\rm jet}$ in a box that measures $48R_{\rm jet}$ in the x- and y-directions and $100R_{\rm jet}$ in the z-direction in a grid that has $512\times512\times1024$ cells with four refinement levels. The initial conditions are set by the jet/ambient density contrast ψ, the jet sonic and Alfvénic Mach numbers $M_s \equiv c/c_s$, and $M_A \equiv c/v_A$, where c, c_s, and v_A are the light, sound, and Alfvén speed, respectively. Our initial parameters are $\psi = 10^{-3}$, M_s =3, and $M_A = 1.67$.

As in MC19, we consider two possible orientations of the jet toroidal magnetic field, $B_\phi \lessgtr 0$, which physically corresponds to a current $J_z \lessgtr 0$ along the jet axis (case A and B, respectively). These cases lead to similar UHECR spectra, and differ only for the angular distribution of the released particles (Figure 11 in

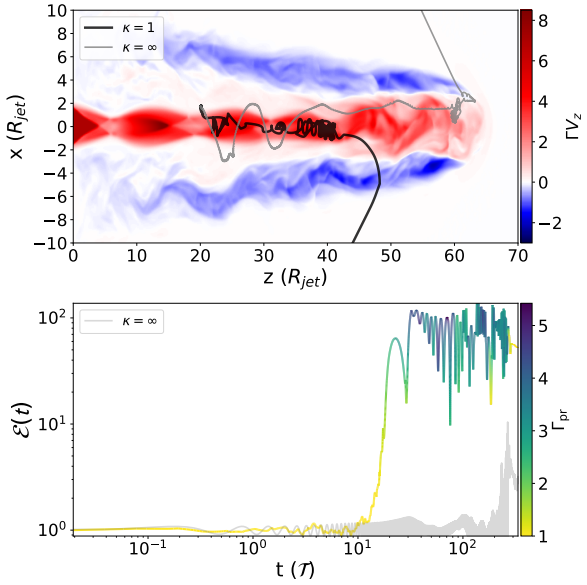

Figure 3.12: Trajectory and energy gain for representative particles with $\kappa = 1$ and $\kappa = \infty$. Top panel: particle trajectories with the same initial conditions overplotted on the 4-velocity component Γv_z of the flow. Bottom panel: energy evolution, color coded with the instantaneous Lorentz factor probed, $\Gamma_{\rm pr}$ for the $\kappa = 1$ particle as a function of the of the gyroperiod $\mathcal{T} \equiv \frac{2\pi m \gamma_i}{qB_0}$ as defined in the text. Such a particle initially gains a factor of < 4 in energy through stochastic acceleration and then experiences multiple *espresso* shots in the high-Γ jet regions. The particle with $\kappa = \infty$ (grey line), on the other hand, only experiences one *espresso* shot. Both particles are initialized with $\alpha_{\rm i} \sim 0.075$.

MC19). When not specified, we plot results for case A only; a synthesis on the differences and similarities between both cases is included in §3.2.1.

We propagate ∼100,000 test-particles in this jet with a wide range of initial gyroradii $\mathcal{R}$ and positions, with the same initial conditions as in MC19 and for the scattering rates discussed in §3.2.1. Particles are homogeneously and isotropically initialized from linearly spaced locations $(r_{\rm i}, \phi_{\rm i}, z_{\rm i})$ around the spine of the jet where $r_{\rm i}/R_{\rm jet} \in [0.2, 5]$, $z_{\rm i}/R_{\rm jet} \in [2, 60]$ and $\phi_{\rm i} \in [0, 2\pi]$. Additionally, their initial pitch angles are also linearly spaced to span all possible angles. It is useful to introduce the particle gyroradius normalized to the jet radius in the reference value of the magnetic field, B_0 as

$$\alpha(E, q) \equiv \frac{\mathcal{R}(E, q)}{R_{\rm jet}}, \tag{3.17}$$

where E and q are the particle's energy and charge, respectively. The particles' injection spectrum is flat in the interval of initial gyroradii $\alpha_{\rm i} \in [2 \times 10^{-4}, 10^{1}]$, where $\alpha_{\rm i}$ goes beyond the jet's Hillas limit, thus probing an extended energy range. Since trajectories only depend on the rigidity E/q, our particles are effectively representative of different nuclei. Note that, since the rigidity scales with the jet radius, there is no absolute energy scale for the particles. When typical values for B_0 and $R_{\rm jet}$ are chosen, the energies of the considered particles are close to those of UHECRs: for instance, $B_0 = 100\mu$G and $R_{\rm jet} = 100$pc would push the Hillas limit to $\sim 10^{20}$eV for iron nuclei (Caprioli, 2015b).

For the given resolution of about 10 cells per $R_{\rm jet}$, our MHD simulations resolve magnetic fluctuations down to scales comparable to the gyroradius of particles with $\alpha \gtrsim 0.1$. Note that particles can be propagated even if their gyroradius is smaller than the grid size, as long as a rigidity-dependent timestep sufficient to resolve their gyration is used. The role of SGS is to model the effect of unresolved

magnetic structures for such particles.

Pitch-angle scattering due to unresolved turbulence

The simulations in MC19 do not include any SGS and hence can be seen as a limiting case with minimum scattering. The opposite limit would be to assume that diffusion occurs in the Bohm regime, in which the mean free path for pitch-angle scattering is as small as the particle's gyroradius. We span across these two regimes by introducing a diffusion coefficient D that is a function of the particle rigidity and the local magnetic field that reads:

$$D(\mathcal{R}) \equiv \frac{\kappa}{3} c\mathcal{R}(E, q, B), \tag{3.18}$$

where $\mathcal{R}$ is the particle gyroradius and κ defines the number of gyroradii per sub-grid scattering (sometimes called the gyrofactor, e.g., Amano et al., 2011). $\mathcal{R}$ is a function of the local magnetic field $B(\mathbf{r})$, which in simulations is scaled to the initial value at the magnetization radius $B(r = R_{\rm jet}) \equiv B_0$ (see MC19 for details).

In this work, we span a wide range of SGS rates by posing $\kappa = 1000,$ 100, 10, and 1 (Bohm diffusion) and investigate their effects on particle acceleration, energy gains, and anisotropy; we compare these cases with the results from MC19, which do not include SGS and correspond to $\kappa = \infty$. For Alfvénic fluctuations, κ is related to the power in modes with wavenumber resonant with the particle gyroradius ($k\mathcal{R} \sim 1$); Bohm diffusion corresponds to the case in which $\delta B(k) \sim B_0$, while for $\delta B(k) < B_0$ one has that $\kappa \propto [B_0/\delta B(k)]^2$ (e.g., Skilling, 1975). In general, the exact relation between diffusion coefficient and magnetic power spectrum depends on the nature of the unresolved turbulence (spectrum, anisotropy, helicity, see e.g., Schlickeiser, 2002).

Pitch-angle diffusion may be accompanied by diffusion in momentum space due to the finite velocity of the scattering centers (e.g., Skilling, 1975; Ptuskin,

1988). We do not include this kind of second-order Fermi acceleration here because it is expected to be underdominant in super-Alfvénic flows and because its efficiency is reduced for particles with gyroradii larger than the largest waves in the system, for which diffusion becomes almost independent of energy (O'Sullivan et al., 2009).

Particle trajectories with scattering

Intuitively, adding SGS is expected to facilitate the diffusion of seed particles in and out of the jet spine, the region with ultra-relativistic flows where *espresso* acceleration occurs. To illustrate that this is actually recovered in simulations, in Figure 3.12 we show a representative trajectory of a particle with $\kappa = 1$, i.e., experiencing Bohm diffusion; the bottom panel shows the particle energy gain $\mathcal{E}$ as a function of its relativistic gyroperiod $\mathcal{T} \equiv \frac{2\pi m \gamma_i}{qB_0}$ where γ_i is the initial Lorentz factor, q the charge, and m the mass.

To assess the role of SGS, we overplot the trajectory of a particle with the same initial conditions but with $\kappa = \infty$ and $\alpha_{\rm i} \sim 0.075$. The $\kappa = 1$ particle in Figure 3.12 follows a more jagged trajectory before entering the spine (where $\Gamma \gtrsim 2$) and experiencing *espresso* gyrations. The reference particle, with the same initial conditions but $\kappa = \infty$, probes a maximum $\Gamma \sim 2$ and leaves the jet with a final energy gain of $\mathcal{E} \sim 3$ (energy diagram in grey in the bottom panel).

We notice that the two particles have a similar evolution until $t \sim 10\mathcal{T}$, with energy oscillating within a factor of ≤ 2. Then, the $\kappa = 1$ particle gets some further acceleration while still in the low-Γ region (yellow color code in the bottom panel of Figure 3.12) and penetrates the high-Γ flow, gaining a factor $\mathcal{E} \sim 120$ in energy by virtue of one canonical *espresso* shot, i.e., the energy gain occurs over a single gyration. This behavior is common to many particles and suggests that SGS leads to a type of stochastic acceleration at the jet-cocoon interface, which fosters

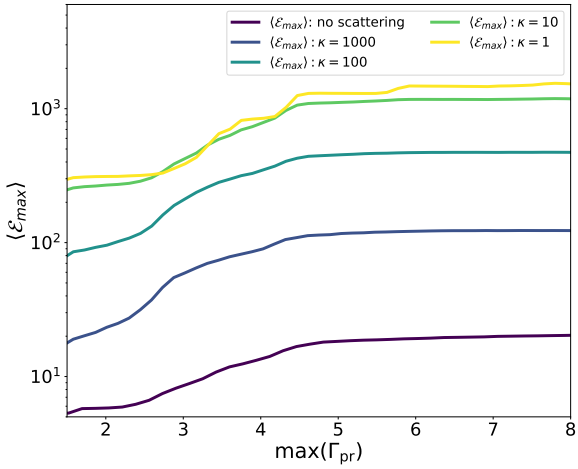

Figure 3.13: Maximum energy gain $\langle \mathcal{E}_{\rm max} \rangle$ averaged on particles with $\mathcal{E} \geq 2$ as a function of the maximum Lorentz factor probed in the flow, $\Gamma_{\rm pr}$. Compare with Figure 6 in Mbarek & Caprioli (2019) for more details.

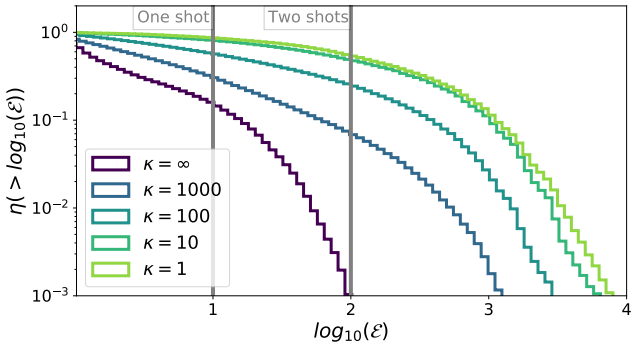

Figure 3.14: Cumulative distribution of the energy gains of particles with a flat injection spectrum in η such that $\alpha_{\rm i} \in [2 \times 10^{-4}, 2 \times 10^{-1}]$ for different SGS rates; η is defined such that $\eta = \frac{\mathcal{E}}{N} \frac{dN}{d\mathcal{E}}$ where N is the number of particles. The two vertical lines correspond to single- and double-*espresso* shots in the effective jet Lorentz factor. Note how increasing SGS allows a larger fraction of seeds to be accelerated to higher energies.

particles to access the high-Γ region and eventually get boosted via the *espresso* mechanism.

Finally, we point out that even in the case of Bohm diffusion, particles that enter the spine experience gyrations reminiscent of those observed without scattering, which are themselves similar to the analytical ones described in MC19 and Caprioli (2018).

In the next sections we quantify how SGS mostly affects: 1) the fraction of particles that can be *espresso* accelerated and 2) the number of *espresso* cycles that a particle may undergo.

Energy gain and injection efficiency

We have previously found that the maximum energy gain of particles $\mathcal{E}_{\rm max}$ correlates with the maximum Lorentz factor that they probe along their trajectory (Figure 6 in MC19). This correlation is recovered also when SGS is introduced, as shown in Figure 3.13, but the overall normalization of the average energy gain depends on κ. Increasing SGS leads to larger energy gains, which saturate for $\kappa \lesssim 10$. The difference with respect to $\kappa = \infty$ lies in the fact that SGS helps to break the correlation between in- and out-going angles, which yields a larger energy gain per cycle.

This claim is further reinforced by the cumulative distribution $\eta(> \log_{10}(\mathcal{E}))$ of the energy gains of particles with $\mathcal{E} \geq 2$ shown in Figure 3.14 for particles with initial gyroradii $\alpha_{\rm i} \in [2 \times 10^{-4}, 2 \times 10^{-1}]$, where η is defined as $\eta = \frac{\mathcal{E}}{N} \frac{dN}{d\mathcal{E}}$. We note a clear increase in the energy boosts that particles experience with increasing SGS. While for $\kappa = \infty$ having more than one *espresso* shot is relatively rare, already for $\kappa = 1000$, about 7% of particles gain a factor of $\geq \Gamma_{\rm eff}^4$ in energy, the equivalent of two *espresso* shots. This fraction increases to about 24%, 48%, and 54% for $\kappa = 100$, $\kappa = 10$, and $\kappa = 1$ respectively. Given the uncertainties in

the seed abundance and spectra in AGN hosts, such efficiencies should not be translated directly into a UHECR luminosity for given AGNs; still, our exercise suggests that the more SGS is added, the easier it is to accelerate pre-existing energetic particles. Note that the observed UHECR flux may be accounted for by reaccelerating as little as $\sim 10^{-4} - 10^{-2}$ of the highest-energy galactic seeds (Caprioli, 2015b), which happens even for large values of κ.

Finally, we note that particle injection does not increase arbitrarily with the SGS level, but rather saturates for $\kappa \lesssim 10$; therefore, even fluctuations at the level of $\delta B/B_0 \lesssim 0.3$ (see §3.2.1) at resonant scales may yield a maximum efficiency in seed re-acceleration.

Effect of the scattering rate on the energy spectra

Figure 3.15 shows the distribution of the gyroradii of escaping particles, $\alpha_{\rm f}$, for different SGS prescriptions. The solid black line represents the total spectrum and is divided in the spectra produced by particles with a given initial $\alpha_{\rm i}$ (colored histograms). The blue vertical line marks the effective Hillas criterion for the jet considered: it corresponds to $\alpha \sim 8$ because the average magnetic field in the spine region is $\sim 8B_0$.

We have already discussed how particles in general undergo larger boosts with increasing SGS rates. Figure 3.15 shows that in more detail by also capturing how the boost enhancement depends on the seed energy. The following features are worth noticing:

(i) Highest-energy particles. For $\alpha \gtrsim 2$ spectra are very similar regardless of the SGS rate, suggesting that the highest-energy particles are always *espresso* accelerated. Close to the Hillas limit, stochastic acceleration, which depends on the level of SGS, does not contribute to either a larger fraction of particles or a larger maximum energy.

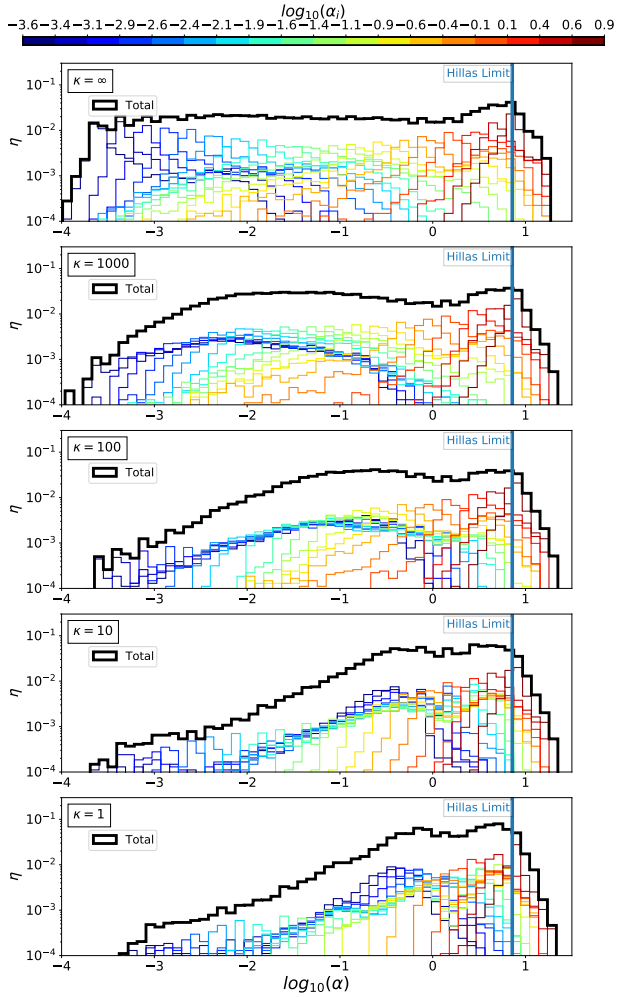

Figure 3.15: Distribution of the gyroradii of reaccelerated particles obtained for an injection spectrum flat in η in the interval $\alpha_{\rm i} \in [10^{-3.6}, 8]$; η is defined such that $\eta \propto \alpha \frac{dN}{d\alpha}$. The thick black line shows the cumulative spectrum, while colored histograms correspond to initial gyroradii as in the color bar. Seeds with $\alpha_{\rm i} \lesssim 1$ can undergo boosts as large as $\sim 50 - 100 \gg \Gamma^2_{\rm eff}$, while for $\alpha_{\rm i} \gtrsim 1$ the energy gain is smaller and saturates at $\alpha_{\rm H} \approx 8$ (longitudinal Hillas criterion).

(ii) Lower-energy particles. As SGS increases, the fraction of low-energy seeds that can be reprocessed by the jet grows considerably and energy gains of order of $\mathcal{E} \gtrsim 10^3$ (corresponding to two/three *espresso* shots) are common;. The increase in the average energy gain shown in Figure 3.13 and 3.14 is driven by these particles.

(iii) Flattening of the spectrum. For $\kappa = \infty$ the UHECR spectrum tends to be only slightly flatter than the injected one, showing a pile-up close to the Hillas limit. With SGS, the spectrum tends to become significantly flatter than the injected one, by about ~ 0.9 in slope for $\kappa = 1$. Again, this effect is driven by a change in the behavior of the lower-energy particles rather than of the higest-energy ones. This recovers results from Monte Carlo simulations of idealized jets, which report spectra as flat as E^{-1} when Bohm diffusion is prescribed (Kimura et al., 2018). Note that rather hard injection spectra are favored by current models for the flux and composition of UHECRs (e.g., Gaisser et al., 2013; Aloisio et al., 2014a; Taylor, 2014).

Angular Distribution of Escaping Particles

Let us focus now on the anisotropy of the accelerated particles, which is important for assessing a possible correlation between the UHECR directions of arrival and local sources. In MC19, we found that without SGS particles preferentially move along the spine of the jet until $z \sim 60$ and get deflected in the cocoon after leaving the relativistic region. In that case, the sign of B_ϕ in the jet, which controls the sign of the motional electric field in the cocoon, either disperses ($E_r > 0$, case A) or collimates ($E_r < 0$, case B) the escaping particles. In both cases the UHECR distribution is never beamed in an angle $1/\Gamma$ as one may expect from a relativistic source; in case A, where the radial (motional) electric field points outward, it is almost isotropic.

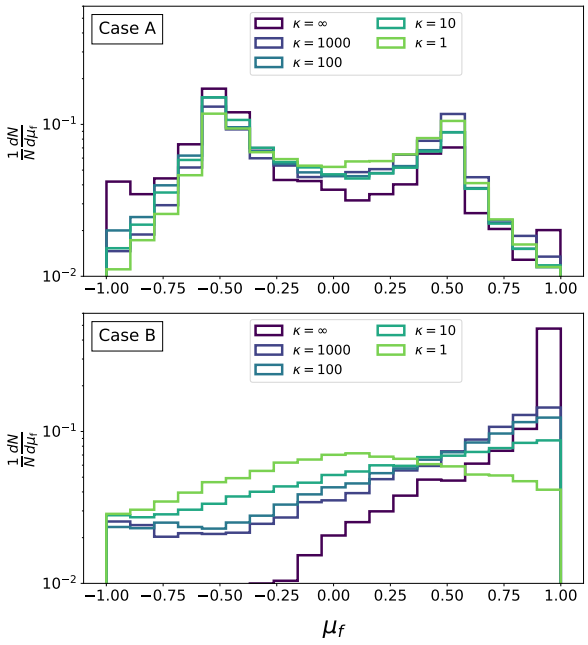

Figure 3.16: Distribution of the cosines of the final angle of flight for accelerated particles with $\mathcal{E} \geq \Gamma^2_{\rm eff}$. In case A particles escape the jet isotropically independently of the scattering rate, while in case B they are less and less beamed as SGS rate increases.

We repeat the same analysis here for all the particles that gain at least a factor of Γ^2 in energy in the presence of SGS. Figure 3.16 shows the distribution of $\mu_{\rm f}$, the cosine of the angle between the final particle velocity and the z-axis, for both case A and case B. While for case A the distribution is isotropic independently of κ, increasing the SGS leads to a progressively more isotropic angular distribution of escaping particles in case B, too (bottom panel of Figure 3.16). This is a natural consequence of introducing additional pitch-angle scattering; it reinforces the idea that relativistic jets may be quite isotropic UHECR emitters and, as a result, we may expect comparable contributions from AGNs that we classify as blazars (with jets along the line of sight) or Fanaroff-Riley radio galaxies.

Since adding SGS induces an isotropization of the outgoing fluxes in both cases, we treat only case-A particles in the remainder of the paper for simplicity. Overall, we find no appreciable differences in particle trajectories or final spectra

between the two cases.

3.2.2 Espresso and Stochastic Acceleration

In §3.2.1 we have showed one instance in which adding SGS may foster injection into *espresso* acceleration. Let us now discuss differences and interplay between *espresso* and stochastic acceleration.

In general, stochastic acceleration relies on repeated crossings of the shearing layers at the interface between the jet and the cocoon (e.g., Ostrowski, 1998, 2000; Fang & Murase, 2018b; Kimura et al., 2018), or repeated diffusive shock acceleration and/or turbulent acceleration in the cocoon (e.g., O'Sullivan et al., 2009; Matthews et al., 2019); *espresso* acceleration, instead, relies on a few Compton-like scatterings against the most relativistic regions of the jet.

Spectral signatures

A natural question is whether the spectral diversity in the sub-Hillas region (see §3.2.1 and Figure 3.15) is due either to a more effective injection of seeds into *espresso* acceleration or to stochastic acceleration. As long as relatively-low Γ factors are involved, the distinction between the two processes is more semantic than factual, in the sense that many acceleration events are invariably needed to achieve large energy gains.

For simplicity, we define the contribution of stochastic acceleration as the contribution to the UHECR spectrum that exceeds the one provided by the $\kappa = \infty$ case, i.e., the case with large-scale turbulence in which particles gain energy only via a few interactions with the highly-relativistic jet spine. Figure 3.15 shows that adding SGS leads to a more and more prominent secondary peak below the Hillas limit that moves towards larger energies ($\alpha \sim 7 \times 10^{-3}, 7 \times 10^{-2}, 0.6$) for κ =1000, 100, 10 respectively.

We interpret such peaks as due to diffusive escape from the side of the jet,

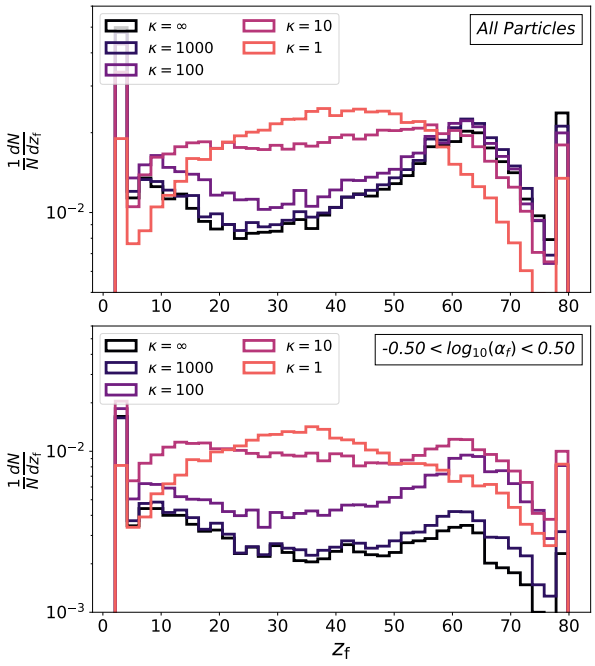

Figure 3.17: Top Panel: Final z position $z_{\rm f}$ of all particles after they escape the jet. Bottom Panel: as above, but only for particles that escape with energies around the stochastic Hillas limit.

which depends on the level of SGS. The diffusion length λ of the particles in the radial direction (transverse to the jet axis) can be expressed as:

$$\lambda_d \approx \frac{D(\alpha)}{V_r}, \tag{3.19}$$

where V_r is the radial velocity component of the jet. Averaging over V_r in our fiducial simulation returns $\langle V_r \rangle \approx 0.01$ and the diffusion length becomes:

$$\lambda \sim 30 \frac{B_0}{B_{\rm coc}} \alpha\kappa \; R_{\rm jet}, \tag{3.20}$$

where $B_{\rm coc} \sim 2B_0$ is the averaged magnetic field in the cocoon. The maximum rigidity that a particle can achieve via stochastic acceleration is set by equating such a diffusion length with the typical transverse size of the shearing region, i.e., $\lambda(\mathcal{R}_{\rm max}) \sim 10 R_{\rm jet}$ (see Figure 3.12). This simple scaling reproduces the position of

each sub-Hillas peak in Figure 3.15, as well as the quasi-linear scaling of such a maximum energy with $1/\kappa$.

To further corroborate this statement, we track where particles leave the jet, defining $z_{\rm f}$ as the value of z where a particle trajectory crosses the surface of a cylinder that shares the jet's axis and has radius $15R_{\rm jet}$ and length $80R_{\rm jet}$. The distribution of $z_{\rm f}$ is shown in Figure 3.17, which highlights how particles are more likely to escape in the transverse direction closer to the base of the jet for larger SGS, i.e., lower values of κ. More precisely, the top panel shows the fraction of all the particles that leave the jet as a function of z_f, while the bottom panel only considers particles with sub-Hillas energies. A comparison between the two panels reveals that for small values of κ the bulk of sub-Hillas particles leaves the jet well before reaching the head; without SGS, instead, most of the particles propagate to the jet's end (peak in the top panel). Intermediate values of κ bridge these two regimes.

It is also interesting to notice that the effect of SGS saturates before reaching the Bohm regime, as attested by the fact that curves for $\kappa = 1$ and $\kappa = 10$ are quite similar in Figures 3.14, 3.15, and 3.17. For such a strong SGS, the sub-Hillas peaks converge to $\alpha \sim 0.7$ and particles tend to escape well before reaching the jet's head (top panel of Figure 3.17); we interpret this as the signature of an intrinsic limitation in maximum energy that applies to particles that escape at $z_{\rm f} < 50R_{\rm jet}$, i.e. the *stochastic Hillas limit*, as explained below in §3.2.2.

The importance of the stochastic Hillas limit

Hillas (1984) discussed how stochastic (statistical) acceleration is characterized by an energy gain per cycle that competes with the particle escape probability, such that the escape time decreases as the particle energy increases. This, in turn, sets a stochastic Hillas limit, more easily achievable for particles that un-

dergo stochastic acceleration, and generally smaller than the Hillas limit corresponding to the potential drop due to the motional electric field on the source diameter. As a result, the maximum energy of particles that undergo stochastic acceleration should depend on the scattering rate (i.e., on κ) and on the parameters (V_r, B, and transverse size) of both the spine and the cocoon. Considering the balance between advection and diffusion outside of the spine of the jet expressed in Equation 3.19, we find that this stochastic Hillas limit sits at $\alpha_{\rm SHL} \sim 0.7/\kappa$ across the whole transverse jet region (spine+cocoon). Indeed, when we estimate such a limit using Equation 3.19 for the relativistic spine's reference values ($\lambda = R_{\rm jet}$, $B \sim 8B_0$, and $\langle V_r \rangle \sim 0.04$), we find that it is comparable with $\alpha_{\rm SHL}$.

From these considerations a simple picture arises: more SGS on one hand increases the fraction of accelerated particles, but on the other hand enhances the probability of leaving the jet sideways; this leads to a pile-up at a maximum energy dictated by the stochastic Hillas limit $\alpha \lesssim 1$, which is intrinsically lower than the energy achievable by the particles that manage to make it throughout the full jet extent (Bottom Panel of Figure 3.17). In terms of acceleration mechanisms, we can conclude that *espresso* acceleration (which happens even without SGS) is responsible for the energization of the highest-energy particles that a jet can produce, i.e., those that can probe the full potential drop. Conversely, stochastic acceleration—which depends on the assumed level of SGS—can be relevant for the energization of lower-energy UHECR. The more effective SGS is at accelerating particles, the more particles pile up close to the stochastic Hillas criterion and the flatter the overall UHECR spectrum.

Let us now study how acceleration occurs in different regions, namely the jet spine (high-Γ) and the shearing region at the jet-cocoon interface.

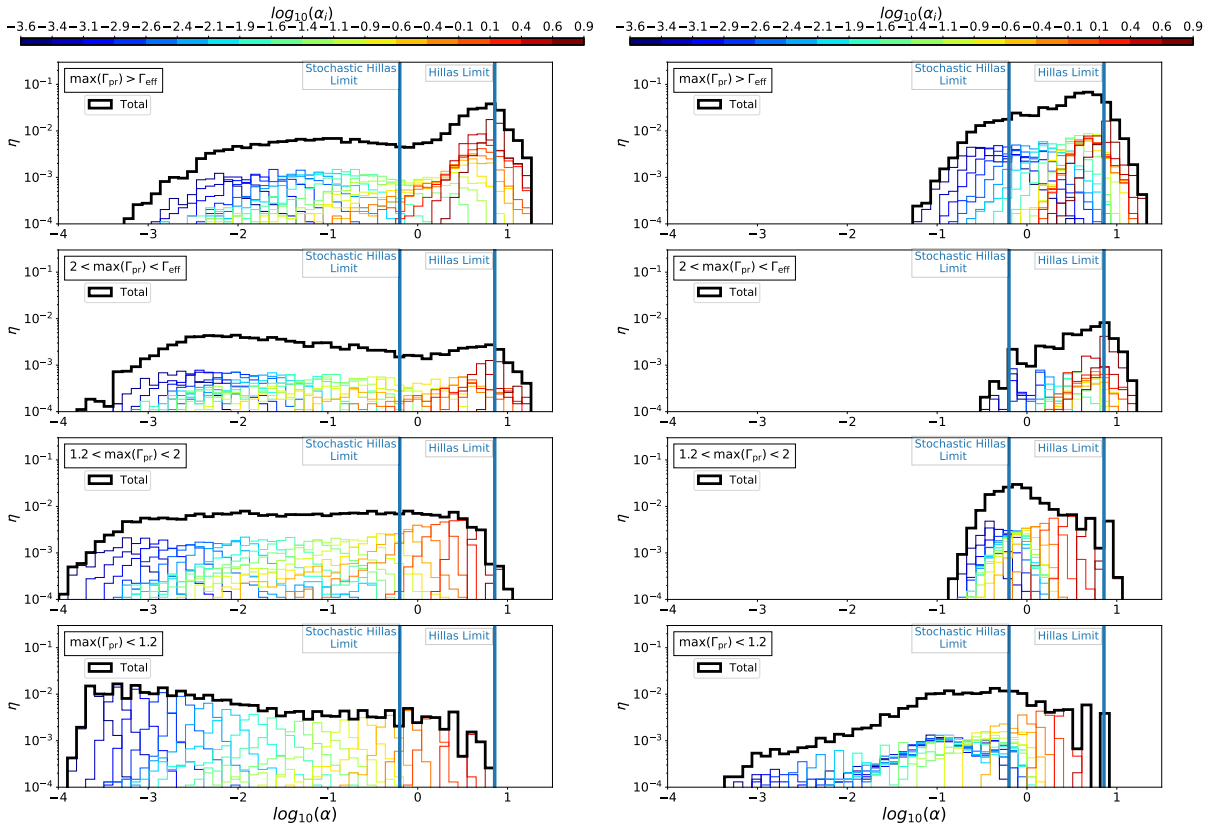

Figure 3.18: Spectrum of accelerated particles separated according to the maximum Lorentz factor that they probe, $\max(\Gamma_{\rm pr})$ (top to bottom, as in the legends); left and right panels correspond to $\kappa = \infty$ and $\kappa = 1$, respectively. Note that: 1) the highest-energy CRs ($\alpha_{\rm f} \gtrsim 1$) systematically go through the most relativistic jet regions (top panels); 2) adding SGS only incrementally enhances the flux of such particles (compare the top two panels); 3) adding SGS significantly boosts the energy of low-energy seeds (cold colors) that probe regions with $\Gamma_{\rm pr} \gtrsim 1.2$.

Acceleration in high-Γ regions

Figure 3.18 shows the impact of the maximum Lorentz factor, $\max(\Gamma_{\rm pr})$, that particles probe along their trajectories on the final spectrum, for the two extreme cases of $\kappa = \infty$ and $\kappa = 1$ (left and right panels, respectively); the color code corresponds to the seed energy.

Let us first focus on the highest-energy particles, those with final gyroradii $\alpha_{\rm f} \gtrsim 1$ (red histograms). Regardless of the amount of SGS, they typically probe the fastest jet regions with $\max(\Gamma_{\rm pr}) > \Gamma_{\rm eff} \sim 3.2$ (top panels in each column). When maximally-effective SGS is added, the number of these particles remains substantially the same (right vs left panels). This is again a manifestation that *espresso* acceleration is sufficient to achieve the Hillas limit and that SGS may allow an incrementally larger fraction of the seeds to be reaccelerated via such a process. A similar conclusion can be drawn for particles that probe slower jet regions (top to bottom): adding SGS does not increase appreciably the amount of particles that achieve large final energies ($\alpha_{\rm f} \gtrsim 1$).

Finally, we can see that as $\max(\Gamma_{\rm pr})$ reaches 1.2 in the bottom panel, particles simply cannot reach the highest energies, even if with Bohm diffusion low-energy particles are still capable of gaining up to a factor of ~ 50 in energy, unlike in the $\kappa = \infty$ case. We can conclude here that particles are not likely to undergo *espresso* in the lowest-Γ regions where $\max(\Gamma_{\rm pr}) < 1.2$.

Acceleration in low-Γ regions

As mentioned in §3.2.2, in low-Γ flows it is hard to unequivocally identify the most important acceleration mechanism, since multiple small *espresso* shots are indistinguishable from stochastic acceleration. Therefore, we limit ourselves to analyzing trajectories and energy gains in comparison with *espresso*'s ordered gyrations that we outlined in e.g., Figure 1 in MC19. Generally speaking, the most

prominent effect of SGS in low-Γ flows is to affect the mostly-ordered gyrations seen when $\kappa = \infty$.

Figure 3.19 shows three representative trajectories of particles that only probe low-Γ regions before escaping, all for the case $\kappa = 1$. The top panel shows their trajectories plotted over the 4-velocity component Γv_z of the jet, while the bottom panels show the energy gain as a function of time, with the color code corresponding to the instantaneous flow properties.

The black trajectory (second panel in Figure 3.19) is representative of particles that probe the trans-relativistic region around the jet spine. In just three gyrations, this particle, initialized with $\alpha_{\rm i} = 1.4 \times 10^{-3}$, experiences three very efficient *espresso* shots—each corresponding to a maximum *espresso* energy boost of a factor of $\sim 2\Gamma_{\rm pr}^2 \sim 8$ (Equation 11 in MC19)—with scattering events at roughly the peak of each gyration. Here the main role of SGS is to break the correlation between in- and out-going angles in the first cycles as, without the presence of SGS, this particle would not have gone through more than one ordered *espresso* gyration. Finally, it lingers around in the cocoon ($\Gamma \sim 1$) before escaping with $\alpha_{\rm f} \sim 0.7$, corresponding to the stochastic Hillas limit.

The maroon trajectory (third panel of Figure 3.19) is representative of particles that gain energy through multiple scattering events in the cocoon, without ever probing the relativistic spine. Such a particle is initialized with $\alpha_{\rm i} = 0.025$ and gains up to a factor of ~ 30 in energy while probing $\Gamma_{\rm pr} \leq 1.3$. This particle escapes when it reaches the stochastic Hillas limit, with a total energy gain $\mathcal{E} \sim 30$. We do not observe similar behavior in the absence of strong SGS, so it is fair to ascribe this kind of acceleration to stochastic acceleration in the jet backflow, as suggested, e.g., by O'Sullivan et al. (2009); Matthews et al. (2019).

Finally, the grey trajectory (bottom panel of Figure 3.19) is representative of particles that only probe non-relativistic regions ($|v_z| \lesssim 0.2c$); in this case, the

trajectory is color-coded with the instantaneous 4-velocity component $\Gamma_{\rm pr} v_{\rm z,pr}$ of the flow. Such a particle, initialized with $\alpha_{\rm i} = 0.025$, experiences a mixture of energy gains and losses when crossing the shear layers as attested by the probed 4-velocity component, and finally exits the jet with an energy gain of ~ 30 without probing the relativistic spine. The last part of the trajectory can be ascribed to stochastic shear acceleration (e.g. Ostrowski, 1998, 2000; Fang & Murase, 2018b; Kimura et al., 2018) due to the alternating sign of v_z.

Overall we find no evidence that particles that *only* undergo stochastic acceleration fostered by the enhanced SGS can achieve boosts in excess of a factor of 50 in energy (bottom panel of Figure 3.18). Some particles, which start with small initial gyroradii can undergo larger boosts (as the black trajectory in Figure 3.19) if they probe relativistic regions; all of these particles, though, make it only to the stochastic Hillas limit.

Our considerations are drawn by examining a large but finite number of particles, which means that we cannot exclude the existence of trajectories along which particles may be accelerated up to the longitudinal limit without undergoing any *espresso* cycle; yet, we can quantitatively assess that this is not common.

We may summarize these findings by saying that, while adding SGS allows particles to be stochastically accelerated also in the cocoon or at the jet interface (where there is free energy in the form of shear, wake shocks, and turbulence), most of the acceleration is bound to occur in the relativistic spine. The particles that are accelerated to the highest energies are those that manage to probe most of its extent, and a more efficient scattering may hinder the process by enhancing lateral escape.

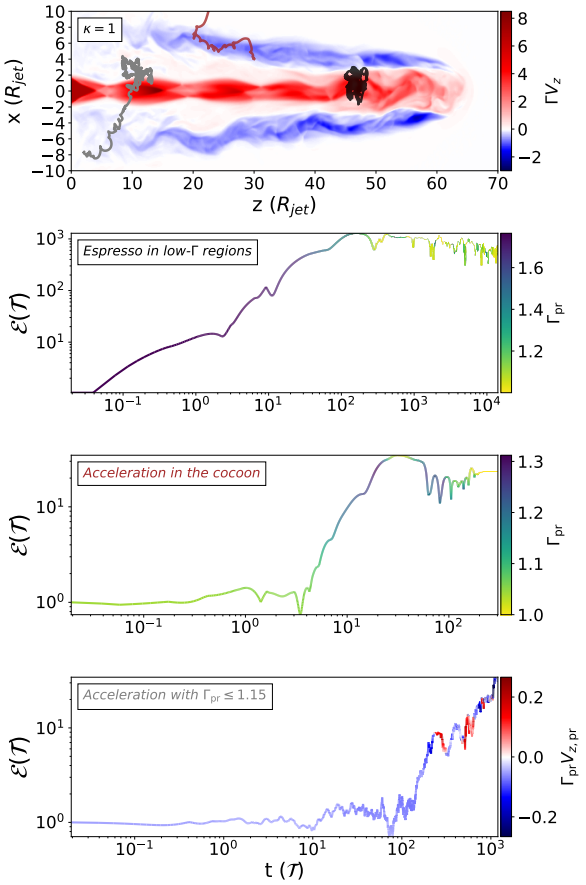

Figure 3.19: 2D projections of typical trajectories (top panel, plotted over the 4-velocity component Γv_z of the flow) and energy gains (bottom panels) for particles that propagated only in low-Γ regions, for $\kappa = 1$. All particles escape the spine/cocoon system. Second panel (black trajectory): energy gain as a function of $\mathcal{T}$, color coded with the instantaneous Lorentz factor probed, $\Gamma_{\rm pr}$. This is representative of particles that undergo multiple (3 in this case) *espresso* shots in trans-relativistic regions around the jet spine. Third panel (maroon): a particle accelerated in the jet backflow. Fourth panel (grey): a particle accelerated in sub-relativistic regions across the cocoon.

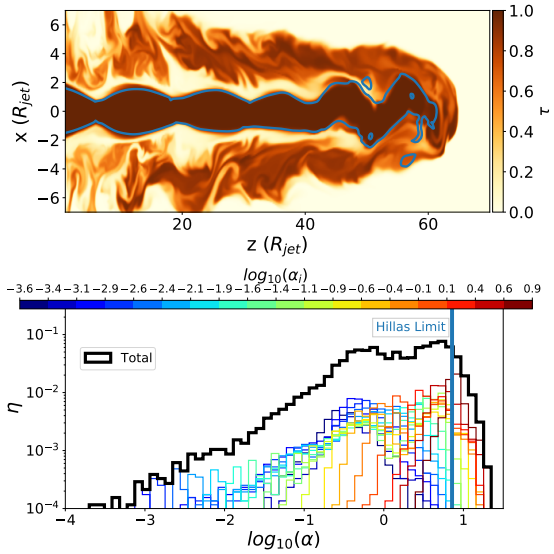

Figure 3.20: Top Panel: 2D cut at $y = 0$ of τ, a tracer of the relative abundance of jet/ambient material. The blue contour plot delimits the spine of the jet, defined as the region with $\Gamma > 2$. Bottom Panel: As in Figure 3.15, but with Bohm diffusion in the spine and galactic-like diffusion in the cocoon, à la Kimura et al. (2018). Note the similarity with the bottom panel of Figure 3.15 ($\kappa = 1$).

A more elaborate diffusion prescription

The calculations above showed how UHECR spectra change when simple prescriptions for SGS are introduced. In reality, pitch-angle scattering depends on the level of turbulence at scales resonant with each particle, and quite different magnetic fluctuations are expected in the jet, the cocoon, and the ambient medium.

For instance, Kimura et al. (2018) recently studied UHECR stochastic acceleration in idealized jets via Monte Carlo simulations with different scattering rates in the cocoon and in the jet. In particular, they assumed Bohm diffusion in the jet (corresponding to our spine) only, while outside the mean free path was chosen as $\lambda_i = l_{\rm c}(\mathcal{R}/\mathcal{R}_{\rm c})^{\delta}$ where $l_{\rm c}$ is the coherence length of the local magnetic turbulence and $\mathcal{R}_c$ the gyroradius for which $\mathcal{R}(E, q) = l_{\rm c}$. For $\mathcal{R} < \mathcal{R}_{\rm c}$, Kolmogorov turbulence is assumed ($\delta = 1/3$); otherwise, particles should only see turbulence on scales

much smaller than their gyroradii, which leads to $\delta = 2$. The coherence length $l_{\rm c}$ is set to be 3% of the radius of the cocoon.

We now investigate a similar prescription for particles propagated in our benchmark simulation and show the results in Figure 3.20. More precisely, we define the spine of the jet as the region with $\Gamma \geq 2$ (delimited by the blue contour plot in the top panel) and the cocoon as the region encompassed by the shocked jet material, traced by the value of τ, a scalar quantity that describes the mixing between jet ($\tau = 1$) and ambient ($\tau = 0$) material.

The bottom panel of Figure 3.20 shows that the spectrum of reaccelerated particles is very similar to the case with Bohm diffusion ($\kappa = 1$) in Figure 3.15. In particular, the peak at $\alpha_{\rm f} \lesssim 1$, corresponding to the stochastic Hillas limit, is quite prominent.

This suggests that CR reacceleration in AGN jets is controlled by the effective scattering rate in the highly-relativistic regions and weakly dependent on the details of how particles diffuse in the cocoon. We stress again that the actual amount of SGS that is realized in realistic environments is highly uncertain, but it is conceivable that in the jet SGS may be enhanced with respect to the ambient medium, which should be described by the galactic diffusion coefficient.

3.2.3 Espresso in Realistic Environments

Let us discuss now how our findings apply to different AGNs from which UHECRs may originate; we limit ourselves to radio-loud AGNs, which are the only ones energetic enough to potentially supply the UHECR luminosity (e.g., Fang & Murase, 2018b; Kimura et al., 2018; Mbarek & Caprioli, 2019, and references therein). Within radio-loud candidates, we distinguish between FR-I and FR-II jets (Fanaroff & Riley, 1974), whose properties are likely determined by both the engine luminosity and the density profile of the ambient medium (Tchekhovskoy

& Bromberg, 2016b). FR-I jets are typically decelerated to trans-relativistic velocities within 1 kpc (e.g., Wardle & Aaron, 1997; Arshakian & Longair, 2004; Mullin & Hardcastle, 2009), while FR-II jets are more powerful and can sustain $\Gamma > 10$ flows over tens of kpc and extend up to hundreds of kpc before they are dissipated (e.g., Sambruna et al., 2002b; Siemiginowska et al., 2002b; Tavecchio et al., 2004; Harris & Krawczynski, 2006b). Strictly speaking, our benchmark simulation should be more similar to a FR-I radio galaxy since the ambient density is homogeneous, rather than rapidly decreasing as in a FR-II case, and the jet is decelerated on a scale of a few tens of $R_{\rm jet}$. A newer family of radio galaxies dubbed FR-0s has also emerged to represent the bulk of the radio-loud AGN population in the near-universe with redshifts $\lesssim 0.05$ (e.g. Baldi et al., 2018; Baldi, R. D. et al., 2018; Torresi et al., 2018; Garofalo & Singh, 2019). With an extent that can reach 3kpc, the only notable difference between FR-0s and extended FR-Is is the former's lack of extended radio emission (Baldi, R. D. et al., 2018; Garofalo & Singh, 2019). FR-0s could be associated with early-type galaxies that can evolve into FR-Is provided that their central black hole's spin is boosted with increasing accreting matter, but FR-0s do not need to be young objects and could also be associated with decelerated FR-IIs with decreasing power considering their important extent (Baldi et al., 2018; Baldi, R. D. et al., 2018; Garofalo & Singh, 2019). Merten et al. (2021) suggested that FR-0 jets can accelerate particles to UHECR levels through stochastic shear acceleration. While this possibility cannot be ruled out, the fact that for low bulk Lorentz factors the stochastic Hillas limit is significantly more stringent than the one due to the motional electric field suggests that UHECR sources may be limited to FR-I and FR-II jets.

As discussed in §3.2.1, the highest energies are achieved by particles that can penetrate into the jet spine; therefore, we expect the extent of the jet to control the highest achievable energy (see Equation 16 in MC19 and §3.2.2). This favors

FR-II jets, which are both faster and longer, as the candidate sources of UHECRs up to 10^{20}eV; this conclusion was already drawn by MC19, but here it is reinforced because we have shown that the highest achievable energies are independent of the level of SGS (see Figure 3.15).

SGS is arguably more important in FR-I jets with relatively small Lorentz factors, where one/two-shot *espresso* acceleration is not enough to produce the highest-energy CRs starting from galactic-like CRs. As shown in section 3.2.2, with quasi-Bohm diffusion, particles can go through multiple acceleration events in low-Γ regions and gain up to a factor of 10^4 in energy, thereby reaching the stochastic Hillas limit (see §3.2.2).

This suggests that FR-I galaxies may also contribute to the bulk of UHECRs around $10^{18} - 10^{19}$eV, with a spectrum which may be more or less flat depending on the amount of SGS (see §3.2.1).

Of course this includes nearby AGNs, such as Centaurus A and M87, as potential sources of UHECRs. Note that they may not look like hotspots in the map of UHECR directions of arrival not only because of particle deflections in the intergalactic medium, but also because their contribution may be swamped in the flux from all the other AGNs on cosmological scales. Such an effect (à la Olbers' paradox) may arise because UHECR protons with energies $\gtrsim 10^{18}$eV may travel almost unhindered across the whole universe; therefore, in this energy window we should expect also the contribution from the most powerful blazars and flat spectrum radio quasars at the cosmological peak of AGN activity, at redshift $z \sim 1-2$. To explain the highest CR energies one would still need local, i.e., within ~ 200 Mpc ($z \lesssim 0.05$), highly-relativistic sources; the catalogue of such AGNs is very likely incomplete, but at least a few sources are present (Caprioli, 2018).

3.3 Conclusions

We have extensively analyzed the *espresso* paradigm for the acceleration of UHECRs in relativistic AGN jets by propagating test particles in both synthetic jet structures and full 3D relativistic MHD simulations. Our bottom-up approach accounts for all of the fundamental ingredients of a universal acceleration theory. We further such an investigation by including subgrid scattering (SGS) to characterize the role of the small-scale magnetic irregularities that are not captured in MHD simulations. Our framework is mechanism-agnostic, i.e., seed trajectories are integrated via standard particle-in-cell techniques (e.g., Birdsall & Langdon, 1991b), augmented with a Monte Carlo treatment of pitch-angle scattering.

Our results can be summarized as:

1. Particles are typically boosted by a factor of $\mathcal{E} \sim \Gamma^2$ in energy regardless of the magnetic structure of the jet, in the sense that $\mathcal{E}$ depends neither on the sign and the radial profile of toroidal magnetic field, nor on its poloidal component.

2. Achieving an energy gain $\mathcal{E} \sim \Gamma^2$ in a jet region of transverse and longitudinal extent $R_{\rm jet}$ and H requires the initial particle Larmor radius to satisfy $\mathcal{R}_{\rm i}/R_{\rm jet} \lesssim \min(1/\Gamma^2, H/\Gamma^3)$ (equation 3.15).

3. Particle trajectories in MHD simulations show many analogies with those in idealized jets; particles exhibit concave or convex trajectories depending on the the sign of J_z and B_ϕ (Figures 3.1 and 3.5), but this has no effect on their energy gain.

4. The trajectories of the most energetic particles are typical of *espresso* acceleration: (i) particles exhibit ordered gyrations, without evidence of pitch-angle scattering (Figure 3.5); (ii) one/two acceleration events are generally

sufficient to reach the Hillas limit (Figure 3.9); and (iii) particle acceleration always occur within the jet, rather than at the jet/cocoon interface or in the cocoon. The presented simulations, while resolving magnetic/shear structures on scales even smaller than the gyroradius of the propagated particles, do not show any evidence of stochastic reacceleration.

5. Adding SGS fosters stochastic acceleration, which can contribute to initially energize the seeds, enabling some of them to penetrate in the higher Γ regions and get *espresso* accelerated (Figure 3.5).

6. The importance of SGS is limited to low-energy UHECRs. The highest-energy particles are invariably *espresso*-accelerated and the spectrum of the particles that reach the Hillas limit is independent of the level of SGS (see Figure 3.18).

7. In terms of AGNs as potential UHECR sources, SGS fosters the reacceleration of a large fraction of seed CRs, but does not change the maximum achievable energy, which is expected to be larger for more extended jets. This suggests that typical radio-bright AGNs should be able to accelerate particles at least to the stochastic Hillas limit, potentially filling the transition between Galactic and extra-galactic CRs and contributing to the lowest-energy UHECRs.

8. *Espresso* acceleration in powerful and extended FR-II jets, where the longitudinal Hillas criterion is maximized (See Equation 16 in MC19), remains the lead candidate for the production of the highest-energy CRs, independently of our poor knowledge of the actual CR diffusion rate in AGN jets.

Chapter 4

Effects of Losses on Ultra-high-energy Cosmic Rays and Neutrino Spectrum

The *espresso* framework suggests that UHECRs can be produced in relativistic AGN jets via the reacceleration of galactic CR seeds. Such seeds, accelerated in supernova remnants up to a few PV in rigidity, penetrate in the highly relativistic regions of the jets and tap in their radial electric field to receive one, or even multiple, $\sim \Gamma^2$ boosts in energy. If the jet is sufficiently powerful with $\Gamma \sim 20 - 30$, a single shot would allow them to reach UHECR energies. In Mbarek & Caprioli (2019); Mbarek & Caprioli (2021), the *espresso* mechanism has been tested by propagating particles in high-resolution magnetohydrodynamical (MHD) simulations of AGN jets (Mignone et al., 2007; Rossi et al., 2008).

In Mbarek & Caprioli (2019), hereafter MC19, we found that the spectra, chemical composition, and anisotropy of the reaccelerated particles are consistent with UHECR phenomenology. Then, in Mbarek & Caprioli (2021), hereafter MC21, we included sub-grid scattering (SGS) to model small-scale magnetic turbulence

that cannot be resolved by MHD simulations, constraining for the first time one potentially crucial but hard-to-model ingredient. We established the relative importance of *espresso* and stochastic acceleration in relativistic jets, finding that strong SGS, on one hand, can promote the injection and acceleration of lower-energy UHECRs, but on the other hand, is irrelevant for the acceleration of the highest-energy CRs, which are invariably *espresso*-accelerated.

In this chapter, we include the effects of photodisintegration and high-energy neutrino production in AGN jets within our self-consistent particle acceleration framework. In particular, we investigate how the intense radiation fields of the blazar zone, the broad-line region, and the dusty torus may affect the chemical composition of the accelerated particles. Moreover, modeling UHECR attenuation in a realistic jet environment allows us to calculate the spectrum of high-energy neutrinos produced in these sources.

Within our bottom-up approach we aim to address, with as few assumptions as possible, some key open questions such as:

- What are the effects of losses on *espresso*-accelerated particles in AGN jets?
- What is the expected spectrum of UHE (Ultra-High-Energy) neutrinos produced by a typical AGN?
- If AGNs are sources of UHECRs, can they be responsible for the observed IceCube flux, too?

This chapter is particularly important to unravel questions associated with Ultra-High-Energy (UHE) neutrinos. UHE neutrinos are created through interactions of UHECRs and are pivotal tools to advance our knowledge of extreme astrophysical environments. Many current and proposed experiments, such as the balloon-borne interferometer ANITA (Gorham et al., 2018a,b), the Askaryan Radio Array (ARA) (Allison et al., 2012, 2016), the In-Ice Radio Array ARIANNA

(Barwick et al., 2017), and the proposed POEMMA mission (Olinto et al., 2017), aim to detect EeV neutrinos for the first time. Theoretical studies have mostly focused on setting limits on the flux of *cosmogenic neutrinos*, i.e., the neutrinos created by UHECRs through interactions with the extragalactic photon background during intergalactic propagation (e.g. Heinze et al., 2016, 2019; Das et al., 2019; Wittkowski & Kampert, 2019; Romero-Wolf & Ave, 2018). On the other and, UHE *source neutrinos*, i.e., neutrinos produced in or around UHECR accelerators, especially in the presence of extreme photon fields, could be crucial to unravel the sites of production of the highest-energy particles in the Universe. This study aims to shed more light on these UHE *source neutrinos*.

The paper is organized as follows. In §4.1, we describe our particle acceleration framework, detailing the different interaction routes that lead to losses and neutrino production. In §4.2, we investigate the effects of losses on the UHECR chemical composition and put constraints on the expected *upper bounds* of the neutrino spectrum resulting from UHECR interactions. We discuss the acceleration mechanism responsible for boosting UHECRs that may contribute to the IceCube flux in §4.2.3.

4.1 Propagating Particles in Realistic Jets

4.1.1 MHD Simulation of a Relativistic Jet

To facilitate the comparison with published results, we model the underlying AGN relativistic jet via the same benchmark simulation used in MC19 and MC21; we refer to those papers for all the details and summarize here the essential information. We consider a 3D relativistic MHD simulation of a powerful AGN jet performed with PLUTO (Mignone et al., 2010), which includes adaptive mesh refinement. The jet, with a magnetization radius $R_{\rm jet}$, is initialized with Lorentz factor $\Gamma_0 = 7$ along the z-direction in a box that measures $48R_{\rm jet}$ in the x- and y-

directions and $100R_{\rm jet}$ in the z-direction in a grid that has $512\times512\times1024$ cells with four refinement levels. The jet/ambient density contrast is set to $\psi = 10^{-3}$, the jet sonic and Alfvénic Mach numbers to M_s =3, and $M_A = 1.67$ respectively. Once the jet has developed, the effective Lorentz factor in the jet spine is $\Gamma_{\rm eff} \sim 3.2$; this value is important to establish how many Γ^2 shots a particle undergoes during acceleration.

4.1.2 Particle Propagation

We propagate $\sim 10^5$ test particles in a snapshot of the benchmark jet with a broad range of initial gyroradii $\mathcal{R}$ and positions. We include the effects of unresolved turbulence by setting the sub-grid scattering (SGS) mean free path to be as small as the particle's gyroradius (Bohm diffusion) to maximize the number of particles within the jet spine and boost the efficiency of particle acceleration (see MC21 for more details on the effects of SGS). This prescription should enhance the effects of photon fields, but does not affect particle acceleration at the highest energies, which are invariably accelerated via the SGS-independent *espresso* mechanism (see MC21).

In addition to protons, we consider four different seed ion species, labelled se =[He, C/N/O,Mg/Al/Si, Fe] with effective atomic number $Z_{\rm se} = [2, 7, 13, 26]$ and mass $A_{\rm se} = [4, 14, 27, 56]$, respectively. The energy flux of these seed galactic CRs below the knee is parameterized as follows:

$$\phi_{\rm se}(E) = K_{\rm se}\left(\frac{E}{10^{12}\ {\rm eV}}\right)^{-q_{\rm se}}, \tag{4.1}$$

We set the normalizations according to the abundance ratios at 10^{12} eV observed in Galactic CRs, such that $K_{\rm se}/K_H \sim$ [0.46, 0.30, 0.07,0.14]. The motivation for using Galactic CR fluxes as fiducial hinges on the fact that the knee feature (the maximum seed energy) should be rather universal (Caprioli, 2015b). We ac-

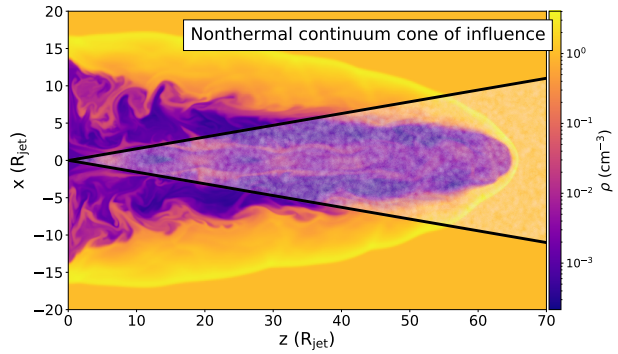

Figure 4.1: Nonthermal continuum cone of influence overlaid on a 2D slice of the density component of the MHD jet. The cone is beamed at an angle $1/\Gamma_{\rm eff}$, Where $\Gamma_{\rm eff} \sim 3.2$ is the effective Lorentz factor of the jet (See Figure 6 in MC19 for more details). The density is normalized based on the assumptions discussed in §4.1.4 to maximize pp-interactions.

knowledge that the actual seed fluxes in AGN hosts may be different due to the different injection and confinement properties of other galaxies but, since the chemical enrichment provided by diffusive shock acceleration of seeds in supernova remnants (Caprioli et al., 2010b, 2017) is rather universal and since the final UHECR fluxes that we consider are normalized to the observed one, the assumptions above are quite genetic. The spectra of different species are calculated as outlined in Appendix 4.4.

Particles are propagated in the MHD simulation even if their gyroradii are smaller than the grid size, which is reasonable as long as a sufficiently small rigidity-dependent timestep is used to resolve their gyration; every particle's gyroradius is resolved with *at least* 10 timesteps.

4.1.3 Photon Field Prescriptions

On top of the jet structure provided by the MHD simulation, we prescribe external photon fields based on the methods presented in Murase et al. (2014), hereafter M14. There is ostensible uncertainty in modeling these external components due to the vast AGN diversity, but the systematic approach of M14 allows us to assess

the individual effect of such fields based on the apparent bolometric luminosity of the jet.

We consider five different photon backgrounds of different origin:

(i) Nonthermal emission: It originates from synchrotron and inverse-Compton radiation of relativistic leptons and/or hadronic emission, emerging from the blazar zone, a sub-pc region close to the base of the jet (See M14 for more details), where the emission is dominated by x/γ-rays and is beamed with an angle $\sim 1/\Gamma$. We refer to this broadband emission region as the nonthermal cone of influence (see Figure 4.1).

(ii) Radiation from the broad atomic line region (BLR): This is the emission from cold gas clumps photoionized by the UV and X-ray produced by the accretion disk. These sub-pc spherical clumps are located closer to the base of the jet (< 1pc away) and have a luminosity $\sim 10\%$ of that of the accretion disk (see M14).

(iii) IR emission from the dusty torus: This is IR from reprocessed accretion dusty disk radiation with a torus size that can reach ~ 1pc. Following M14, we model it as a spherical grey body with temperature $\sim$500K.

(iv) Stellar light: The photons from the host-galaxy stars have been shown to have large energy densities compared to other photon fields at a few hundred pc, which makes them important targets for accelerated particles in powerful AGN jets. In the remainder of the paper, we will consider the starlight emission profile for Centaurus A as our fiducial case (Tanada et al., 2019).

(v) The cosmic microwave background (CMB) radiation: Besides affecting every particle regardless of its location, accounting for the CMB contribution serves as a benchmark to compare the effect of the prescribed photon fields.

In the remainder of the paper, all photon fields are assumed to be isotropic except for the nonthermal component, which is beamed within a cone of aper-

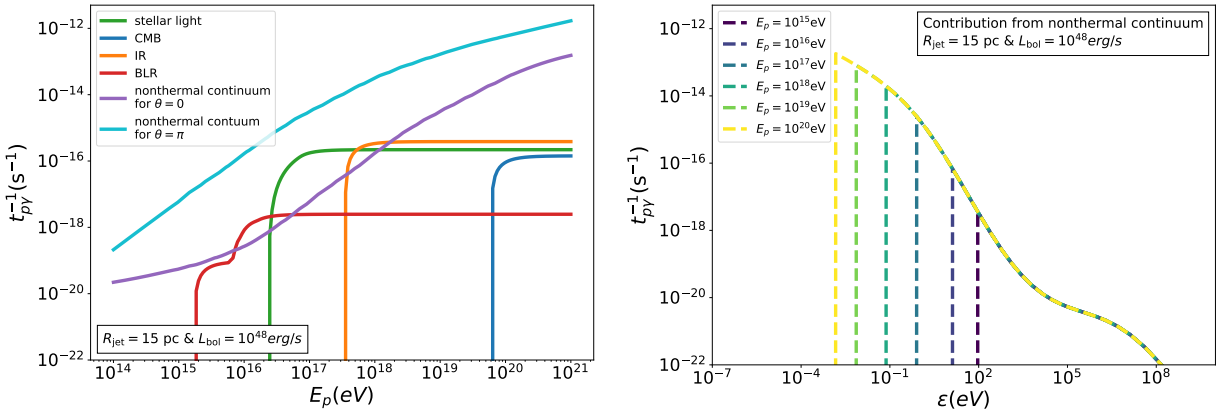

Figure 4.2: Left Panel: Photomeson cooling time for a proton located at a position (0,0,750pc) for a jet with $R_{\rm jet} = 15$pc and $L_{\rm bol} = 10^{48}$erg s^{-1}. Contributions from the isotropic photon fields (BLR, IR, stellar light, and CMB) are calculated based on equation 4.14. Contributions from the beamed nonthermal continuum are calculated based on equation 4.16. Here, θ denotes the angle between the momentum of the proton and the target photon such that $\theta = \pi$ for head-on interactions and $\theta = 0$ for tail-on interactions. Right Panel: Photomeson cooling time for protons with different energies located at the same position as a function of the photon energy ϵ. This plot only considers head-on interactions ($\theta = \pi$) with the nonthermal continuum as an example.

ture $1/\Gamma_{\rm eff}$, where $\Gamma_{\rm eff}$ is the effective Lorentz factor of the jet. The BLR, IR and nonthermal contributions have intensities that are inversely proportional to the square of the distance from their emitting regions.

4.1.4 Particle Interactions

When propagating our test particles, at every time step we: (i) calculate the probability of interaction with the thermal plasma (assuming it is electron–proton) and photon fields; (ii) keep track of each particle's atomic mass A and charge Z; (iii) monitor secondary particle production including neutrinos and secondary protons. Finally, secondary protons and ions are further propagated until parent and secondary nuclei have travelled a distance of at least 100 $R_{\rm jet}$. Produced neutrinos are assumed to escape without experiencing further interactions; their place of production and escaping direction are recorded, though.

	Process	Reactions	Energy Frac.
p	proton-proton (pp)	$\mathrm{p} + \mathrm{p} \rightarrow \mathrm{p} + \mathrm{n} + \pi^{+}$ $\rightarrow \mathrm{p} + \mathrm{n} + e^{+} + \nu_e + \nu_\mu + \bar{\nu}_\mu$	p:$\nu \sim$ 20:1
	photomeson ($p\gamma$)	$\mathrm{p} + \gamma \rightarrow \mathrm{n} + \pi^{+}$ $\rightarrow \mathrm{n} + e^{+} + \nu_e + \nu_\mu + \bar{\nu}_\mu$	p:$\nu \sim$ 20:1
N	photomeson ($N\gamma$)	$\mathrm{N} + \gamma \rightarrow {}^{\mathrm{A}-1}\mathrm{N} + \mathrm{n} + \pi^{+}$ $\rightarrow {}^{\mathrm{A}-1}\mathrm{N} + \mathrm{n} + e^{+} + \nu_e + \nu_\mu + \bar{\nu}_\mu$	N:$\nu \sim$ 20:1
	photodisintegration	${}^{\mathrm{A}}\mathrm{N} + \gamma \rightarrow {}^{\mathrm{A}-1}\mathrm{N} + \mathrm{n}$ $\rightarrow {}^{\mathrm{A}-1}\mathrm{N} + \mathrm{p} + e^{-} + \bar{\nu}_e$	N:$\nu \sim 10^3$A:1
	& neutron decay	${}^{\mathrm{A}}\mathrm{N} + \gamma \rightarrow {}^{\mathrm{A}-1}\mathrm{N} + \mathrm{p}$	—

Table 4.1: Neutrino production mechanisms for protons (p) and nuclei (N) of atomic mass A. The last column gives the ratio of the energy of the neutrino with respect to the parent particle (the parameter α introduced in Appendix 4.4).

In order to study the effects of UHECR photodisintegration and the resulting neutrino flux, we consider the most relevant attenuation mechanisms, i.e., inelastic proton-proton (pp), photomeson ($p\gamma$), and neutron decay following photodisintegration of heavy nuclei. More specifically, photomeson interactions of photons and nucleons also result in the production of pions that subsequently decay to create photons and neutrinos. On the other hand, photodisintegration interactions are nuclear processes that cause the photon-absorbing nucleus to change to another chemical specie and release either a proton or a neutron. Table 4.1 summarizes the interaction routes that lead to neutrinos and photodisintegration of heavy elements. A more detailed explanation of the interaction probabilities at every time step is included below.

Proton-proton (pp) Interactions

Accelerated particles can experience pp scattering to create charged pions and hence ν_e and ν_μ neutrinos. At every time step, depending on the particle's energy E_p and position x, there is an interaction probability $P(E_p, \mathrm{x}) \sim n(\mathrm{x})\sigma_{pp}(E_p)R_{\mathrm{jet}}\Delta t$, where σ_{pp} is the pp interaction cross section (Tanabashi et al., 2018), n is the

position-dependent density, and Δt is the time step. The neutrino spectrum that results from every pp interaction is calculated based on the parametrization by Kelner et al. (2006).

Powerful AGN jets are predominantly inside clusters of galaxies (e.g., Begelman et al., 1984; Best et al., 2007; Fang & Murase, 2018b), so that the ambient medium density should reflect that of the intra-cluster medium, which is of order of $n_{\rm ICM} \sim 10^{-3}{\rm cm}^{-3}$ (Walg et al., 2013). This reference value is used in Figure 4.1, which also shows that the jet itself is expected to have an even lower density; Generally, pp interactions are not expected to contribute much to the overall neutrino spectrum.

Photomeson ($p\gamma$) Interactions

At every time step Δt, a photopion production probability $f_{p\gamma}$ is calculated such that $f_{p\gamma} = t_{p\gamma}^{-1}\Delta t$, where $t_{p\gamma}$ is the photomeson cooling time. A detailed account of $t_{p\gamma}$ calculations for isotropic photon fields and interactions at a known angle for both protons and nuclei with atomic mass A is provided in Appendix 4.4.

In general, the cooling time depends on the particle position and on the AGN luminosity; therefore, we cannot use dimensionless quantities but need to introduce physical scales for the magnetic field strength and for the jet size and luminosity. For instance, the left panel of Figure 4.2 shows the cooling time for protons of different energies located 750 pc away from the base of the jet along the spine (z-direction in Figure 4.1), for a jet with radius $R_{\rm jet} = 15{\rm pc}$ and an apparent bolometric luminosity $L_{\rm bol} = 10^{48}{\rm erg\ s}^{-1}$. In this characteristic example, we show the contribution from isotropic photon fields (BLR, IR, stellar light, and CMB, as in the legend) and the angle-dependent interactions with the beamed nonthermal continuum (cyan and purple lines). The left panel of Figure 4.2 shows that the nonthermal contribution provides the shortest photomeson cooling time (even for

tail-on interactions, i.e., $\theta = 0$). These cooling curves depend on the particle position (distance from the base of the jet and position with respect to the nonthermal continuum cone of influence) as will be further discussed below.

The right panel of Figure 4.2 shows the dependence of the cooling time on the photon energy ϵ when the proton energy is fixed. Only the nonthermal contribution is shown here for simplicity as it is the dominant photon field. We can see that the shortest cooling time—which depends on the proton energy— occurs at the threshold energy $\bar{\epsilon}_{\rm th}$ for photomeson interactions (See Appendix 4.4 for more details). Importantly, the contribution of x/γ-ray photons with $\epsilon \geq> 100$eV to cooling is only significant for lower energy protons. This paints a picture where a potential correlation between $\gamma-$ray flares and neutrino detection would be mostly relevant for interactions with galactic CRs with energies $E_{CR} \lesssim 10^{15}$eV.

Photodisintegration Interactions

On the same photon fields, nuclei with atomic mass A can also undergo photodisintegration with probability $t_{A\gamma}^{-1}\Delta t$ per time step. Appendix 4.4 details our calculations, in particular the use of the giant dipole resonance (GDR) cross-section (e.g., Wang et al., 2008) as a fiducial case (see Figure 4.3). We also account for photomeson interactions of heavy nuclei (as described in Equation 4.15 in Appendix 4.4), and find that their cooling time is comparable to that of protons. Also for nuclei, the most important photon background is typically the nonthermal component, as shown by a comparison of Figure 4.3 with Figure 4.2 and Equation 4.15. Higher-energy nuclei are more likely to be photodisintegrated, as expected.

While propagating particles, we keep track of the atomic mass and charge of nuclei, considering that after photodisintegration event, the nucleus loses either one neutron or one proton. Neutrons produced as a result of photodisintegration

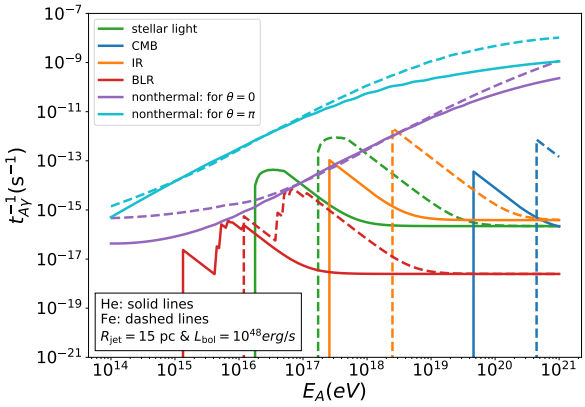

Figure 4.3: Same as the left panel of Figure 4.2 but for photodisintegration interactions of nuclei with energy E_A, including photomeson interactions and interactions based on the GDR photodisintegration total cross section (see Equation 4.19 and 4.20).

decay within a distance $9.15(E_n/10^9\text{GeV})$kpc (Anchordoqui et al., 2007); since secondary particles cannot achieve energies beyond $\sim 10^{10}$GeV, we assume that all the secondary neutrons β-decay and produce neutrinos on their way to Earth.

Dependence on the Distance from the AGN

Since different photon backgrounds have different spatial extents, the cooling time for both photodisintegration and $p\gamma$ interactions depend on the magnitude of the distance from the base of the jet, D, such that close to the base of the jet $t^{-1} \propto D^{-2}$ where photon fields other than the CMB are most relevant. For a jet with bolometric luminosity $L_{\rm bol} = 10^{45}$erg s^{-1}, nonthermal emission is dominant until $D \sim 3$kpc, beyond which the CMB becomes important. Considering that the photon fields we assume are generated close to the base of the jet, CR interactions beyond a few kpc would not increase with large jet extents, usually associated with the more luminous FR-II jets.

4.1.5 From Scale-free MHD Simulations to Realistic Environments

In our simulations, CR gyroradii are normalized to the jet radius $R_{\rm jet}$ and magnetic field B_0; therefore, setting a physical value to $R_{\rm jet}$ and B_0 is equivalent to associating physical energies to the seed particles of charge Ze. In order to calculate the actual neutrino fluxes from realistic AGNs, we need to fix a reference magnetic field and two physical quantities of the jet: its bolometric luminosity, which controls the photon fields, and its radius.

Our simulations have extensively shown that particles are routinely *espresso*-accelerated up to the jet Hillas limit (MC19, MC21). In our 3D relativistic MHD simulations we launch the jet with $\Gamma = 10$; yet, the effective Lorentz factor of evolved jets turns out to be $\Gamma_{\rm eff} \sim$ a few, too small to promote CR seeds with rigidities of a few PeV to actual UHECRs with a single $\Gamma^2_{\rm eff}$ boost. Therefore, in order to achieve realistic UHECR energies, we fix the normalization of our jet radius and magnetization such that CR seeds have rigidities as large as 3×10^{17}V, two orders of magnitude above the CR knee. This choice allows us to include the attenuation losses discussed for realistic photon fields and to calculate the fluxes of UHECRs and HE neutrinos expected from different kinds of AGNs.

When contemplating assigning B-field, radius, and $L_{\rm bol}$ prescriptions to our jet, one needs to consider different types of radio-loud AGNs, which at minimum can be split into FR-I and FR-II sources. FR-I jets are typically decelerated to nonrelativistic bulk flows within 1 kpc (e.g., Wardle & Aaron, 1997; Arshakian & Longair, 2004; Mullin & Hardcastle, 2009), while FR-II jets, show $\Gamma \gtrsim 10$ at scales of tens of kpc and beyond (e.g., Sambruna et al., 2002b; Siemiginowska et al., 2002b; Tavecchio et al., 2004; Harris & Krawczynski, 2006b). The FR dichotomy likely reflects a combination of jet power and ambient density (Bromberg

& Tchekhovskoy, 2016), and our fiducial jet propagating in a homogeneous density profile may resemble a FR-I jet more than a FR-II one, with a relatively low $\Gamma_{\rm eff}$ and a small $R_{\rm jet}/H_{\rm jet}$ ratio, where $H_{\rm jet}$ is the extent of the jet. Yet, in this work we consider here a broad range of luminosities that should span the appropriate parameter space. More precisely, we consider the two following cases.

Case I: Extremely High-luminosity AGNs As a benchmark for a quite powerful jet of limited ($\sim$ 1kpc) extent, we consider $L_{\rm bol} = 10^{48}$erg s^{-1}, $R_{\rm jet} = 15$pc ($H_{\rm jet} \sim 1$kpc), and $B_0 = 100\mu$G. Such a large magnetic field is routinely inferred in powerful FR-II jets, but should also pertain to the spines of FR-I jets (e.g., Hardcastle et al., 2004; Hawley et al., 2015). This $L_{\rm bol}$ prescription is reminiscent of blazars, including flat-spectrum radio quasars (FSRQs) and BL Lac objects, that have $L_{\rm bol}$ that go beyond $10^{48}\,{\rm erg\ s^{-1}}$ (e.g. Ghisellini et al., 2010). This should enhance the effects of photodisintegration and the production of neutrinos considering that this $L_{\rm bol}$ is deemed quite large (Ajello et al., 2013; Tadhunter, 2016; Blandford et al., 2019; Mingo et al., 2019) and particles propagate closer to the base of the jet—where most photons are emitted—compared to the expected size of FR-IIs where $H_{\rm jet}$ can reach hundreds of kpc.

Case II: High-luminosity AGNs A jet with a more moderate bolometric luminosity $L_{\rm bol} = 10^{45}$erg s^{-1}, $R_{\rm jet} = 1$pc, and $B_0 = 150\mu$G is assumed here. Just as in Case I, the strong magnetic field prescription serves only to study the effect of photodisintegration on UHECRs and the production of astrophysical UHE neutrinos. We choose to set the jet radius to 1pc to further increase the probability of particle interactions as the bulk of the photon field energy is emitted at the base (See §4.1.4 for a discussion on the distance dependence), by setting $H_{\rm jet}$ to the smallest FR-I scales (Hawley et al., 2015).

4.1.6 The UHECR Injection Spectrum

While the spectrum of UHECRs detected at Earth is measured to be $\propto E^{-2.7}$, the actual spectrum injected by their sources is not well constrained because of the uncertainties in the cosmological distribution of sources and in adiabatic and inelastic losses. While several authors have considered an injection spectrum E^{-q}, with $q = 2$ (e.g., Waxman, 1995; Katz et al., 2013; Aloisio et al., 2011), more recent Auger data favor a harder injection spectra with $1 \leq q \leq 1.6$ (e.g., Aloisio et al., 2011; Gaisser et al., 2013; Aloisio et al., 2014a; Taylor et al., 2015; Aab et al., 2017c) to explain the observed heavy chemical composition. For steeper spectra, the rate of injection $Q_{\rm UHECR}$ has been calculated to be $Q_{\rm UHECR}(q = 2) \sim 5 \times 10^{43}\,{\rm erg\ s^{-1}\,Mpc^{-3}}$for $E \gtrsim 10^{19}$eV (e.g., Katz et al., 2013). On the other hand, flatter injection spectra would require a slightly larger rate, such that $Q_{\rm UHECR}(q = 1) \sim 2 \times 10^{44}\,{\rm erg\ s^{-1}\,Mpc^{-3}}$for $E > 10^{16}$eV (e.g. Aloisio et al., 2014a).

In this paper, in which we do not account for propagation effects, we bracket our ignorance of actual UHECR spectrum by considering injection slopes $1 \leq q \leq 2$. In the *espresso* framework, the injection spectrum turns out to be flatter than the spectrum of the CR seeds, which should be a power law $\propto E^{-q_{\rm se}}$, with $q_{\rm se} \sim 2-2.7$ (Caprioli, 2015b), because reacceleration tends to push particles close to the jet's Hillas limit (MC19, MC21). A systematic study of *espresso* acceleration in different kinds of AGN jets is ongoing, but in general we find that $q - q_{\rm se} \sim 0.5-1$, consistent with the flatter spectra required to explain Auger data (e.g., Aloisio et al., 2014a; Taylor et al., 2015).

In general, the spectrum of secondary particles and UHE neutrinos is a function of q; therefore we show results for different values of $q_{\rm se}$. In the remainder of this paper, we fix the value of the UHECR injection spectrum q such that $1 \leq q \leq 2$.

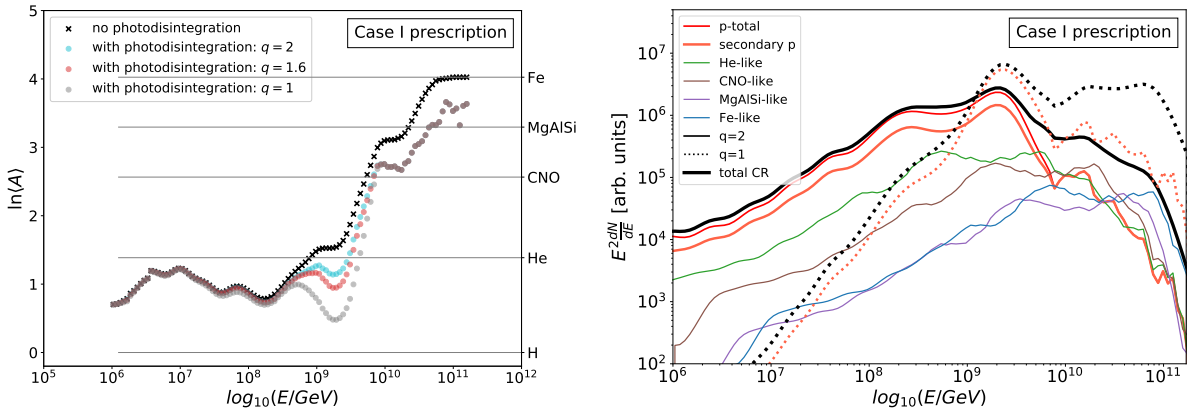

Figure 4.4: Left Panel: Average atomic mass A as a function of energy for the spectrum from the left panel for Case I prescription. The horizontal solid lines correspond to the atomic masses of the injected chemical species. Right Panel: UHECR spectrum including secondary particle spectra. He-like are particles with atomic mass A$\in [3, 8]$; CNO-like with A$\in [9, 18]$; MgAlSi-like with A$\in [19, 35]$; Fe-like with A$\in [36, 56]$.

4.2 Results

4.2.1 Effects of losses on UHECR spectra

Let us start the discussion of our main findings by assessing the role of losses on the spectra of reaccelerated UHECRs. As discussed above, the parameters for Case I are chosen in order to maximize the potential losses for UHECRs: a powerful, yet compact, source would in fact force particles to propagate closer to the AGN and hence be exposed to the bulk of its nonthermal emission (see, e.g., Dermer, 2007).

The left panel of Figure 4.4 shows the average atomic mass and spectrum of UHECRs for Case I, with the contribution of different chemical species and for values q =1, 1.6, and 2. The interesting result is that the UHECR spectrum is not significantly affected by photodisintegration, even with a prescription that may magnify its effects. A large fraction of the heavy nuclei survives losses because seed reacceleration occurs throughout the jet extent, and not just in the blazar

region. The light component cuts off at a few times 10^{18}eV, and the overall spectrum gets heavier with increasing energy, consistent with Auger observations (Aab et al., 2014b; Aab et al., 2017a; Yushkov, 2019). The right panel of Figure 4.4 breaks down the contribution of each chemical species for $q = 2$ (solid lines, color coded) and also shows the total spectrum for $q = 1$ (dotted line).

Unger et al. (2015) suggested that heavy ions may be photodisintegrated if the UHECR confinement time were increased around sources due to the presence of magnetic irregularities. In this picture the secondary nuclei originating in these regions would account for the light composition observed below 10^{18} eV. Here we observe a similar phenomenology, in the sense that particle scattering in the cocoon produces a light-element bump of reaccelerated secondary protons around 10^{18} eV, provided that the seed spectrum is sufficiently flat. This would correspond to the so-called EeV component that is often invoked to fit the low-energy section of the UHECR spectra (e.g, Gaisser et al., 2013; Aloisio et al., 2014a). Note that the position of this bump does not depend on the assumed SGS, in that it corresponds to the Hillas limit for protons; also, increased scattering does not significantly increase the confinement time of particles because particles are more likely to escape sideways from the jet as SGS increases (see MC21).

4.2.2 Neutrinos from interactions of UHECRs inside their sources

UHE neutrino flux expeted from a given AGN

The black and red curves in Figure 4.5 show the expected UHECR and neutrino spectra for two different AGNs (Case I and II, left and right panel, respectively) and for $q = 1, 2$ (dashed, solid lines), as examples of spectral slopes. Extrapolations to other q's are straightforward based on the results in Appendix 4.4.

Three main trends arise, as expected: 1) the neutrino flux is proportional to the jet luminosity (compare left and right panels in Figure 4.5); 2) flatter injec-

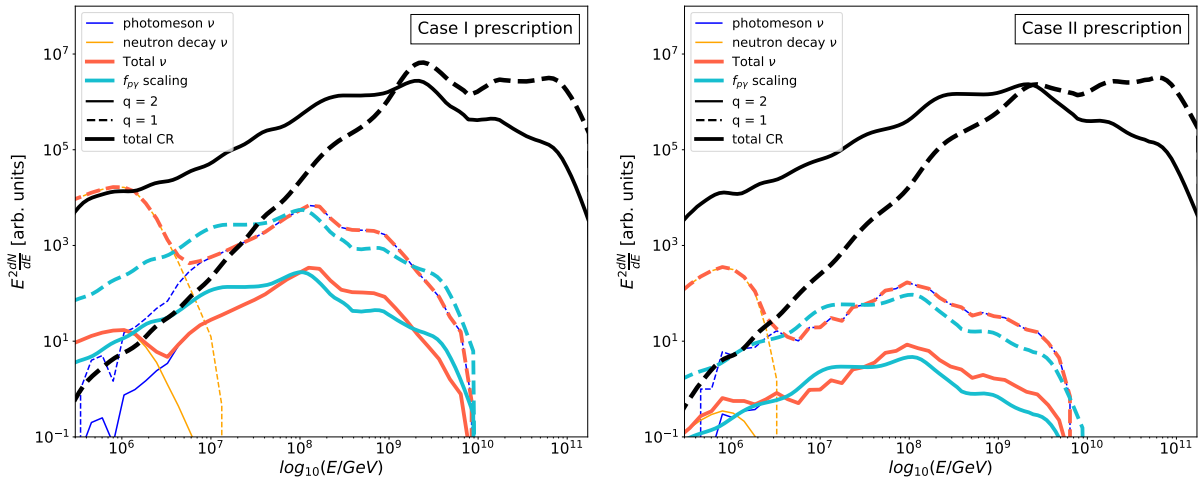

Figure 4.5: Left Panel: Overall CR spectrum including secondary particles in black for the examples of q= 1, 2 assuming the same power at 10^{18}eV. Note that the CR spectrum is not affected by the bolometric luminosity prescriptions because photodisintegration does not play a major role in this energy range. Blue and Orange lines: neutrino spectra that ensued from neutron decay, and $p\gamma$ and pp interactions for different radius and bolometric luminosity prescriptions. The spectra are computed based on the methods presented in §4.4 and §4.4. The teal lines show the expected neutrino based on the ν scaling from Equation 4.2. Right Panel: Same as the left panel but for the Case II prescription.

tion slopes produce more neutrinos (see Appendix 4.4); 3) the highest-energy neutrinos are produced via photomeson interactions (thin blue curves), while at lower energies ($\lesssim$10 PeV) neutrinos from the neutron decay of photodisintegrated UHECRs dominate the flux (thin yellow curves). Finally, we point out that all the neutrinos produced here are from $p\gamma$ interactions; *pp* collisions are negligible and not visible in the plots. These results do not depend on the level of assumed SGS, since most of the HE neutrinos are produced by the highest-energy UHECRs, which are always *espresso* accelerated (MC21).

The red lines in Figure 4.5 are calculated based on the propagation of test-particles in our fiducial jet, but it is instructive to also calculate the neutrino spectrum resulting from a much simpler approach that ignores the actual jet structure. Such an analytical *one-zone model* is fully described in Appendix 4.4; in a nutshell, a neutrino flux can be estimated via a rescaling of the UHECR flux

based on an effective optical depth $f_{p\gamma}$ for $p\gamma$ interactions, with $f_{p\gamma}$ given by:

$$f_{p\gamma} \equiv \frac{F_{\mathrm{UHE}\nu}(E_\nu)}{F_{\mathrm{UHECR}}(E)} \sim \alpha^{q-1}\sigma_{\mathrm{eff}}\xi\frac{L_{\mathrm{bol}}}{2\pi H_{\mathrm{jet}}c}\frac{1}{\epsilon_{\mathrm{max}}} \tag{4.2}$$

where $F_{\mathrm{UHE}\nu}$ and F_{UHECR} are their respective fluxes at the source, H_{jet} the extent of the jet, ϵ_{max} the most probable photon energy, L_{bol} the bolometric luminosity of the jet, ξ the average energy fraction lost to the pion, and $E_\nu = \alpha E$ (see Table 4.1). f_ν can be thought of as an effective optical depth for UHECR interactions, which captures the order of magnitude of the full kinetic approach (compare red and teal curves in Figure 4.5) and which can be used to quickly estimate the expected neutrino flux from a given AGN that is active as a UHECR source.

Total Expected Flux of UHE Source Neutrinos

We move now to estimating the overall flux of UHE neutrinos produced by a realistic distribution of AGNs. The energy flux in neutrinos that comes from the convolution over the cosmological distribution of their sources can be expressed as (e.g. Ahlers & Halzen, 2017):

$$E_\nu^2\phi_\nu \sim \frac{c}{4\pi}\int_0^{z_{\mathrm{max}}}\frac{dz}{H(z)}\rho(z)E_\nu^2\mathcal{J}_\nu[(1+z)E_\nu] \tag{4.3}$$

where $\rho(z)$ is the number density of sources, $H(z) = H_0\sqrt{(1+z)^3\Omega_M + \Omega_\Lambda}$ is the Hubble parameter, with $\Omega_M \approx 0.3$ and $\Omega_\Lambda \approx 0.7$ for standard ΛCDM cosmology, and $H_0 = 70$km s^{-1} Mpc^{-1} is the Hubble constant. The $\mathcal{J}_\nu[(1+z)E_\nu]$ term is the average neutrino source luminosity.

In this paper, we consider a scenario in which all the UHECRs are produced in environments with strong photon fields, which should get us closer to an upper limit on the possible neutrino flux. Such a flux must be anchored to some expected UHECR luminosity, hence we scale the $\rho(z)E_\nu^2\mathcal{J}_\nu$ term with $Q_{\mathrm{UHECR}}(E =$

10^{19}eV) (see §4.1.6), since most CR interactions leading to neutrinos occur at 10^{19}eV.

Both the photon and the UHECR luminosities for an AGN jet should scale with its bulk power (also see MC19). Ghisellini et al. (2009) found that there may be hints that could relate the jet bulk power to accretion disk luminosity; this study was later complemented by findings from Ghisellini et al. (2014) where it was asserted that there is a clear correlation between the accretion luminosity and γ-ray jet luminosity. The UHECR injection rate at any redshift can then be written as a function of the local one such that:

$$Q_{\rm UHECR}(z,q) = Q_{\rm UHECR}(z\sim 0,q)\zeta_z(L_{\rm x},z), \tag{4.4}$$

where ζ_z is a cosmological evolution factor defined in Equation 4.30 of Appendix 4.4 and $L_{\rm x}$ the X-ray luminosity of the AGN sources. The prescribed photon fields in our framework are related to $L_{\rm x}$ such that $L_{\rm bol}/L_{\rm x} = 10^{4.21}$ where the constant of proportionality is obtained by modeling the γ-ray luminosity function through the observed X-ray luminosity (see, e.g., Inoue & Totani, 2009; Inoue et al., 2010; Harding & Abazajian, 2012).

Assuming that there are different classes of high-luminosity AGNs, we can then rewrite Equation 4.3 as:

$$E_\nu^2\phi_\nu \sim \frac{c}{4\pi}\int_0^{z_{\rm max}}\frac{dz}{H(z)}Q_{\rm UHECR}(z\sim 0,q)\sum_i w_i f_\nu(L_i,E,q)\zeta_z(10^{-4.21}L_i,z) \tag{4.5}$$

where the weights w_i of the different classes are defined as the relative X-ray injection in Mpc^{-3} of each AGN type:

$$w_{\log({\rm L_{bol}})} = w(L_{\rm x}) = \frac{L_{\rm x}\frac{d\psi}{dL_{\rm x}}}{\sum_k L_k\frac{d\psi_k}{dL_k}} \tag{4.6}$$

such that $\frac{d\psi}{dL_{\rm x}}(L_{\rm x}, z)$ is the z-dependent X-ray luminosity function of the AGN sources per luminosity per comoving volume (see Appendix 4.4 for more details). As discussed in §4.1.6, $Q_{\rm UHECR}$ depends on the injection slope q, and in particular we have that $Q_{\rm UHECR}(z \sim 0, q = 2) \sim 5 \times 10^{43}$ erg Mpc^{-3} yr^{-1} (Katz et al., 2013) at $\sim 10^{19}$eV and $Q_{\rm UHECR}(z \sim 0, q = 1) \sim 2 \times 10^{44}$ erg Mpc^{-3} yr^{-1} for $E_{\rm CR} > 10^{16}$eV (Aloisio et al., 2014a; Aab et al., 2017c); we also assume a rate equivalent to $Q_{\rm UHECR}(z \sim 0, q = 1)$ for $q \leq 1.6$ (Aloisio et al., 2014a).

In this study, we consider contributions from two types of AGN jets with two different bolometric luminosities: i) extremely high-luminosity AGNs with $L_{\rm bol} = L_{48} \sim 10^{48}$erg s^{-1} (Case I), and ii) high-luminosity AGNs with $L_{\rm bol} = L_{45} \sim 10^{45}$erg s^{-1} (Case II). From Equation 4.29, we note that $L_{\rm x}\frac{d\psi}{dL_{\rm x}} \approx L_{\rm x}^{-2}$, so the relative contribution of each AGN type in this case is roughly the same, i.e., $w_{45} \sim w_{48}$ and the total energy injected per unit time in UHECRs should be contributed equally by both AGN types. Note that they could, in principle, accelerate particles to different maximum energies (see the discussion in MC21).

We finally obtain:

$$E_\nu^2 \phi_\nu \sim \frac{c}{4\pi} \int_0^{z_{\rm max}} \frac{dz}{H(z)} Q_{\rm UHECR}(q) \Big[w_{45} f_\nu(L_{45}, E, q) \zeta_z(10^{-4.21} L_{45}, z) + w_{48} f_\nu(L_{48}, E, q) \zeta_z(10^{-4.21} L_{48}, z) \Big] \tag{4.7}$$

Figure 4.6 shows the resulting UHE source neutrino fluxes (black lines) based on Equation 4.7 and expected cosmogenic neutrino fluxes (blue lines, from Batista et al., 2019) with IceCube observations (yellow data points). Shown are also the CR data from Auger (Aab et al., 2020), Telescope Array (Jui, 2016), and KASCADE-GRANDE (Apel et al., 2013a) for reference.

A few points are worth noticing.

- At a fixed UHECR injection rate, the normalization of the source neutrino

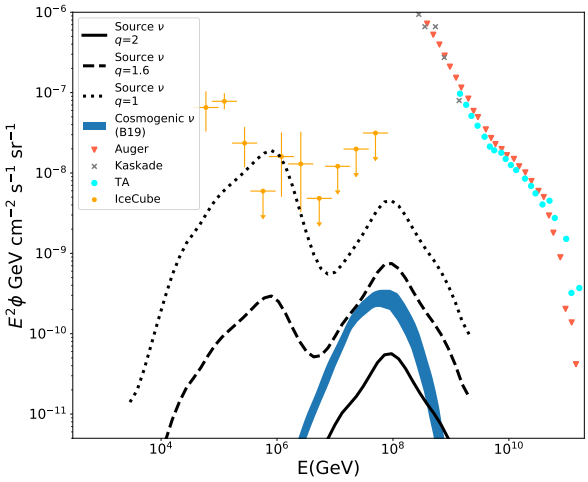

Figure 4.6: Expected upper bounds for the source neutrino flux (black) from UHECR interactions for three different injection slopes q=2 (solid) q=1.6 (dashed), and q = 1 (dotted) including cosmological effects. This flux is compared to the expected cosmogenic neutrino flux (blue bands) based on models that fit Auger's spectral features with different confidence levels (Batista et al., 2019). Such a cosmogenic flux is modeled according to an AGN source evolution. IceCube neutrino data, along with UHECR data from Auger, KASKADE, and TA are also included for reference.

flux is strongly dependent on the spectral slope of their parent UHECRs such that $f_\nu(E_\nu)/f(E_\nu) = \alpha^{q-1}$ with $E_\nu = \alpha E$ (See Appendix 4.4 and Table 4.1 for more details). The flatter the injection spectra, the more neutrinos are produced because the more power is available in CRs with energies above 10^{18}eV.

- If injection spectra are sufficiently flat, the flux of source neutrinos may dominate the expected flux of cosmogenic neutrinos (also see Rodrigues et al., 2021). Even for a moderately flat spectrum of $q = 2$, their relative contribution at $\sim 10^{17}$eV turns out to be comparable.

- Given the strong dependence of the source neutrino flux on q and α, neutrinos from the β-decay of photodisintegration byproducts ($\alpha = 10^{-3}$) may become a sizable fraction of the flux observed by IceCube below a few PeV for flatter spectra.

These results should be regarded as close to *upper limits* of the neutrino flux since we assumed that all UHECRs are produced in AGNs with pretty high bolometric luminosities (between 10^{45} and 10^{48} erg s^{-1}); if also low-luminosity AGNs (and/or other classes of sources) were to contribute to the observed UHECR flux, the expected neutrino flux would be reduced. Moreover, we have considered jets with a limited extent to maximize the effect of the photon fields that are generated close to the base of the jet. In fact, relaxing any of these assumptions would reduce the contribution of the non-thermal photon background to $p\gamma$ collisions; the CMB, BLR, and dusty torus contributions alone would provide a source neutrino flux that would be a few orders of magnitude smaller (see left panel of Figure 4.2), underdominant with respect to both the cosmogenic neutrino flux and the astrophysical neutrino flux in the IceCube band.

These results lead to two very general consideration. On one hand, neutrinos produced by the β-decay of secondary neutrons should always be accounted for when calculating the flux of expected UHE neutrino; their flux, especially for the flattest UHECR spectra consistent with Auger data, may be comparable with the one measured by IceCube.

On the other hand, in order to explain the whole IceCube flux with neutrinos from UHECR sources, photodisintegration would need to happen at a much higher rate than what is estimated here, which would be inconsistent with the presence of heavy elements at the highest energies. In other words, the optical depth f_ν required to produce a sizable source neutrino flux would necessarily lead to the complete photodisintegration of heavy UHECRs; this result is general and independent of the UHECR source or acceleration mechanism. Overall, better UHECR chemical composition measurements and constraints on the UHECR injection slopes may pose more stringent limits on the expected contribution of neutron-decay neutrinos to the observed IceCube flux.

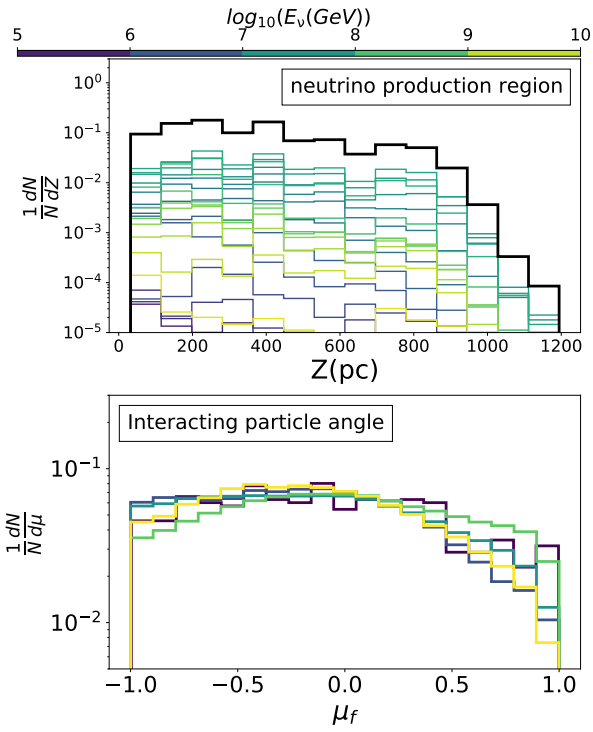

Figure 4.7: Upper Panel: Distribution of the final angles of escaping neutrinos. Neutrinos escape the jet quasi-isotropically. Lower Panel: Final z position of neutrinos for the Case I prescription to trace the regions where neutrinos are most likely to be produced. Neutrinos are preferentially produced close to the base of jet such that most neutrinos are produced within ~ 800pc, but a non-negligible fraction of neutrinos is produced at larger distances.

Site of Production and Angular Distribution of Escaping Neutrinos

In our simulations we keep track of where neutrinos are produced and in which direction they escape. The top panel of Figure 4.7 shows that a considerable fraction of neutrinos is produced at relatively large distances (~ 1 kpc) away from the base of the jet as a result of two competing effects: on one hand, the photon field intensity declines as D^{-2}; on the other hand the nonthermal emission cone affects a greater volume as we move away from the base of the jet. We observe similar trends for all of our prescriptions, so we argue that photodisintegration of heavy UHECRs and neutrino production should mainly occur at intermediate distances, not too close to the blazar region but well before the jet's end.

The bottom panel of Figure 4.7, instead, shows the distribution of the cosines of the final angles of flight of the neutrinos produced through $p\gamma$ interactions and neutron decay for Case I. Neutrinos are released quasi-isotropically, essentially because UHECRs are efficiently isotropized in the cocoon (see also MC19, M21).

This is important for neutrino astronomy because any correlation between neutrino directions of arrival and the AGN population[1] is intrinsically connected to how neutrinos are released from their sources. If neutrinos are strongly beamed along the jet axis, then they would preferentially be associated with AGN jets that point towards us such as blazars and flat-spectrum radio quasars. On the other hand, if the emission were less beamed, we might expect all radio-loud AGNs to contribute to the flux, generally producing a more isotropic signal. Our results suggest that we should receive neutrinos from non-blazar AGNs, too, which makes it harder to assess AGNs as UHE neutrino sources *on a statistical basis*. This however does not preclude the association of individual events with given sources, as we discuss in section 4.2.3.

4.2.3 The Dawn of Multimessenger Astronomy

This paper's results, together with the fact that accelerated particles are mainly located within the spine inside the nonthermal cone of influence (see Figure 4.1 and MC19 for more details), suggests that neutrino production could correlate with AGN luminosities and, potentially, with AGN flares. Even if AGN jets can hardly account for the bulk of the neutrinos measured by IceCube (see §4.2.2), it is still possible that some of them may come from AGNs, especially during periods of enhanced activity. Kadler et al. (2016) first reported a positional and temporal correlation between AGN flares and neutrino emission, and later the IceCube collaboration found 3.5σ evidence for neutrino excess emission from the direction

1. Note that the sample of known AGNs is far from complete and systematically biased towards those whose jets point at us (Caprioli, 2018).

of TXS 0506+056 (Aartsen et al., 2018a,b), a flaring blazar. It is worth remembering that calculating the exact time lag between GeV and neutrino emissions is however non trivial: the γ-ray emission is highly beamed and likely produced by relatively low-energy (GeV-TeV) electrons, while HE neutrinos require PeV protons, which may be accelerated later and/or in different regions of the jet. We should also keep in mind that, in flaring phases, neutrinos would most likely be produced in interactions with lower-energy photons (See §4.1.4 for more details), which would explain why the sources of neutrinos are not in phase with the peaks of γ-ray emission (e.g. Kun et al., 2021).

Within our framework, this correlation is however quite natural because the jet's nonthermal photons are the dominant background for $p\gamma$ interactions and thus flares may be associated with increased neutrino production. In general, an enhanced neutrino flux should be due mostly to an enhancement of the optical depth for photodisintegration, rather than an increase in the production rate of UHECRs, which in a flare may happen on a much longer timescale (if ever, considering that AGN flares are likely leptonic and due to local magnetic reconnection events in the jet spine (e.g. Sironi et al., 2015)). Taking this into consideration, a time correlation between AGN flares and IceCube neutrinos could be produced by the decay of the neutrons produced in the photodisintergration of heavy nuclei with energies above 10^{18}eV that are continuously being *espresso*-accelerated in the jet.

4.3 Conclusions

In this chapter, we tested the effect of photodisintegration on UHECRs accelerated in powerful AGN jets and estimate the ensuing flux of high-energy neutrinos. UHECRs are generically accelerated in such environments via *espresso* reacceleration of galactic-like CRs (Caprioli, 2015b), independently of the jet morphology (MC19) and on the details of particle transport (MC21). We used a bottom-up

approach in which test particles (CR seeds) are propagated in a fiducial 3D MHD simulation of a ultra-relativistic jet, augmented with realistic modeling (à la M14) of the photon fields responsible for UHECR losses and hence for neutrino production via different channels (see Table 4.1). We considered different prescriptions for AGN size and luminosity (§4.1.5) to maximize the interaction rate and hence put an upper limit on the expected source neutrino flux, under the additional assumption that powerful AGNs are responsible for the total flux of UHECRs at Earth. In fact, relaxing any of these hypotheses would generally lead to a lower neutrino flux. The main findings are as follows:

1. For typical densities and photon fields, pp interactions are negligible with respect to $p\gamma$ collisions; moreover, the most relevant photon field is provided by the non-thermal jet emission, which dominates over the IR dusty torus emission, the optical stellar light, and even the CMB.

2. UHECRs are not heavily affected by photodisintegration, even in the most luminous AGNs; the spectrum of the highest-energy particles gets heavier with increasing energy, as reported by Auger (Aab et al., 2014a).

3. In general, the expected neutrino flux scales with the AGN luminosity and with the slope of the seed and the reaccelerated CR spectra (Figure 4.5); the rather flat spectra ($q \lesssim 1.5$) required to explain Auger data (see, e.g., Aloisio et al., 2014a; Taylor, 2014) would maximize the neutrino yield with respect to softer UHECR spectra.

4. Even if AGNs sustained the totality of the UHECR luminosity of the universe, their steady neutrino emission could not account for the entire IceCube astrophysical neutrino flux (Figure 4.6). The only major contribution to the IceCube flux would be from the β-decay of photodisintegration byproducts especially for flatter UHECR injection spectra ($q = 1$).

5. Since the production of source neutrinos strongly depends on the non-thermal continuum, the case for AGNs to be prominent multimessenger sources is strong; AGN γ-ray flares, in fact, should be associated with enhanced neutrino production, as suggested by the case of TXS 0506+056.

6. For the most optimistic scenarios (flat injection spectra), UHE neutrinos produced inside AGN jets may dominate, or at least be comparable to, the expected flux of cosmogenic neutrinos produced during UHECR propagation across the universe (Figure 4.6).

7. Neutrinos are released quasi-isotropically which strongly suggests that non-blazar jets should contribute to the UHE astrophysical neutrino flux.

4.4 Appendix

Spectra of nuclei We propagate particles of given rigidity R, which for different species with different atomic charge Z corresponds to an energy $E = RZ$. The normalizations of the different ion species are chosen according to the abundance ratios at 10^{12} eV such that $K = K_{\rm se}/K_H \sim$ [1, 0.46, 0.30, 0.14] for He, CNO, MgAlSi and Fe respectively. Hence:

$$f(E_i) = Kf(ZR) \tag{4.8}$$

With $f(R) = f_0 R^{-q}$ where q is the spectral slope. Then:

$$f(E_i) = f_0 K Z^{-q}\Big(E_i\Big)^{-q} \tag{4.9}$$

where $E_{\rm i}$ is the ion energy and R is the rigidity.

Photomeson interactions We introduce $t_{p\gamma}$ as the cooling time of a proton with energy E_p due to photomeson interactions, i.e.:

$$t_{p\gamma}(E_p) = \frac{E_p}{dE_p/dt} \sim \frac{E_p}{\Delta E_p/\Delta t}. \tag{4.10}$$

If we pose $\Delta E_p = \xi E_p$, with $\xi \sim 0.17$ the average fraction of the energy lost to pions, we obtain:

$$t_{p\gamma}(E_p) \sim \frac{E_p}{\xi E_p c} \frac{1}{n_\gamma \sigma_{p\gamma}}, \tag{4.11}$$

where $1/(n_\gamma \sigma_{p\gamma})$ is the mean free path for a photon density n_γ and $\sigma_{p\gamma}$ is the photomeson cross section. Eventually, we get:

$$t_{p\gamma}^{-1} \sim n_\gamma \sigma_{p\gamma} \xi c \tag{4.12}$$

We follow Stecker (1968) and for an isotropic photon field we have:

$$t_{p\gamma}^{-1}(\gamma_p) \sim \frac{\xi c}{2\gamma_p^2} \int_{\bar{\epsilon}_{\rm th}/2\gamma_p}^{\infty} d\epsilon n_\gamma(\epsilon) \epsilon^{-2} \int_{\bar{\epsilon}_{\rm th}}^{2\gamma_p \epsilon} \epsilon' \sigma(\epsilon') d\epsilon' \tag{4.13}$$

where ϵ is the photon energy in the black hole frame, ϵ' its energy in the proton frame, and $\bar{\epsilon}_{\rm th} \sim 0.15$ GeV is the threshold energy in the proton frame. We integrate over $\epsilon' = \gamma_p \epsilon (1 - \beta \cos\theta)$, where θ is the angle between the particle momentum vectors in the black hole frame and $\beta \sim 1$, for $0 \leq \epsilon' \leq 2\gamma_p \epsilon$, we can introduce the effective cross section $\sigma_{\rm eff} \sim 70 \mu$b (Dermer et al., 2014) and obtain:

$$t_{p\gamma}^{-1}(\gamma_p) \sim \sigma_{\rm eff} \xi c \int_{\bar{\epsilon}_{\rm th}/2\gamma_p}^{\infty} d\epsilon n_\gamma(\epsilon, d_p) [1 - \frac{\bar{\epsilon}_{\rm th}^2}{4\epsilon^2 \gamma_p^2}], \tag{4.14}$$

where d_p expresses the spatial dependence of n_γ.

When considering interactions between the photons and a nucleus of atomic number A and energy E_A, we assume $\sigma_{\rm eff,A} = A\sigma_{\rm eff}$ and $\xi_A = \xi/A$. Based on equation 4.14, the cooling time for nuclei $t_{N\gamma}^{-1}$ eventually reads:

$$t_{N\gamma}^{-1}(\gamma_A) \sim \sigma_{\rm eff} \xi c \int_{\bar{\epsilon}_{\rm th}/2\gamma_A}^{\infty} d\epsilon n_\gamma(\epsilon, d_p) [1 - \frac{\bar{\epsilon}_{\rm th}^2}{4\epsilon^2 \gamma_A^2}]; \quad \gamma_A \equiv \frac{E_A}{A m_p c^2}. \tag{4.15}$$

Nonthermal emission in jets is typically beamed; hence, the angle θ between the proton momentum and the target photon is fixed and we can express $t_{p\gamma}^{-1}(\gamma_p)$

for an individual proton interacting with a beamed photon field as:

$$t_{p\gamma}^{-1}(\gamma_p) = \xi c \int_{\frac{\bar{\epsilon}_{\rm th}}{\gamma_p(1-\beta\cos\theta)}}^{\infty} d\epsilon \sigma_{p\gamma}(\epsilon') n_\gamma(\epsilon) = \sigma_{\rm eff} \xi c \int_{\frac{\bar{\epsilon}_{\rm th}}{\gamma_p(1-\beta\cos\theta)}}^{\infty} d\epsilon n_\gamma(\epsilon) \tag{4.16}$$

such that again $\epsilon' = \epsilon\gamma_p(1-\beta\cos\theta)$.

Photodisintegration interactions due to the Giant Dipole Resonance We follow Murase et al. (2008); Murase & Beacom (2010) in calculating the photodisintegration interaction time $t_{A\gamma}$ (for an isotropic background), obtaining an expression similar to equation 4.13, with γ the ion Lorentz factor:

$$t_{A\gamma}^{-1}(\gamma) \sim \frac{c}{2\gamma_A^2} \int_{\bar{\epsilon}_{\rm th}/2\gamma}^{\infty} d\epsilon n_\gamma(\epsilon, d_p) \epsilon^{-2} \int_{\bar{\epsilon}_{\rm th}}^{2\gamma\epsilon} \sigma_{\rm A\gamma}(\epsilon') \epsilon' d\epsilon'; \tag{4.17}$$

here $\sigma_{\rm A\gamma}$ is the giant dipole resonance (GDR) photodisintegration total cross section, which reads (Wang et al., 2008):

$$\sigma_{\rm A\gamma} = \frac{\sigma_G \epsilon'^2 (\Delta\epsilon'_{\rm G})^2}{[\epsilon'^2_{\rm G} - \epsilon'^2]^2 + \epsilon'^2 (\Delta\epsilon'_{\rm G})^2} \tag{4.18}$$

where $\sigma_G = 1.45 \times 10^{-27} A{\rm cm}^2$, $\epsilon'_{\rm G} = 42.65 A^{-0.21}$ MeV ($0.925 A^{2.433}$ MeV) for $A > 4$ ($A \leq 4$), and $\Delta\epsilon'_{\rm G} \sim 8$MeV.

For soft isotropic photon spectra, we can simplify equation 4.18 by posing $\sigma_{\rm A\gamma} \sim \sigma_{\rm G} \Delta\epsilon'_{\rm G} \delta(\epsilon' - \epsilon'_{\rm G})$. Equation 4.17 becomes:

$$t_{A\gamma}^{-1}(\gamma) \sim \frac{c\sigma_{\rm G}}{2\gamma_A^2} \Delta\epsilon'_{\rm G} \int_{\bar{\epsilon}_{\rm th}/2\gamma}^{\infty} d\epsilon n_\gamma(\epsilon, d_p) \epsilon^{-2} \int_{\bar{\epsilon}_{\rm th}}^{2\gamma\epsilon} \delta(\epsilon' - \epsilon'_{\rm G}) \epsilon' d\epsilon' \sim \frac{c\sigma_{\rm G}}{2\gamma_A^2} \Delta\epsilon'_{\rm G} \epsilon'_{\rm G} \theta(\epsilon'_{\rm G} - \bar{\epsilon}_{\rm th}) \Xi(d_p) \tag{4.19}$$

where $\gamma_A = E_A/(m_A c^2)$, with

$$\theta(x) = \begin{cases} 0, & \text{if } x < 0 \\ 1/2, & \text{if } x = 0 \\ 1, & \text{if } x > 0 \end{cases}$$

We assume that $\epsilon'_{\rm G} - \bar{\epsilon}_{\rm th} > 0$ where $\bar{\epsilon}_{\rm th}$ is the threshold energy (10 MeV for photodisintegration) and $\epsilon'_{\rm G}$ is the energy at which the cross section peaks. Also, $\Xi(d_p) = \int_{\bar{\epsilon}_{\rm th}/2\gamma}^{\infty} d\epsilon n_\gamma(\epsilon, d_p)\epsilon^{-2}\theta(2\gamma\epsilon - \epsilon'_{\rm G})$. For example, if we deal with two prominent BLR emission lines $\epsilon_{\rm HI} = 10.2$ eV and $\epsilon_{{\rm Ly}\alpha}$ =40.8 eV, then:

$$\Xi(d_p) = \frac{n_\gamma(\epsilon_{\rm HI}, d_p)\theta(2\gamma\epsilon_{\rm HI} - \epsilon'_{\rm G})}{\epsilon^2_{\rm HI}} + \frac{n_\gamma(\epsilon_{{\rm Ly}\alpha}, d_p)\theta(2\gamma\epsilon_{{\rm Ly}\alpha} - \epsilon'_{\rm G})}{\epsilon^2_{{\rm Ly}\alpha}} \tag{4.20}$$

For a nucleus interacting with a beamed photon field, the angle θ between the photon and nucleus momenta is known and we can write $t^{-1}_{A\gamma}(\gamma_p)$ as:

$$t^{-1}_{A\gamma}(\gamma_A) = c\int_{\frac{\bar{\epsilon}_{\rm th}}{\gamma_A(1-\beta\cos\theta)}}^{\infty} d\epsilon\sigma_{A\gamma}(\epsilon')n_\gamma(\epsilon) \tag{4.21}$$

where $\sigma_{A\gamma}(\epsilon')$ is given by equation 4.18.

Secondary particle spectra The spectra of secondary particles are intrinsically dependent on the the slopes of the primary spectra, which in turn depend on the slope of the seed spectrum. Let us consider primary spectra as power laws in energy $f(E) = f_0 E^{-q}$; from particle number conservation we get:

$$f(E)dE = f'(E')dE' \tag{4.22}$$

where E is the energy of the primary particle and $E' = \alpha E$ is the energy of the secondary particle. Then $dE' = \alpha dE$ and we obtain:

$$f'(E') = f(E)\frac{dE}{dE'} = f_0\frac{E^{-q}}{\alpha} \tag{4.23}$$

and therefore:

$$f'(E') = f_0(E')^{-q}\alpha^{q-1} = f_0 E'^{-q}\alpha^{q-1} \tag{4.24}$$

And finally:

$$f_s(E_s)/f(E_s) = f_0 E_s^{-q}\alpha^{q-1}/f(E_s) = \alpha^{q-1} \tag{4.25}$$

where E_s is the energy of the secondary particle. Eventually, the relative normalization of primary and secondary spectra reads $f_s(E_s)/f(E_s) = \alpha^{q-1}$. α can be read in the last column of Table 4.1 for the different processes that yield neutrinos.

UHE neutrino scaling We consider the photomeson optical depth $f_{p\gamma}$—a proxy for the neutrino production efficiency produced through photomeson interactions—to estimate the expected astrophysical UHE neutrino spectrum based on the average bolometric luminosity and extent of the jet in the black hole frame. We can express $f_{p\gamma}$ as a ratio of the UHECR to UHEν fluxes such that $F_{\mathrm{UHE}\nu}(E_\nu) \equiv f_{p\gamma} F_{\mathrm{UHECR}}(E)$. Considering that UHECRs up the jet's Hillas limit are *espresso*-accelerated, we can estimate their propagation time t_{prop} to be close to ballistic such that $t_{\mathrm{prop}} \sim \frac{H_{\mathrm{jet}}}{c}$. $f_{p\gamma}$ can then be estimated as:

$$f_{p\gamma} \sim \alpha^{q-1} \langle t_{p\gamma}^{-1} \rangle t_{\mathrm{prop}} \sim \alpha^{q-1} H_{\mathrm{jet}} \langle n_\gamma \rangle \sigma_{p\gamma} \xi \tag{4.26}$$

where $E_\nu = \alpha E$ and:

$$\langle n_\gamma \rangle \sim \frac{L_{\mathrm{bol}}}{4\pi c} \frac{1}{\epsilon_{\mathrm{m}}} \frac{1}{H_{\mathrm{jet}}^2}, \tag{4.27}$$

where ϵ_m the most likely photon energy. ϵ_m depends on the considered particle energy such that $\epsilon_{\mathrm{m}} \sim \bar{\epsilon}_{\mathrm{th}}/\gamma_{\mathrm{min}}$ where $\bar{\epsilon}_{\mathrm{th}} \sim 0.15$GeV is the photomeson interaction threshold and γ_{min} is the minimum proton energy contributing to the neutrino flux. Finally we get an estimate for $F_{\mathrm{UHE}\nu}$ such that:

$$F_{\mathrm{UHE}\nu}(E_\nu) \sim \alpha^{q-1} \sigma_{\mathrm{eff}} \xi \frac{L_{\mathrm{bol}}}{2\pi H_{\mathrm{jet}} c} \frac{1}{\epsilon_{\mathrm{max}}} F_{\mathrm{UHECR}}(E) \tag{4.28}$$

In the example in the left panel of Figure 4.4, $L_{\mathrm{bol}} = 10^{48}$erg s^{-1}, $H_{\mathrm{jet}} \sim 1$kpc, and $\gamma > 10^7$ so $\epsilon_{\mathrm{m}} \sim 15$eV in the black hole frame; the values of α, σ_{eff}, and ξ are discussed more in detail in Appendix 4.4.

Source Luminosity Function Following the calculations in M14 based on studies by Ueda et al. (2003); Inoue & Totani (2009); Harding & Abazajian (2012), the redshift-dependent X-ray luminosity function of sources can be expressed as:

$$\frac{d\psi}{dL_{\rm x}}(L_{\rm x},z)=\frac{A_{\rm x}\zeta_z(L_{\rm x},z)}{L_{\rm x}\Big[\Big(\frac{L_{\rm x}}{L_{\rm x}^*}\Big)^{\alpha_1}+\Big(\frac{L_{\rm x}}{L_{\rm x}^*}\Big)^{\alpha_2}\Big]} \tag{4.29}$$

where $\zeta_z(L_{\rm x},z)$ is the cosmological evolution factor, z the redshift, $A_{\rm x}=5\times10^{-6}$Mpc^{-3}, $L_{\rm x}^*=10^{43.96}$erg s^{-1}, $\alpha_1=0.43$, and $\alpha_2=2.23$. $\zeta_z(L_{\rm x},z)$ is expressed as follows:

$$\zeta_z(L_{\rm x},z)=\begin{cases}(1+z)^{4.23} & \text{if } z\le z_l(L_{\rm x})\\ [1+z_l(L_{\rm x})]^{4.23}\left[\frac{1+z}{1+z_l(L_{\rm x})}\right]^{-1.5}, & \text{if } z>z_l(L_{\rm x})\end{cases} \tag{4.30}$$

with

$$z_l(L_{\rm x})=\begin{cases}z_c & \text{if } L_a\le L_{\rm x}\\ z_c(L_{\rm x}/L_a)^{0.335} & \text{if } L_a>L_{\rm x}\end{cases}$$

such that $z_c\simeq1.9$ and $L_a\simeq10^{44.6}$erg s^{-1}.

Chapter 5

Magnetic reconnection as a potential explanation for AGN flares

Studying the nonthermal radiation of AGN jets is paramount to understanding the effects of UHECR losses and neutrino production. This chapter provides initial work on a path to finding solutions to problems pertaining to nonthermal radiation in AGN jets.

AGN jets are magnetically-dominated structures associated with multiwavelength high-energy observations, crucial attributes in answering the outstanding questions associated with UHECR, neutrino, and x/γ-ray production at the highest energies. Within these environments, magnetic energy can be dissipated through turbulence to inject a population of nonthermal particles from relativistically reconnecting current sheets (e.g. Comisso & Sironi, 2018, 2019). Considering the turbulent nature of AGN jets, asymmetric reconnection can potentially be the main driver of nonthermal lepton acceleration. This is why, We study the effect of relativistic asymmetric reconnection on particle energization in relativistic astrophysical systems (Mbarek et al., 2022), such as these jets, analytically and with kinetic PIC simulations (TRISTAN-MP from Spitkovsky, 2005). In a nut-

shell, we present the first steps in understanding asymmetric reconnection in the relativistic regime, i.e. systems with $\sigma > 1$, where σ is the ratio between the magnetic energy density and the plasma rest mass energy density. We derive basic scaling predictions for relativistic asymmetric reconnection, which reproduce both the symmetric relativistic and non-relativistic asymmetric limits. We then test predictions with a survey of 2D PIC simulations, and show good agreement. Finally, we examine the effects of inflowing asymmetry on nonthermal particle acceleration.

Magnetic reconnection is a fundamental plasma process through which energy stored in magnetic fields is converted into thermal and nonthermal particle energy. This process is a candidate for explaining impulsive nonthermal emission from magnetically dominated astrophysical objects such as gamma-ray bursts (GRBs) (e.g. Zhang & Yan, 2011; McKinney & Uzdensky, 2011), pulsar winds (e.g. Lyubarsky & Kirk, 2001; Arons, 2012), and jets from active galactic nuclei (e.g. Giannios, 2010; Sironi et al., 2021). As the magnetic energy density becomes larger than the rest mass energy density of the plasma, reconnection generates power law distributions of energetic ($> \mathrm{MeV}$) leptons (Guo et al., 2014, 2015; Sironi et al., 2015; Werner et al., 2016).

There have been significant efforts to understand the basics of relativistic reconnection including: (i) its dynamics and scaling Blackman & Field (1994); Lyubarsky (2005); Lyutikov (2003); Takahashi et al. (2011), (ii) the rate at which magnetic energy is dissipated, i.e., the reconnection rate Zenitani & Hoshino (2007); Hesse et al. (2011); Liu et al. (2015), and (iii) nonthermal particle acceleration Zenitani & Hoshino (2001, 2005); Sironi & Spitkovsky (2011b, 2014); Liu et al. (2015); Zenitani & Hesse (2008); Jaroschek et al. (2004); Kagan et al. (2013, 2015); Bessho & Bhattacharjee (2012); Cerutti et al. (2012, 2013, 2014a,b); Rowan et al. (2017); Ball et al. (2018). These works have shown that relativistic recon-

nection efficiently accelerates nonthermal particles. However, such studies have assumed that the magnetic field strength, temperature and density of the reconnecting plasma regions are equal (symmetric case). Nevertheless, systems in which the inflowing parameters differ, i.e., asymmetric reconnection, is not an odd or rare event, with in-situ observations of asymmetric reconnection frequently reported in the heliosphere (Øieroset et al., 2004; Paschmann et al., 2013; Phan et al., 2013; Burch et al., 2016; Mistry et al., 2017). Because of the prevalence of asymmetric reconnection in near-Earth systems, asymmetric reconnection has been thoroughly detailed Swisdak et al. (2003); Cassak & Shay (2008); Malakit et al. (2010); Shay et al. (2016). Albeit extensive, this body of work is limited to non-relativistic systems, and presently, the description for asymmetric reconnection has not been extended to relativistic plasma, i.e., systems where the magnetic energy density is larger than the rest mass energy density of the plasma. The ubiquity of asymmetric reconnection in the heliosphere suggests that asymmetric reconnection can be as important to astrophysical environments. Likely examples include the boundary layer between the jet and accretion flow in active galactic nuclei (AGNs) or shear flow boundaries warped by Kelvin-Helmholtz instabilities in AGN jets (e.g. Lyubarsky & Kirk, 2001; Ripperda et al., 2020; Sironi et al., 2021).

With this in mind, we present the first step in understanding asymmetric reconnection in the relativistic regime. We derive basic scaling predictions for relativistic asymmetric reconnection which reproduce both the symmetric relativistic and non-relativistic asymmetric limits. We show that for asymmetric inflow density and magnetic fields, the reconnection rate and the outflow speed are set by the inflow with the weaker ratio of magnetic energy density to rest mass energy density, i.e., the magnetization σ. The predictions are tested with a survey of two-dimensional (2D) particle-in-cell (PIC) simulations, and show good agreement.

Finally, we examine the effects of inflowing asymmetry on nonthermal particle acceleration, and show that the efficiency of particle acceleration is again controlled by the weaker-magnetization region.

5.1 Scaling of Asymmetric Reconnection

If reconnection is occurring at a steady state, the characteristics of the outflowing plasma can be related to the inflowing properties by enforcing the conservation of mass and energy around a given X-line.[1] To this end, we consider an asymmetric diffusion region, with two distinct plasmas flowing in from below and above the current sheet; each with its own density and magnetic field strength flowing into a side with length L and with bulk velocities v_1 and v_2 (the 1 & 2 subscripts denote the distinct regions below and above the current sheet respectively). The two populations mix as the magnetic energy is dissipated and the plasma is accelerated out of either side of the diffusion region with width δ. For simplicity, we assume that the temperature of the inflowing plasma is non-relativistic and the inflowing magnetic fields are anti-parallel, i.e., the guide field is negligible.

The field on both sides of the current sheet is characterized by the magnetization, defined in this paper as $\sigma \equiv B'^2/4\pi\rho' c^2$ where B' is the magnetic field strength, ρ' is the mass density, and c is the speed of light. Note that throughout the paper, unless otherwise stated, un-primed variables are measured in the X-line (or simulation) frame and primed variables are measured in the rest frame, i.e. the frame co-moving with the fluid velocity v with Lorentz factor $\gamma = 1/\sqrt{1-(v/c)^2}$.

1. Note that the conservation of momentum flux only provides a pressure balance constraint, and does not connect the inflow properties to to the outflow one.

The equation governing the conservation of mass in the X-line frame is:

$$L(\gamma_1 \rho_1' v_1 + \gamma_2 \rho_2' v_2) = 2\gamma_{\rm out}\rho_{\rm out}' v_{\rm out}\delta \tag{5.1}$$

The conservation of energy density flux (Lichnerowicz, 1967; Lyutikov & Uzdensky, 2003) yields:

$$\begin{aligned} L\left[\left(w_1' + \frac{B_1'^2}{4\pi}\right)\gamma_1^2 v_1 + \left(w_2' + \frac{B_2'^2}{4\pi}\right)\gamma_2^2 v_2\right] \\ = 2\delta\left(w_{\rm out}' + \frac{B_{\rm out}'^2}{4\pi}\right)\gamma_{\rm out}^2 v_{\rm out}, \end{aligned} \tag{5.2}$$

where $w' = \rho' c^2 + \Gamma P_0'/(\Gamma - 1)$ is the enthalpy density, Γ is the adiabatic index of the plasma, and P' is the pressure. We take the reconnection region to be in steady state and apply Stokes' theorem to Faraday's law to obtain $\vec{\nabla} \times \vec{E} = 0$; as a result, the inductive electric field driving reconnection E_z is uniform. The inflowing velocities are expressed as $v_i/c = |\vec{E} \times \vec{B}_i|/B_i^2 \approx E/B_i$, implying that $\gamma_1 v_1 B_1' = \gamma_2 v_2 B_2'$, since E_z is the same on both sides of the current sheet.

Using these considerations, assuming that $B_{\rm out}'$ is negligible compared to B_1' and B_2', and dividing Eq. 5.2 by Eq. 5.1, we obtain,

$$\left(1 + \frac{\Gamma P_{\rm out}'}{(\Gamma - 1)\rho_{\rm out}' c^2}\right)\gamma_{\rm out} = \frac{\gamma_1(1+\sigma_1) + \xi\gamma_{\mathbf{2}}(\mathbf{1}+\sigma_{\mathbf{2}})}{1+\xi} \tag{5.3}$$

where $\xi \equiv \frac{B_1'\rho_2'}{B_2'\rho_1'} = \sqrt{\frac{\sigma_1\rho_2'}{\sigma_2\rho_1'}}$ and the inflowing initial temperatures are assumed to be non-relativistic, $w_{1,2}' \approx \rho_{1,2}' c^2$. This equation provides a prediction for the Lorentz factor of the outflowing plasma $\gamma_{\rm out}$, provided we know the outflowing pressure and density. Previous works on the scaling of reconnection have made diverging assumptions about the role of the thermal pressure in the exhaust: some works have assumed the pressure is negligible compared to the outflowing bulk kinetic

energy density (e.g. Cassak & Shay, 2008; Lyutikov, 2003), while others take the pressure to be relativistically hot and comparable to the outflowing energy density (e.g. Lyubarsky, 2005; Zenitani & Hesse, 2008). For completeness, in this work we present both cases and show that simulations agree with the hot exhaust scenario.

In the limit of negligible pressure in the exhaust, $w'_{\rm out} \approx \rho'_{\rm out}c^2$, i.e. the magnetic energy is fully utilized to accelerate the plasma, Eq. 5.3 becomes

$$\gamma_{\rm out} = \frac{\gamma_1(1+\sigma_1) + \gamma_2\xi(1+\sigma_2)}{1+\xi}, \tag{5.4}$$

This equation can be verified by considering the limiting behaviour. For the symmetric relativistic case, as $\sigma_1 = \sigma_2 = \sigma_{\rm in}$ and $\xi \to 1$, Eq. 5.4 becomes $\gamma_{\rm out} \approx \gamma_{\rm in}(1+\sigma)$, identical to the super-Alfvénic prediction in Lyutikov & Uzdensky (2003); in the non-relativistic limit, we obtain the familiar $v_{\rm out} \sim v_A = B_{\rm in}/\sqrt{4\pi\rho_{\rm in}}$. Next, we consider the non-relativistic asymmetric limit. Expanding Eq. 5.4 in the $v_{\rm out} \ll c$ limit, we find $v_{\rm out}^2 \approx 2c^2(\sigma_1+\xi\sigma_2)/(1+\xi)$, which can be rewritten in terms of the magnetic fields and densities: $v_{\rm out}^2 \approx B_1B_2/(2\pi\rho_{\rm tot})$, where $\rho_{\rm tot} = (\rho_1B_2+\rho_2B_1)/(B_1+B_2)$, in agreement with the well-established predictions for non-relativistic asymmetric outflows Cassak & Shay (2007); Birn et al. (2010).

In the alternative case, in which the outflowing pressure is much larger than the rest mass energy density and cannot be neglected in the scaling derivation, an expression is needed for the exhaust pressure. In non-relativistic magnetic reconnection, the energy per particle in the bulk flow is found to be comparable with the exhaust temperature in simulations, observations and experiments Shay et al. (2014); Haggerty et al. (2017, 2018); Phan et al. (2013); Phan et al. (2014); Yamada et al. (2015). Motivated by this and by results from the simulations preformed for this work, the exhaust pressure is taken to be, $P'_{\rm out} \sim \rho'_{\rm out}\gamma_{\rm out}v_{\rm out}^2 \sim$

$\rho'_{\rm out}\gamma_{\rm out}c^2$, and in this limit, the left hand side of Eq. 5.3 is equal to $4\gamma^2_{\rm out}$, where we have used the relativistic adiabatic index of $\Gamma = 4/3$. Applying this to Eq. 5.3 yields

$$\gamma_{\rm out} \approx \sqrt{\frac{\gamma_1(1+\sigma_1)+\gamma_2\xi(1+\sigma_2)}{4(1+\xi)}}. \tag{5.5}$$

Taking this equation in the symmetric case, we recover the scaling relation of $\gamma_{\rm out} \propto \sqrt{\sigma}$, consistent with the Alfvénic outflow predictions of Lyubarsky (2005) and Liu et al. (2015).

Next we consider the limiting behaviour of Eq. 5.5 for $\sigma_2 \gg \sigma_1 \gg T/mc^2$. In this limit, balancing magnetic and thermal pressure requires that $\rho'_1/\rho'_2 \sim \sigma_2/\sigma_1$, $B'_2 \sim B'_1$ (hence $\gamma_1 \sim \gamma_2$), and $\xi \sim \sigma_1/\sigma_2 \ll 1$, the prediction for the outflowing Lorentz factor (Eq. 5.5) becomes:

$$\gamma_{\rm out} \sim \frac{\sqrt{\gamma_1(1+2\sigma_1)}}{2} \tag{5.6}$$

Thus, for $\sigma_2 \gg \sigma_1$, the outflow speed is set by the weaker-σ side, or equivalently the larger density side. This prediction should hold for both relativistic and non-relativistic values of σ_1.

Finally, we can use the outflow prediction to estimate the reconnection rate $R \equiv v_1/v_{\rm out}$, which is $\approx v_2/v_{\rm out}$, for systems where the upstream thermal energy is much smaller than the magnetic energy per particle. In such systems, $v_1 \sim v_2$ since $B'_2 \sim B'_1$ and $\xi \sim \sigma_1/\sigma_2$, and hence, we can rewrite Eq. 5.1 in terms of the reconnection rate. In the limit where the inflow velocity is not ultra relativistic ($\sigma < 100$ and $\gamma_{\rm in} \gtrsim 1$), we find an approximation for the asymmetric reconnection rate by taking the exhaust density as $\rho_{\rm out} \sim (\rho_1+\rho_2)/2$ following Cassak & Shay (2007):

$$R \approx \frac{\delta}{2L}\sqrt{1+\frac{2\sigma_1\sigma_2}{\sigma_1+\sigma_2}} \tag{5.7}$$

This prediction is again only valid for mildly relativistic cases ($\gamma_{\rm in} \gtrsim 1$); nevertheless, considering that the weaker-σ side sets the reconnection rate, such a scaling is pertinent for asymmetric environments with $\min(\sigma_1, \sigma_2) \lesssim 100$, and consequently for symmetric environments with $\sigma \lesssim 100$.

5.2 Simulation Setup

To test the scaling predictions outlined above, we perform 2.5D (2D real space, 3D velocity space) particle-in-cell (PIC) simulations of electron-positron (pair-plasma) reconnection with TRISTAN-MP (Buneman, 1993; Spitkovsky, 2005). The plasma is comprised of electron-positron pairs, typical of high-energy astrophysical environments such as pulsar winds and AGN jets (e.g. Sturrock, 1971; Wardle et al., 1998). Both electrons and positrons are initialized with a constant temperature, $\Delta\gamma \equiv k_B T'/mc^2 = 0.25$. Throughout the simulations, no notable differences between electron and positron properties are observed.

Initializing a single stable current sheet in the simulations requires balancing pressure across the current sheet; and thus the density and magnetic field on the two sides are uniquely determined for a fixed temperature and a particular combination of σ_1 and σ_2[2]. Note that pressure balance stipulates that the magnetic field is roughly similar across the sheet if the initial temperature is relatively low as discussed above. For additional details on the simulations, the setup and the normalization see the Appendix.

5.3 Simulation Results

We study relativistic asymmetric reconnection by performing a survey of simulations where the upper magnetization scans between $\sigma_2 = 10^{-1}$ and 10^3; the lower is fixed at $\sigma_1 = 10$. Fig. 5.1 compares the mass density (ρ) and outflow velocities (v_x) for the $\sigma_2 = 10$ case (i.e. symmetric) and the $\sigma_2 = 0.25$ case (i.e. asymmetric),

2. The ratio of the magnetic fields across the exhaust is given by $B_2'/B_1' = \sqrt{\frac{1+4\Delta\gamma/\sigma_1}{1+4\Delta\gamma/\sigma_2}}$.

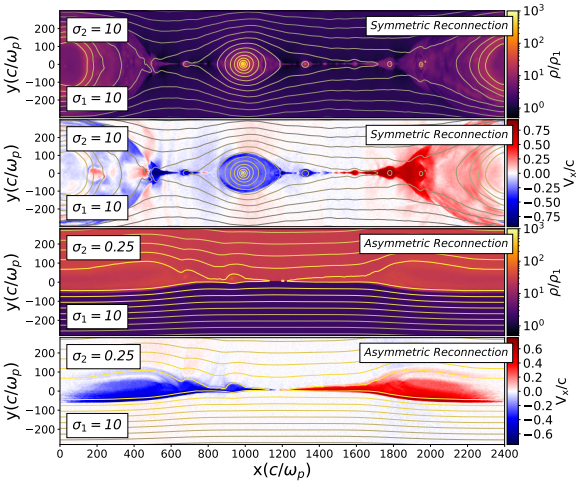

Figure 5.1: Reconnection layer at $t\omega_p \sim 400$ for both symmetric and asymmetric reconnection. The magnetization σ is specified in the plot on both sides of the current sheet. Contour maps of the magnetic scalar potential are also shown for reference. Top Panels: mass density map normalized to the mass density in the lower region ρ_1. Bottom Panels: Outflow speed v_x in units of c.

at $t\omega_p \approx 400$ for positrons. Note, that for the latter asymmetric case the assumption $\sigma_2 \gg T/mc^2$ is not satisfied, however we include this limit to show the effect two reconnecting regions with σ's that differ by orders of magnitude. The most notable difference between the symmetric and asymmetric cases is the shape of the exhaust that morphs from round islands to a more elongated shape, preferentially protruding into the inflow region with the weaker magnetic field strength because it has a faster inflow velocity. The island bulges into this side to replace the higher volume of plasma that has reconnected (Krauss-Varban et al., 1999; Cassak & Shay, 2007). Additionally, more plasmoids are present in the symmetric simulation compared to the asymmetric case, which may be due to a combination of the apparent broader asymmetric exhaust and the documented reduction of plasmoids for weaker σ in symmetric reconnection Sironi et al. (2016). Finally, the area of the islands suggest that less magnetic flux has been reconnected in the asymmetric simulation, consistent with the scaling predictions associated with Eq. 5.5. For the $\sigma_2 \gg \sigma_1$ case (not shown), the shape of the exhaust looks

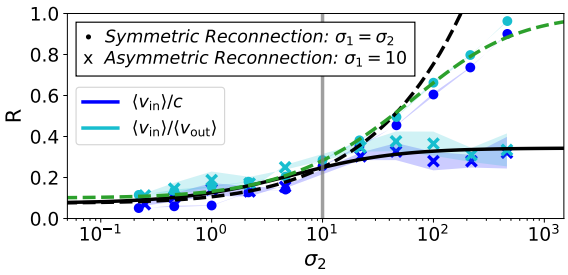

Figure 5.2: Reconnection rate for different magnetization parameters in simulations of symmetric and asymmetric cases. The green dashed curve shows the expected symmetric reconnection rate based on Liu et al. (2015)'s prediction including the plasma thermal pressure. The teal and blue dots (crosses) show the averaged measured values of $\langle v_{\rm in}\rangle$ normalized to $\langle v_{\rm out}\rangle$ and c respectively for symmetric (asymmetric) reconnection. The averages are determined over a $5d_e$ window just upstream of the X-line. The black dashed (solid) line shows the prediction for the for symmetric (asymmetric) reconnection rate determined by Eq. 5.7; such a prediction is only valid for environments with $\min(\sigma_1, \sigma_2) \lesssim 100$ as explained in the text. For the asymmetric cases, $\sigma_1 = 10$ is fixed and the reconnection rate is controlled by the weaker σ.

similar to symmetric reconnection, with the island expanding both inflow regions equally.

To further verify the scaling predictions, the reconnection rates in the survey of symmetric and asymmetric simulations are measured and shown in Fig. 5.2 as a function of σ_2. The teal dots and crosses show $v_{\rm in}/v_{\rm out}$, where $v_{\rm out}$ is a spatially averaged absolute value in the center of the exhaust ($y \sim 0$) and $v_{\rm in}$ is the absolute value of the average of both sides within $5c/\omega_p$ away from the X-line in the inflow region. The blue dots and crosses show a similar value, but with the outflow velocity assumed to be c (appropriate for $\sigma_1, \sigma_2 \gg 1$); The dashed green line shows the prediction for the reconnection rate from Eq. 5 of Liu et al. (2015) [3]. The black dashed and solid lines show the expected reconnection rate based on Eq. 5.7 for $\delta/L = 0.15$ (the best fit for our simulation results), which is comparable with Liu et al. (2015)'s favored aspect ratio. Finally, the edges of the corresponding shaded

3. For Eq. 3 from Liu et al. (2015), we use $r_{n'}\delta/L = 0.1$ and include the thermal contribution to enthalpy with $k_B T' = mc^2/4$.

regions are defined by the values measured on either upstream regions, e.g., the upper extent will be the average reconnection rate determined from the upper half of the current sheet (σ_2 region) and the lower extent of the shaded region will be the averaged value below the current sheet (σ_1 region). Considering that $v_1 \sim v_2$ for small values of $k_B T/mc^2 \ll \sigma_1,\ \sigma_2$, we expect the shaded regions to have a limited extent especially as $\sigma_2 \to \sigma_1$. The simulation measurements were taken at $400\omega_p^{-1}$. This is not the longest timescale for all runs, but we choose this time as a representative steady-state snapshot, well after reconnection has started, but before island size inhibits efficient reconnection.

Symmetric simulations in Fig. 5.2 yield results consistent with predictions from previous studies; the reconnection rate increases from the standard non-relativistic 0.1 value, up to almost nearly 1 for simulations with $\sigma \gg 1$ Takahashi et al. (2011); Liu et al. (2015). For the asymmetric simulations, σ_1 is fixed to 10 and σ_2 is varied over ~ 4 orders of magnitude. For the asymmetric simulations, the reconnection rates are set by the weaker-σ regions. For $\sigma_2 < \sigma_1$, asymmetric reconnection rates are comparable to the symmetric σ_2-counterparts, and for $\sigma_2 > \sigma_1$, the rate becomes insensitive to increases in σ_2. This can primarily be attributed to the exhaust field lines becoming mass loaded by the weaker σ_1 (i.e., larger density) inflow. From these considerations, our simulations verify that the reconnection rate is quenched by the side of the exhaust with the weaker magnetization parameter, as predicted by Eq. 5.6, even in the extreme limit where $n_2' \to 0$ or vacuum, i.e., $\sigma_2 \to \infty$ (as shown in the Appendix).

5.4 Nonthermal Particle Spectra

To examine particle acceleration, we show the energy distribution functions in Fig. 5.3 for different symmetric and asymmetric conditions at different times, averaged over the entire domain, with the time stamp of representative distributions, color coded based on the color bar shade. We show the distributions for five

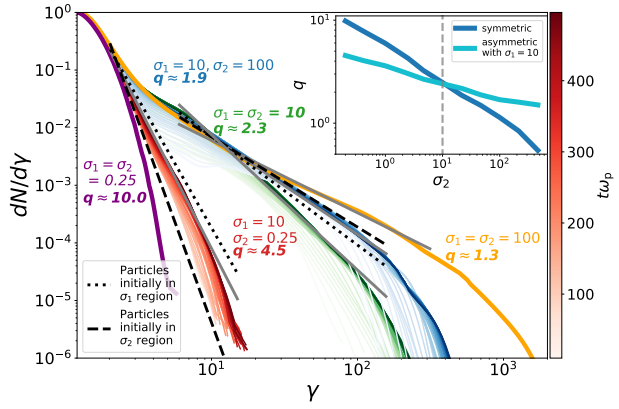

Figure 5.3: Time evolution of particle energy spectra for symmetric and asymmetric reconnection with different magnetization parameters. The time stamp of each distribution is color coded based on the color bar shade for one representative example ($\sigma_1 = 10, \sigma_2 = 0.25$). The spectrum tends towards a power law slope as time progresses. The dashed and dotted lines show the best fit values for slopes of the power law spectra based on particles originating from the lower and upper inflow regions respectively, while the gray solid lines show the best fit for the combined population. The upper right plot shows the dependence of the slope for different magnetization parameters for both symmetric and asymmetric reconnection.

different characteristic example simulations in Fig. 5.3 that exhibit nonthermal, extended tails reaching ultra-relativistic energies. The spectra with the red, blue, and green color correspond to $\sigma_2 = 0.25,\ 10,\ \&\ 100$ respectively, with σ_1 fixed to 10 and are fitted at $t\omega_p \sim 450$ with a spectral slope $q \equiv -d\log \mathrm{N}/\log\gamma$. We also show the spectra for the symmetric cases $\sigma = 0.25$ and $\sigma = 100$ (the purple and orange lines, respectively) at $t\omega_p \sim 450$ with their power law fit.

Asymmetric simulations develop power-law spectral slopes between those of their symmetric counterparts. Following similar trends, we find that the spectra associated with $\sigma_2 = 0.25$ (red curves) are much steeper than those with a symmetric $\sigma = 10$ prescription, and can conclude that a power law distribution essentially does not form. The symmetric $\sigma = 0.25$ case has the steepest distribution as expected.

The inset of Fig. 5.3 shows the power law slopes for symmetric and asymmetric

($\sigma_1 = 10$ for asymmetric cases) simulations over a range of σ's and exhibits the same trend for a range of different magnetizations. Overall, it appears from these simulations that for asymmetric reconnection, the accelerated particle spectra are steepened relative to the larger σ side, and hardened relative to the weaker σ side.

Finally, for spectra associated with asymmetric reconnection, we separately present the spectra of positrons coming from either the upper or lower half of the domain; dotted lines correspond to particles initialized on the lower half of the current sheet (σ_1), and dashed lines for particles from the upper domain (σ_2). We note that particles starting in the higher σ regions have a flatter slope and tend towards higher energies as can be seen in more detail in Fig. 5.3.

5.5 Appendix

Reconnection Region

The rate at which magnetic energy is converted during magnetic reconnection can be estimated by considering the diffusion region around a given X-line. The Figure below shows the expected layout of the X-line with the different physical parameters defined in the text.

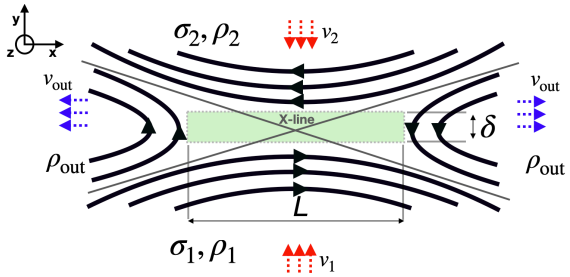

Reconnection region with variables defined in the text.

Simulation Setup

To test the scaling predictions outlined in the text, we perform 2.5D (2D real space, 3D velocity space) particle-in-cell (PIC) simulations of electron-positron (pair-plasma) reconnection with TRISTAN-MP Buneman (1993); Spitkovsky (2005). The simulations are performed in the $x,\ y$ plane with the reconnecting magnetic field pointing in the $\pm\hat{x}$ direction. The simulations are periodic in the outflow direction and open in the inflow direction with receding injectors to allow the simulations to continuously feed in upstream plasma and magnetic flux; this technique has been used in various other studies of relativistic reconnection to efficiently reduce the simulation's computational cost Sironi & Spitkovsky (2014); Sironi et al. (2016); Rowan et al. (2017); Ball et al. (2018). The magnetic field is initialized with $\mathbf{B}' = [0.5(B'_2 + B'_1)\tanh(2\pi y/\delta) + 0.5(B'_2 - B'_1)]\hat{\mathbf{x}}$; the field on both sides of the current sheet is characterized by the magnetization $\sigma = B'^2/4\pi m n' c^2$. The plasma is comprised of electron-positron pairs, typical of high-energy astrophysical environments such as pulsar winds and AGN jets (e.g. Sturrock, 1971; Wardle et al., 1998). Throughout the simulations, no notable differences between electron and positron properties are observed. The simulation dimensions are $840\ c/\omega_p$ in the periodic direction (x), where ω_p is the electron plasma frequency based on the density of the lower half of the simulation, $\omega_p = \sqrt{4\pi n'_1 e^2/m}$. We check for convergence by performing additional test simulations with x domains up to $3360\ c/\omega_p$ (An example with $1200\ c/\omega_p$ is shown in Figure 1 of the text), with no significant differences found. We also run the simulations with better particle statistics by increasing the number of particles per cell by an order of magnitude and noted no difference in the scaling and the non-thermal spectra. The reconnection process is initialized by creating a localized low temperature perturbation in the center of the simulation, thereby collapsing the current sheet in a prede-

termined location and shortening the time it takes for a dominant X-line to form, as described in Sironi et al. (2016).

Simulation Normalizations

Unless otherwise stated in the text the simulations are initialized as follows: The length of the simulation in the x direction is $420\ c/\omega_p$, based on the density of the subscript 1 side (lower half of the simulation). Each simulation uses four positrons+electrons per cell with 20 cells per c/ω_p. The magnetization parameter is defined as $\sigma = B^2/4\pi\rho c^2$. The time step is set by the speed of light, $0.45\Delta x/\Delta t = c$. The electrons and positrons are initialized with a constant temperature, $\Delta\gamma \equiv k_B T'/mc^2 = 0.25$. The parameters that change between simulations are the lower magnetization (σ_1), the upper magnetization (σ_2), the upper to lower mass density ratio (ρ_2/ρ_1) and the upper to lower magnetic field strength ratio (B_2/B_1). These values are given in the table below.

Simulations with $\sigma_2 \to \infty$

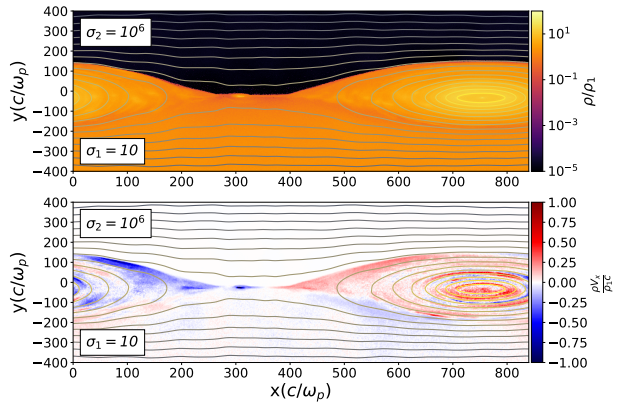

Same as Fig. 1 in the main text but for $\sigma_1 = 10$ and $\sigma_2 \to \infty$. We can see that reconnection occurs even if one side is in vacuum.

We present below a unique extension of this work that would be inadequately described with previous theories of relativistic or asymmetric reconnection. We consider an environment where in one of the reconnecting regions $\sigma \to \infty$ (de

σ_1	σ_2	ρ_2/ρ_1	B_2/B_1
0.22	0.22	1	1
0.46	0.46	1	1
1	1	1	1
2.15	2.15	1	1
4.64	4.64	1	1
10	10	1	1
21.5	21.5	1	1
46.41	46.41	1	1
100	100	1	1
215	215	1	1
464	464	1	1
10	0.1	10	0.316
10	0.22	9.01	0.445
10	0.25	8.8	0.469
10	0.46	7.53	0.589
10	1	5.5	0.742
10	2.2	3.437	0.869
10	4.6	1.964	0.95
10	22	0.478	1.025
10	46	0.234	1.038
10	100	0.109	1.043
10	220	0.0497	1.046
10	460	0.0238	1.046

facto vacuum). If one were to analyze this system employing the existing theories of magnetic reconnection, one would face two significant obstacles. First, in the relativistic symmetric framework, the lack of plasma implies that no magnetic energy could be dissipated, resulting in insignificant particle energization and no reconnection for that matter. Second, in the standard asymmetric framework, $V_A \to \infty$, where V_A is the Alfvén speed on the vacuum side, which is an inherently inaccurate description of the system. However, the model presented in this manuscript is applicable to this extreme regime and predicts that reconnection will occur with a given outflow and reconnection rate. We also recover a power law spectrum in this simulation, and observe the nonthermal particle spectrum to be enhanced by reconnecting with vacuum.

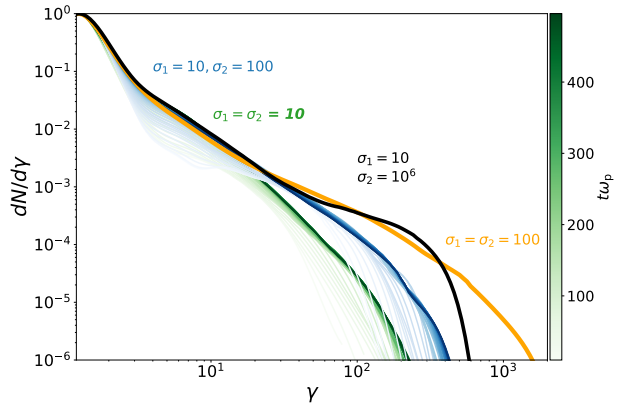

Same as Fig.3 in the main text but including the particle energy spectrum for a system with $\sigma_1 = 10$ and $\sigma_2 \to \infty$.

Part III

Particle Propagation: From cosmic to galactic scales

Chapter 6

Introduction

From a theoretical standpoint, CR propagation has been studied either by following individual particles including their spectra and interactions during their journey, or as a relativistic gas with a certain pressure and energy that interacts with the interstellar medium (ISM). The latter method is particularly interesting to study the effect of CRs on the ISM. However, following single particles enables a better understanding of various CR observations that were discussed in the introduction. Therefore, combining studies relying on individual CR trajectories with observations is an important first step to model CRs more realistically.

In this section, I study particle propagation from i) a theoretical perspective to study the effect of magnetic fields on the delay incurred on particles during propagation on an extended scale and ii) an experimental perspective to measure the abundances of clock isotopes and thus the confinement time of CRs in the galaxy (Please refer to the introduction for more details). When applied to galactic propagation of CRs, the theoretical perspective complements my experimental work to have a clearer picture of the confinement time of CRs in the galaxy.

Chapter 7

The effects of Magnetic Field Line Wandering on Particle Propagation

In this chapter, we propagate particles in magnetic fields over a large span of distances and examine the impact of magnetic field line wandering and particle scattering on the delay incurred during propagation and the arrival direction.

7.1 Particle Propagation Framework

We have a rather simple setup in which particles are propagated with a Boris Pusher (e.g., Birdsall & Langdon, 1991b) in a magnetic field $\vec{B}$ with different initial pitch angles. Generally speaking, our propagated particles have trajectories that are only dependent on the rigidity E/Z, where E is the particle's energy and Z its charge. A rigidity-dependent timestep is chosen to resolve gyrations, such that every particle is propagated for *at least* 50 timesteps per gyroradius. These particles are representative of different species at different energies. We eventually compare the particle's propagation time t with the ballistic time t_b to the sources (photon travel time) assuming different initial conditions as explained more in detail below. Here, we do not include the effects of losses during propagation to test particle propagation within a well-defined scheme and, more importantly, set

lower limits on the delay time $t_d = t - t_b$.

The magnetic field magnitude is kept constant throughout particle propagation, but is augmented with a turbulent component. We choose to include two different prescriptions of the magnetic field turbulence: i) a Magnetic Field Line Wandering (MFW) prescription, and ii) an MFW in addition to a Monte Carlo Spatial Diffusion (SD) prescription, i.e., the MFW-SD prescription. The MFW prescription should be regarded as more realistic since the magnetic field is changed every coherence length and particles are propagated without any added scattering. The MFW-SD prescription helps us to disentangle the contribution of MFW and SD to delaying particles. We do not include a standalone SD prescription as the definition of the particle mean free path is dependent on a coherence length of the magnetic field, which requires variations in the field, i.e., a wandering component.

7.2 The Magnetic Field Line Wandering (MFW) component

Particles are propagated in a magnetic field whose direction changes with a random angle $\in [0, \pi/2]$ according to a random walk based on $L_{\rm c}$, the coherence length of the local magnetic turbulence. This effectively introduces a perpendicular diffusion coefficient, critically altering particle transport.

Seminal works characterized the diffusion tensor from which we obtain the parallel and perpendicular diffusion coefficients, $\kappa_{\parallel}$ and $\kappa_{\perp}$ (e.g. Parker, 1965; Jokipii, 1966; Forman & Gleeson, 1975; Chapman et al., 1990), focusing on the regimes where $\kappa_{\perp}/\kappa_{\parallel}$ is relatively low. However, the transport perpendicular to the B-field could play a more important role, and this wandering effect could have significant effects on particle propagation when $\kappa_{\perp}/\kappa_{\parallel} \to 1$, as was later pointed out (e.g. Giacalone & Jokipii, 1999; Casse et al., 2001; Plotnikov, I. et al., 2011).

To help us understand the trajectory properties we obtain, we can introduce a scattering distance, equivalent to a mean free path, such that $\lambda \sim \eta^{-1}\mathcal{R}^2/L_{\rm c}$ for

$\mathcal{R}/L_{\rm c} \gg 1$ and $\lambda \sim \eta^{-1} L_{\rm c}(\mathcal{R}/L_{\rm c})^{2-\beta}$ for $\mathcal{R}/L_{\rm c} \ll 1$ (See Eq. 9 in Plotnikov, I. et al., 2011); where β is the spectrum index ($\beta = 5/3$ for Kolmogorov (Kolmogorov, 1941) and $\beta = 2/3$ for Iroshnikov/Kraichnan (Iroshnikov, 1964; Kraichnan, 1965)) and η is a level of turbulence parameter relating the mean $\mathbf{B_0}$ and turbulent component of the magnetic field δB such that $\eta = \frac{\langle \delta \mathbf{B^2} \rangle}{\langle \delta \mathbf{B^2} \rangle + \langle \mathbf{B_0^2} \rangle}$. Within our framework, the B-field direction changes every coherence length as defined above and we can estimate $\eta \to 1$ such that $\lambda \sim (\mathcal{R}/L_{\rm c})^{2-\beta} L_{\rm c}$, with $\beta = 0$ for $\mathcal{R}/L_{\rm c} \gg 1$ and $\beta = 5/3, 2/3$ for $\mathcal{R}/L_{\rm c} \ll 1$.

Monte Carlo Elastic Scattering, i.e., the spatial diffusion (SD) component In order to mimic spatial diffusion effects, particles are assigned a mean free path to be $\lambda = L_{\rm c}(\mathcal{R}/L_{\rm c})^{\delta}$ where $\mathcal{R}$ is the particle gyroradius, and $\delta = 2 - \beta$. For $\mathcal{R} < L_{\rm c}$, particles are resonantly scattered and we obtain instabilities at smaller scales where the magnetic field has a kolmogorov or an Iroshnikov/Kraichnan spectrum. There is no consensus on the phenomenology dictating magnetohydrodynamic (MHD) turbulence (e.g. Ng et al., 2010; Treumann et al., 2015); however, both resulting turbulence spectral indices are quite close, and thus, have no significant effect on the particle delays. For simplicity, we only show results for Kolmogorov turbulence where $\delta = 1/3$ (Stawarz & Petrosian, 2008). As for $\mathcal{R} \geq L_{\rm c}$, particles are scattered on scales smaller than their gyroradii which leads to $\delta = 2$ (Sironi et al., 2013). In this case, particles are scattered based on their mean free path with a random scattering scattering angle, but the overall magnetic field is unchanged.

7.3 Results

General considerations: Figure 7.1 shows the normalized time delay t_d/t_b map of particle propagation as a function of the particle gyroradius $\mathcal{R}$ and coherence length L_c normalized to the source distance D. The different panels show the dependence of t_d/t_b on the magnetic field setup and the initial pitch angle of the

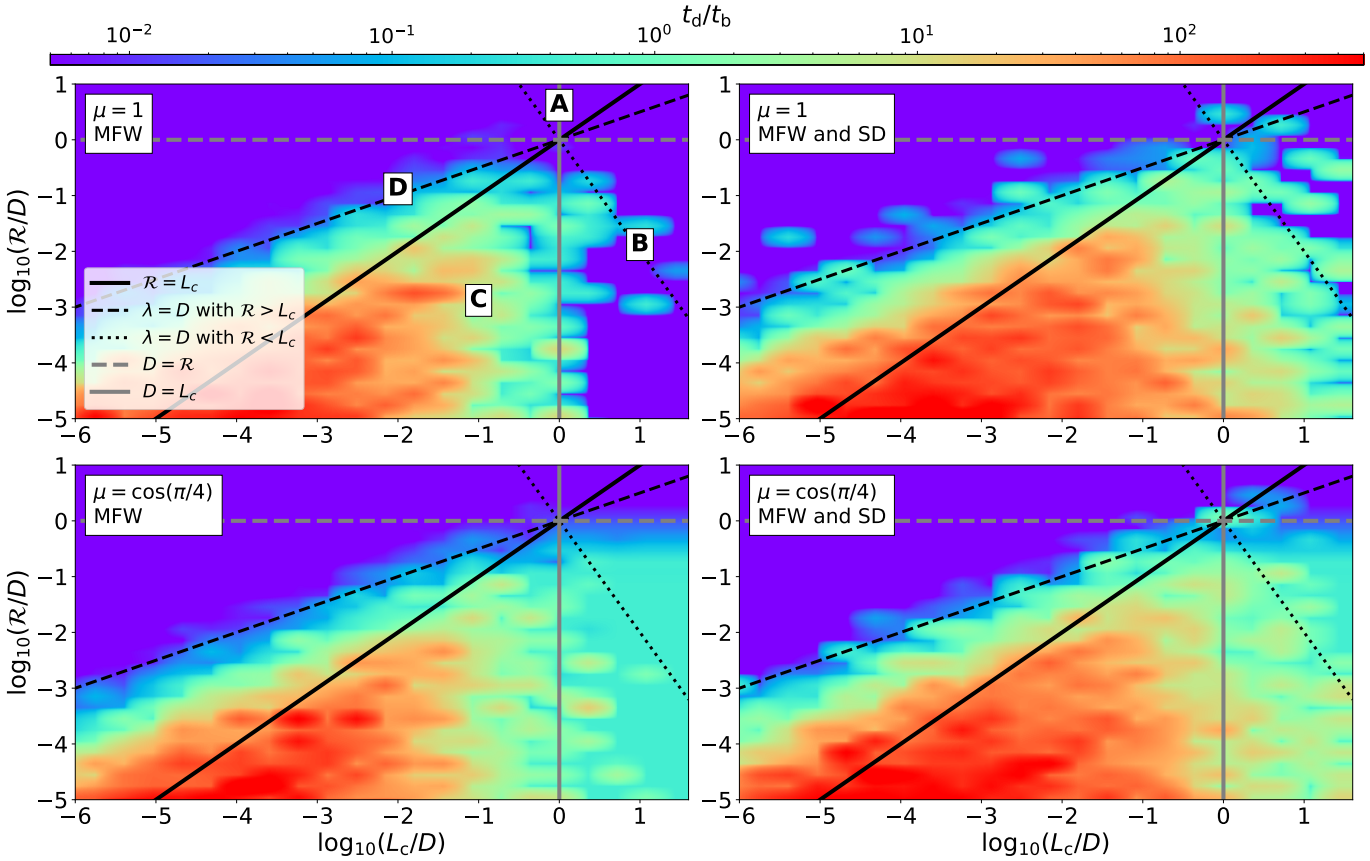

Figure 7.1: Time delay maps of particle propagation as a function of the particle gyroradius $\mathcal{R}$ and coherence length L_c normalized to the source distance D. The color bar denotes the ratio of the time delay $t_d = t - t_b$ and the ballistic time t_b. The solid black line characterizes the boundary $\mathcal{R} = L_c$. Within the spatial diffusion model, the particle gyroradius is expressed as $\mathcal{R} = \lambda^{1/2} L_c^{1/2}$ for $\mathcal{R} > L_c$, and the limiting case where $\lambda = D$ is plotted in dashed black for reference. For $\mathcal{R} < L_c$, $\mathcal{R} = \lambda^3 L_c^{-2}$, and the limiting case where $\lambda = D$ is plotted in dotted black. The different maps show the impact of the magnetic field setup and initial pitch angle.

particle μ, defined as the cosine of the angle between the particle momentum and the magnetic field.

We can analytically relate $\mathcal{R}$ to L_c based on the definition of the mean free path λ in §7.1 such that:

$$\mathcal{R} \equiv \lambda^{1/\delta} L_c^{1-1/\delta} \tag{7.1}$$

where δ depends on the turbulence regime as discussed above. We disregard the extra factor associated with η that we obtain in the MFW discussion since $\eta \to 1$.

In Figure 7.1, we plot the dependence of $\mathcal{R}$ on $L_{\rm c}$ based on Eq. 7.1 for $\mathcal{R} > L_{\rm c}$ (dashed line) and $\mathcal{R} < L_{\rm c}$ (dotted line), such that the mean free path $\lambda = D$. For distances beyond λ, we do not expect much of a delay.

In the following, we examine our results by analyzing different parts of the delay maps (lettered A to D) as shown in the upper left panel of Figure 7.1 to facilitate the discussion. Overall, we do not find major differences between the MFW and MFW-SD maps as discussed more in detail below.

Region A This is the part of the map where the gyroradius exceeds the distance to be covered $\mathcal{R} > D$. Hence, delays are minimal and would only be associated with a slight bending from ballistic trajectories. This is corroborated in all the maps of Figure 7.1 where $t_d/t_b \sim 10^{-3}$.

Region B This is the part of the map where $L_{\rm c} > D$. In the MFW only maps, particles can travel in a relatively uniform magnetic field since the field is coherent over the distance traveled, and hence do not expect any scattering event. On the other hand, particles are delayed more significantly till $\lambda = D$ (dotted line) if we include spatial diffusion.

We find that, as expected, delays associated with these trajectories are negligible for $\mu = 1$ as the particle travels in a quasi-ballistic way. However, for $0 < \mu < 1$, a delay associated directly with the pitch angle is recovered in both

setups. In the absence of scattering events, particle propagation is helical and can be approximated as the total distance traveled by the particle in region B as $d \approx N\sqrt{D_h^2 + (2\pi\mathcal{R})^2}$, where D_h is the distance traveled along the axis of the helical path after one rotation, and N is the number of rotations. Employing the expression for the particle's gyroperiod, we get $D_h = 2\pi\mu\mathcal{R}$. In region B, the source distance can be expressed as $D = ND_h$ and we get,

$$d \approx D\sqrt{\frac{\mu^2 + 1}{\mu^2}} \tag{7.2}$$

for $0 < \mu < 1$. Hence, assuming an average pitch angle $\langle\mu\rangle \sim \cos\frac{\pi}{4}$, we can predict the expected delay in this part of the map to be $t_d/t_b \sim 0.7$. This prediction is corroborated by our propagation results in the lower left plot of Figure 7.1.

Additionally, the MFW prescription gives us virtually no delays for $L_c > D$ which is expected, but the MFW-SD consideration results in delays till the dotted line corresponding to $\mathcal{R} = \lambda^3 L_c^{-2}$ where $\lambda = D$. This is due to the nature of the SD consideration where particle scattering is set up synthetically.

In general, we do not expect an IGMF configuration where $L_c > D$ since that would result in a discernible anisotropic signal. Therefore, UHECRs cannot be associated with region B.

Region C This is the part of the map where $\mathcal{R} < L_c$ and $L_c < D$. Here, particles are more likely to scatter resonantly, and as a result, time delays are more significant. This is apparent in the MFW-only maps and are more prominent in MFW-SD maps because of the increased scattering, but both cases show relatively similar delays. We can see from Figure 7.1 that all pitch angle initializations result in time delays that can go beyond $t_d/t_b \gtrsim 10^3$.

Region D This is the part of the map where $\mathcal{R} > L_c$ and $\mathcal{R} < D$. We can see that t_d/t_b drops sharply beyond $\lambda = D$, to reach inconsequential delay levels ($t_d/t_b \lesssim$

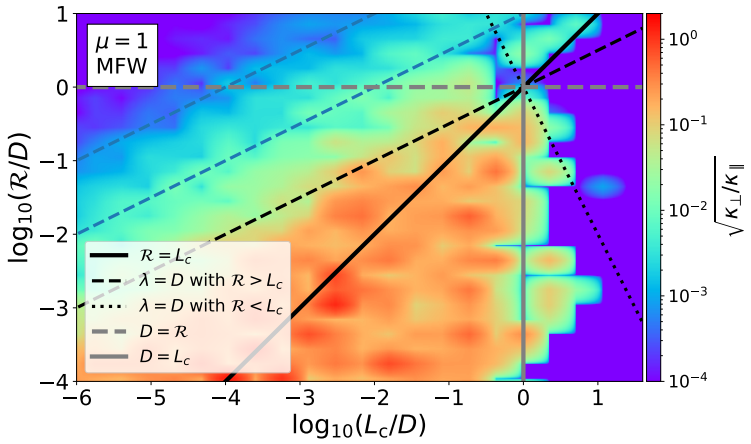

Figure 7.2: Map of the ratio of the transverse diffusion and spatial diffusion $\sqrt{\kappa_\perp/\kappa_\parallel}$ as a function of the normalized Larmor radius $\mathcal{R}$ and coherence length L_c. The solid, dashed, and dotted black and grey lines are as defined in Figure 7.1. The blue and red dashed lines serve to reiterate the $\sqrt{\kappa_\perp/\kappa_\parallel} \propto (\mathcal{R}/L_c)^{-1}$ relationship as explained in the text.

10^{-3}). Overall, in the extended $\lambda < D$ region (encompasses part of region D), the pitch angle does not have any effect as particles are more likely isotropized resulting in considerable time delays.

It is critical to mention here that UHECRs are most likely scattered on scales much smaller than their gyroradii, and hence, the region where $\mathcal{R} > L_c$ (delimited with a solid black line) is more representative of potential delays; we show an extended map here for completeness.

Magnetic Field Line Wandering and Transverse Diffusion For our MFW trajectories, we can define a spatial diffusion coefficient $\kappa_\parallel$ such that $\kappa_\parallel \sim \frac{\langle \Delta r_\parallel^2 \rangle}{2\Delta t}$ where $r_\parallel$ is the coordinate of a particle moving along $\mathbf{B_0}$ and $\langle \Delta r_\parallel \rangle$ its displacement. There is in turn a transverse diffusion coefficient $\kappa_\perp \sim \frac{\langle r_\perp^2 \rangle}{2\Delta t}$ where $\langle \Delta r_\perp \rangle$ is the perpendicular displacement. We study the behavior of transverse diffusion by plotting the ratio $\sqrt{\kappa_\perp/\kappa_\parallel}$ in Figure 7.2 and compare our results with the trends shown in the Monte Carlo numerical simulations from Casse et al. (2001) and Plotnikov, I. et al. (2011).

- $\mathcal{R} < L_c$: Casse et al. (2001) find that $\sqrt{\kappa_\perp/\kappa_\parallel}$ is maximized at and independent of the ratio $\mathcal{R}/L_c$ for systems exhibiting strong turbulence. This is consistent with our results where $\sqrt{\kappa_\perp/\kappa_\parallel} \to 1$ in this region till $L_c = D$. For $L_c > D$, we do not expect much of an effect of MFW as described above.

- $\mathcal{R} > L_c$: In this region, we note that $\sqrt{\kappa_\perp/\kappa_\parallel} \to 1$ till $\lambda = D$ (black dashed line). Casse et al. (2001) study the relationship between $\sqrt{\kappa_\perp/\kappa_\parallel}$ and $\psi \equiv \mathcal{R}/L_{\max}$, where $L_{\max}$ is the maximal scale of the turbulent spectrum. They find that as $\eta \to 1$, $\sqrt{\kappa_\perp/\kappa_\parallel} \to 1$ for $\psi < 1$ (consistent with Giacalone & Jokipii, 1999) and $\kappa_\perp/\kappa_\parallel \propto \psi^{-2}$ for $\psi > 1$. Within our framework, $\mathcal{R} = L_{\max}$ is equivalent to the black dashed line in Figure 7.2 as $\lambda = D$ defines the maximal scale of the effect of turbulence ($\psi = 1$ in our maps). As ψ increases beyond the black dashed line, we can see that $\kappa_\perp/\kappa_\parallel \propto \psi^{-2}$ as attested by the dashed blue lines that mark the value of $\sqrt{\kappa_\perp/\kappa_\parallel}$ for every order of magnitude decrease in ψ.

We note that our results are consistent with the diffusion effects presented in the simulations from Giacalone & Jokipii (1999), Casse et al. (2001), and Plotnikov, I. et al. (2011). This further shows that our propagation framework is consistent with the analytical and Monte Carlo simulations presented in these studies.

7.4 Astrophysical Implications

The results presented above are largely general and should be regarded as applicable to different parts of a particle's journey. This is also applicable to different types of CRs in different environments, from UHECRs in the ICM to electrons in the interstellar medium (ISM). In the following, we discuss the implications for delays of UHECRs from AGN jets and TeV electrons from galactic pulsars.

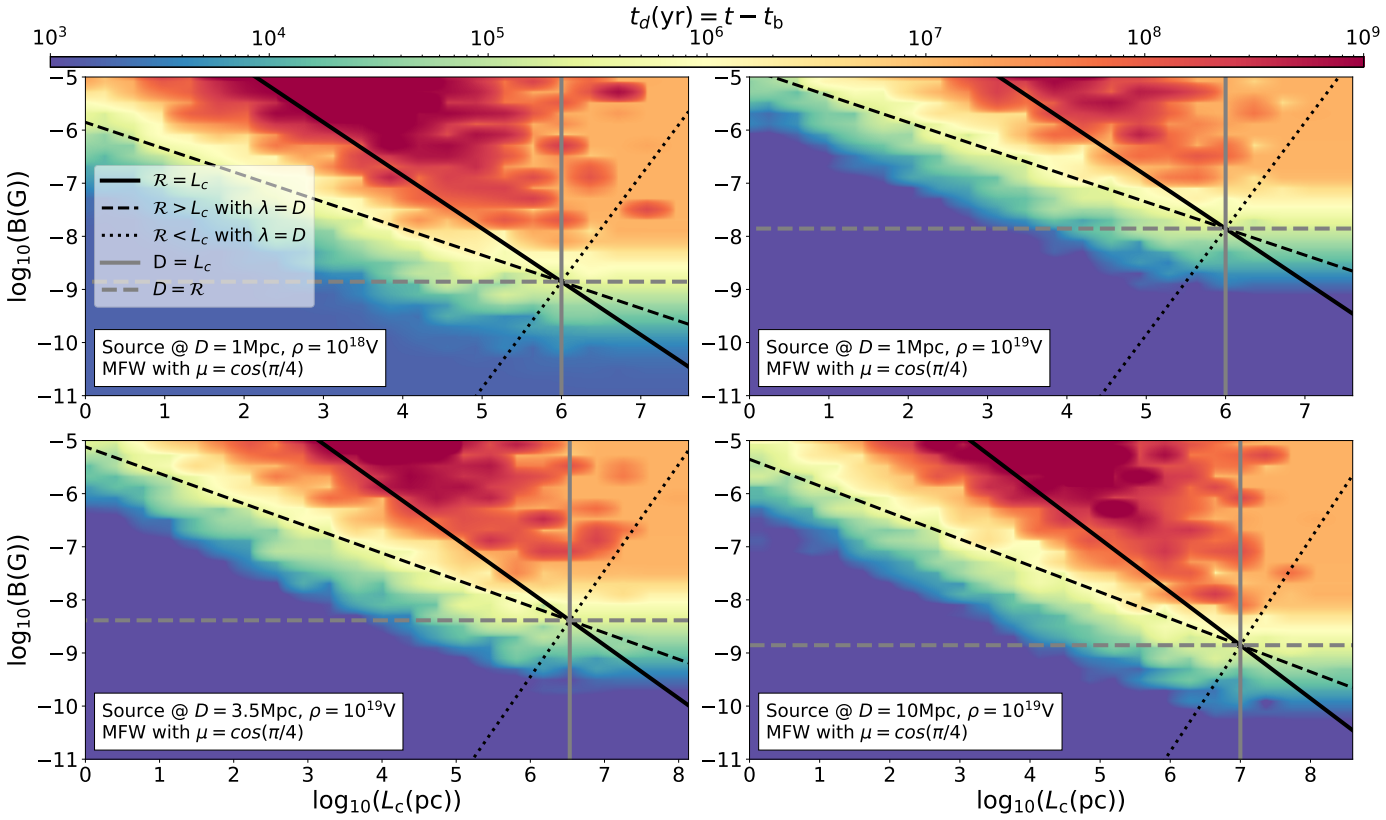

Figure 7.3: Time delay map t_d(yr) as a function of the coherence length L_c(pc) and the magnetic field B(G) that UHECRs with rigidity $\rho = E/Z = 10^{18}$V $\rho = 10^{19}$V probe over different distances as specified. Particle propagation in these plots is augmented with a wandering component as explained in the text. Particles are initialized with a pitch angle of $\mu = \cos \pi/4$. More details about the different panels are provided in the text.

Implications for the origin of UHECRs:

The origin of UHECRs has not been unequivocally determined. In this respect, newly-born millisecond pulsars (e.g., Blasi et al., 2007; Fang et al., 2012), γ-ray bursts (e.g., Vietri, 1995; Waxman, 1995), and tidal disruption events (e.g., Farrar & Piran, 2014b) have all been suggested as potential sources. However, AGN jets with radii $\sim 10 - 100$pc and magnetic fields with $\lesssim \mu$G are regarded as one of the most promising astrophysical sources (e.g. Ostrowski, 2000; Murase et al., 2012; Caprioli, 2015b; Matthews et al., 2019; Mbarek & Caprioli, 2019; Mbarek & Caprioli, 2021), as they satisfy the Hillas criterion up to 10^{20}eV and have luminosities that can explain the energy injection rate necessary to sustain the UHECR flux (e.g., Katz et al., 2013).

Discussions on the correlation between potential sources and UHECR arrival delays have largely focused on transient sources (e.g. GRBs, neutron stars) as the origin of UHECRs (e.g. Miralda-Escudé & Waxman, 1996; Kalli, S. et al., 2011; Takami & Murase, 2012; Harari et al., 2021; van Vliet et al., 2021). One of main concerns in these studies is the short dissipation time of such phenomena, that eventually renders spatial correlations with electromagnetic counterparts quite challenging. As for AGN jets, studies have mainly focused on flaring phases that would be coincident with acceleration (e.g., Biermann & Strittmatter, 1987; Murase et al., 2012; Farrar & Gruzinov, 2009) and their impact on correlation studies. They have, however, largely disregarded analyzing propagation delays that might be comparable to the AGN duty cycle.

Here we argue that the properties of the intergalactic magnetic field (IGMF)—which determine the pitch angle of particles, their potential deflections, and subsequent delays—play an essential role in constraining the AGNs responsible for the production of UHECRs. More specifically, particle propagation within the

IGMF can introduce delays comparable to AGN duty cycles, thus rendering correlations with potential sources challenging.

Constraining the properties of the magnetic fields between potential sources and Earth is paramount to analyzing the propagation of UHECRs, and eventually evaluating the effects of propagation delays. There have been numerous studies that attempted to constrain the properties of the IGMF (e.g. Neronov & Vovk, 2010; Tavecchio et al., 2010, 2011; Huan et al., 2011; Taylor et al., 2011; Finke et al., 2015) and its corresponding coherence length (e.g. Vovk et al., 2012). However, the scarcity of observational data and the difficulties associated with measurements of magnetic fields (Alves Batista & Saveliev, 2021) have made this challenging. Overall, within the context of UHECR propagation over cosmological baselines, it has been proposed that magnetic fields in voids are the most decisive component (Alves Batista & Saveliev, 2021), and an upper limit for their values could be set at $\lesssim 1$nG (e.g. Blasi et al., 1999; Kronberg et al., 2007; Planck Collaboration et al., 2016; Pshirkov et al., 2016). Moreover, in the context of quasars, outflows such as jets can inject a quite substantial galactic magnetic fields (GMF) (e.g. Kulsrud & Zweibel, 2008; Vallée, 2011; Ryu et al., 2012) in the intergalactic medium (IGM) (Furlanetto & Loeb, 2001). This renders the IGM in galaxy clusters more prone to having non-negligible fields, especially that filaments of galaxy clusters have also been observed to have magnetic fields reaching $B \sim 0.1 - 10$nG (e.g. Vazza et al., 2017). As for the intra-cluster medium (ICM), Faraday rotation observations suggest that the magnetic field can reach $\sim \mu$G (e.g. Clarke et al., 2001; Carilli & Taylor, 2002; Govoni et al., 2004). Galaxy superclusters, on the other hand, were found to have a statistically significant Faraday screen acting on radio-waves suggesting that $B \sim 0.3\mu$G in the local supercluster (Vallée, 2002). Similarly, the plane of the coma supercluster could have a magnetic field $\sim 0.5\mu$G (Kim et al., 1991). Finally, simulated magnetic fields in the local supercluster find

that they can reach ~ 10nG (Ryu et al., 2008).

Needless to say that there is a substantial body of work that attempts to constrain the properties of magnetic fields in galaxies, galaxy clusters and beyond; nevertheless, basic properties of the IGMF including its mean value or its associated coherence length remain poorly known. However, we can assume average values based on the aforementioned studies, and estimate that the magnetic field in galaxy clusters is $\sim 1\mu$G over a scale of $\sim$1Mpc and $\sim 0.1\mu$G in superclusters over a scale of $\sim$10Mpc.

In Figure 7.3, we show examples of the time delay t_d(yr) map of particle propagation as a function of the coherence length L_c(pc) and the magnetic field B(G) that particles with rigidities $\rho_{18} = 10^{18}$V and $\rho_{19} = 10^{19}$V probe over a distance of 1Mpc, 10Mpc, and 3.5Mpc ($\sim$ the distance to Centaurus A (e.g. Ferrarese et al., 2007; Majaess, 2010)). The rigidity examples are chosen to probe the delays of protons at the EeV level where $E = \rho_{18}$ and heavier elements at the highest energies (e.g. Aab et al., 2017a) reaching $E = Z\rho_{19} \sim 10^{20}$eV. These maps are based on a propagation in a wandering magnetic field (MFW only) since it should be regarded as more realistic, as discussed above. The solid and dashed lines are the boundaries introduced in Figure 7.1.

The most important features from each panel could be summarized as follows:

- Upper Left Panel: This shows the expected delay for particles with rigidity ρ_{18} depending on the coherence length of the magnetic field $L_{\rm c}$ and its magnitude B, for every 1Mpc that particles cover. We can see that for a $B \sim 1\mu$G, EeV protons are delayed by more than $t_d = 20$Myr for every Mpc they cover for $L_{\rm c} > 10$pc. At $B \sim 1$nG, delays are less significant such that $t_d > 2 \times 10^5$yr if $L_{\rm c} > 10^5$pc.

- Upper Right Panel: This shows the expected delay for particles with rigidity ρ_{19} for every 1Mpc that is covered.

- Lower Left Panel: Expected delays for particles with ρ_{19} traveling a distance equivalent to that to Centaurus A in a uniform magnetic field.
- Lower Right Panel: Expected delays for particles with ρ_{19} traveling a distance equivalent to that to Centaurus A in a uniform magnetic field.

While considering the effects of diffusion on particle propagation, Waxman & Miralda-Escude (1996) suggested that the induced time delay from the deflection angle of a proton propagating a distance D is $t_{\rm WM96} \sim 200{\rm yr}\ (D/100{\rm Mpc})^2(L_c/10{\rm Mpc})(B/10^{-11}{\rm G})^2(E/10^{20}{\rm eV})^{-2}$. This makes $t_{\rm WM96} \gtrsim 10^5$yr for $L_c = 1$Mpc, B$= 10^{-8}$G, E$= 10^{20}$eV, and $D = 10$Mpc. We find that the delay t_{20} associated with these conditions in our calculations (not shown in plots) is consistent with $t_{\rm WM96}$ such that $t_{20} \sim 3 \times 10^5$yr. However, we do not expect to get protons at these energies as the spectrum gets heavier with increasing energies (e.g. Aab et al., 2017a).

The AGN Duty Cycle and the Origin of UHECRs

AGN duty cycles $t_{\rm AGN}$ are uncertain phenomena that may depend on the mass and luminosity of the considered galaxies (e.g. Shabala et al., 2008). Several studies have focused on local radio galaxies with $z < 0.1$ (Shabala et al., 2008) and radio-loud galaxies including FRIs and FRIIs (e.g. Hardcastle et al., 2019; Shabala et al., 2020) and found observational evidence that place $t_{\rm AGN} \gtrsim 10^{6-7}$yr. We can also get clues on $t_{\rm AGN}$ by examining studies that constrain the average lifetime of quasars t_Q assuming that $t_{\rm AGN} \sim t_Q$. There are 3 main methods that have been introduced to estimate t_Q. The first of such methods is the transverse proximity effect or the Lyα forest absorption in a quasar spectrum from another quasar along the line of sight (e.g. Kirkman & Tytler, 2008; Schmidt et al., 2017; Bosman et al., 2020), which puts quasar lifetimes $t_Q \gtrsim 10^{5-7}$yr. The second method uses the extents of ionized nebulae around quasars to probe their repro-

cessed radiation field, and hence their radiative history (e.g. Trainor & Steidel, 2013; Borisova et al., 2016). This method constrains quasar lifetimes such that $t_Q \gtrsim 10^{6-7}$yr. The third method, dubbed quasar clustering, provides clues on t_Q by comparing the relative abundance of quasars with their host halos (Martini & Weinberg, 2001; Haiman & Hui, 2001), unfortunately with large uncertainties that place $t_Q \gtrsim 10^{6-8}$yr (Martini & Weinberg, 2001; Hopkins et al., 2005; Shen et al., 2009). Overall, AGN duty cycle measurements are highly uncertain, but we can assume that $t_{\rm AGN} \gtrsim 10^{5-8}$yr, a quite substantial interval.

These duty cycles are less important or comparable to the ballistic propagation time from potential AGN sources within the GZK radius (Greisen, 1966; Zatsepin & Kuz'min, 1966; Abbasi et al., 2008). So if particles are delayed during their propagation from AGN jets by a fraction of their ballistic propagation time–with delays 1-100Myr comparable to AGN duty cycles—correlation studies between UHECRs and their sources may prove challenging if not misleading.

It is worth stressing that particles do not feel the same magnetic field as they propagate from their sources. Powerful AGN jets are found to be predominantly inside clusters of galaxies (e.g., Begelman et al., 1984; Best et al., 2007; Fang & Murase, 2018b), and hence, UHECRs produced in such jets are likely to spend part of their journey within clusters with average magnetic field 1μG further delaying their propagation. For every 1Mpc that is covered by a UHECR with ρ_{19}, we can expect *at least* a delay $t_d > 10$Myr for $L_{\rm c} \geq 10^4$pc. For sources relatively close-by sources at 10Mpc away, delays exceed the maximum expected AGN duty cycles if propagating in such magnetic fields. Lower-energy particles are affected even more. If we assume larger values of the magnetic field by more than an order of magnitude, we still obtain delays much greater than the lower limits of the expected $t_{\rm AGN}$. It has also been argued that UHECRs can be affected by galactic magnetic fields (GMF) (Takami et al., 2012; Jansson & Farrar, 2012; Unger &

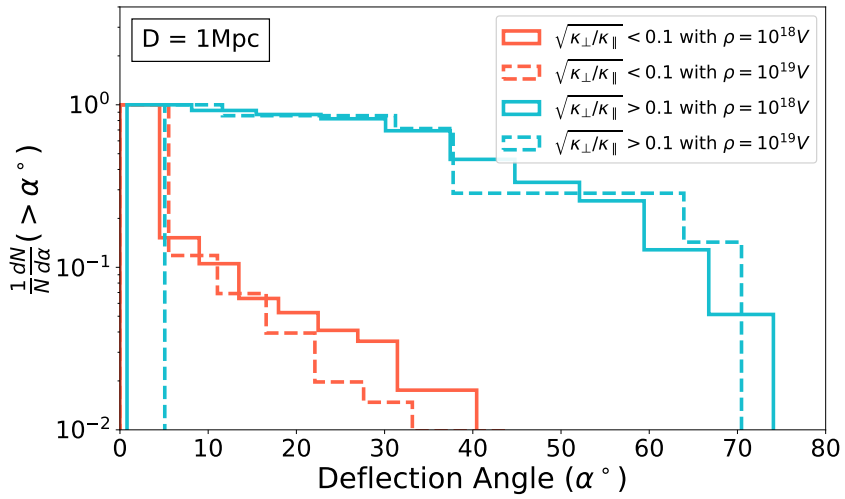

Figure 7.4: Cumulative distribution $\frac{1}{N}\frac{dN}{d\alpha}(> \alpha^\circ)$ of the deflection angles of particles with rigidity $\rho = 10^{18}$V & 10^{19}V in regions with $L_c < D$, depending on the ratio of the transverse diffusion and spatial diffusion $\sqrt{\kappa_\perp/\kappa_\parallel}$ (See Figure 7.2 for a more detailed discussion). N is the total number of particles.

Farrar, 2017), further delaying particles.

In general, our results paint a picture in which even if particles spend a modest part of its journey within the cluster on their way to Earth or where they originate from, they can be sufficiently delayed by time intervals comparable to the duty cycles of AGNs. We then expect that less active AGNs, that currently do not satisfy the power requirements to generate UHECRs, might have been much more powerful in the past to accelerate the presently detected UHECRs. Previously powerful FRI/FRII galaxies within the GZK radius could have produced the bulk of UHECRs that we observe today, considering that the UHECR propagation time can be comparable to that of AGN duty cycles. This would mean that correlation studies between the location of AGNs and the expected arrival directions of UHECRs (e.g. Aab et al., 2018b) are unlikely to accurately detect an anisotropic signal. A study of the expected deflection angles follows to further reiterate these claims.

Deflection of Arrival Angles

In Figure 7.4, we show the impact of $\sqrt{\kappa_\perp/\kappa_\parallel}$ on the expected deflection angles that ensue particle propagation in our simple numerical setup. We include the cumulative distribution of the deflection angles of particles propagating over 1 Mpc for different B-field values (See Figure 7.3) spanning a range of coherence lengths such that $L_{\rm c}$ <1Mpc.

As discussed in §7.3, $\sqrt{\kappa_\perp/\kappa_\parallel}$ is a good probe for the B-$L_{\rm c}$ maps that are affected by the turbulent magnetic field differently. First, we note that particles are deflected almost similarly for different rigidities. We expect ∼20% of UHECRs in regions where $\sqrt{\kappa_\perp/\kappa_\parallel} < 0.1$ to be deflected by at least 5° and almost all particles to be deflected by at least $> 10^\circ$ for $\sqrt{\kappa_\perp/\kappa_\parallel} > 0.1$.

Estimates of deflection angles of particles as they propagate towards Earth from their sources have important repercussions for anisotropy studies. These results show that it is only possible to point back to the sources of UHECRs if $\sqrt{\kappa_\perp/\kappa_\parallel} > 0.1$ or $\lambda > D$ (for $\mathcal{R} > L_{\rm c}$). These results, along with the comparison of propagation time with the AGN duty cycle, only serve to reiterate that it is challenging to pinpoint the location of UHECR sources based on their arrival directions.

The significant deflections we find are not anomalous compared to other studies. For instance, Waxman & Miralda-Escude (1996) followed a diffusive propagation approach, and estimated the expected deflection of UHECRs as they reach Earth. If B is a homogenous magnetic field with coherence length L_c such that $\mathcal{R} > L_c$, the average deflection will be $\langle\theta\rangle \sim \frac{L_c}{2\mathcal{R}}$ and the overall deflection θ_d will be $\theta_d \sim \langle\theta\rangle\sqrt{D/L_c}$ after a distance D undergoing random deflections. In the fiducial example introduced earlier (B = 10nG, E = 10^{20}eV, $L_c = 1$Mpc, and D = 10Mpc), the expected deflection reaches 8°, a significant value. Several other groups have

further discussed the deflections associated with propagation (e.g. Alves Batista et al., 2016); and others found that UHECRs can be significantly deflected up to 30° for iron above 5EeV because of the GMF (Jansson & Farrar, 2012). These significant deflections further reiterate the results of our propagation scheme.

7.5 Conclusions

In this chapter, we propagate particles in a turbulent magnetic field and check the effect of the wandering field properties on the time delay and deflection of particles as they propagate towards Earth. We eventually compare these time delays to AGN duty cycles and find that they are comparable.

The main conclusions of the paper can be summarized as follows:

1. The propagation delay results shown in Figure 7.1 are general in that they are applicable to galactic propagation of CRs as well as intergalactic propagation of UHECRs.

2. If the particle gyroradius is less than the distance to the potential source, the propagation time of UHECRs is at least doubled compared to the ballistic time.

3. The spectrum of turbulence that we assume does not have much of an effect on the expected delays for the lowest magnetic field values.

4. UHECRs could originate from AGNs that were active in the past since their duty cycles is comparable to the expected propagation delay.

5. We expect significant deflections of the arrival directions of UHECRs. These results render correlation studies with potential AGN sources quite challenging.

Chapter 8

The Cosmic Ray confinement Time in the Milky Way: The HELIX Experiment

The propagation framework discussed above enables us to calculate the expected delay time that particles could experience on their way to Earth depending on the magnetic field and its coherence length. Here, I discuss my contribution to the HELIX experiment, which will make measurements of CR isotope ratios to more directly measure the confinement time of CRs in the galaxy.

8.1 HELIX: A Quick Overview

In a nutshell, the High Energy Light Isotope eXperiment or HELIX is a magnet spectrometer designed to make measurements of the composition of light CR isotopes. This NASA funded experiment is outfitted with a suite of modern, high-precision particle detectors designed specifically to make measurements of CR isotope ratios in the energy range ~ 0.2 GeV/n to ~ 10 GeV/n, a range that is not accessible to any current or planned instrument. Most importantly, it will determine astrophysically significant isotopic abundance ratios such as $^{10}\mathrm{Be}/^{9}\mathrm{Be}$.

8.1.1 Background & Motivation

Over the past decade, new successful balloon-borne and space-based missions with unparalleled precision and energy reach have challenged our conventional understanding of the field. The sophistication with which we can interpret data has also dramatically evolved to enable us to test theoretical models pertaining to CR sources and their propagation. Many questions, however, remain unresolved. Studying the propagation of CRs in the galaxy is one of such important questions. This transport has proven challenging to tackle because microphysical processes alter the large scale propagation of CRs in the interstellar medium (ISM). CR propagation is most commonly studied through the diffusion-convection equation such that small scale complexity is averaged out. Ultimately, these equations characterize the spatial dependence of the CR spectrum. The spectrum observed at Earth then becomes a convolution of variables dependent on the CR confinement time in the galaxy and the source spectrum. In the context of the diffusion-convection model, CR flux ratios are employed to characterize such a transport.

Precise measurements of CR ratios are not only important for galactic astrophysics, but also for cosmological models of galaxy formation and evolution. Understanding CR transport and the CR halo size through $^{10}\mathrm{Be}/^{9}\mathrm{Be}$ ratio measurements is crucial in unraveling the role of CRs in galaxy evolution. Modern galaxy formation models are very sensitive to CR dynamics because of the effect of CRs on the circumgalactic medium (CGM) (Ji et al., 2019). Additionally, it is found that different modes of CR transport have a significant impact on the properties of Milky Way-like galaxies in cosmological magneto-hydrodynamical simulations (Buck et al., 2019).

The ^{10}Be/^{9}Be ratio, a crucial measurement The description of CR propagation and its observable consequences (secondary particles and radiation) has become increasingly more sophisticated due to the improvement in the numerical resources to explain CR transport. GALPROP (Strong & Moskalenko, 1998), DRAGON (Evoli et al., 2008), PICARD (Kissmann, 2014), and Usine (Maurin, 2011) are numerical codes that rely heavily on precise CR ratio measurements to eventually explain the CR spectrum at Earth and understand CR sources in our galaxy.

More importantly, precise ratio measurements will pave the way for explaining the most widely publicized recent discrepancy in CR physics: the observed increase in the positron fraction $e^+/(e^+ + e^-)$ reported by the PAMELA, AMS-02, and Fermi/LAT collaborations. Before this discovery, it had been long believed that the measured secondary-to-primary ratios of nuclei decrease with increasing energy. This means that the grammage—the total mass per unit surface that CRs interact with as they roam the galaxy—associated with diffusive propagation also decreases with increasing energy. The fluxes of positrons, supposed to be products of CR interactions, are also expected to decrease with energy. However, this discovery suggests the exact opposite. Following the positron excess discovery, a clear interpretation and analysis still has not been attained because of the lack of important CR ratio measurements needed to inform and constrain the CR propagation framework. This excess contradicts traditional models of CR propagation which prompted many research teams to attribute it to particle production in nearby pulsars, propagation physics, and even the annihilation or decay of DM particles. (Simon, 1999; et al., 2004; Putze et al., 2009). High-quality $^{10}\mathrm{Be}/^{9}\mathrm{Be}$ measurements are important model inputs for interpreting CR and DM-related data (Strong et al., 2007; Putze et al., 2009; Ptuskin & Soutoul, 1998; Delahaye et al., 2010; Blum, 2011; Tomassetti, 2012; Delahaye & Grefe, 2013; Cholis &

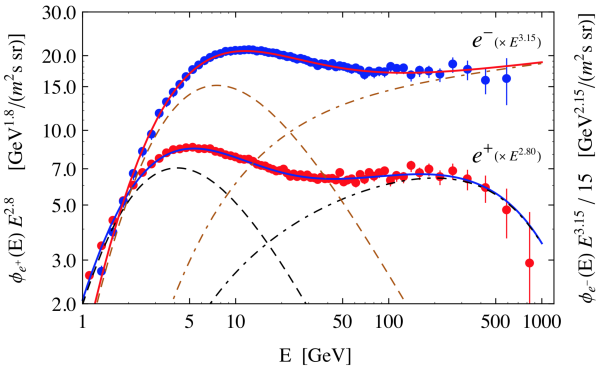

Figure 8.1: Spectra of CR positrons et al. (2019) and electrons et al. (2014) measured by AMS-02. The fluxes are plotted as a function of energy in the form $E^{2.8}\phi(E)$ for positrons and $E^{3.5}\phi(E)$ for electrons. Lipari (2019) presents the solid lines as the sum of contributions from models in the dashed lines. These models depend directly on the CR residence time in the galaxy.

Hooper, 2013) and can provide strong discrimination between these models. For example, the positron spectrum ϕ_{e+} in Figure 8.1 Lipari (2019) depends directly on the properties of the residence time τ of CR particles in the galaxy. Measurements of the isotope abundances in the Be flux inform us on τ and eventually constrain DM and positron accelerator models.

HELIX and ^{10}Be/^{9}Be measurements The AMS-02 instrument was anticipated to provide these important ratio data; however, key ratios cannot be measured anymore because the instrument's original superconducting magnet was replaced with a longer-lifetime, but lower-strength permanent magnet. HELIX, with its superconducting magnet spectrometer system equipped with a set of modern, high-precision particle detectors designed specifically to detect CR isotope ratios, will make these measurements in an energy range that is not accessible to any current or planned instrument. Existing measurements have indeed been limited to sub-GV rigidities (e.g. et al., 2004; Connell, 1998). The HELIX spectrometer is outfitted with a 1T superconducting magnet from the HEAT instrument (et al., 1997), which has been used with great success in five previous balloon campaigns. This magnet will also be combined with a gas drift chamber, a fast time-of-flight system, and a high-precision ring-imaging Cherenkov detector. HELIX will eventually make high statistics measurements of important isotopic abun-

dances such as $^{10}\mathrm{Be}/^{9}\mathrm{Be}$ in energy ranges an order of magnitude higher than previously achieved.

8.1.2 HELIX: Measurement Techniques and Current Status

As stated above, one of the main goals of HELIX is to measure the isotopic composition of CRs. However, it is experimentally much more difficult to measure isotopes than the elemental secondary-to-primary ratios. In the HELIX energy range, magnet spectrometers are the instrument of choice for measuring isotopic compositions. In this case, we need to measure the charge Z of the particle, its rigidity R and the velocity β in order to obtain the particle mass m. The charge Z is usually determined through measurements of energy loss by ionization; the velocity β is determined, on the other hand, by time-of-flight measurements or from signals in Cherenkov counters at higher energies. As for the rigidity, the particle is tracked through the magnetic field of the spectrometer. The mass resolution can be expressed as follows: $\left(\frac{\Delta m}{m}\right)^2 = \left(\frac{\Delta R}{R}\right)^2 + \gamma^4\left(\frac{\Delta\beta}{\beta}\right)^2$, where γ is the Lorentz factor of the particle. From the above formula, we can see that the overall success of the experiment hinges on an excellent rigidity resolution $\Delta R/R$ and velocity resolution $\Delta\beta/\beta$. For this reason, it is insufficient to merely have an effective detector system, but also innovative tracking techniques. Tracking techniques are numerical methods for fitting tracks of particles in magnetic fields to obtain their rigidities (e.g. Myrheim & Bugge, 1979) as they pass through the whole detector system.

As of 04/22, we are in the final stages of assembling the detector system which will be ready for launch in Antarctica in 12/22. Over the past $\sim$5 years, I have been heavily involved in the detector systems' building and testing including accurately measuring and analyzing the magnetic field map of the magnet, mapping the relative positions of different subsystems, designing and testing thermal so-

lutions for the science flight computer (SFC) for precise data collection, testing the payload batteries, and designing thermal solutions for the RICH. The following sections will have a more detailed mapping of my contributions to the HELIX experiment.

8.2 Contribution to The HELIX Experiment

8.2.1 Initial Predictions of the ^{9}Be/^{10}Be ratio

The most prominent experiment that mesaured the ^{9}Be/^{10}Be ratio is The Isotope Magnet Experiment (ISOMAX), a balloon-borne superconducting magnet spectrometer that was designed to measure the isotopic composition of the light isotopes ($3 \leq Z \leq 8$) cosmic radiation up to 4 GeV nucleon^{-1}. Figure 8.2 shows the main results pertaining to the ISOMAX measurements compared with known models. The lines show the expected beryllium ratio assuming different propagation models that will be discussed in the following subsections. The solid line represents a prediction in a diffusion-halo model with reacceleration. The dotted line represents a Leaky Box Model (LBM) with a hydrogen density of $n_H = 0.2$cm^{-3} and the dashed line represents an LBM in which the solar system is part of a low-density Local Bubble and the remainder of the Galaxy has a higher hydrogen density $n_H = 0.5$cm^{-3}.

More recently during the 2021 International Cosmic Ray Conference (ICRC), the AMS-02 collaboration has shown—although not published yet—hints that ^{9}Be/^{10}Be increases more slowly with energy than previously thought relying on current diffusion-based models (See Figure 8.3 from Lipari (2022)). This would imply that either the common description of nuclear fragmentation cross sections or diffusion models commonly used to interpret CR observations is inadequate. However, these results are not direct measurements of the ^{9}Be/^{10}Be ratio and should be considered with caution while awaiting the official AMS publication.

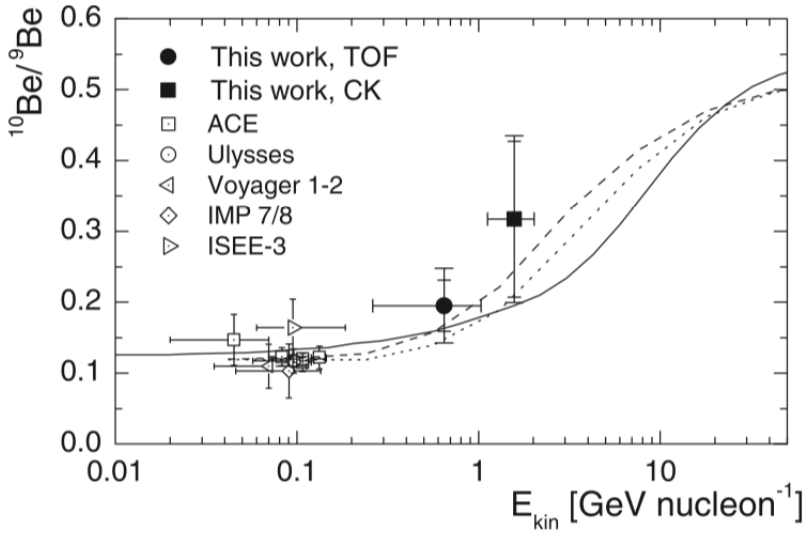

Figure 8.2: Beryllium ratio of ISOMAX (Hams et al., 2004) compared with satellite measurements.

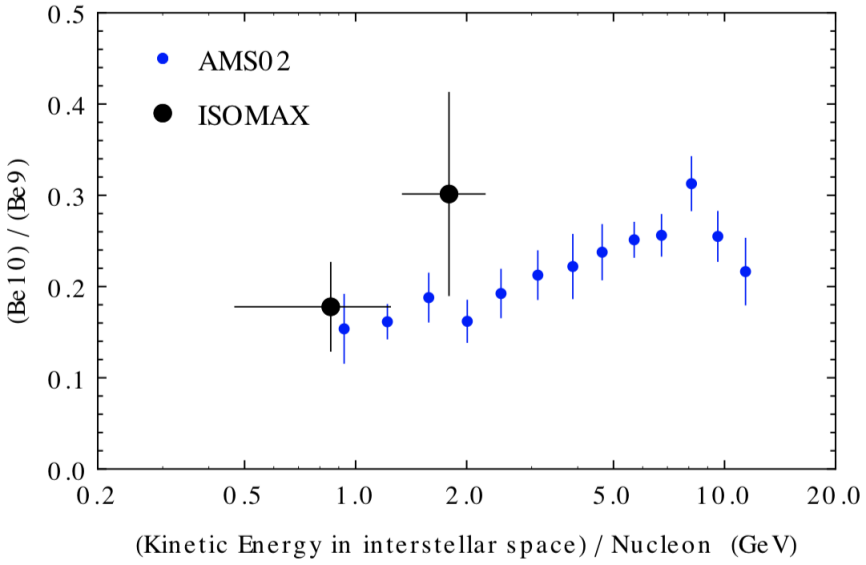

Figure 8.3: Beryllium ratio of ISOMAX (Hams et al., 2004) compared with the newest measurements of the AMS02 of the ^{9}Be/^{10}Be ratio (Adapted from Lipari, 2022)

Propagation of CRs in the galaxy

Equation 8.1 governs the distribution of sources and propagation of particles in the galaxy. If sources inject particles of type i at a rate $Q(E, x, t)$ such that Q also depends on time and position in the galaxy, the density N of particle i becomes:

$$\begin{aligned} &\frac{\partial N_i(E,x)}{\partial t} + V.\nabla N_i(E,x) - \nabla.[D(r)\nabla N_i(E,x)] \\ &= Q_i(E,x,t) - p_i N_i(E,x) + \frac{v\rho(x)}{m_p}\sum_{k\geq i}\int \frac{d\sigma_{i,k}(E,E')}{dE} N_k(E',x)dE' \end{aligned} \tag{8.1}$$

The second and third terms in the left hand side represent convection and diffusion such that D is the diffusion coefficient and V is the flow velocity. Basically, those are the propagation terms.

The second term in the right hand side of equation 8.1 represents the loss of nuclei of type i with collisions or decay such that:

$$p_i = \frac{v\rho\sigma_i}{m_p} + \frac{1}{\gamma\tau_i} = \frac{v\rho}{\lambda_i} + \frac{1}{\gamma\tau_i} \tag{8.2}$$

where $\gamma\tau_i$ is the dilated lifetime of the particle. $\frac{v\rho\sigma_i}{m_p}$ represents the rate at which nuclei i interact in Hydrogen of number density $n_H = \rho/m_p$ (although 10% should be Helium). The last term is the cascade term to include nuclear fragmentation and feed-down from higher energies. If a particle occurs from a radioactive decay of another particle, an extra term is added.

Leaky Box model

For a galactic cosmic ray (GCR) of species i at a particular ISM energy per nucleon E, the steady-state equation (equation 8.1) governs its number density, N_i. Meneguzzi et al. (1971) suggested that CRs are transported in a 'leaky box' assuming a simple exponential path length distribution. Basically CRs propagate

freely in a containment volume, with a constant probability per unit time of escape $1/\tau_{\rm esc} \ll c/h$ (The approximation is relevant only if $c\tau_{\rm esc} \gg h$ where h defines the galaxy thickness. The MW is assumed as a uniform thin cylinder of thickness $2h \sim 200pc$). $\tau_{\rm esc}$ is the mean time in the containment volume and $\lambda_{\rm esc} = \rho\beta c\tau_{\rm esc}$ is the mean amount of matter traversed by the particle in units of g/cm^2. Diffusion and convection are replaced by a characteristic escape time:

$$V.\nabla N_i(E,x) - \nabla.[D(r)\nabla N_i(E,x)] \rightarrow N/\tau_{\rm esc} \tag{8.3}$$

The probability of a particle staying in this 'box' becomes $e^{-t/\tau_{\rm esc}}$.

In the Leaky box model, equation 8.1 then becomes:

$$\frac{N_i(E,x)}{\tau_{\rm esc}} = Q_i(E) - p_i N_i(E,x) + \frac{v\rho(x)}{m_p} + \frac{\beta c\rho}{m_p}\sigma_{i,k}N_k(E',x) \tag{8.4}$$

This enables us to compute secondary-to-primary ratios such as Boron to Carbon in order to understand how particles are propagated in the galaxy. It is in fact assumed that Boron is not produced at the CR sources and is solely the result of CR propagation. We can compute the density of Boron as :

$$\frac{N_B(E)}{\tau_{\rm esc}(E)} + \frac{\beta c\rho}{\lambda_B}N_B(E) = \frac{\beta c\rho}{m_p}[\sigma_{C\rightarrow B}N(C) + \sigma_{O\rightarrow B}N(O)] \tag{8.5}$$

since we get B mainly from O and C.

We end up with:

$$\frac{N_B(E)}{N_C(E)} = \frac{\lambda_{\rm esc}(E)}{1+\lambda_{\rm esc}(E)/\lambda_B}\frac{[\sigma_{C\rightarrow B} + \sigma_{O\rightarrow B}]}{m_p} \tag{8.6}$$

since we get B mainly from O and C. $\lambda_B = m_p/\sigma_B$ is the grammage associated with B, and .$\lambda_{\rm esc}$ is defined as the energy-dependent escape length where:

$$\lambda_{\rm esc}(E) = \beta c\rho\tau_{\rm esc}(E) \tag{8.7}$$

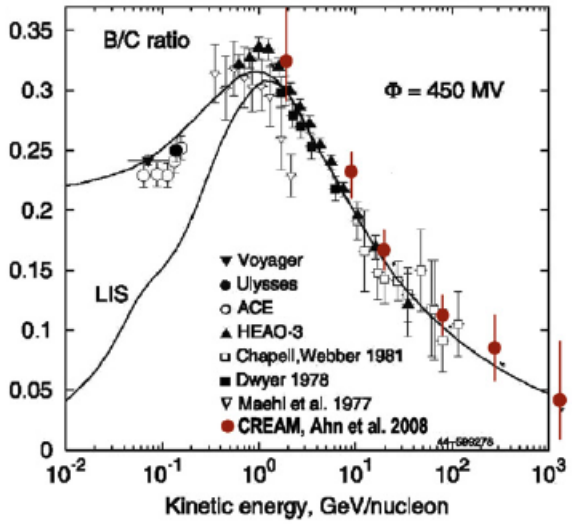

Figure 8.4: B/C ratio as a function of kinetic energy (Gaisser et al., 2016).

We can parameterize $\lambda_{\rm esc}$ using data from the Figure below from Ptuskin (2012) such that:

$$\lambda_{\rm esc} = 19\beta^3\left(\frac{R}{3GV}\right)^{\delta} \tag{8.8}$$

with $\delta \sim -0.4$. The energy dependence of $\lambda_{\rm esc}$ is a power law

Radioactive isotopes with the Leaky Box model

Within the leaky box model and following the same procedure as with primary to secondary ratios, we should pbtain for Be isotopes:

$$\frac{^{10}Be}{^{9}Be} = \frac{\sigma_{\rm p\to 10}}{\sigma_{\rm p\to 9}}\frac{1+\lambda_{\rm esc}/\lambda_9}{1+\lambda_{\rm esc}/\lambda_{10}+\tau_{\rm esc}/(\gamma\tau_{10})} \tag{8.9}$$

where σ_p is the production cross-section for Be (Yanasak et al., 2001), $\tau_{\rm esc}$ is the confinement time in the galaxy, $\lambda_i = m_p/\sigma_i$ are the grammage associated with Be isotopes (values of σ_i from Letaw et al. (1983)), and τ_{10} is the decay time of ^{10}Be. Since $\lambda_{\rm esc} = \beta c\rho\tau_{\rm esc}$, the ratio depends on average density ρ and $\tau_{\rm esc}$ separately.

With the simplistic analysis that we introduced, we get the results shown in Figure 8.5. We note that the ratios that we obtain from the Leaky box model

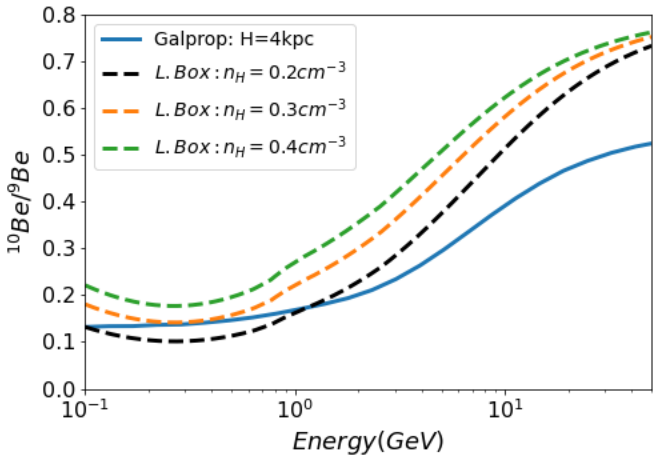

Figure 8.5: Ratio simulations based on the Galprop code (Strong & Moskalenko, 1998) and Leaky Box Model as explained in the text.

are overly simplistic and do not allow us to extract correct values because energy losses during propagation are not accounted for. Additionally, ^{10}Be is created from ^{11}B which is as we learned earlier, a secondary. Therefore we need to solve a set of equations according to equation 8.1 to get better results.

Fitting to the Leaky Box Model

With the simple analysis that we introduced, we can obtain fit potential HELIX data generated with a Monte Carlo routine using test routines that rely on the Least Square (LS) and Maximum Likelihood (ML) methods. This enables us to test the robustness of methods we would employ after a HELIX flight. We get the results shown in Figure 8.6. A 2D counterpart to the ML method.

Flaws of Leaky Box Model The ratios that we obtain from the Leaky box model are overly simplistic and do not allow us to extract correct values because energy losses during propagation are not accounted for. Also ^{10}Be is created from ^{11}B which is as we learned earlier, a secondary. Therefore, the results we obtain are still overly simplistic. In the Leaky Box model:

1. Diffusion and Advection are replaced with a characteristic confinement time

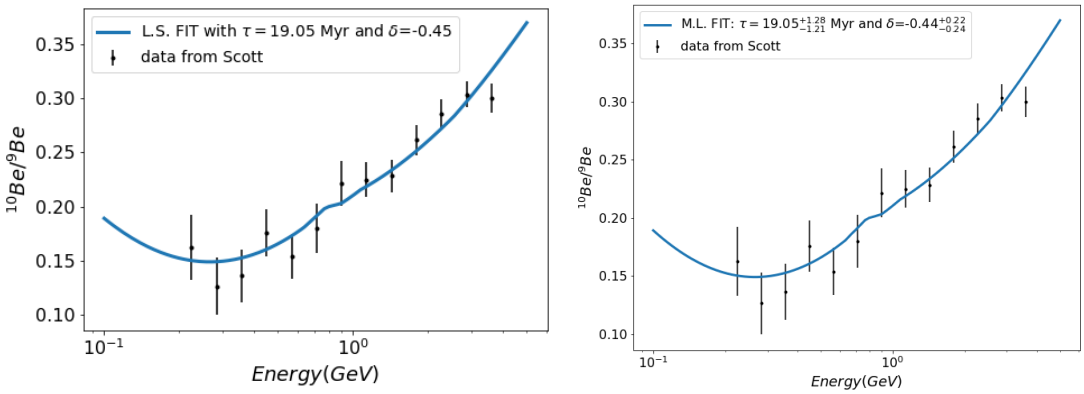

Figure 8.6: Least Square (SQ) and Maximum Likelihood (M.L) fit to Monte Carlo generated data. These plots show the robustness of the methods that will be employed to fit HELIX data.

2. The CR age and escape time distributions are identical and determined by τ_{esc}. However, age is the time elapsed between the instants of injection and observation of a particle, while escape time is the total time spent in the galaxy after injection.

8.2.2 Magnetic Field Mapping of the Super-Conducting Magnet & Trajectory Reconstruction

Magnetic Field Mapping

In order to map the magnetic field, we used a 3D stage with 3 stepper motors to move a Hall probe around the two coils of the magnet after fully charging it as shown in Figure 8.8. At every position, all magnetic field components are measured, which eventually enables us to make a field map in and between the magnet coils.

We can then compare these experimental B-field measurements with theoretical ones that we can calculate based on the Biot-Savart law. Figure 8.9 shows the overall layout of the coils along with the initial conditions that we compare the experimental values with.

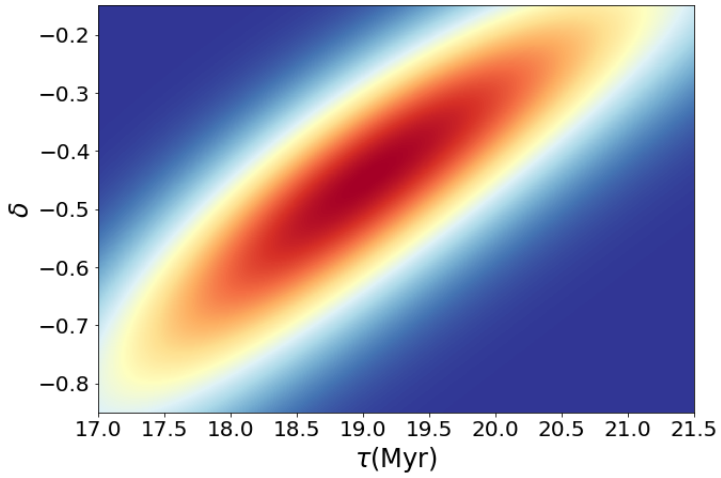

Figure 8.7: Same as Figure 8.6 but showing the maximum likelihood fit for τ and δ.

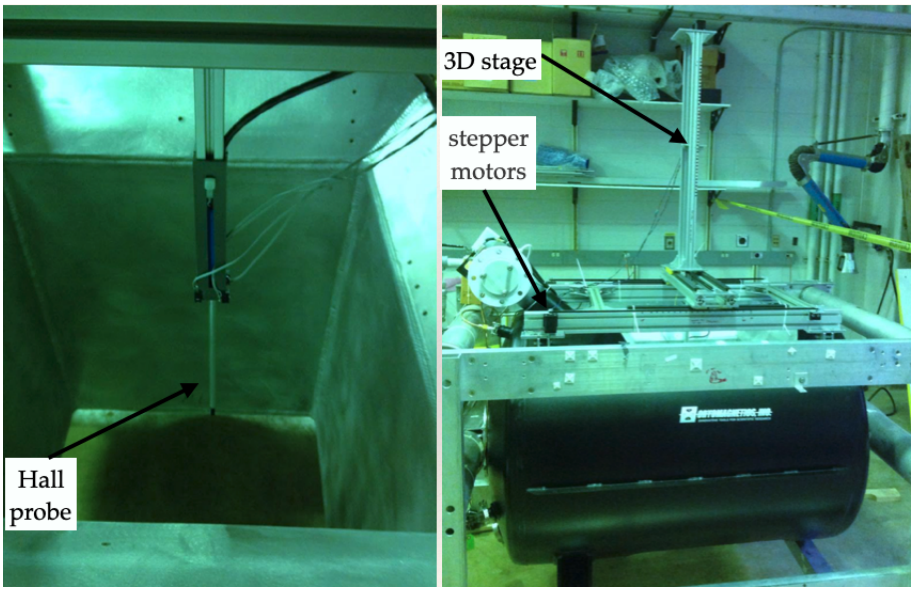

Figure 8.8: Left Panel: Hall probe used to make the measurements. Right Side: Overall setup on top of the charged magnet.

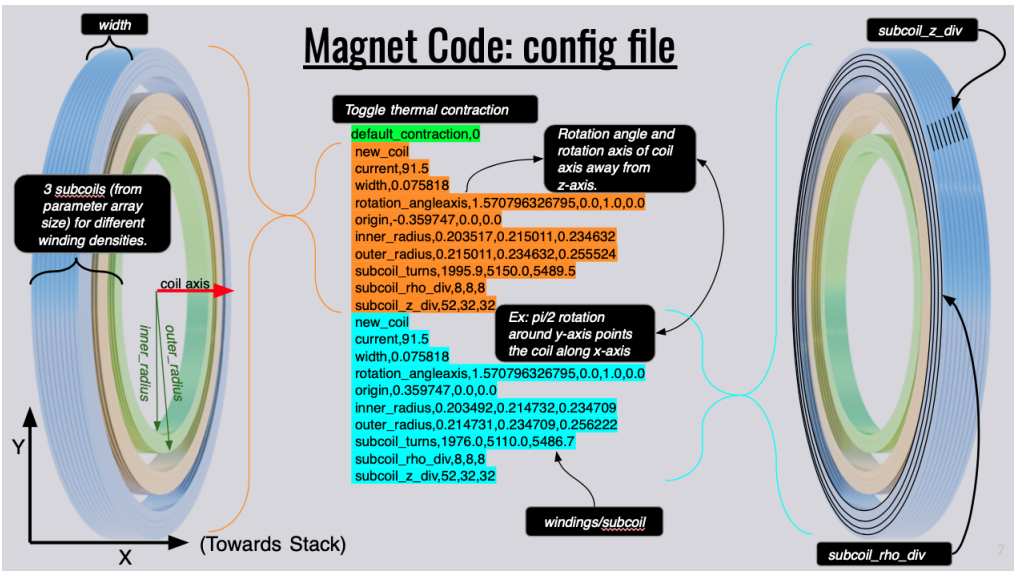

Figure 8.9: Layout of Magnet's coils along with initial conditions used to generate the magnetic field map. Credit: Noah Green.

Trajectory Reconstruction

The magnet has been charged multiple times and every time the coils heat up or if the magnet quenches, there is a non-negligible chance that the coils move from their initial positions which could result in changes in the magnetic field. This could result in different bends in particle trajectories and thus different conclusions about particle properties. Figure 8.10 shows a 2D slice of the measured and analytical magnetic field maps in the same position, along with the percentage difference between the two maps. We can see that the maps are quite similar. However, rotations along all possible axes of rotation is not to be excluded. After performing a Least square fit to the measured maps by rotating the coils along all 3 axes in the theoretical maps, we find that the coils could not have moved by more 2°. These results could not be satisfactory unless we simulate particle propagation in the measured maps to check whether particle rigidity retrieval is affected.

As a result, we propagate 1000 particles in the magnetic field map with a

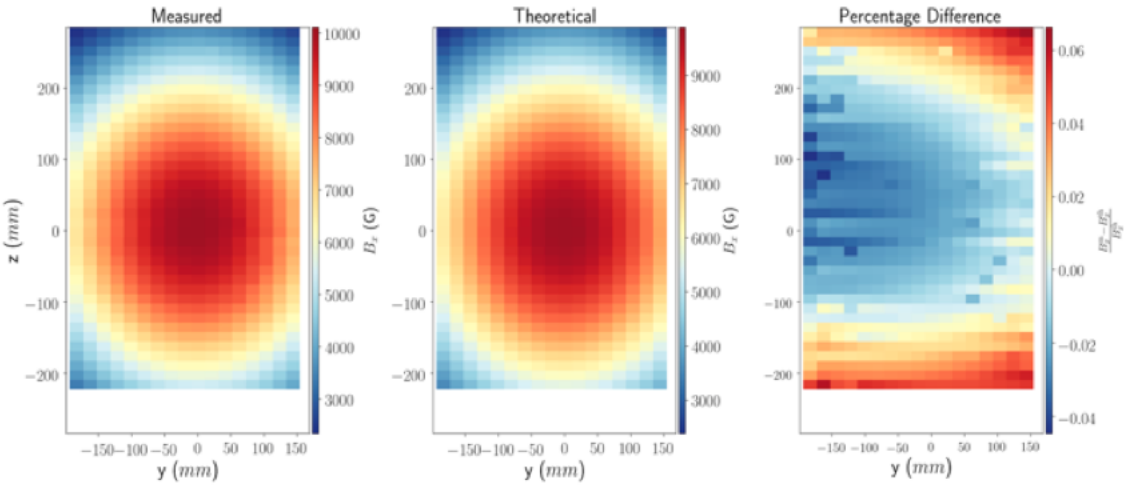

Figure 8.10: Left Panel: 2D slices of the measured magnetic field maps. Middle: Same as the left panel but for the theoretical maps. Right Panel: Percentage difference between the left and right maps.

known rigidity and later reconstruct their rigidity based on their bend. Figure 8.11 shows the reconstructed rigidity within the measured magnetic field with two different reconstruction methods (See presentation from 05/2019 on tracking codes). We find no differences between the theoretical and experimental maps.

8.2.3 Science Flight Computer Thermal Management

The Science Flight Computer (SFC) has 4 main components:

1. An INTEL® Perfectron motherboard (CPU Maximum Temperature ~ 90C)
2. An PCI merger board: SYNOPSIS® board (Maximum Temperature ~ 85C)
3. An ATX-M4® power supply (Temperature range -40—85C)
4. Four Industrial Innodisk® Solid State Disk (SSD) with an 8TB capacity (Temperature range -40—85C)

As specified above, each component has a specific temperature range that needs to be accounted for both in vacuum and in atmosphere. While running the PCI

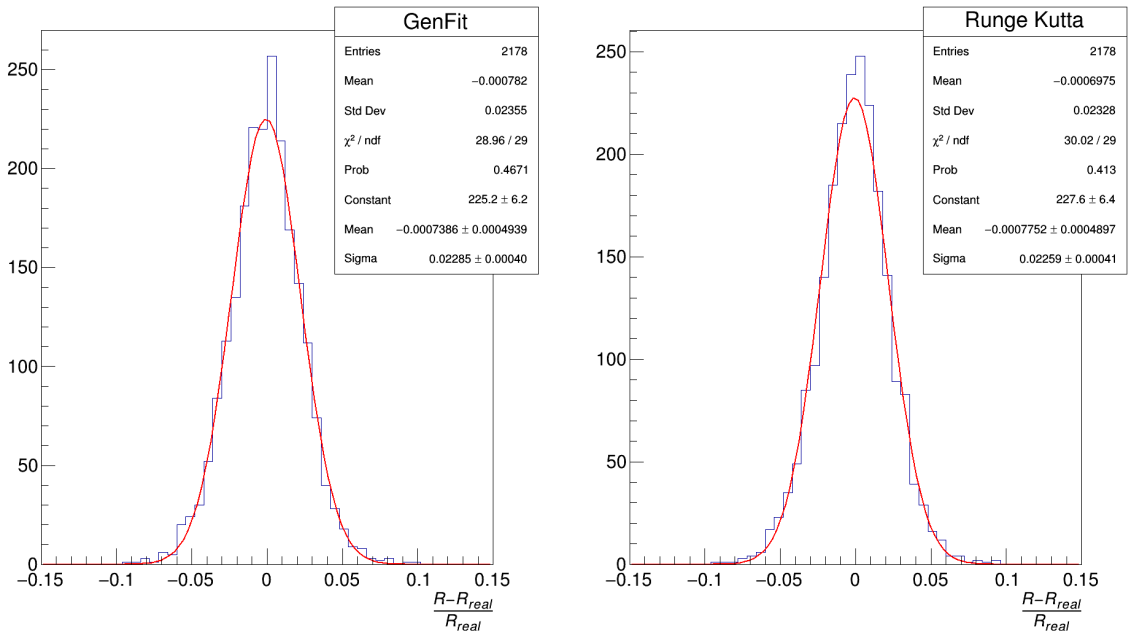

Figure 8.11: Particle rigidity reconstruction

board for a few minutes, we can see in Figure 8.12 that the temperature increases fast and dramatically. Therefore, adequate thermal solutions that work out for all four components above is necessary.

Thermal Solutions In order to remedy to these problems, we use a combination of heat sinks, fans (while running in atmosphere), and water heat pipes (See Figure 8.14) to enable a fast flow of heat. Figure 8.13 shows the solution that we

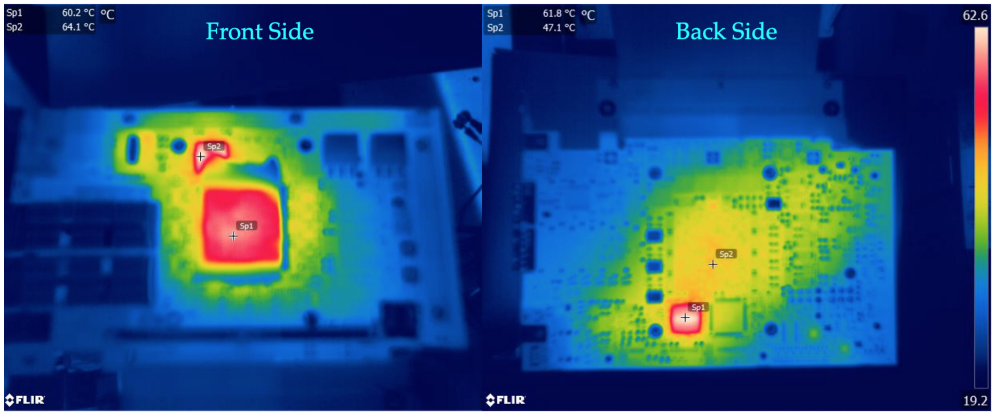

Figure 8.12: Snapshot from a FLIR IR camera of the PCI merger after running it for 15 seconds. We can see that the FPGA warms up very fast.

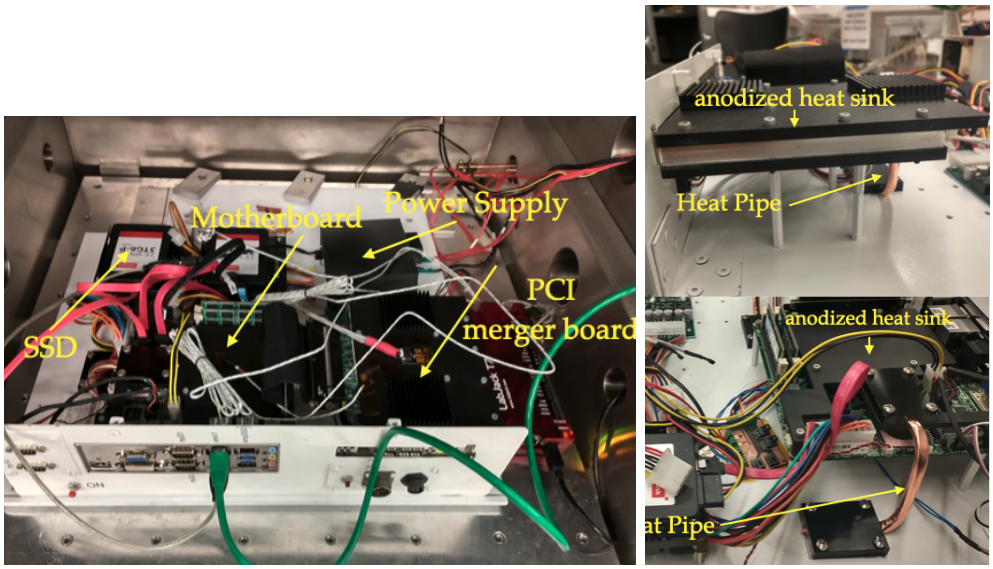

Figure 8.13: Left Panel: Components of the Science Flight computer (SFC) covered with their respective heat sinks. Right Panel: Close-up pictures of the thermal management solutions of the SFC including the anodized heat sinks and heat pipes.

had to deal with the temperature constraints.

Then, we run the SFC at maximum capacity by maximally stressing the CPU and PCI board in the thermal vacuum chamber. Figure 8.15 shows the results of this test for the CPU and PCI board (DINI in the Figure). We find that the water heat pipes conduct heat properly in the temperature range where they are supposed to operate (heat pipe regime). As the base plate temperature—which is a proxy for the Gondola temperature with which the SFC is in direct contact—decreases, the working fluid in the pipe starts freezing (transition regime) and the heat pipe do not conduct heat as efficiently. Finally, when the working fluid is completely frozen, the heat pipes conduct heat as hollow copper pipes. Considering that the base plate temperature is quite low in this conduction regime, there is significant heat that still flows out of the motherboard and PCI board. This setup enables us to use a quite simple setup and be able to have an operational SFC within a substantial temperature range.

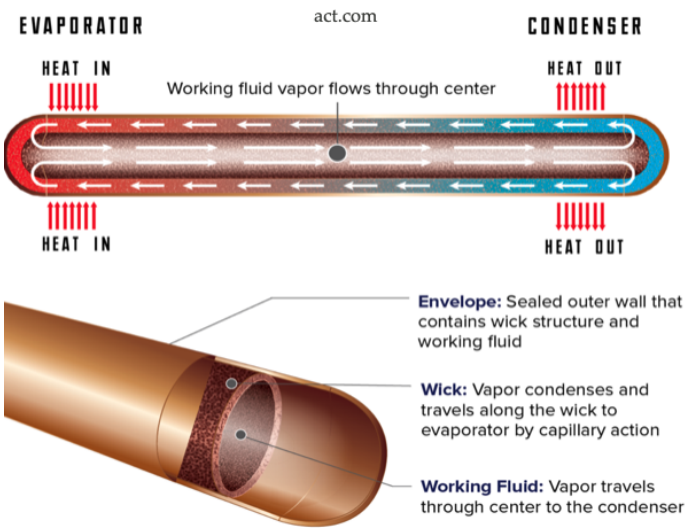

Figure 8.14: Heat pipes are copper enclosures that have a working fluid (water in our case) that evaporates and condenses depending on the temperature. The working fluid defines the temperature range in which the pipe operates.

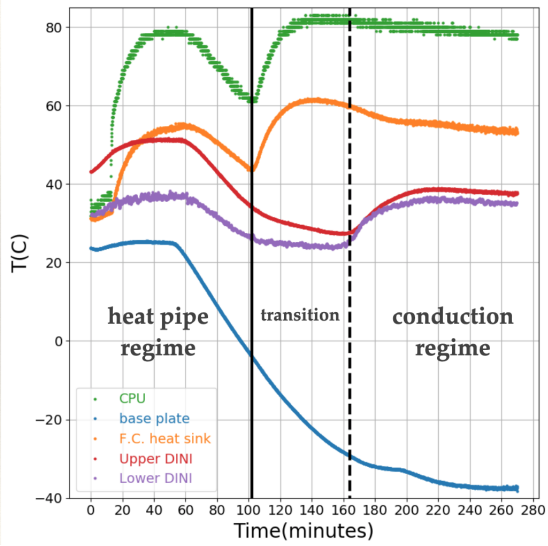

Figure 8.15: Motherboard and PCI merger (DINI) maximum temperatures as a function of the base plate temperature. There are 3 regimes that the setup stabilizes to depending on the base plate temperature as explained in the text. Overall, the temperature of the SFC stays within a reasonable range independent of the temperature of the base plate, a proxy for the gondola.

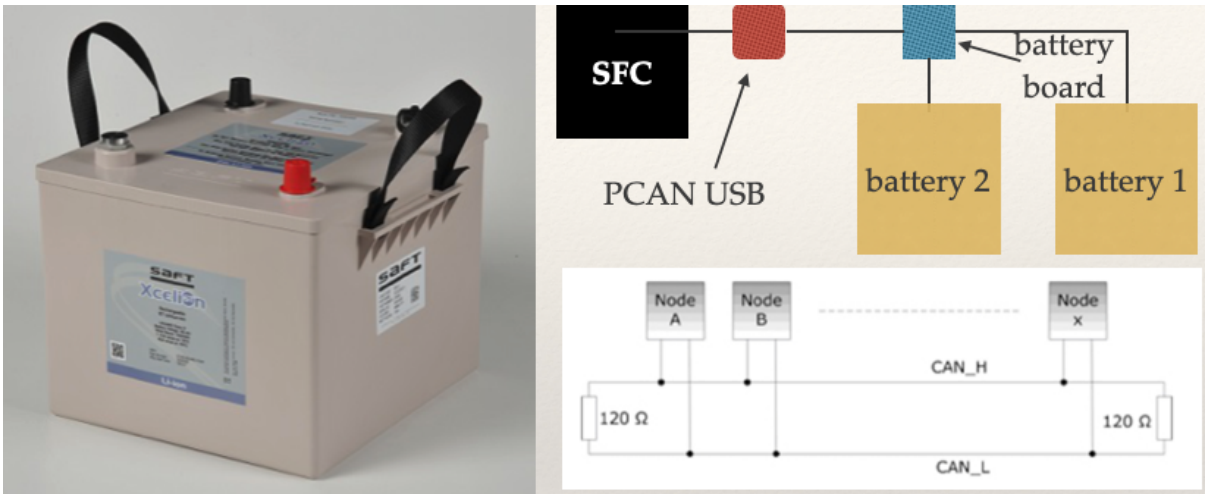

Figure 8.16: Left Panel: SAFT Battery used for the HELIX payload. Right Panel: Battery charge-discharge test in the vacuum chamber.

8.2.4 Payload Battery

In this section we try to figure out

1. How can we communicate with the battery during flight?

2. Can we get enough power out of two batteries before the solar panels get us extra power?

Battery communication

The Battery communicates over a 250kbps CAN bus, using a J1939 CAN 2.0B protocol. We have been able to successfully communicate with the battery by designing a board and writing code routines that are based on the CAN Bus communication protocol. Figure 8.16 shows the simple layout we used in order to communicate with 2 batteries.

Power requirements

We set the battery in the vacuum chamber to test whether:

1. the battery survives in the vacuum chamber

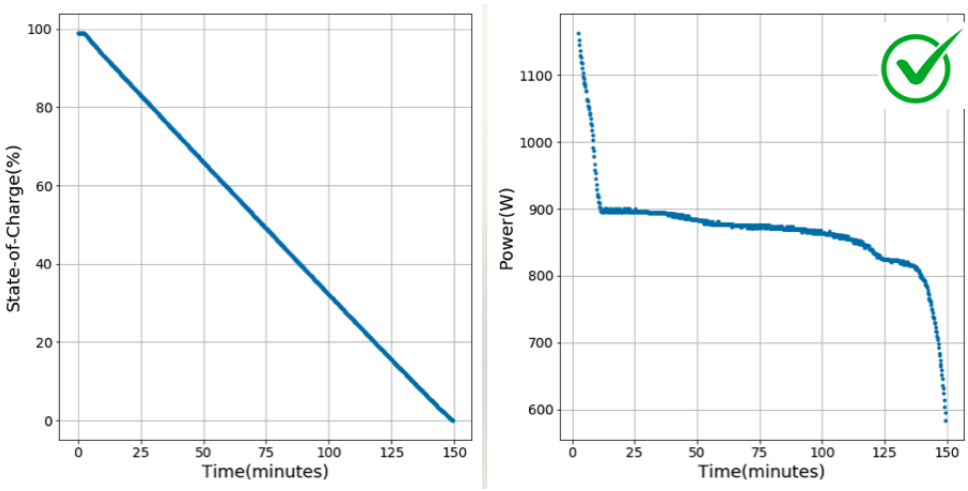

Figure 8.17: Battery discharge test in the vacuum chamber.

2. having two batteries meets the power requirements

Fortunately, we had no issues with the battery test in the chamber. As for the power requirements, we find that a single battery can sustain the payload for more than 2h if the power consumption does not exceed 750W as shown in Figure 8.17.

8.2.5 RICH Thermal Management

After initial thermal simulations, we found out that the RICH was getting too hot and needs to be cooled. Considering the location of the RICH within the gondola and the fact that we need to control the temperature quite well, we decided to use a liquid cooling circuit to transfer heat from the RICH to a radiator. We need to move an amount of heat Q between the RICH and the radiator.

In order to make a liquid cooling circuit, we need:

- a heat exchanger: Transfers heat from the source to the coolant
- a reservoir: coolant tank that contains the liquid to be circulated. The reservoir holds extra liquid to allow air bubbles to be replaced by the coolant as the liquid circulates
- a pump: connects to the reservoir and pumps the coolant

- a radiator: cools down the coolant inside the liquid loop. When the coolant runs through the tubing, the radiator absorbs heat from the coolant.
- tubing, fittings and a coolant

Calculations relevant for cooling pump

We use the following heat exchange formula to approximate the heat flow between the heater (RICH) and the liquid coolant:

$$Q_1 = \xi m_t C_p \Delta T \tag{8.10}$$

Where Q_1 is the heat dissipated by the RICH, ξ is the efficiency of heat transfer between the heater and the coolant, m_t is the rate at which the coolant mass is heated in units of $\frac{[mass]}{[time]}$, C_p the specific heat of the coolant, and ΔT is the temperature difference between the heater and the coolant (Here we assume $\Delta T \sim 1K$ as a minimum difference possible. Lower ΔTs enable us to test the worst case scenario because they result in a larger flow).

Power dissipated We can then calculate the coolant flow q that is needed to dissipate power Q_1. Since $q = m_t/\rho$ where ρ is the density of the coolant, we get:

$$q = \frac{Q_1}{\xi \rho C_p \Delta T} \tag{8.11}$$

We can also calculate the efficiency of the heat exchanger either empirically or through Newton's formula:

$$Q_N = UAD_T \tag{8.12}$$

where U is the heat transfer coefficient, A the area of contact, and D_T is the log temperature difference. Here we don't use Newton's formula for simplicity and just assume that $\xi = 0.9$.

Application to cooling system In addition to heat from the RICH, pumps also add hydraulic power P_h into the system such that:

$$P_h = q\rho gh \tag{8.13}$$

where q is the flow, g is the acceleration due to gravity and h is the head produced by the pump (basically the height to which it has to take up the coolant). So the total power dissipated is:

$$Q_T = Q_1(1 + \frac{gh}{\xi C_p \Delta T}) \tag{8.14}$$

Coolant The EBEX experiment successfully used Dynalene HC-40 in their experiment. We can use Dynalene HC-50 because it goes to lower temperatures (-X in HC-X represents the lowest temperature the coolant goes to). We can compare the heat transfer capability of Dynalene with other coolants in Figure 8.18.

Using the Thermophysical properties for Dynalene HC-50, we can compute the expected flow rate using equation 8.11 that we need in the liquid cooling system. The expected flow rate associated with this coolant is shown in Figure 8.19 as a function of the coolant temperature. Also shown below is the differential pressure associated with an exaggerated pump head of 4 meters (we are studying the worst case scenario).

With Dynalene HC-50, we can also compute the total heat that needs to be dissipated assuming that the RICH needs to dissipate Q_1 =20W in power. The hydraulic power only adds $\sim$ 1W to be dissipated. Overall, $Q_T \sim 21W$ (equation8.14).

Radiator The radiator area and emissivity determine the dissipated power. We also take into account that solar irradiance may play a role in heating the radiator.

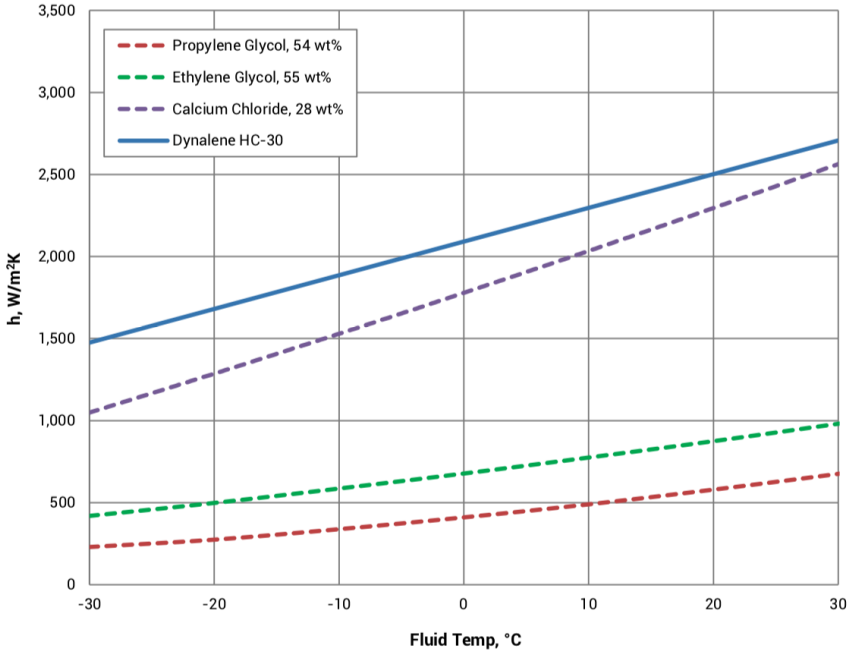

Figure 8.18: Heat transfer performance comparison of Dynalene HC-30 vs propylene glycol, ethylene glycol, and calcium chloride solutions with a coolant temperature $T = -40C$.

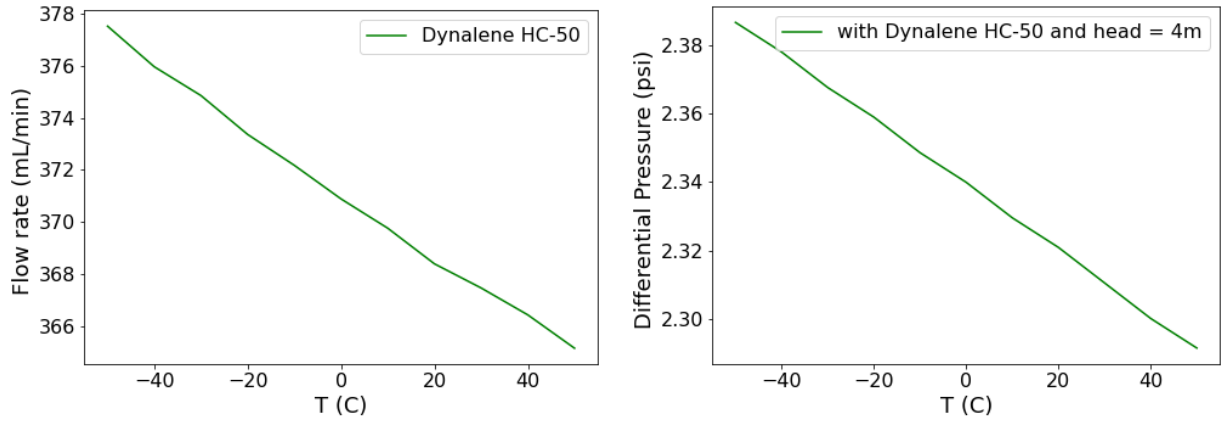

Figure 8.19: Left Panel: The expected flow rate associated with this coolant is as shown in Figure 8.19 as a function of the coolant temperature. Right Panel: Differential pressure associated with pump head.

Total power that needs to be dissipated by radiator:

$$Q_T = A_R \epsilon \sigma T_M^4 \tag{8.15}$$

where T_M is maximum temperature of the radiator due to heating from coolant, ϵ is the emissivity of the radiator, and A_R is the area of the radiator and for a painted aluminum radiator: $\epsilon = 0.8$ and $\Sigma = 0.2$.

$$A_R = \frac{Q_T}{\epsilon \sigma T_M^4} \tag{8.16}$$

In this model, the temperature T_M is unknown and is dependent on the heat provided from the coolant and the solar irradiance. Since we expect that the solar irradiance should not have much of an effect, we can assume that T_M is roughly the maximum temperature of the RICH at ~ 273K. Calculating A_R for the size of our radiator, we get $\sqrt{A_R} = 30$cm.

Pump The EBEX experiment successfully used a GJ-Series external gear pump from micropump.

Highlights:

1. Applications: Aerospace and Aircraft, Automotive, Biotechnology, Chemical Processing, Clinical and Analytical Lab, Electronics, Energy/Fuel...

2. perfect temp. range for HELIX

3. can sustain up to 80 psi in differential pressure

4. Compact, magnetically driven gear pump that features a cavity style design (Take a look at the appendix for an explanation) with no dynamic seals for applications that cannot tolerate leaks. It is chemically resistant, has smooth pumping and pulseless delivery.

5. Works with brushless motor

6. We can order it directly online.

We choose to use the GJ-N21 pump with specs specified in Figure 8.20. Assuming that we need a flow of 380mL/min (maximum calculated flow) or less and after looking at all the pumps that micropump offers, the GJ-N21-DEMSE with a performance graph in Figure 8.20 is a good fit. It offers the following advantages compared to other pumps:

1. For the differential pressure of our system (~ 2.5psi), the pump operates within the flow range we are interested in.

2. It offers the lowest power consumption (≈ 10W for water as a coolant) for a flow rate of 380 mL/min compared to the other models. A lower flow needs a lower power consumption(200 mL/min needs 5 W for 24Vdc). It is also possible to run the pump at a lower voltage (12V).

3. The external gear pump and the motor are already assembled (The pump the EBEX experiment used needed two separate components: an external gear and a drive).

A more complete list of the specs is available on the micropump website.

Peltier element We discuss the power needs of the different elements in the cooling system (pump+Peltier). The pump's DC Input is 12-36 V. The lowest voltage at 12V enables us the get the lowest flow which is closer to what we may need. At 24V, we draw 80mA and get double the lowest flow. Driving the pump with a lower voltage gives us more options (wattage closer to 1W).

We have chosen a Laird Peltier element with the following specs. To power and control the Peltier element, we can use the following thermoelectric cooling (TEC) controllers: TEC-1089-SV or TEC-1091 from Meerstetter.

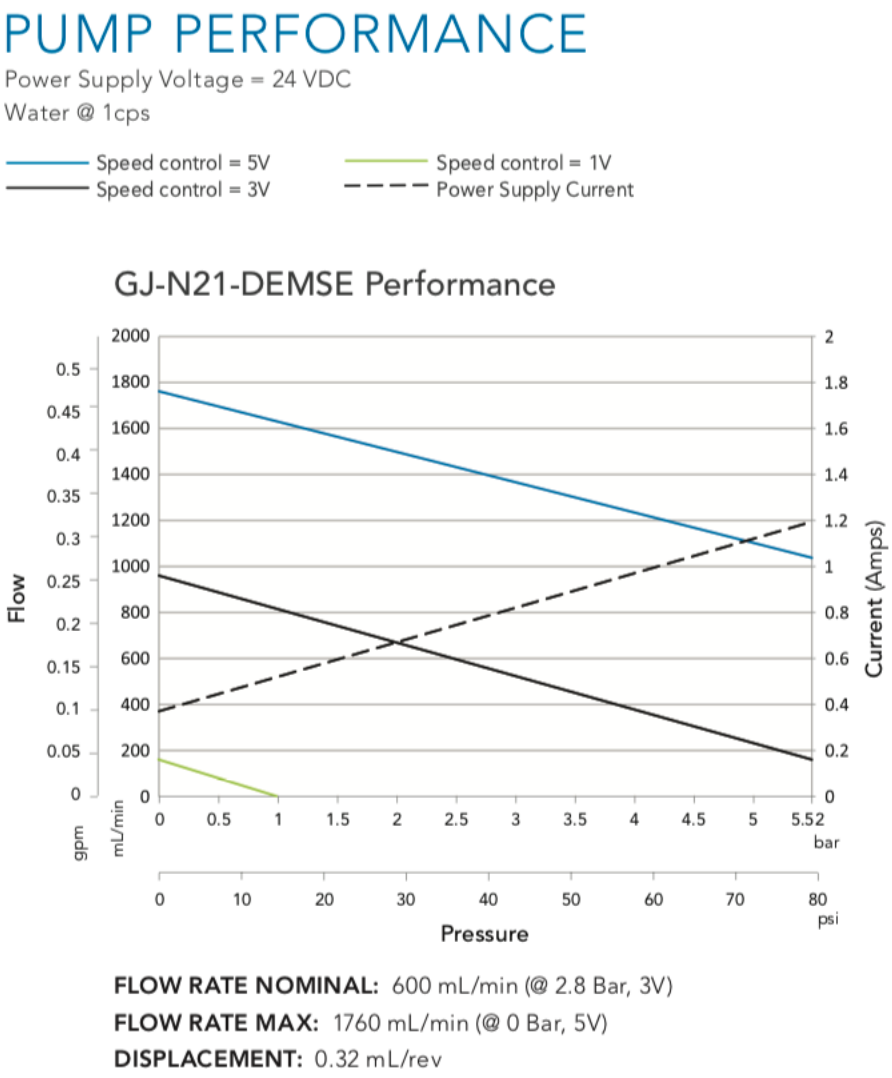

Figure 8.20: Left Panel: The expected flow rate associated with this coolant is as shown in Figure 8.19 as a function of the coolant temperature. Right Panel: Differential pressure associated with pump head.

Typical cooling power	**TEC-1091(±4 A/±21 V)**	**TEC-1089-SV(±10 A/±21 V)**
Typical cooling power	42 W	105 W
DC Input	5-24 V/4 A	12-24 V / 10 A
Bipolar Output	0-21V/±4 A	0-21 V/±10 A
Temp. Probe Input	NTC	NTC
Temp. Probe example	from Digikey	from Digikey
Communication	RS485, RS232 TTL, USB	RS485, USB
dimensions(mm)	65x38x14	75x 60x18

These TEC controllers can heat and cool. They can be remotely-controlled, script-controlled, or operated as a stand-alone unit. They can also be used as digitally controlled power supplies.

Power consumption:

Element	voltage (V)	Power consumption (W)	Remarks
Pump	12	0.72	maximum RPM: 1700
Pump	24	1.96	
Pump	28	2.8	
Launchpad+DAC	5	1.3	

Rich Thermal Design

Taking into account the above design considerations, we build a RICH cooling system based on the layout presented in Figure 8.21. A more detailed payout of the electronics is presented in Figure 8.22.

Based on the characteristics of our setup, we can simulate the temperature distribution on the focal plane. A heat map of the focal plane is provided in Figure 8.23 fo reference.

The final setup on the gondola is provided in Figure 8.24 and 8.25.

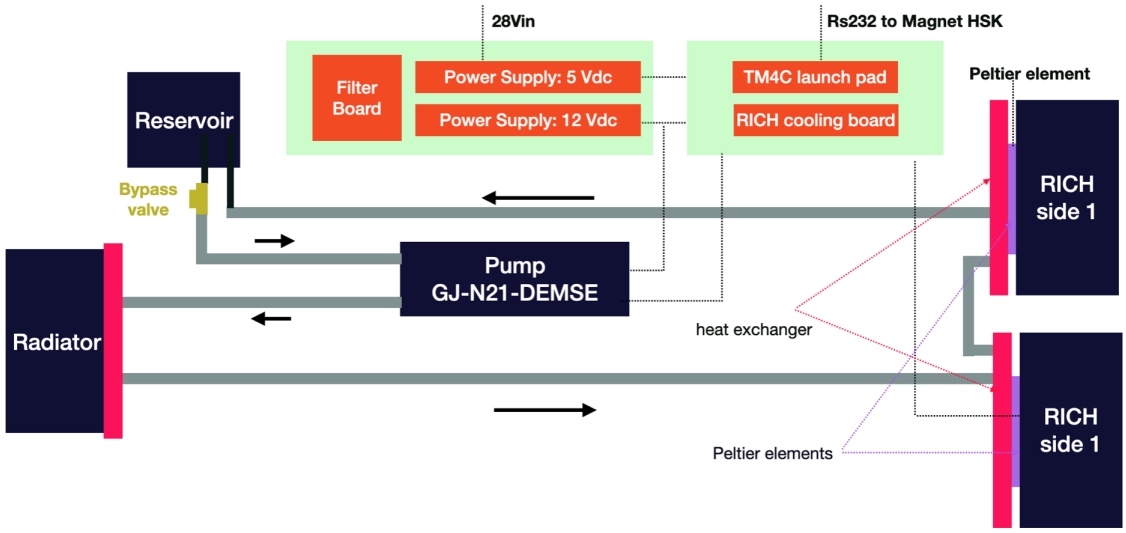

Figure 8.21: Layout of the thermal management setup of the RICH. The coolant flows through heat exchangers attached to Peltier elements on the RICH and then heat is radiated away through the radiator. The loop is controlled by self-designed electronics board and and a Thermo-electric cooler controller (Meerstetter® 1161-4A).

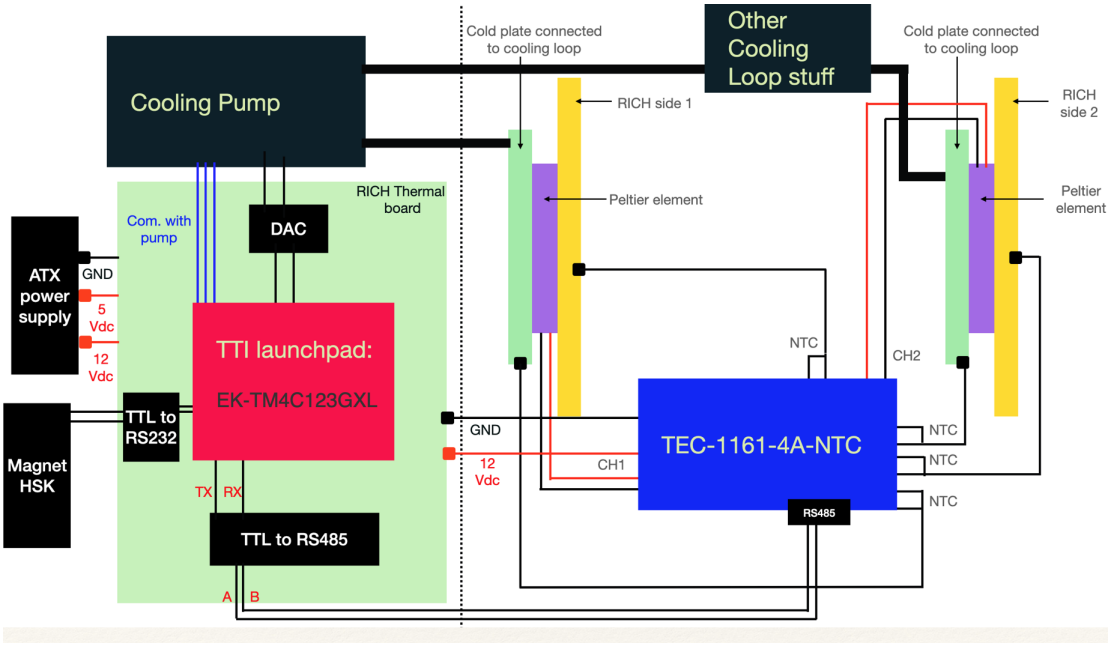

Figure 8.22: Same as Figure 8.21, but supplying more information on the electronics controlling the cooling pump and Peltier elements.

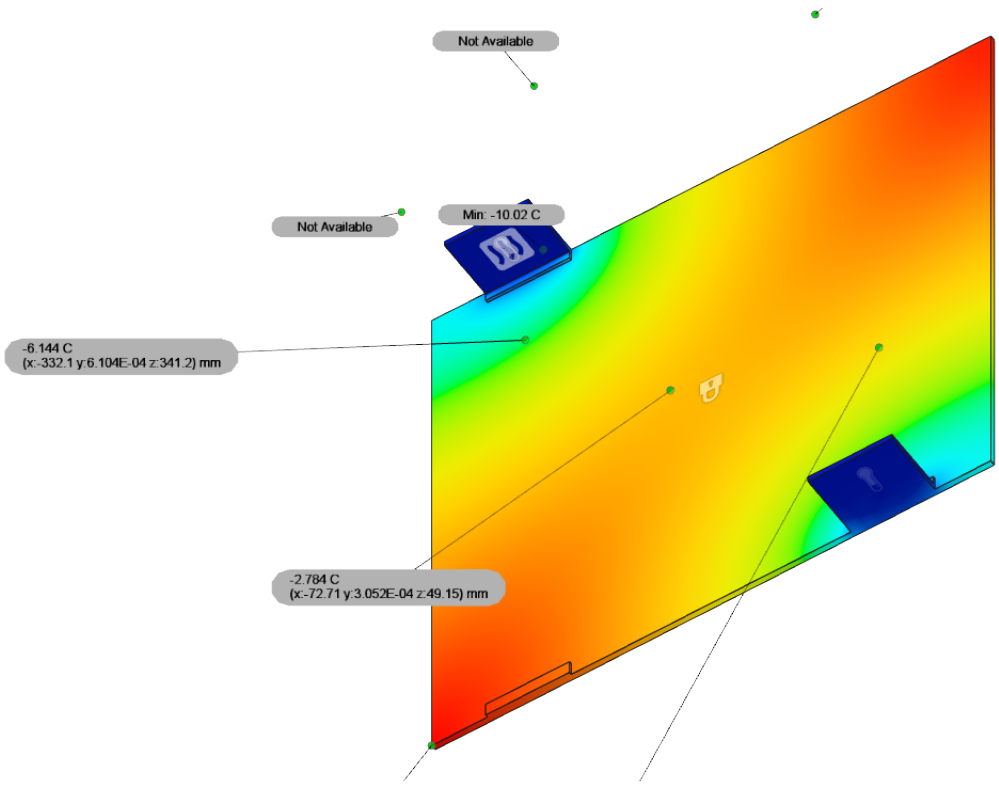

Figure 8.23: Simple Thermal simulation of the RICH focal plane if we have two heat exchangers on opposite sides.

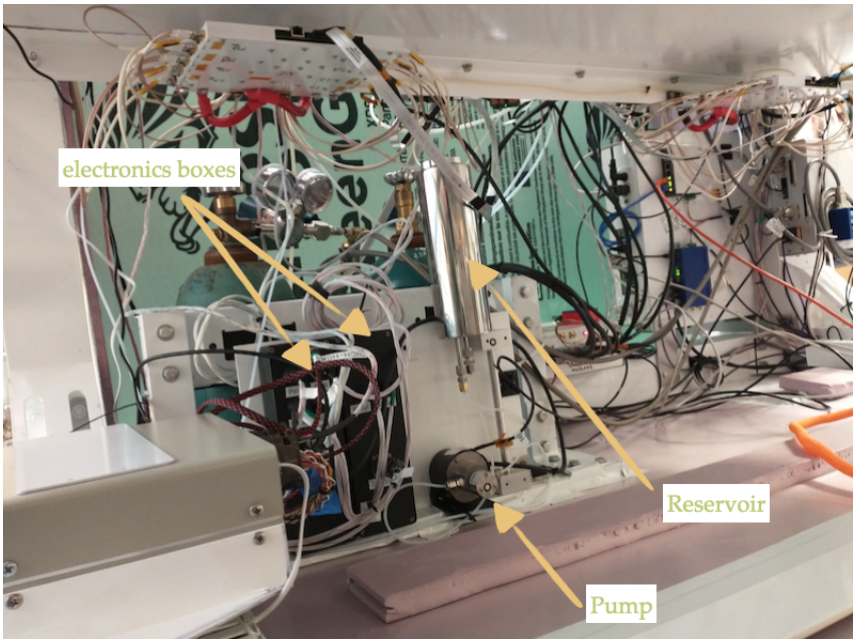

Figure 8.24: Final position of the RICH thermal management system on the gondola

Figure 8.25: Position of one of the RICH heat exchangers after assembling the payload.

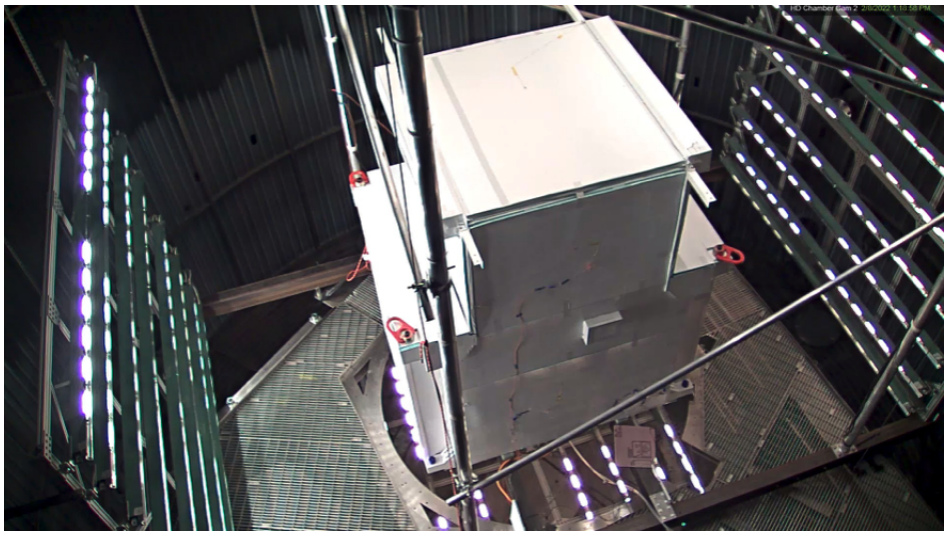

Figure 8.26: Assembled payload at NASA's Neil A. Armstrong Test Facility. Lamps mimicking the sun radiation are placed in the vacuum chamber, while cold walls mimic temperature expected at the payload altitude.

8.2.6 Payload Metrology

Measuring the coordinates of each subsystem in the payload within one generalized coordinate system is crucial for particle event reconstruction. After assembling the whole system in Antarctica, we need to measure the relative position of each subdetector with respect to the other components. In order to perform this task, we will use a total station and retro-reflectors placed on all of the subdetectors and make our measurements. In this memo, we will provide a quick and comprehensive tutorial on how to make quick measurements with the total station from different positions and how to use a computer code to move from one station (coordinate system) to another. Finally, we end up with one coordinate system that encompasses all of the points.

8.2.7 Total Station use: A quick tutorial

In this section, we provide a quick tutorial on how to use the total station. The total station has many features and options that enable us to map the positions of all of the detector subsystems. However, considering potential time constraints and potential mistakes associated with using the total station, we decided to use the simplest options available. In this case, we will measure the coordinates fo each point regardless of the coordinate system. Then, we will perform coordinate transformations afterwards.

8.2.8 Measurements

Coordinate Transformation

The goal of these transformations is to simplify and expedite the use of the total station in Antarctica while measuring the coordinates of different components relative to one another.

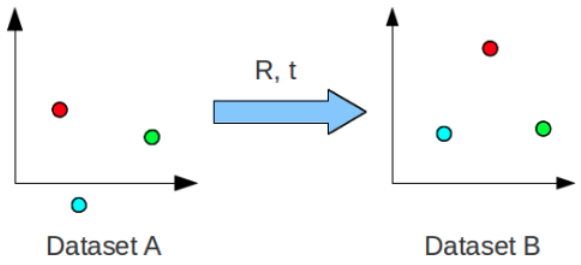

Figure 8.27: Cartoon showing the overall transformation that needs to be performed.

These are the main steps that will be facilitated:

1. Make n coordinate measurements from one station
2. Move to another station and measure the coordinates of at least 3 points from the initial measurement. Save these points
3. Make your measurements within the new station
4. Use the computer code to get the transformation (rotation+translation) associated with moving from one coordinate system to the other
5. Apply the transformation and now you have everything in the same coordinate system.
6. Repeat

Transformation: the basics We want to find the rotation R and transformation t that describe the rotation and translation we made using the total station. we make the same 3 point measurements with two different stations each time to enable us to make the coordinate transformation. This is equivalent to a translation+rotation transformation as shown in Figure 8.27.

First, as in Figure 8.28, we define a centroid (central point) and move points according to this point. By demeaning our data, we are effectively moving the

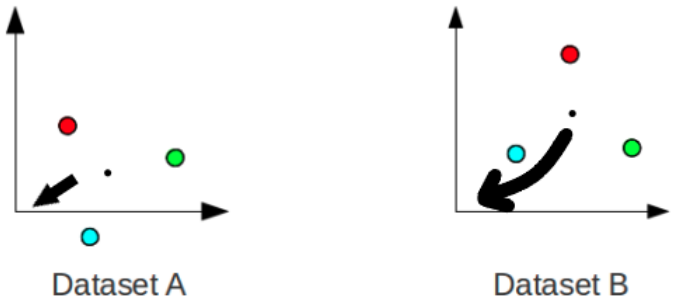

Figure 8.28: Cartoon showing the centroid transformation.

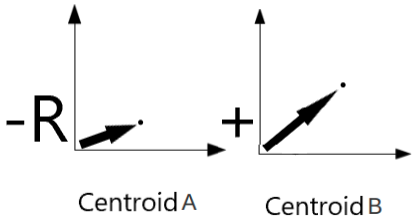

Figure 8.29: 3D vectoral picture represents the translation, $t = -R\text{centroid}_\text{A} + \text{centroid}_\text{B}$. We now have R and t from our original diagram.

centroid (black point) to the origin. Using some arbitrary rotations of the original picture for visual effect, we now use Singular Value Decomposition (SVD), a decomposition method that reduces a matrix to its constituent parts, to find the 3D rotation matrix that maps one set of these points to the other. At the end of this stage, we only need the translation. (N.B. The algorithm also checks the determinant to ensure handedness remains the same.)

All that's left is to apply the rotation matrix R that we just got from SVD to the centroid of dataset A, and rearrange $RA + t = B$ with centroids, solving for the translation t. Note: we apply these to centroids to make t a column vector, e.g.

$$t = \begin{bmatrix} 10 \\ 3.8 \\ 7 \end{bmatrix}$$

We have thus found R and t, the rotation and translation matrices that define

our coordinate transform. To check our work, we can use these matrices to see that for each point i, $RA_i + t = B_i$ for noiseless data, or print the results of $RA_i + t - B_i$, which should be very close to 0 ($\sim 10^{-15}$ in the Jupyter Notebook example). For a more robust check, the testing software computes the Root Mean Square Error, with the arbitrarily chosen threshold RMSE$< 10^{-5}$.

The Python Computer code We provide a python notebook that provides a user tutorial for determining the optimal rotation and translation of 3D points from one coordinate system to another, useful for total station measurements.

The concepts were originally outlined in this page. The main function and testing code were also written by the same individual who outlined the concepts.

8.2.9 Results

After applying the steps described above, we find that:

1. On average, a 1 meter increase in the physical distance between 2 points in real space (d_{meas} in Figures) leads to a $\sim 0.3\%$ increase in fractional uncertainty.

2. For points 2 meters away, the fractional uncertainty will on average be 0.2%.

3. All fractional uncertainties are within 1 percent.

Figure 8.30 reiterate these claims. Our results are valid for:

1. Multiple reference frames (making measurements with total station in multiple positions) between 4 and 8 meters away from the points.

2. Spacing between points on the order of 1 meter.

We also find no sign of increasing error with multiple transforms. Our next steps involve:

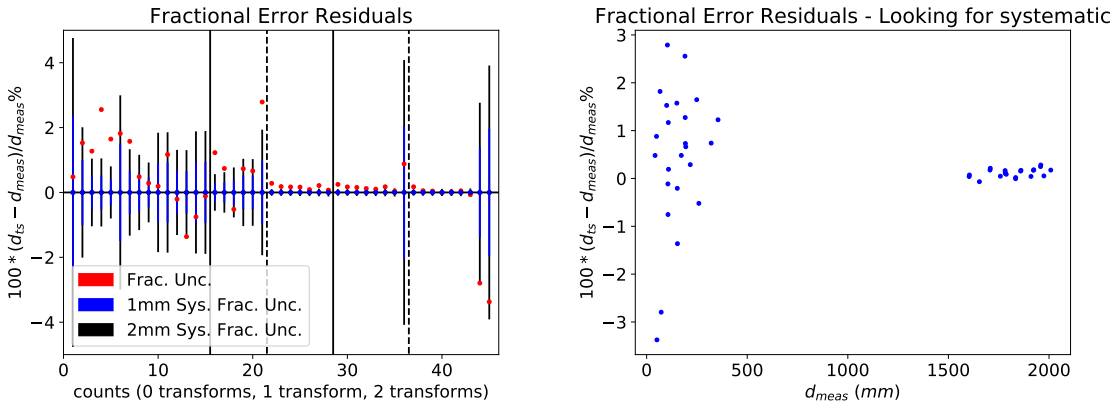

Figure 8.30: Fractional Uncertainty through: transforms, aka moving total station (left), and physical space (right). Credit: Nial Coffey

OLS Regression Results

Dep. Variable:	y	R-squared:	0.188
Model:	OLS	Adj. R-squared:	0.145
Method:	Least Squares	F-statistic:	4.397
Date:	Wed, 16 Sep 2020	Prob (F-statistic):	0.0496
Time:	09:31:46	Log-Likelihood:	23.886
No. Observations:	21	AIC:	-43.77
Df Residuals:	19	BIC:	-41.68
Df Model:	1		
Covariance Type:	nonrobust		

	coef	std err	t	P>|t|	[0.025	0.975]
const	-0.4649	0.278	-1.673	0.111	-1.046	0.117
x1	0.3195	0.152	2.097	0.050	0.001	0.638

Figure 8.31: Example of Linear Regression Output

1. Analyzing data recorded on payload.

2. Writing an instructional tutorial so anyone can use the total station and Python script to make measurements.

3. Testing accessibility of tutorial through an undergraduate user without knowledge of this.

4. Use a 3D handheld distance scanner to compare results with.

Part IV

Conclusions

Chapter 9

Thesis Summary

During my PhD, I have acquired the required independence to improve my research skills, and implement my own ideas with valuable help from my advisors and colleagues. I have been trained in an uncommon way especially that I have combined theoretical and experimental work. Overall, I have attempted to answer the following outstanding questions in astrophysics:

- How are UHECRs accelerated? Where do they come from?
- Where do the highest energy neutrinos come from?
- What is the confinement time of CRs in the galaxy? Can we devise a generic way of computing the delay of CR propagation?
- What are the main properties of relativistic magnetic reconnection? What are the astrophysical implications of our results?

In doing so, I have combined plasma physics, high energy astrophysics, and experimental physics. The main conclusions pertaining to each question are discussed in detail in each relevant section.

My aim going forward is to have a comprehensive—and more importantly falsifiable—theoretical framework that combines data from x/γ-ray observatories,

neutrino experiments, and UHECR detectors to enable a much-needed modeling refinement in High-Energy Astrophysics and beyond. It could potentially relate physics on the kinetic scales in AGN jets to detectable data. Considering their relative simplicity and convincing testability, my current and future projects can have a long-lasting impact for future experiments, as they offer a holistic approach to predicting multi-messenger signals.

References

Aab, A., Abreu, P., Aglietta, M., et al. 2014a, PhRvD, 90, 122005

—. 2014b, PhRvD, 90, 122006

Aab, A., Abreu, P., Aglietta, M., et al. 2017a, Science, 357, 1266

—. 2017b, PhRvD, 96, 122003

—. 2017c, JCAP, 2017, 038

—. 2018a, ApJ, 868, 4

—. 2018b, The Astrophysical Journal, 853, L29

—. 2020, Phys. Rev. Lett., 125, 121106

Aartsen, M., Ackermann, M., Adams, J., et al. 2018a, Science, 361, 147

—. 2018b, Science, 361

Aartsen, M. G., Ackermann, M., Adams, J., et al. 2019, PhRvD, 100, 082002

Aartsen, M. G., Ackermann, M., Adams, J., et al. 2019, Phys. Rev. D, 100, 082002

Abbasi, R., Bellido, J., Belz, J., et al. 2015, ArXiv e-prints. https://arxiv.org/abs/1503.07540

Abbasi, R. U., Abu-Zayyad, T., Allen, M., et al. 2008, PhRvL, 100, 101101

Abbasi et al., R. U. 2014, ApJ Lett., 790, L21

Achterberg, A., Gallant, Y. A., Kirk, J. G., & Guthmann, A. W. 2001, MNRAS, 328, 393

Ackermann et al., M. 2013, Science, 339, 807

Adriani, O., Barbarino, G. C., Bazilevskaya, G. A., et al. 2011, Science, 332, 69

Agudo, I., Gómez, J.-L., Martí, J.-M., et al. 2001, ApJ, 549, L183

Aguilar, M., Aisa, D., Alpat, B., et al. 2015, PhRvL, 114, 171103

Aguilar, M., Ali Cavasonza, L., Ambrosi, G., et al. 2016, Phys. Rev. Lett., 117, 231102

Aharonian, F. A., Belyanin, A. A., Derishev, E. V., Kocharovsky, V. V., & Kocharovsky, V. V. 2002, PhRvD, 66, 023005

Ahlers, M., & Halzen, F. 2017, Progress of Theoretical and Experimental Physics, 2017

Ahn, H. S., Allison, P., Bagliesi, M. G., et al. 2010, The Astrophysical Journal, 714, L89

Ajello, M., Romani, R. W., Gasparrini, D., et al. 2013, The Astrophysical Journal, 780, 73

Alfaro, R., Alvarez, C., Álvarez, J. D., et al. 2017, PhRvD, 96, 122001

Allison, P., Auffenberg, J., Bard, R., et al. 2012, Astroparticle Physics, 35, 457

Allison, P., Bard, R., Beatty, J. J., et al. 2016, Phys. Rev. D, 93, 082003

Aloisio, R., Berezinsky, V., & Blasi, P. 2014a, JCAP, 10, 20

—. 2014b, JCAP, 10, 20

Aloisio, R., Berezinsky, V., & Gazizov, A. 2011, APh, 34, 620

Alves Batista, R., & Saveliev, A. 2021, Universe, 7

Alves Batista, R., Dundovic, A., Erdmann, M., et al. 2016, JCAP, 2016, 038

Amano, T., Torii, K., Hayakawa, T., & Fukui, Y. 2011, Publications of the Astronomical Society of Japan, 63, L63

Amato, E. 2014, International Journal of Modern Physics D, 23, 1430013

Amenomori, M., Bi, X. J., Chen, D., et al. 2008, ApJ, 678, 1165

An, Q., Asfandiyarov, R., Azzarello, P., et al. 2019, Science Advances, 5, eaax3793

Anchordoqui, L. A. 2019, Physics Reports, 801, 1

Anchordoqui, L. A., Beacom, J. F., Goldberg, H., Palomares-Ruiz, S., & Weiler, T. J. 2007, PhRvD, 75, 063001

Apel, W., Arteaga-Velázquez, J., Bekk, K., et al. 2013a, Astroparticle Physics, 47, 54

Apel, W. D., Arteaga-Velàzquez, J. C., Bekk, K., et al. 2013b, Phys. Rev. D, 87, 081101

Araudo, A. T., Bell, A. R., Blundell, K. M., & Matthews, J. H. 2018, MNRAS, 473, 3500

Archer, A., Benbow, W., Bird, R., et al. 2018, PhRvD, 98, 062004

Arons, J. 2012, Space Science Reviews, 173, 341

Arshakian, T. G., & Longair, M. S. 2004, MNRAS, 351, 727

Baldi, R. D., Capetti, A., & Giovannini, G. 2018, MNRAS, 482, 2294

Baldi, R. D., Capetti, A., & Massaro, F. 2018, A&A, 609, A1

Ball, D., Sironi, L., & Özel, F. 2018, ApJ, 862, 80

Bartoli, B., Bernardini, P., Bi, X. J., et al. 2015, Phys. Rev. D, 92, 092005

Barwick, S., Besson, D., Burgman, A., et al. 2017, Astroparticle Physics, 90, 50

Batista, R. A., de Almeida, R. M., Lago, B., & Kotera, K. 2019, Journal of Cosmology and Astroparticle Physics, 2019, 002

Begelman, M. C., Blandford, R. D., & Rees, M. J. 1984, Reviews of Modern Physics, 56, 255

Bell, A. R. 1978, MNRAS, 182, 147

Bell, A. R., Araudo, A. T., Matthews, J. H., & Blundell, K. M. 2018, MNRAS, 473, 2364

Bell, A. R., Schure, K. M., Reville, B., & Giacinti, G. 2013, MNRAS, 431, 415

Berezhko, E. G., & Völk, H. J. 2007, ApJL, 661, L175

Berezinsky, V., Gazizov, A., & Grigorieva, S. 2006, Phys. Rev. D, 74, 043005

Bertaina, M., Apel, W. D., Arteaga-Velázquez, J. C., et al. 2015, in International Cosmic Ray Conference, Vol. 34, 34th International Cosmic Ray Conference (ICRC2015), 359

Bessho, N., & Bhattacharjee, A. 2012, ApJ, 750, 129

Best, P. N., von der Linden, A., Kauffmann, G., Heckman, T. M., & Kaiser, C. R. 2007, MNRAS, 379, 894

Biermann, P. L., & Strittmatter, P. A. 1987, ApJ, 322, 643

Birdsall, C. K., & Langdon, A. B. 1991a, Plasma Physics via Computer Simulation (CRC Press)

—. 1991b, Plasma Physics via Computer Simulation (CRC Press)

Birn, J., Borovsky, J. E., Hesse, M., & Schindler, K. 2010, Physics of Plasmas, 17, 052108

Blackman, E. G., & Field, G. B. 1994, Phys. Rev. Lett., 72, 494

Blandford, R., Meier, D., & Readhead, A. 2019, ARA&A, 57, 467

Blandford, R., Simeon, P., & Yuan, Y. 2014, Nuclear Physics B Proceedings Supplements, 256, 9

Blandford, R. D., & Ostriker, J. P. 1978, ApJL, 221, L29

Blasi, P. 2013, A&A Rv, 21, 70

Blasi, P., & Amato, E. 2012a, JCAP, 1, 10

—. 2012b, JCAP, 1, 11

Blasi, P., Amato, E., & Caprioli, D. 2007, MNRAS, 375, 1471

Blasi, P., Amato, E., & Serpico, P. D. 2012, Physical Review Letters, 109, 061101

Blasi, P., Burles, S., & Olinto, A. V. 1999, The Astrophysical Journal, 514, L79

Blum, K. 2011, Journal of Cosmology and Astro-Particle Physics, 2011, 037

Borisova, E., Cantalupo, S., Lilly, S. J., et al. 2016, The Astrophysical Journal, 831, 39

Bosman, S. E. I., Kakiichi, K., Meyer, R. A., et al. 2020, The Astrophysical Journal, 896, 49

Bromberg, O., & Tchekhovskoy, A. 2016, MNRAS, 456, 1739

Buck, T., Pfrommer, C., Pakmor, R., Grand, R. J. J., & Springel, V. 2019, arXiv e-prints, arXiv:1911.00019. https://arxiv.org/abs/1911.00019

Budnev, N. M., Chiavassa, A., Gress, O. A., et al. 2020, Astroparticle Physics, 117, 102406

Buneman, O. 1993, Computer Space Plasma Physics: Simulation Techniques and Software (ed. H. Matsumoto & Y. Omura (Tokyo: Terra Scientific))

Burch, J. L., Torbert, R. B., Phan, T. D., et al. 2016, Science, 352, aaf2939

Bustard, C., Zweibel, E. G., & Cotter, C. 2017, ApJ, 835, 72

Caprioli, D. 2011, JCAP, 5, 26

—. 2012, JCAP, 7, 38

—. 2015a, ApJL, 811, L38

—. 2015b, ApJL, 811, L38

Caprioli, D. 2018, Nuclear and Particle Physics Proceedings, 297-299, 226

Caprioli, D., Amato, E., & Blasi, P. 2010a, APh, 33, 160

—. 2010b, APh, 33, 160

Caprioli, D., Blasi, P., & Amato, E. 2011, APh, 34, 447

Caprioli, D., & Spitkovsky, A. 2014, ApJ, 783, 91

Caprioli, D., Yi, D. T., & Spitkovsky, A. 2017, Phys. Rev. Lett., 119, 171101

Caprioli, D., Yi, D. T., & Spitkovsky, A. 2017, PhRvL, 119, 171101

Cardillo, M., Amato, E., & Blasi, P. 2015, Astroparticle Physics, 69, 1

Carilli, C. L., & Taylor, G. B. 2002, Annual Review of Astronomy and Astrophysics, 40, 319

Casandjian, J., & Grenier, I. A. 2008, A&A, 489, 849

Cassak, P. A., & Shay, M. A. 2007, Physics of Plasmas, 14, 102114

Cassak, P. A., & Shay, M. A. 2008, Geophys. Res. Lett., 35, L19102

Casse, F., Lemoine, M., & Pelletier, G. 2001, Phys. Rev. D, 65, 023002

Cavallo, G. 1978, A&A, 65, 415

Cerutti, B., Uzdensky, D. A., & Begelman, M. C. 2012, ApJ, 746, 148

Cerutti, B., Werner, G. R., Uzdensky, D. A., & Begelman, M. C. 2013, ApJ, 770, 147

—. 2014a, Physics of Plasmas, 21, 056501

—. 2014b, ApJ, 782, 104

Chapman, S., Cowling, T., Burnett, D., & Cercignani, C. 1990, The Mathematical Theory of Non-uniform Gases: An Account of the Kinetic Theory of Viscosity, Thermal Conduction and Diffusion in Gases, Cambridge Mathematical Library (Cambridge University Press)

Chiaberge, M., Capetti, A., & Celotti, A. 2001, MNRAS, 324, L33

Cholis, I., & Hooper, D. 2013, Phys. Rev. D, 88, 023013

Clarke, T. E., Kronberg, P. P., & Böhringer, H. 2001, The Astrophysical Journal, 547, L111

Comisso, L., & Sironi, L. 2018, PhRvL, 121, 255101

—. 2019, ApJ, 886, 122

Connell, J. J. 1998, ApJ, 501, L59

Contopoulos, I., & Kazanas, D. 1998, ApJ, 508, 859

Das, S., Razzaque, S., & Gupta, N. 2019, Phys. Rev. D, 99, 083015

Delahaye, T., & Grefe, M. 2013, Journal of Cosmology and Astro-Particle Physics, 2013, 045

Delahaye, T., Lavalle, J., Lineros, R., Donato, F., & Fornengo, N. 2010, A&A, 524, A51

Dembinski, H., Engel, R., Fedynitch, A., et al. 2017, International Cosmic Ray Conference, 35, 533. https://arxiv.org/abs/1711.11432

Dembinski, H. P., Arteaga-Velázquez, J. C., Cazon, L., et al. 2019, in European Physical Journal Web of Conferences, Vol. 210, European Physical Journal Web of Conferences, 02004

Dermer, C. D. 2007, ArXiv e-prints. https://arxiv.org/abs/0711.2804

Dermer, C. D., Murase, K., & Inoue, Y. 2014, Journal of High Energy Astrophysics, 3-4, 29

Engelmann, J. J., Ferrando, P., Soutoul, A., et al. 1990, A&A, 233, 96

et al., A. 2008, Astroparticle Physics, 30, 133

—. 2014, Phys. Rev. Lett., 113, 121102

—. 2019, Phys. Rev. Lett., 122, 041102

et al., B. 1997, Nuclear Instruments and Methods in Physics Research Section A: Accelerators, Spectrometers, Detectors and Associated Equipment, 400, 34

et al., H. 2004, ApJ, 611, 892

Evoli, C., Gaggero, D., Grasso, D., & Maccione, L. 2008, JCAP, 2008, 018

Evoli, C., Morlino, G., Blasi, P., & Aloisio, R. 2019, arXiv e-prints, arXiv:1910.04113. https://arxiv.org/abs/1910.04113

Fanaroff, B. L., & Riley, J. M. 1974, MNRAS, 167, 31P

Fang, K., Kotera, K., & Olinto, A. V. 2012, ApJ, 750, 118

Fang, K., & Murase, K. 2018a, Nature Physics, 14, 396

—. 2018b, Nature Physics, 14, 396

Farrar, G. R., & Gruzinov, A. 2009, The Astrophysical Journal, 693, 329

Farrar, G. R., & Piran, T. 2014a, arXiv e-prints. https://arxiv.org/abs/1411.0704

—. 2014b, arXiv e-prints. https://arxiv.org/abs/1411.0704

Fermi, E. 1949, Physical Review, 75, 1169

—. 1954, Ap. J., 119, 1

Ferrarese, L., Mould, J. R., Stetson, P. B., et al. 2007, The Astrophysical Journal, 654, 186

Finke, J. D., Reyes, L. C., Georganopoulos, M., et al. 2015, The Astrophysical Journal, 814, 20

Forman, M. A., & Gleeson, L. J. 1975, Ap&SS, 32, 77

Furlanetto, S. R., & Loeb, A. 2001, The Astrophysical Journal, 556, 619

Gaisser, T. K., Engel, R., & Resconi, E. 2016, Cosmic Rays and Particle Physics, 2nd edn. (Cambridge University Press)

Gaisser, T. K., Stanev, T., & Tilav, S. 2013, Frontiers of Physics, 8, 748

Garofalo, D., & Singh, C. B. 2019, The Astrophysical Journal, 871, 259

Ghisellini, G., Tavecchio, F., & Chiaberge, M. 2005, A&A, 432, 401

Ghisellini, G., Tavecchio, F., Foschini, L., et al. 2010, Monthly Notices of the Royal Astronomical Society, 402, 497

Ghisellini, G., Tavecchio, F., & Ghirlanda, G. 2009, MNRAS, 399, 2041

Ghisellini, G., Tavecchio, F., Maraschi, L., Celotti, A., & Sbarrato, T. 2014, Nature, 515, 376

Giacalone, J., & Jokipii, J. R. 1999, The Astrophysical Journal, 520, 204

Giannios, D. 2010, MNRASL, 408, L46

Giannios, D., Uzdensky, D. A., & Begelman, M. C. 2009, MNRAS, 395, L29

Giovannini, G., Cotton, W. D., Feretti, L., Lara, L., & Venturi, T. 2001, ApJ, 552, 508

Gorham, P. W., Allison, P., Banerjee, O., et al. 2018a, Phys. Rev. D, 98, 022001

Gorham, P. W., Rotter, B., Allison, P., et al. 2018b, Phys. Rev. Lett., 121, 161102

Govoni, F., Markevitch, M., Vikhlinin, A., et al. 2004, The Astrophysical Journal, 605, 695

Granger, D. E., Lifton, N. A., & Willenbring, J. K. 2013, Geological Society of America Bulletin, 125, 1379

Grebenyuk, V., Karmanov, D., Kovalev, I., et al. 2019, Advances in Space Research, 64, 2546

Greisen, K. 1966, Physical Review Letters, 16, 748

Guo, F., Li, H., Daughton, W., & Liu, Y.-H. 2014, PhRvL, 113, 155005

Guo, F., Liu, Y.-H., Daughton, W., & Li, H. 2015, ApJ, 806, 167

Haggerty, C. C., Parashar, T. N., Matthaeus, W. H., et al. 2017, Physics of Plasmas, 24, 102308

Haggerty, C. C., Shay, M. A., Chasapis, A., et al. 2018, Physics of Plasmas, 25, 102120

Haiman, Z., & Hui, L. 2001, The Astrophysical Journal, 547, 27

Harari, D., Mollerach, S., & Roulet, E. 2021, PhRvD, 103, 023012

Hardcastle, M. J., Cheung, C. C., Feain, I. J., & Stawarz, Ł. 2009, MNRAS, 393, 1041

Hardcastle, M. J., Harris, D. E., Worrall, D. M., & Birkinshaw, M. 2004, The Astrophysical Journal, 612, 729

Hardcastle, M. J., Lenc, E., Birkinshaw, M., et al. 2016, MNRAS, 455, 3526

Hardcastle, M. J., Williams, W. L., Best, P. N., et al. 2019, A&A, 622, A12

Hardee, P. E. 2000, ApJ, 533, 176

Harding, J. P., & Abazajian, K. N. 2012, Journal of Cosmology and Astroparticle Physics, 2012, 026

Harris, D. E., & Krawczynski, H. 2006a, ARA&A, 44, 463

—. 2006b, ARA&A, 44, 463

Hawley, J. F., Fendt, C., Hardcastle, M., Nokhrina, E., & Tchekhovskoy, A. 2015, Space Sci. Rev., 191, 441

Heinze, J., Boncioli, D., Bustamante, M., & Winter, W. 2016, The Astrophysical Journal, 825, 122

Heinze, J., Fedynitch, A., Boncioli, D., & Winter, W. 2019, The Astrophysical Journal, 873, 88

Hesse, M., Neukirch, T., Schindler, K., Kuznetsova, M., & Zenitani, S. 2011, Space Sci. Rev., 160, 3

Hillas, A. 1967, Physics Letters A, 24, 677

Hillas, A. M. 1984, Ann. Rev. of A&A, 22, 425

—. 2005, Journal of Physics G Nuclear Physics, 31, 95

Hopkins, P. F., Hernquist, L., Martini, P., et al. 2005, ApJL, 625, L71

Hörandel, J. R. 2005, astro-ph/0508014

Hörandel et al., J. R. 2006, Journal of Physics Conference Series, 39, 463

Huan, H., Weisgarber, T., Arlen, T., & Wakely, S. P. 2011, ApJL, 735, L28

Inoue, Y., & Totani, T. 2009, ApJ, 702, 523

Inoue, Y., Totani, T., & Mori, M. 2010, PASJ, 62, 1005

Iroshnikov, P. S. 1964, Soviet Astronomy, 7, 566

Jansson, R., & Farrar, G. R. 2012, ApJL, 761, L11

Jaroschek, C. H., Lesch, H., & Treumann, R. A. 2004, ApJL, 605, L9

Ji, S., Chan, T. K., Hummels, C. B., et al. 2019, arXiv e-prints, arXiv:1909.00003. https://arxiv.org/abs/1909.00003

Jiang, L., Fan, X., Ivezić, Ž., et al. 2007, ApJ, 656, 680

Jokipii, J. R. 1966, ApJ, 146, 480

Jones, F. C., & Ellison, D. C. 1991, Space Science Reviews, 58, 259

Jui, C. 2016, PoS, ICRC2015, 035

Kadler, M., Krauß, F., Mannheim, K., et al. 2016, Nature Physics, 12, 807

Kagan, D., Milosavljević, M., & Spitkovsky, A. 2013, ApJ, 774, 41

Kagan, D., Sironi, L., Cerutti, B., & Giannios, D. 2015, Space Sci. Rev., 191, 545

Kalli, S., Lemoine, M., & Kotera, K. 2011, A&A, 528, A109

Kampert, K.-H., & Unger, M. 2012, Astroparticle Physics, 35, 660

Kang, H., Ryu, D., & Jones, T. W. 1996, ApJ, 456, 422

Katz, B., Waxman, E., Thompson, T., & Loeb, A. 2013, ArXiv e-prints. https://arxiv.org/abs/1311.0287

Kelner, S. R., Aharonian, F. A., & Bugayov, V. V. 2006, Phys. Rev. D, 74, 034018

Kim, K. T., Tribble, P. C., & Kronberg, P. P. 1991, ApJ, 379, 80

Kimura, S. S., Murase, K., & Zhang, B. T. 2018, PhRvD, 97, 023026

Kirkman, D., & Tytler, D. 2008, Monthly Notices of the Royal Astronomical Society, 391, 1457

Kissmann, R. 2014, Astroparticle Physics, 55, 37–50

Kolmogorov, A. 1941, Akademiia Nauk SSSR Doklady, 30, 301

Kotera, K., & Olinto, A. V. 2011, ARA&A, 49, 119

Kraichnan, R. H. 1965, Physics of Fluids, 8, 1385

Krauss-Varban, D., Karimabadi, H., & Omidi, N. 1999, Geophys. Res. Lett., 26, 1235

Kronberg, P. P., Kothes, R., Salter, C. J., & Perillat, P. 2007, ApJ, 659, 267

Kulsrud, R. M., & Zweibel, E. G. 2008, Reports on Progress in Physics, 71, 046901

Kun, E., Bartos, I., Tjus, J. B., et al. 2021, The Astrophysical Journal Letters, 911, L18

Letaw, J. R., Silberberg, R., & Tsao, C. H. 1983, ApJS, 51, 271

Lichnerowicz, A. 1967, Relativistic Hydrodynamics and Magnetohydrodynamics (W.A. Benjamin, Inc, San Francisco)

Lipari, P. 2019, arXiv e-prints. https://arxiv.org/abs/1902.06173

—. 2022, arXiv e-prints, arXiv:2204.13085. https://arxiv.org/abs/2204.13085

Lister, M. L., Homan, D. C., Hovatta, T., et al. 2019, ApJ, 874, 43

Liu, R.-Y., Rieger, F. M., & Aharonian, F. A. 2017, The Astrophysical Journal, 842, 39

Liu, Y.-H., Guo, F., Daughton, W., Li, H., & Hesse, M. 2015, Phys. Rev. Lett., 114, 095002

Lusso, E., Comastri, A., Simmons, B. D., et al. 2012, MNRAS, 425, 623

Lyubarsky, Y., & Kirk, J. G. 2001, The Astrophysical Journal, 547, 437

Lyubarsky, Y. E. 2005, Monthly Notices of the Royal Astronomical Society, 358, 113

Lyutikov, M. 2003, Monthly Notices of the Royal Astronomical Society, 346, 540

Lyutikov, M., & Uzdensky, D. 2003, The Astrophysical Journal, 589, 893

Majaess, D. 2010, Acta Astronomica, 60, 121. https://arxiv.org/abs/1006.2458

Malakit, K., Shay, M. A., Cassak, P. A., & Bard, C. 2010, Journal of Geophysical Research (Space Physics), 115, A10223

Malkov, M. A., & O'C. Drury, L. 2001, Rep. Prog. Phys., 64, 429

Martini, P., & Weinberg, D. H. 2001, ApJ, 547, 12

Matthews, J., & Telescope Array Collaboration. 2017, in International Cosmic Ray Conference, Vol. 301, 35th International Cosmic Ray Conference (ICRC2017), 1096

Matthews, J. H., Bell, A. R., Blundell, K. M., & Araudo, A. T. 2019, MNRAS, 482, 4303

Maurin, D. 2011, in Cosmic Rays for Particle and Astroparticle Physics, ed. S. Giani, C. Leroy, & P. G. Rancoita, 420–434

Mbarek, R., & Caprioli, D. 2019, ApJ, 886, 8

Mbarek, R., & Caprioli, D. 2021, ApJ, 921, 85

Mbarek, R., Haggerty, C., Sironi, L., Shay, M., & Caprioli, D. 2022, Phys. Rev. Lett., 128, 145101

McKinney, J. C., & Uzdensky, D. A. 2011, Monthly Notices of the Royal Astronomical Society, 419, 573

Meneguzzi, M., Audouze, J., & Reeves, H. 1971, A&A, 15, 337

Merten, L., Boughelilba, M., Reimer, A., et al. 2021, Astroparticle Physics, 128, 102564

Mignone, A., Bodo, G., Massaglia, S., et al. 2007, ApJS, 170, 228

Mignone, A., Rossi, P., Bodo, G., Ferrari, A., & Massaglia, S. 2010, MNRAS, 402, 7

Mignone, A., Zanni, C., Tzeferacos, P., et al. 2012, ApJS, 198, 7

Mingo, B., Croston, J. H., Hardcastle, M. J., et al. 2019, Monthly Notices of the Royal Astronomical Society, 488, 2701

Miralda-Escudé, J., & Waxman, E. 1996, The Astrophysical Journal, 462

Mistry, R., Eastwood, J. P., Phan, T. D., & Hietala, H. 2017, Journal of Geophysical Research (Space Physics), 122, 5895

Morlino, G., & Caprioli, D. 2012, A&A, 538, A81

Mullin, L. M., & Hardcastle, M. J. 2009, MNRAS, 398, 1989

Murase, K., & Beacom, J. F. 2010, Phys. Rev. D, 81, 123001

Murase, K., Dermer, C. D., Takami, H., & Migliori, G. 2012, ApJ, 749, 63

Murase, K., Inoue, Y., & Dermer, C. D. 2014, Phys. Rev. D, 90, 023007

Murase, K., Ioka, K., Nagataki, S., & Nakamura, T. 2008, Phys. Rev. D, 78, 023005

Myrheim, J., & Bugge, L. 1979, Nuclear Instruments and Methods, 160, 43

Neronov, A., & Vovk, I. 2010, Science, 328, 73

Ng, C. S., Bhattacharjee, A., Munsi, D., Isenberg, P. A., & Smith, C. W. 2010, Journal of Geophysical Research (Space Physics), 115, A02101

Øieroset, M., Phan, T. D., & Fujimoto, M. 2004, Geophys. Res. Lett., 31, L12801

Olinto, A. V., Adams, J. H., Aloisio, R., et al. 2017, PoS, ICRC2017, 542

Ostrowski, M. 1998, A&A, 335, 134

—. 2000, MNRAS, 312, 579

O'Sullivan, S., Reville, B., & Taylor, A. M. 2009, MNRAS, 400, 248

O'Sullivan, S. P., & Gabuzda, D. C. 2009, MNRAS, 400, 26

Pacini, D. 1912, Il Nuovo Cimento, 3, 93

Parfrey, K., Philippov, A., & Cerutti, B. 2019, Phys. Rev. Lett., 122, 035101

Parker, E. N. 1965, Planet. Space Sci., 13, 9

Particle-Data-Group, Zyla, P. A., Barnett, R. M., et al. 2020, Progress of Theoretical and Experimental Physics, 2020

Paschmann, G., Øieroset, M., & Phan, T. 2013, Space Sci. Rev., 178, 385

Phan, T., Drake, J., Shay, M., et al. 2014, Geophysical Research Letters, 41, 7002

Phan, T. D., Shay, M. A., Gosling, J. T., et al. 2013, Geophys. Res. Lett., 40, 4475

Pierog, T. 2013, Journal of Physics Conference Series, 409, 012008

Planck Collaboration, Ade, P. A. R., Aghanim, N., et al. 2016, A&A, 594, A19

Plotnikov, I., Pelletier, G., & Lemoine, M. 2011, A&A, 532, A68

Pshirkov, M. S., Tinyakov, P. G., & Urban, F. R. 2016, PhRvL, 116, 191302

Ptuskin, V. 2012, Astroparticle Physics, 39-40, 44

Ptuskin, V., Zirakashvili, V., & Seo, E.-S. 2010, ApJ, 718, 31

Ptuskin, V. S. 1988, Soviet Astronomy Letters, 14, 255

Ptuskin, V. S., & Soutoul, A. 1998, A&A, 337, 859

Putze, A., Derome, L., Maurin, D., Perotto, L., & Taillet, R. 2009, A&A, 497, 991

Ripperda, B., Bacchini, F., & Philippov, A. A. 2020, ApJ, 900, 100

Rodrigues, X., Heinze, J., Palladino, A., van Vliet, A., & Winter, W. 2021, Phys. Rev. Lett., 126, 191101

Romero-Wolf, A., & Ave, M. 2018, Journal of Cosmology and Astroparticle Physics, 2018, 025

Rossi, P., Mignone, A., Bodo, G., Massaglia, S., & Ferrari, A. 2008, A&A, 488, 795

Rowan, M. E., Sironi, L., & Narayan, R. 2017, ApJ, 850, 29

Ryu, D., Kang, H., Cho, J., & Das, S. 2008, Science, 320, 909

Ryu, D., Schleicher, D. R. G., Treumann, R. A., Tsagas, C. G., & Widrow, L. M. 2012, Space Sci. Rev., 166, 1

Sambruna, R. M., Maraschi, L., Tavecchio, F., et al. 2002a, ApJ, 571, 206

—. 2002b, ApJ, 571, 206

Schlickeiser, R. 2002, Cosmic Ray Astrophysics (Springer)

Schmidt, T. M., Worseck, G., Hennawi, J. F., Prochaska, J. X., & Crighton, N. H. M. 2017, The Astrophysical Journal, 847, 81

Shabala, S. S., Ash, S., Alexander, P., & Riley, J. M. 2008, MNRAS, 388, 625

Shabala, S. S., Jurlin, N., Morganti, R., et al. 2020, MNRAS, 496, 1706

Shay, M. A., Phan, T. D., Haggerty, C. C., et al. 2016, Geophysical Research Letters, 43, 4145

Shay, M. A., Haggerty, C. C., Phan, T. D., et al. 2014, Physics of Plasmas, 21, 122902

Shen, Y., Strauss, M. A., Ross, N. P., et al. 2009, ApJ, 697, 1656

Shikaze, Y., Haino, S., Abe, K., et al. 2007, Astroparticle Physics, 28, 154

Siemiginowska, A., Bechtold, J., Aldcroft, T. L., et al. 2002a, ApJ, 570, 543

—. 2002b, ApJ, 570, 543

Simon, M. 1999, International Cosmic Ray Conference, 4, 211

Simpson, J. A., & Garcia-Munoz, M. 1988, Space Sci. Rev., 46, 205

Sironi, L., Giannios, D., & Petropoulou, M. 2016, MNRAS, 462, 48

Sironi, L., Petropoulou, M., & Giannios, D. 2015, MNRAS, 450, 183

Sironi, L., Rowan, M. E., & Narayan, R. 2021, ApJL, 907, L44

Sironi, L., & Spitkovsky, A. 2011a, ApJ, 726, 75

—. 2011b, ApJ, 741, 39

—. 2014, ApJL, 783, L21

Sironi, L., Spitkovsky, A., & Arons, J. 2013, ApJ, 771, 54

Skilling, J. 1975, MNRAS, 172, 557

Slane, P., Lee, S.-H., Ellison, D. C., et al. 2014, ApJ, 783, 33

Spitkovsky, A. 2005, in American Institute of Physics Conference Series, Vol. 801, Astrophysical Sources of High Energy Particles and Radiation, ed. T. Bulik, B. Rudak, & G. Madejski, 345–350

Stawarz, Ł., & Ostrowski, M. 2002, ApJ, 578, 763

Stawarz, Ł., & Petrosian, V. 2008, ApJ, 681, 1725

Stecker, F. W. 1968, Phys. Rev. Lett., 21, 1016

Stecker, F. W., Baring, M. G., & Summerlin, E. J. 2007, ApJ, 667, L29

Strong, A. W., & Moskalenko, I. V. 1998, The Astrophysical Journal, 509, 212

Strong, A. W., Moskalenko, I. V., & Ptuskin, V. S. 2007, Annual Review of Nuclear and Particle Science, 57, 285

Sturrock, P. A. 1971, ApJ, 164, 529

Swisdak, M., Rogers, B. N., Drake, J. F., & Shay, M. A. 2003, Journal of Geophysical Research (Space Physics), 108, 1218

Swordy, S. P., Mueller, D., Meyer, P., L'Heureux, J., & Grunsfeld, J. M. 1990, ApJ, 349, 625

Tadhunter, C. 2016, A&A Rv, 24, 10

Takahashi, H. R., Kudoh, T., Masada, Y., & Matsumoto, J. 2011, The Astrophysical Journal, 739, L53

Takami, H., Inoue, S., & Yamamoto, T. 2012, Astroparticle Physics, 35, 767

Takami, H., & Murase, K. 2012, The Astrophysical Journal, 748, 9

Tanabashi, M., Hagiwara, K., Hikasa, K., et al. 2018, Phys. Rev. D, 98, 030001

Tanada, K., Kataoka, J., & Inoue, Y. 2019, ApJ, 878, 139

Tavecchio, F. 2021, MNRAS, 501, 6199

Tavecchio, F., Ghisellini, G., Bonnoli, G., & Foschini, L. 2011, Monthly Notices of the Royal Astronomical Society, 414, 3566

Tavecchio, F., Ghisellini, G., Foschini, L., et al. 2010, Monthly Notices of the Royal Astronomical Society: Letters, 406, L70

Tavecchio, F., Ghisellini, G., Ghirlanda, G., Foschini, L., & Maraschi, L. 2010, MNRAS, 401, 1570

Tavecchio, F., Maraschi, L., Sambruna, R. M., et al. 2004, ApJ, 614, 64

Taylor, A. M. 2014, Astroparticle Physics, 54, 48

Taylor, A. M., Ahlers, M., & Hooper, D. 2015, PhRvD, 92, 063011

Taylor, A. M., Vovk, I., & Neronov, A. 2011, A&A, 529, A144

Tchekhovskoy, A., & Bromberg, O. 2016a, MNRAS, 461, L46

—. 2016b, MNRAS, 461, L46

Tomassetti, N. 2012, Astrophysics and Space Science, 342, 131

Torresi, E., Grandi, P., Capetti, A., Baldi, R. D., & Giovannini, G. 2018, MNRAS, 476, 5535

Trainor, R., & Steidel, C. C. 2013, The Astrophysical Journal, 775, L3

Treumann, R., Baumjohann, W., & Narita, Y. 2015, Frontiers in Physics, 3, 22

Turatto, M., Cappellaro, E., & Benetti, S. 1994, AJ, 108, 202

Ueda, Y., Akiyama, M., Ohta, K., & Miyaji, T. 2003, ApJ, 598, 886

Unger, M., & Farrar, G. R. 2017, in International Cosmic Ray Conference, Vol. 301, 35th International Cosmic Ray Conference (ICRC2017), 558. https://arxiv.org/abs/1707.02339

Unger, M., Farrar, G. R., & Anchordoqui, L. A. 2015, ArXiv e-prints. https://arxiv.org/abs/1505.02153

Vallée, J. P. 2002, AJ, 124, 1322

Vallée, J. P. 2011, New Astronomy Reviews, 55, 91

van Vliet, A., Palladino, A., Taylor, A., & Winter, W. 2021, arXiv e-prints, arXiv:2104.05732. https://arxiv.org/abs/2104.05732

Vay, J.-L. 2008, Physics of Plasmas, 15, 056701

Vazza, F., Brunetti, G., Brüggen, M., & Bonafede, A. 2017, Monthly Notices of the Royal Astronomical Society, 474, 1672

Verzi, V. 2019, in International Cosmic Ray Conference, Vol. 36, 36th International Cosmic Ray Conference (ICRC2019), 450

Vietri, M. 1995, ApJ, 453, 883

Vovk, I., Taylor, A. M., Semikoz, D., & Neronov, A. 2012, The Astrophysical Journal, 747, L14

Walg, S., Achterberg, A., Markoff, S., Keppens, R., & Meliani, Z. 2013, MNRAS, 433, 1453

Wang, X.-Y., Razzaque, S., & Mészáros, P. 2008, The Astrophysical Journal, 677, 432

Wardle, J. F. C., & Aaron, S. E. 1997, MNRAS, 286, 425

Wardle, J. F. C., Homan, D. C., Ojha, R., & Roberts, D. H. 1998, Nature, 395, 457

Waxman, E. 1995, Physical Review Letters, 75, 386

Waxman, E., & Miralda-Escude, J. 1996, ApJL, 472, L89

Webber, W. 1997, Advances in Space Research, 19, 755

Webber, W. R. 2000, in American Institute of Physics Conference Series, Vol. 528, Acceleration and Transport of Energetic Particles Observed in the Heliosphere, 410–412

Werner, G. R., Uzdensky, D. A., Cerutti, B., Nalewajko, K., & Begelman, M. C. 2016, ApJL, 816, L8

Wittkowski, D., & Kampert, K.-H. 2019, MNRAS: Letters, 488, L119

Woo, J.-H., & Urry, C. M. 2002, ApJ, 579, 530

Wykes, S., Croston, J. H., Hardcastle, M. J., et al. 2013, A&A, 558, A19

Yamada, M., Yoo, J., Jara-Almonte, J., et al. 2015, Physics of Plasmas, 22, 056501

Yanasak, N. E., Wiedenbeck, M. E., Mewaldt, R. A., et al. 2001, ApJ, 563, 768

Yushkov, A. 2019, PoS, ICRC2019, 482

Zatsepin, G. T., & Kuz'min, V. A. 1966, Soviet Journal of Experimental and Theoretical Physics Letters, 4, 78

Zenitani, S., & Hesse, M. 2008, The Astrophysical Journal, 684, 1477

Zenitani, S., & Hoshino, M. 2001, ApJL, 562, L63

—. 2005, ApJL, 618, L111

—. 2007, ApJ, 670, 702

Zhang, B., & Yan, H. 2011, ApJ, 726, 90

Zhang, B., Zhao, X., & Cao, Z. 2014, IJAA, 4, 499